



**Università  
degli Studi  
di Ferrara**

**DOCTORAL COURSE IN  
PHYSICS**

CYCLE XXXIII

COORDINATOR Prof. ssa Eleonora Luppi

# Probing the Equation of State of Neutron Stars through astrophysical observations

Scientific/Disciplinary Sector (SDS) FIS/02

**Candidate**

Dott. Traversi Silvia

**Supervisor**

Prof. Drago Alessandro

---

Year 2017/2020



University of Ferrara

Department of Physics and Earth Science

**Ph.D. in Physics**

Probing the Equation of State of Neutron Stars  
through astrophysical observations

**Supervisor:**  
**ALESSANDRO DRAGO**

**Candidate:**  
**SILVIA TRAVERSI**

---

Years 2017-2020 - XXXIII Cycle  
Coord. Prof. Eleonora Luppi

---

# *Abstract*

One of the most exiting theoretical and experimental challenges is the understanding of the Equation of State of Neutron Stars. The proliferation of data from astrophysical observations in the last years has brought new developments to the study of the Equation of State, providing increasingly stringent limits.

This thesis contains a collection of works aimed to translate these data into constraints on the Equation of State, through a comparison between the experimental evidence and the prediction of different employed models. To fulfill these task, several methods, such as simulations, Bayesian inferences and machine learning approaches, have been exploited.

---

# *Sommario*

Una delle sfide più stimolanti sia da un punto di vista teorico che sperimentale è la comprensione dell'Equazione di Stato delle Stelle di Neutroni. La proliferazione di dati da osservazioni astrofisiche negli ultimi anni ha dato nuova linfa allo studio dell'Equazione di Stato, fornendo dei limiti sempre più stringenti.

Questa Tesi contiene una collezione di lavori il cui obiettivo è di tradurre questi dati in vincoli riguardanti l'Equazione di Stato, attraverso la comparazione tra le evidenze sperimentali e le previsioni dei diversi modelli adottati. A questo scopo sono stati utilizzati vari metodi come simulazioni, inferenza Bayesiana e machine learning.

---

# Contents

<b>Introduction</b>	<b>1</b>
<b>1 Neutron stars and equations of state: the basics</b>	<b>5</b>
1.1 The structure of neutron stars and the problem of the equation of state at high density . . . . .	5
1.2 General features of the Equation of State . . . . .	8
1.3 Types of Equations of State . . . . .	10
1.4 TOV equations and M-R sequence . . . . .	12
1.5 General constraints . . . . .	15
1.5.1 Compactness . . . . .	15
1.5.2 Spin rate . . . . .	16
1.5.3 Maximum mass . . . . .	17
<b>2 Laboratory and astrophysical measurements</b>	<b>19</b>
2.1 Saturation properties . . . . .	19
2.2 Laboratory experiments . . . . .	22
2.2.1 Nuclear masses . . . . .	22
2.2.2 Nuclear Resonances . . . . .	22
2.2.3 Neutron skin thickness . . . . .	23
2.2.4 Heavy ions collisions . . . . .	25
2.3 Astrophysical constraints . . . . .	27
2.3.1 Mass measurements . . . . .	27
2.3.2 Radii measurements . . . . .	30
<b>3 The Equations of State</b>	<b>40</b>
3.1 Relativistic mean field model . . . . .	40
3.1.1 The $\sigma$ - $\omega$ model . . . . .	41

---

3.1.2	Extensions of the model . . . . .	43
3.1.3	SFHo . . . . .	46
3.2	The hyperon puzzle and its possible solutions . . . . .	49
3.2.1	Hyperons in RMFT . . . . .	50
3.2.2	The hyperon puzzle . . . . .	52
3.2.3	The small radii problem . . . . .	55
3.2.4	The MIT bag model . . . . .	56
3.2.5	Hybrid stars (HyS) . . . . .	60
3.2.6	Strange quark stars (QsS) . . . . .	64
3.3	The two families scenario . . . . .	66
3.3.1	The hadronic and the quark EOSs . . . . .	67
3.3.2	The mass radius relation for the two families . . . . .	70
3.3.3	QsS formation and astrophysical implications . . . . .	72
<b>4</b>	<b>Binary neutron star mergers</b>	<b>75</b>
4.1	The main observables . . . . .	75
4.2	The Merger of Two Compact Stars: A Tool for Dense Matter Nuclear Physics	78
4.2.1	Introduction . . . . .	78
4.2.2	State of the art before 17 August 2017 . . . . .	79
4.2.3	GW170817-GRB170817A-AT2017gfo . . . . .	85
4.2.4	A different hypothesis: a hadronic star - quark star merger . . . . .	89
4.3	from $\tilde{\Lambda}$ to radii constraints . . . . .	90
4.4	GW190425 . . . . .	91
<b>5</b>	<b>Merger of Compact Stars in the Two-families Scenario</b>	<b>93</b>
5.1	Introduction . . . . .	93
5.2	Equations of state of hadronic matter and quark matter . . . . .	95
5.2.1	Transition from hadronic matter to quark matter . . . . .	95
5.2.2	Static and rotating configurations . . . . .	97
5.3	Classification of the mergers . . . . .	99
5.3.1	Quark deconfinement in the merger of compact stars . . . . .	100
5.3.2	Possible outcomes of a merger . . . . .	101
5.4	Numerical simulations of the merger of HS-HS . . . . .	103
5.4.1	Numerical methods . . . . .	104
5.4.2	Initial data: EOS approximation . . . . .	105
5.4.3	GW extraction . . . . .	109
5.4.4	Estimate of the ejected mass and disk mass . . . . .	112
5.4.5	Results of the numerical simulations . . . . .	113
5.4.6	Estimate of the Threshold mass . . . . .	120
5.4.7	Trigger of the phase conversion . . . . .	123

---

5.5	Rates of the mergers from population synthesis analysis . . . . .	125
5.6	GW170817 and its interpretation as a HS-QS merger . . . . .	127
5.7	Discussions and Conclusions . . . . .	129
<b>6</b>	<b>The fate of quark matter: strangelets evaporation</b>	<b>131</b>
6.1	Criticisms to QSs existence . . . . .	132
6.2	Strangelets in cosmological context vs stranglets from the merger . . . . .	134
6.3	QS-QS merger simulations . . . . .	136
6.4	Abstract . . . . .	137
6.5	Formation and evaporation of strangelets during the merger of two compact stars . . . . .	137
6.5.1	Ejection of quark matter . . . . .	138
6.5.2	Fragmentation of quark matter . . . . .	138
6.5.3	Evaporation of strangelets . . . . .	141
6.5.4	Phenomenological implications . . . . .	144
<b>7</b>	<b>Bayesian analysis of RMF models</b>	<b>147</b>
7.1	Bayes theorem and sampling methods . . . . .	147
7.2	Model selection . . . . .	150
7.3	Previous works . . . . .	152
7.4	Extended abstract . . . . .	154
7.5	Bayesian inference of dense matter EOS within RMF models using astrophysical measurements . . . . .	155
7.5.1	Equation of State . . . . .	156
7.5.2	Bayesian Analysis . . . . .	157
7.5.3	Conditions on the priors . . . . .	158
7.5.4	Observational Data . . . . .	160
7.5.5	Simulation Results . . . . .	161
7.5.6	Discussion and conclusions . . . . .	173
7.5.7	Additional material . . . . .	176
<b>8</b>	<b>Neural networks vs Bayesian analysis: a study on quark matter</b>	<b>186</b>
8.1	Introduction to Neural Networks . . . . .	186
8.2	EOS inference through NN: previous works . . . . .	191
8.3	Abstracts . . . . .	193
8.4	Structure of Quark Star: A Comparative Analysis of Bayesian Inference and Neural Network based modelling . . . . .	194
8.4.1	Quark Stars within the two families scenario . . . . .	195
8.4.2	Observational Data: Candidate Quark Stars . . . . .	196
8.4.3	Bayesian Inference . . . . .	198

---

8.4.4	Deep Learning . . . . .	198
8.4.5	Results and discussions . . . . .	200
8.4.6	Summary and Conclusions . . . . .	206
8.5	Speed of sound and quark matter . . . . .	207
8.5.1	What if GW190814 has a $2.6M_{\odot}$ compact star component? . . . . .	209
8.5.2	Summary . . . . .	211
	<b>Conclusions</b>	<b>212</b>
	<b>Appendices</b>	<b>216</b>
	<b>A Numerical relativity and Einstein Toolkit</b>	<b>218</b>
	<b>B Treatment of thermodynamical integrals</b>	<b>228</b>
	<b>C Supplementary material for chapter 6</b>	<b>231</b>
	<b>References</b>	<b>237</b>
	<b>Acknowledgments</b>	<b>281</b>

---

# *Introduction*

The Equation of State (EOS) of Neutron Stars (NS) has been an exiting subject of investigation in the scientific community in the last decades. Because of the high densities reached in their core, NS can be regarded as living laboratories for the study of matter under extreme physical conditions and they allow to access an unexplored region of the QCD phase diagram. On the other hand, the absence of terrestrial experiments able to reproduce the same conditions, makes the determination of the high density EOS an incredibly challenging task. As a consequence, the degrees of freedom in the NS interior and the interactions among them are, at the present, still affected by large uncertainties.

The most discussed topics concern the internal composition and the state of matter characterizing the core of a NS: many models suggest the appearance of new particles, such as hyperons or  $\Delta$  resonances, or Bose condensate of pions or kaons. On the other side, there are theories which suggest a phase transition to quark matter in the most massive NS which therefore becomes hybrid stars, or even the possibility of an absolutely stable quark matter that would imply the existence of Quark Stars (QSs).

In the recent years, the increasing numbers and the precision improvements of the astrophysical observations have opened a new cycle in the research fields connected with the investigation of the EOS. First of all, the measurements of the mass of NS of  $\sim 2M_{\odot}$  have tighten the lower limit on the maximum mass allowing to rule out many EOSs. Moreover, significant progresses have been achieved in the simultaneous measurements of mass and radius both of low mass X-ray binaries in the quiescent phase (qLMXBs) and of thermonuclear bursters (TBs). At the same time, the Neutron Star Interior Composition Explorer (NICER), installed on the International Space Station in 2017, determined an important step forward in the application of pulse profile modelling to rotation-powered millisecond pulsars (MSPs). Finally, a completely new era opened in 2017 with the first observation of a binary NS (BNS) merger: the contemporary detection of a signal in gravitational waves (GWs) (GW170817),  $\gamma$ -rays (GRB170817A) and optical (AT2017gfo) has marked the beginning of the so called "multimessenger astronomy".

---

The EOS can be constrained by different observables, estimated both through laboratory measurements near to the saturation point and also from astrophysical observations. In this regard, chapters 1-4 provide the necessary background for the original works presented later in this thesis. They are organized as follow:

- chapter 1 gives a basic introduction on NS and on the EOS and the general constraints concerning the NS observables;
- chapter 2 contains a summary of the available data from both laboratory experiments and astrophysical observations which can constrain the EOS. This data have been exploited in the EOS inference analyses presented in 7 and 8.
- chapter 3 explores the EOS models employed in our studies with a particular focus on the "hyperons puzzle" and its possible solutions.
- chapter 4 provides a list of the most important observables connected with a BNS merger and the specific constraints obtained from the two events GW170817 and GW190425. These constraints will be used, directly or indirectly, in all my Ph.D. works.

Once the EOS is specified, the equations of stellar structure can be solved and they give a mass-radius (M-R) relation that is uniquely linked to the input EOS. Lindblom (1992) developed a method to invert these equations, thus in principle a way to solve the so called inverse stellar problem: given a series of astrophysical measurements of masses and radii, they can be mapped to the EOS. However, this formal inversion needs data spanning over the entire M-R curve, meaning for NS masses in the range between  $\sim 0.2M_{\odot}$  and  $2M_{\odot}$ . Even the subsequent improvements of this approach (see Lindblom (2015)) would require extremely precise measurements. This condition makes the method of Lindblom (1992, 2015) not suitable to be applied to the "real world" EOS problem.

As a consequence, one has to adopt more indirect approaches to infer the EOS starting from astrophysical observations. In this context, at least four different methods can be used, each one of them involving a comparison between a theoretical model and its results with the measurements. Each of the original works presented in this thesis in chapters 5,6,7,8, is representative of one of these approaches:

- **simulations**

This method is mostly adopted to study hydrodynamic and chemical phenomenon taking place in an astrophysical context. Examples are the merger of BNS and the possible consequent nucleosynthesis chain leading to the formation of heavy elements, but also the birth of a NS through the explosive episode of core-collapse supernova (CCSN). The simulations try to reproduce these processes and to give as output an estimate of all the connected observables. The EOS usually enters as initial condition in

---

the simulation and influences in many ways the results: this allows to make predictions or comparisons with the observative evidence that can possibly confirm or rule out that particular model. In chapter 5 the results of a hydrodynamical simulation of BNS merger is presented with the aim to investigate the consequences of assuming two EOS models with different degrees of freedom. One of these is part of the so called "two families scenario": the phenomenological implications of this EOS are investigated and compared with the constraints from GW170817.

- **theoretical calculations**

In the same way as simulations, also theoretical calculations can be used to probe a model through the comparison with the experimental data. Indeed, using as assumptions the conditions typical of some astrophysical framework, one can check if a particular model is able to reproduce the observations. The simplest example among all is the calculation of the M-R curve starting from an EOS to see if it is able to fulfill the maximum mass constraint. Here this approach is used to check if, in the conditions typical of the post-merger phase, an eventual ejecta in the form of quark matter can evaporate back to normal matter (see chapter 6). The consequences, both in terms of the possible detection of strangelets and of an eventual Kilonova signal associated to a GW event, are studied.

- **Bayesian analysis**

This procedure in the context of NS physics has been developed for the first time by [Steiner et al. \(2010\)](#) and it is becoming an increasingly widely used technique for the EOS inference problem. Instead of mapping out the full functional form of the EOS from a complete M-R sequence, it allows to constrain some features of the EOS from a more sparse sampling of masses and radii of an even small number of NS (or other observables, such as tidal deformability).

The approach is based on the estimation of the probability to obtain certain measurements starting from an EOS described by a certain number of parameters. The Bayesian analysis not only provides a probability distribution function (PDF) for the values of the parameters but also allows to compare in a quantitative way among different models. In addition the prior knowledge can also be incorporated in a quite rigorous manner.

In chapter 7, a work is described with the results of a Bayesian analysis of a Relativistic mean Field (RMF) EOS model using astrophysical sources and prior nuclear matter constraints. The aim of this study is mainly to find the most probable values for the saturation properties of nuclear matter and to check if there is a tension between the prior knowledge from nuclear physics and the new astrophysical limits.

- **machine learning**

[Fujimoto et al. \(2018\)](#) introduced a new machine learning technique to infer the EOS

---

from a set of mass-radius data with observational errors. This uses a deep neural network (NN) which is trained with data generated to mimic the real observational sources assuming a model for the EOS. Finally, the NN, when fed with the real measurements, would provide an estimate of best values for the EOS parameters. A comparison of this new technique with the Bayesian analysis is presented in chapter 8, employing a simple EOS for quark matter based on MIT bag model (see chapter 3.2.4 for details). In addition, the squared sound speed of quark matter is treated as a free parameter allowing to explore the validity of the conformal limit in the context of the two family scenario.

# 1

## *Neutron stars and equations of state: the basics*

### *1.1 The structure of neutron stars and the problem of the equation of state at high density*

Neutron stars (NSs) are the most compact objects in the universe without event horizons: their densities ranging from a few  $g\text{ cm}^{-3}$  at the surface to more than  $10^{15}\text{ g cm}^{-3}$  in the interior make them peerless resources for dense matter studies.

With a central pressure that can exceed  $10^{36}\text{ dyn cm}^{-2}$ , NSs are characterized typically by a mass of  $1.4M_{\odot}$  and a radius of about only  $10\text{ km}$ .

The binding force of these exceptionally dense objects is gravity: despite the nuclear is the strongest among forces, it is short-ranged and can affect only its neighbors while the gravitational force is able to act on the entire star. One can easily evaluate the gravitational energy for a typical configuration:

$$E_{grav} \sim \frac{3M^2}{5R} \sim 10^{53}\text{ erg} \sim 10^{59}\text{ MeV} \quad (1.1.1)$$

Considering a rough estimate of the baryon number of a NS,  $A \sim 2.6 \cdot 10^{57}$  (Glendenning, 1997), the above formula results in  $\sim 157\text{ MeV}$  per nucleon. Nevertheless this number does not represent the binding energy of a star: in fact, the energy associated to the Fermi pressure and to the nuclear force must also be considered.

Indeed, the matter of NSs is compressed up to densities above the saturation density of nuclear matter ( $\rho_0$  or  $n_0$ ), reaching a regime in which the nuclear force become repulsive.

To evaluate the binding energy one must compare the gravitational mass ( $M$ ) of a NS with the so called baryon mass  $M_A = Am_n$  equal to the energy associated to the same

number of neutron  $A$  at rest at an infinite distance:

$$\frac{B}{A} = \frac{(M_A - M)}{A} \quad (1.1.2)$$

The repulsive Fermi energy and nuclear compression energy reduce the net binding energy of a NS up to about 100 MeV per nucleon. Therefore, the nuclear force gives a negative contribution to the binding of a NS, but it represent the fundamental ingredient of the equation of state (EOS) which determines its structure and its dynamical properties.

The EOS is a relation between thermodynamic state variables: in particular it is specified by a set of equations which describes the state of matter under the given physical conditions. In NSs, the EOS expresses the dependence of the pressure on the energy density:

$$p = p(e) \quad (1.1.3)$$

or, alternatively, the variation of the pressure with the baryon or mass density ( $p(n)$  or  $p(\rho)$ ). In a more general case, also the temperature plays an important role and thus the EOS becomes:

$$p = p(e, T) \quad (1.1.4)$$

If the object to be studied is a single cold neutron star, the temperature dependence is negligible and the EOS can be calculated at  $T = 0$ . Often the term EOS means also a description of the composition of matter and a choice of a particular microphysical model.

As a matter of fact, within the typical ranges of densities of a NS, the composition and the state of matter changes dramatically. To schematically represent this feature, the structure of a NS is usually divided into the atmosphere and four main regions ([Haensel, 2007](#)): the outer crust, the inner crust, the outer core and the inner core.

- the outer crust is located between the bottom layer of the atmosphere and a density  $\rho = \rho_{ND} = 4 \cdot 10^{11} g cm^{-3}$  with a thickness of few hundreds meters. The matter is composed of a lattice of ordinary nuclei in the iron group immersed in a sea of electrons. The latter give the main contribution to the pressure and constitute a degenerate ideal gas, that becomes ultra-relativistic for  $\rho > 10^6 g cm^{-3}$ . Going to larger density, the neutron chemical potential increases and nuclei become more massive and more neutron-rich.
- the inner crust begins in correspondence with the neutron drip density  $\rho_{ND}$  where the neutron chemical potential is sufficiently high so that it becomes energetically favourable for the neutrons to "leak" out of the neutron-rich nuclei. As a consequence, the matter in this layer is composed of electrons, free neutrons and neutron-rich nuclei

and the fraction of free neutrons increases with the density. Eventually, at the border of the inner crust, the nuclei starts to be deformed, giving birth to the so-called "pasta" phase.

The inner crust extends up to  $\sim 0.5 \rho_0$  where the nuclei disappear and the phase transition to uniform nuclear matter begins.

- the outer core is the part that occupies the density in the range between  $0.5 \rho_0$  and  $2 \rho_0$ . In this layer, the matter is composed of a uniform liquid with a large fraction of neutrons with a few protons, electrons, and eventually muons (for this reason sometimes called  $npe\mu$  matter). Electron and muons form an almost ideal Fermi gas, while neutrons and protons interact by means of nuclear strong force. Therefore the matter is described with a microscopic model of many-body nucleon interactions with the constraints of charge neutrality and  $\beta$  equilibrium (see the following section).
- the inner core extends from  $\rho > 2 \rho_0$  and in the most massive NSs can reach values about  $\sim 7-8 \rho_0$ . The composition of matter in this layer is model dependent and many different scenarios for the state of matter have been suggested. The main hypotheses concern the appearance of hyperons, pion and kaon condensates and finally, eventually, the transition to quark matter.

Concerning the crust, the EOS has been evaluated with sufficient accuracy. Indeed, the calculations can rely on experimental data on atomic nuclei, nucleon scattering, and on the theory of strongly coupled Coulomb systems.

Also in the case of the outer core, the composition of matter is well known: as mentioned, at such densities the only baryons present in the ground state of the matter are nucleons, surrounded by electrons and possibly muons. Here, the nuclear many-body theory allows to calculate the EOS in a rather reliable way.

On the other hand, there are no laboratory experiments which can reproduce the conditions in the NS inner core: this indeed access an uncharted region of the QCD phase diagram characterized by low temperature and high density. As a consequence, the structure and the internal composition in this region remain deeply uncertain. To determine the EOS, first of all, the relevant degrees of freedom have to be identified and then their interactions need to be properly specified. And finally, after fixing the Hamiltonian, one has to find a state which minimize the energy as a function of the baryon density. The complexity of the interaction and the dependence on the choice of the degrees of freedom make this an extraordinarily complex task. Moreover, a unique and precise many-body theory describing nuclear interactions in this regime is still missing. Instead there is a variety of theoretical models whose reliability decreases with growing density.

Regarding the composition of matter, the eventual appearance of new exotic degrees of freedom has been suggested.

First of all, the possibility for mesons to form condensates has been investigated (Glendenning, 1997): the matter would consequently become inhomogeneous and it would contain Bose condensates of pions (Pandharipande et al., 1995; Akmal et al., 1998a; Mukherjee, 2009) or kaons (Kaplan & Nelson, 1986; Brown et al., 1992; Glendenning & Schaffner-Bielich, 1998) arranged in a periodic structures.

In addition, due to the large densities, other particles are predicted to occur, such as nuclear resonances like  $\Delta$  baryon (Drago et al., 2014b) and also strange degrees of freedom in the form of hyperons (Glendenning, 1982b; Schulze et al., 1995; Chatterjee & Vidaña, 2016). Indeed the appearance of such particles, through the strangeness changing weak interaction, becomes at some point energetically favoured because of the Pauli principle. The threshold density is usually thought to be placed in the interval  $(2 - 4) \rho_0$ .

Moreover, many models state that at high densities matter can no longer be described by nucleons and suggest a transition to a deconfined quarks (Alford et al., 2005; Bombaci, 2017a; Kojo et al., 2015). In addition, quark matter could be in a color superconducting phase (Alford et al., 2008) or even form different crystalline structures (Anglani et al., 2014; Buballa & Carignano, 2015; Carignano & Buballa, 2020).

Concerning all the possible phase transitions, the ground state of the matter can be described either by a single phase at a given pressure or by two coexisting phases in thermodynamic equilibrium.

Finally, in Witten (1984) the hypothesis of quark matter being the absolute ground state of matter has been formulated: this implies that a compression of matter and/or an increase of temperature can trigger a phase transition which ultimately would convert the entire star. The newly born strange quark star (QS), in contrast to a normal NS, is self-bound (Farhi, 1986; Haensel et al., 1986).

Therefore many possible types of compact stars can be found in literature: nucleonic, hyperonic, hybrid or even quark stars.

In conclusion, the calculation of the EOS of NS core remains still a mystery and constitutes a formidable intellectual challenge. Despite the constant improvements of nuclear theories, the major hope to make progress will continue to rely on astrophysical observations and models.

## ***1.2 General features of the Equation of State***

The EOS of NS is usually expressed in terms of hydrodynamic variables assuming local thermodynamic equilibrium. This statement implies the validity of a set of equilibrium

conditions which concerns the main intensive thermodynamic variables: the temperature for thermal equilibrium, the pressure for mechanical equilibrium and finally the chemical potential for the chemical equilibrium.

As a consequence, a standard approach is to construct the EOS starting from a thermodynamical potential and derive all the required variables using standard thermodynamic relations: this method assure the thermodynamic consistency to hold.

Examples of frequently adopted thermodynamic potentials are the Helmholtz Free energy  $F(T, (N_i), V)$  or the grand canonical potential  $\Omega(T, (\mu_i), V) = F - \sum_i \mu_i N_i$ : the first one is a function of the temperature  $T$ , of particle numbers  $N_i (i = 1; \dots; N_{part})$  and of the volume  $V$ . The second one instead depends directly on the chemical potential defined as  $\mu_i = \frac{\delta F}{\delta N_i}$ . In the thermodynamic limit the extensive variables can be replaced by the corresponding intensive ones, such as, for example, the particle number density  $n_i = \frac{N_i}{V}$ .

These variables are not all independent, but are linked through the aforementioned equilibrium conditions, in particular the chemical equilibrium. This holds only if the time scales of the possible chemical reactions are much shorter than the time scales of the system's hydrodynamic evolution, like in a cold NS. However the latter represent the ground state reached by the star after an evolution which involves many reactions able to convert particle species  $i$  to different ones. For example, hyperons and kaons can be produced and subsequently decay through the weak interaction: they produce finally leptons but also photons and neutrinos which leave the star. This mechanism can proceed until the loss of energy prevents the possibility of further reactions.

This is finally the equilibrium state which is defined by a number of charges that are the attributes which are conserved on a timescale longer than the lifetime of the star or the epoch of observation.

The most general set of conserved charges includes the baryon, the electric, the lepton, and the strangeness charges.

However, since during the evolution neutrinos have been diffused out, the lepton charge is not conserved and we can set the corresponding chemical potential to zero  $\mu_\nu = 0$ . The same holds for the strangeness charge: being the weak interaction timescale of the order of  $10^{-10}$  s, at the equilibrium strangeness cannot be considered an independent thermodynamic variable.

Therefore the only conserved charges left are the baryon and the electric ones and correspondingly only two independent chemical potentials:  $\mu_n$  for neutrons and  $\mu_e$  for electrons. Using, for example the  $\beta$ -decay  $n \leftrightarrow p + e^- + \bar{\nu}_e$  one can obtain:

$$\mu_p = \mu_n - \mu_e \tag{1.2.1}$$

remembering that the chemical potential of neutrinos is set to zero. When  $\mu_e$  reaches the value of the muon mass, the reaction  $e^- \leftrightarrow \mu^- + \nu_e + \bar{\nu}_\mu$  will populate also the muon sector

and at equilibrium:

$$\mu_\mu = \mu_e \tag{1.2.2}$$

With a similar procedure all the chemical potentials can be inferred. At the end, the chemical potential of all the particles can be written as a linear combination of  $\mu_n$  and  $\mu_e$ :

$$\mu = b\mu_n + q\mu_e \tag{1.2.3}$$

where  $b$  and  $q$  are the particle's baryon and electric charge respectively.

This statement is true also for nuclei in equilibrium (in this case called nuclear statistical equilibrium NSE):

$$\mu_a = (N_a + Z_a)\mu_n + Z_a\mu_e \tag{1.2.4}$$

where  $N_a$  and  $Z_a$  are the numbers of neutrons and protons inside the nucleus  $a$ .

As for muons, any particle type can in principle be populated if there is enough energy and if the reaction is energetically favoured, i.e. if it lowers the energy state of the system. The first requirement is fulfilled if the chemical potential of the involved particle exceeds its rest mass. Moreover, the baryons must satisfy the Pauli principle and thus sharing the conserved baryon numbers among many species of fermions would decrease the energy in the system. Thus the appearance of hyperons or even quarks in the massive NS core is to be expected.

Beside the aforementioned equilibrium conditions, another requirement constrains NS EOS: charge neutrality, written as

$$\sum_i q_i n_i = 0 \tag{1.2.5}$$

This is a local condition, but in the cases of inhomogeneous matter the charge distribution is locally imbalanced, thus charge neutrality holds only on a global scale. The consequence could be the creation of clusters or complex structures such as the "pasta phase" present in the inner crust.

### **1.3 Types of Equations of State**

All the aforementioned conditions and the basic thermodynamic properties of a many-body system need to be properly included in any theoretical model of strongly interacting matter. Fulfilling this task is extremely hard due to multiple reasons: first of all, one has to identify the degrees of freedom which characterize the problem and which depend on the physical conditions under investigation. Indeed, if at low densities and temperatures only nucleons and nuclei are present, one may need to consider hyperons or quarks to describe matter at

high densities or finite temperatures.

Once the degrees of freedom are chosen, one has to specify and properly describe the interactions among them. Since direct QCD calculations are not available or very complex to implement in the realistic astrophysical conditions, the interactions have to be approximated through a model which is hopefully constrained by experiments. Moreover, an extrapolation procedure is required for the phase space regions which cannot be probed by nuclear physics measurements.

A plethora of many-body approaches exists, but they can roughly be divided in two main classes (see [Oertel et al. \(2017\)](#) and [Fiorella Burgio & Fantina \(2018\)](#) for reviews):

- **Ab initio or microscopic many-body methods:** these are based on realistic two- or three-body interactions fitted to the experimental data collected studying both nucleon scattering and bound system with a limited number of nucleons. Among the mostly used techniques one can cite Green's function approaches, (Dirac)-Brueckner-Hartree-Fock, coupled cluster, variational, and Monte-Carlo methods.

Some of the shortcomings of this class of models are their inability to describe large nuclear systems or clustered matter. Moreover, technical issues can limit these approaches like in the case of Monte-Carlo calculations.

- **Phenomenological methods:** these make use of effective interactions which are functions of a certain number of parameters. The values of these parameters are optimized by fitting the available data on nuclei and nuclear matter.

The approaches which are mostly used to calculate EOS for high density matter are the one based on mean fields (MFs). Among these, one can find non-relativistic methods such as the ones based on Skyrme or Gogny forces or relativistic mean field (RMF) calculations. A widely adopted approach is also the so called liquid drop model, where the energy is given by the sum of singular contributions which express global properties of the system. Very similar to RMF models are also the methods used to describe quark matter. The simplest is the "bag model" born originally to model hadrons as finite size quark bound states.

In the works presented in this thesis, EOSs based on RMF theory and bag model have been employed. For this reason, these two approaches will be further explained being the subject of chapter 3 of this thesis.

## 1.4 TOV equations and M-R sequence

The equations which describe the structure of a star are the Tolman- Oppenheimer - Volkoff equations (TOV):

$$\frac{dp}{dr} = - \frac{[e(r) + p(r)][M(r) + 4\pi r^3 p(r)]}{r(r - 2M(r))} \quad (1.4.1)$$

$$dM(r) = 4\pi r^2 e(r) dr \quad (1.4.2)$$

where  $r$  is the radial distance from the center,  $M$  the enclosed mass,  $p$  the pressure and  $e$  the energy density. The first equation represents the balance between the force acting on a shell of matter due to material pressure from within, and the gravitational force from without. The second expresses just the relation between mass and energy density in this shell.

Thus these equations are nothing else than the equations of hydrostatic equilibrium in General Relativity (GR).

In order to close the system of differential equations, one needs to specify the EOS, i.e. the pressure-energy density relation.

Therefore the EOS represents the way in which the properties of dense matter enter the equations of stellar structure.

Once the EOS is settled, the two TOV equations can be integrated from the origin  $r = 0$  with the initial condition  $M(0) = 0$  and a chosen value of the central pressure  $p_c$  or central energy density  $e_c$ . Then the integration stops when the pressure reaches the value  $p = 0$ , corresponding to the stellar surface: the point  $R$ , at which this condition is satisfied, represents the radius of the star and the associated value of  $M$ , its mass.

The energy density at the surface of the NS is equal to zero in the case of an hadronic EOS, while it remains finite for QS containing strange quark matter. At this point the radius  $R$  and the mass  $M = M(R)$  for the chosen central density are known.

Selecting a series of increasing values for the central density results in developing a sequence of stars of increasing mass, parameterized by the central density  $M = M(\rho_c)$ ,  $R = R(\rho_c)$  and therefore also the mass of the star as a function of the radius  $M(R)$  is known.

Some feature of the  $M(R)$  curve are generic and in first approximation, independent from the underlying EOS (at least for hadronic ones). First of all, high-mass hadronic stars are smaller than low-mass stars. Indeed for the latter, the gravitational attraction is weak allowing stars to be large and diffuse. On the other hand, the gravitational attraction felt by high mass stars is strongest forcing the radius to be small at equilibrium. Therefore, defining the compactness parameter  $\frac{M}{R}$  as the ratio between mass and radius of a stellar configuration, one can note that it increases together with the mass and/or the central density.

Figure 1.4.1 shows a representative  $M(R)$  sequence evaluated for schematic hadronic and

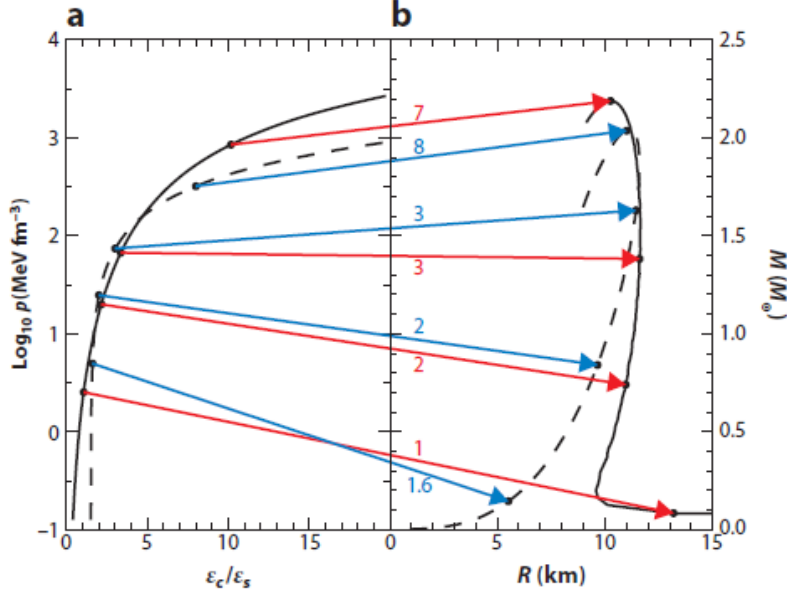


**Figure 1.4.1:** from [Lattimer \(2012\)](#). Example of mass-radius sequences for hadronic stars with a polytropic EOS (solid line) and a QS (dashed line). Republished with permission of Annual Reviews, Inc., permission conveyed through Copyright Clearance Center, Inc..

pure QM EOSs. The hadronic EOS is described through polytropes,  $p = Kn^{\gamma}$ , while for strange quark matter (SQM) the EOS is parametrized with a simple MIT bag model (see chapter 3.2.4 for details).

In first approximation, a polytropic EOS leads to scaling relations between the radius  $R$  and total mass  $M$ :

$$R \propto M^{\frac{\gamma-2}{3\gamma-4}}; \quad M \propto R^{\frac{3\gamma-4}{\gamma-2}}. \quad (1.4.3)$$

At low densities, the polytrope for hadronic matter is characterized by  $\gamma \sim \frac{4}{3}$  which results in  $M \propto R^0$ , meaning that the mass of these configurations is independent from the radius. The opposite happens at higher densities ( $\sim e_0 - 3e_0$ ) where  $\gamma \sim 2$  for the hadronic EOS. Indeed, here the scaling is  $R \sim M^0$ , and therefore the radii remain constant at the increase of the mass.

On the other hand for SQM at low densities  $\gamma \rightarrow \infty$  and so the scaling relation becomes  $R \propto M^{\frac{1}{3}}$ .

Therefore the behavior of the hadronic and SQM stars is very different at low densities but, on the contrary, one can note from figure 1.4.1 that both the EOS result in a very similar curve for masses  $1.5 < \frac{M}{M_{\odot}} < 2$ .

All the M(R) configurations which are solutions of the TOV equations are in hydrostatic equilibrium. However, the equilibrium can be realized either in a minimum or in a maximum of the energy, meaning that not all the stars of the sequence are necessarily stable.

This sequence presents at least two branches of stable configurations: white dwarfs and NS and eventually a third branch of hybrid stars (see for example [Alford & Han \(2014\)](#); [Benic et al. \(2015\)](#); [Burgio & Zappalà \(2016\)](#)).

In the instability region between white dwarfs and NS, radial oscillations destroy the configurations by dispersal or cause their collapse to NS. On the other hand, above the stable NS or hybrid star sequence, no forces exist able to counteract the gravity: the density at the center become so high that the central region is inside the Schwarzschild radius and the star collapse to a black hole (BH).

Therefore NS have a minimum and a maximum mass: those are the boundaries between stability and instability and are characterized by the condition:

$$\frac{\delta M(e_c)}{\delta e_c} = 0 \tag{1.4.4}$$

In between the minimum and the maximum mass, there is the sequence of stable stars satisfying:

$$\frac{\delta M(e_c)}{\delta e_c} > 0 \tag{1.4.5}$$

Indeed, if a star on the stable branch is compressed, this condition assures that the new equilibrium mass would be larger. Therefore the squeezed star present a deficit in mass, i.e. the gravitational force can not contrast the increased central pressure working to decompress the star to return in the original configuration. If, on the other hand, the central density decreases then the surplus of gravitational force will again restore the initial state. On the contrary, if the condition [1.4.5](#) is not fulfilled either gravity or matter pressure would move away the perturbed star from the equilibrium configuration. Therefore [1.4.5](#) is a necessary condition for stability which leads to the existence of a maximum mass, regardless of the features of matter, but the specific value of this mass is strongly dependent on the EOS.

Usually the EOSs are categorized on the basis of their compressibility, i.e. the easiness to change their volume as a result of pressure. An EOS is defined as "soft" and as "stiff" if the compressibility is high and low respectively. A stiffer EOS has a higher pressure for a given energy density and can therefore sustain configurations with a larger mass. As a consequence, the maximum mass for a soft EOS is always smaller than the one for a stiff EOS.

In conclusion, the TOV equations provide a one-parameter family of stellar models which are uniquely linked to the input EOS. Moreover the nature of the strong force between constituent particles and the composition determine the stiffness of NS matter.

This opens the possibility to put constraints on the EOS and on the properties of ultradense matter by mapping out the M-R relation observationally.

## 1.5 General constraints

### 1.5.1 Compactness

As discussed in the previous section, in principle the TOV equations should be integrated using a realistic EOS. However it is possible to infer interesting limits on many NS observables considering just the properties of the equation itself or using simplified and extreme EOSs to describe NS matter.

First of all, the limit for any static star which satisfies the TOV equations, allows to set a constraint on the compactness:

$$\frac{2M}{R} < \frac{8}{9} \quad (1.5.1)$$

which is completely independent of the EOS (Weinberg, 1972).

The same result was obtained by Schwarzschild in the unphysical approximation of an incompressible star of uniform density. The corresponding radius and mass for this model are:

$$M_{lim} = \frac{4}{9} R_{lim} \quad (1.5.2)$$

implying  $R > 2.25M$ .

It is interesting to underline that the existence of a limit on the compactness for a stable configuration depends directly on the nature of GR and it is not found in the Newtonian theory.

More strict results are obtained adding general conditions on NS matter.

For example, assuming  $p < e$ :

$$\frac{2M}{R} < \frac{3}{4}; \quad R > 2.66M \quad (1.5.3)$$

Moreover, if the EOS satisfies the constraints  $e > 0$ ,  $p > 0$ , and  $\frac{dp}{de} < 1$  a similar limit on the radius  $R > 2.56M$  is obtained (Bondi, 1964). A further possibility has been exploited by Koranda et al. (1997) who considered the maximally stiff EOS at high density, and the maximally soft EOS at low density: this, indeed, can sustain the largest mass with the smallest radius. The EOS can be written as:

$$p = 0 \text{ for } e < e_f; \quad p = e - e_f \text{ for } e > e_f \quad (1.5.4)$$

where  $e_f$  is the surface energy density and the limit on the stiff high density EOS is imposed by causality. The integration of the TOV equations gives for the maximally compact solution:

$$R \geq 2.824M \quad (1.5.5)$$

The constraints on the compactness can also be expressed in terms of redshift:

$$z = \frac{1}{\sqrt{1 - \frac{2M}{R}}} \leq 0.8512 \quad (1.5.6)$$

This result is very similar to the one obtained by Lindblom (1984),  $z \leq 0.863$  and consequently  $R \geq 2.83M$ .

### 1.5.2 Spin rate

In connection with the constraints on compactness, one can calculate the limit on the spin rate of a NS which is the so called Keplerian frequency. This is the frequency at which the matter at the equatorial surface is shed, i.e. its velocity is equivalent to the orbital velocity above that surface.

In the Newtonian approximation, the Kepler limit on the rotational period is calculated as:

$$P_{min}^N = 2\pi \sqrt{\frac{R^3}{M}} = 0.545 \left(\frac{M_\odot}{M}\right)^{\frac{1}{2}} \left(\frac{R}{10km}\right)^{\frac{3}{2}} \quad (1.5.7)$$

This result is similar to one obtained for the maximum mass NS considering full GR (Haensel & Zdunik, 1989; Friedman et al., 1986; Lattimer et al., 1990):

$$P_{min} = k \left(\frac{M_\odot}{M_{max}}\right)^{\frac{1}{2}} \left(\frac{R_{max}}{10km}\right)^{\frac{3}{2}} \quad (1.5.8)$$

where  $k$  has been estimated using the compact EOS of equation 1.5.4 as 0.74, with a realistic hadronic EOS as 0.83 (Lattimer & Prakash, 2007) and finally phenomenologically as 0.96 in Lattimer & Prakash (2004).

Here the authors also found a relation which apply to any NS mass not to close to the maximum:

$$P_{min} \simeq (0.96 \pm 0.03) \left(\frac{M_\odot}{M}\right)^{\frac{1}{2}} \left(\frac{R}{10km}\right)^{\frac{3}{2}} \quad (1.5.9)$$

which could be useful to constrain masses and radii from the measurements of the rotation period.

### 1.5.3 Maximum mass

The first attempt to study the structure of a NS and to investigate its maximum mass has been done by [Oppenheimer & Volkoff \(1939\)](#): they assumed that NS matter is composed only by non-interacting relativistic neutrons and they obtained a maximum mass of only  $0.72M_{\odot}$ . Although their picture of NS EOS is fairly too simplified, their result remains worth mentioning: indeed the contribution of interactions, in particular the repulsive nuclear forces in the core, can just provide an additional positive contribution to the pressure. In this respect the value estimated in [Oppenheimer & Volkoff \(1939\)](#) can be regarded as the theoretical lower bound for the maximum mass of NS.

On the other hand, [Rhoades & Ruffini \(1974\)](#) tried to estimate an upper bound for the maximum mass. The EOS they used is based on a few simple assumptions. First of all the validity of the so called Le Chatelier's principle, i.e.  $\frac{dp}{de} \geq 0$ ; secondly the causality constraint  $\sqrt{\frac{dp}{de}} < 1$  must be fulfilled: the stiffest equation of state that is compatible with this condition has a speed of sound equal to the light speed in vacuum. Finally, the high density EOS needs to match in a continuous way with a low density EOS. Since in the maximum mass configuration the energy falls to zero very rapidly near the surface, the choice of the low density EOS is almost irrelevant.

Finally the EOS looks like:

$$p(e) = p_{BPS}, \quad e \leq e_f ; \quad p(e) = e - e_f + p_f, \quad e \geq e_f \quad (1.5.10)$$

where  $e_f$  is the matching energy density and  $p_f$  is the corresponding pressure.

With a chosen value of  $e_f = 4.636 \cdot 10^{14} \text{ g cm}^{-3}$  (corresponding to a density  $\sim 2n_0$ ), the numerical integration of the TOV results in:

$$M = 3.14M_{\odot} \quad (1.5.11)$$

Since adding other constraints to obtain a more realistic equation of state would just lower the bound, this value can be considered a safe upper limit on the NS maximum mass.

Subsequently, [Hartle & Sabbadini \(1977\)](#) demonstrated the existence of a scaling relation for this limit with  $e_f$  in the form:

$$M_{max} = 4.2 \sqrt{\frac{e_f}{e_0}} M_{\odot} \quad (1.5.12)$$

As already discussed, the limiting mass of a sequence of stars depends on the stiffness or softness of the EOS. Therefore for a realistic model which takes nuclear forces into account is expected to have the maximum mass to lie between these extreme cases.

In conclusion, all these calculations represent a brief summary of some of the most important theoretical limits and they were the first steps to gain some knowledge on the structure of NS. Obviously the window of allowed values for the NS observables is consistently being narrowed by measurements, in particular astrophysical observations. This will be the subject of the next chapter.

# 2

## *Laboratory and astrophysical measurements*

The EOS of NS matter can be constrained by different observables, which can be estimated through laboratory measurements of nuclear properties and reactions and also from astrophysical observations.

These experiments investigate different parts of the space of thermodynamic variables and of the phase diagram and allow to test various aspects of an EOS model (Klahn et al., 2006; Lattimer & Prakash, 2007; Lattimer & Lim, 2013; Tsang et al., 2012; Oertel et al., 2017; Özel & Freire, 2016).

### *2.1 Saturation properties*

It is well known that the total mass of a nucleus can be written approximately with the "semiempirical mass formula" as

$$M(A, Y_p) = A \left[ \frac{4}{3} \pi r_0^3 e_0 + S(1 - 2Y_p)^2 \right] + 4\pi r_0^2 A^{\frac{2}{3}} e_{surf} + a_{Coul} \frac{Z^2}{A^{\frac{1}{3}}} \quad (2.1.1)$$

where  $A$  is the number of nucleons and  $Y_p$  is the proton fraction  $\frac{Z}{A}$ .  $r_0$  is a constant appearing in the expression for nuclear radius  $R = r_0 A^{\frac{1}{3}}$ . The first term is the volume contribution, while the second arises from the variation of the energy connected with asymmetric matter (in which densities of protons and neutrons are different). The last two are respectively the surface and Coulomb energy.

The so called nuclear matter approximation is obtained by neglecting the Coulomb contribution and by assuming symmetric matter  $Y_p = \frac{1}{2}$ . In this way, by subtracting  $Am_N$ , the

total binding energy is obtained and in the limit for  $A \rightarrow \infty$  just the volume term survives. Thus the value of the binding energy for infinite, symmetric, nuclear matter is (Glendenning (1997)):

$$B_{sat} \simeq -16.3 \text{ MeV} \quad (2.1.2)$$

The corresponding value of particle density at equilibrium, the saturation density, is formally defined as:

$$n_0 = \left[ \left( \frac{4\pi}{3} \right) r_0^3 \right]^{-1} \simeq 0.15 \text{ fm}^{-3} \quad (2.1.3)$$

that corresponds to a Fermi momentum of:

$$k_F \simeq 1.3 \text{ fm}^{-1} \quad (2.1.4)$$

Given an EOS  $e(n)$ , the relation between the equilibrium energy density  $e_0$  and the binding energy is:

$$B_{sat} = \left( \frac{e}{n} \right)_0 - m_N = E_0(n = n_0) - m_N \quad (2.1.5)$$

where  $E_0(n)$  is the energy per nucleon.

These relations are valid when  $n = n_0$  and for symmetric matter, i.e. the number of neutrons equals the numbers of protons; but NS matter is characterized by densities which exceed the nuclear saturation density and by a high degree of asymmetry. In order to link the description of this matter with the properties of symmetric nuclear matter which can be experimentally probed, it is conventional to express the energy per baryon at higher density and at higher neutron fraction as a parametric expansion in terms of the ratio  $x = \frac{(n-n_0)}{3n_0}$  and the neutron excess  $\delta = (1 - 2Y_p)$ :

$$E(n, \delta) = E_0(n) + E_{sym}(n)\delta^2 + O(\delta^4) \quad (2.1.6)$$

Both the energy per nucleon of symmetric matter

$$E_0(n) = m_{nuc} + B_{sat} + \frac{1}{2}Kx^2 + \frac{1}{6}Qx^3 + \dots \quad (2.1.7)$$

and the symmetry energy:

$$E_{sym}(n) = S + Lx + \frac{1}{2}K_{sym}x^2 + \dots \quad (2.1.8)$$

can be expanded close to nuclear saturation. Note that in the limit  $x = 0$  and  $Y_p = \frac{1}{2}$  equation 2.1.5 is recovered from 2.1.6 and 2.1.7.

In this expansions, K is the so called incompressibility or compression modulus that expresses

the curvature of  $\frac{e}{n}$  at  $n_0$  and is defined as:

$$K = \left[ k^2 \frac{d^2}{dk^2} \left( \frac{e}{n} \right) \right]_{k_F} = 9 \left[ n^2 \frac{d^2}{dn^2} (E_0(n)) \right]_{n_0} \quad (2.1.9)$$

The larger the value of  $K$ , the stiffer is the EOS, so the compression modulus influences directly the maximum mass of the NS sequence associated with that EOS.

The cubic term in  $x$  in formula 2.1.7 is the skewness parameter  $Q$ .

The dependence of the energy on the asymmetry of the system is expressed through the symmetry energy  $E_{sym}(n)$  which varies as function of the baryon density as in 2.1.8. Here  $S$  is the symmetry energy at the nuclear density:

$$S = \frac{1}{2} \left( \frac{\partial^2}{\partial t^2} \left( \frac{e}{n} \right) \right)_{t=0}, t \equiv \frac{n_n - n_p}{n} \quad (2.1.10)$$

On the other hand,  $L$  is related to the derivative of the symmetry energy with respect to density:

$$L = 3n_0 \left( \frac{\delta E_{sym}}{\delta n} \right)_{n=n_0} \quad (2.1.11)$$

and  $K_{sym}$  is called symmetry incompressibility.

In this scheme, the pressure can be expressed as:

$$P(\delta, x) = \frac{n_0(3x+1)}{3} \left[ Kx + \frac{1}{2} + \frac{1}{2}Qx^2 + \frac{\delta E_{sym}}{\delta x} \delta^2 \right] \quad (2.1.12)$$

As a consequence, close to  $x = 0$  and with  $Y_p \ll 1$ , the pressure is almost completely determined by  $\frac{\delta E_{sym}}{\delta x}$  and therefore by  $L$ .

In general, the saturation variables are strongly correlated to the properties of NS (see for example [Lattimer & Steiner \(2014\)](#)). This is the reason for the recent efforts in finding more and more precise constraints on these parameters, in particular the symmetry energy and its density dependence ([Li et al., 2014](#)).

Naturally, at high density and high neutron fraction, these approaches also enter a regime where the expansions are not valid.

## 2.2 *Laboratory experiments*

### 2.2.1 *Nuclear masses*

The experiments that allow to obtain the most precise data and the least model-dependent results consist in fitting nuclear masses (Audi et al., 2002; Wang et al., 2012) and density distributions (De Vries et al., 1987; Angeli & Marinova, 2013).

From these measurements the determination of the various parameters entering Eq. 2.1.1 is possible. Once the equation is extrapolated to infinite mass number (see previous section) one obtains the saturation density and the corresponding value of the binding energy, but also constraints on the symmetry energy  $E_{sym}$  and its density dependence.

The results coming from ground-state binding energies show a strong correlation between  $S$  and  $L$  (Lattimer & Lim, 2013; Lattimer & Steiner, 2014), which is also confirmed theoretically. In particular, Kortelainen et al. (2010), using the universal nuclear energy density functional to fit nuclear masses, found in the  $S$ - $L$  plane a confidence ellipse characterized by  $S \simeq 30.5$  MeV,  $L \simeq 45$  MeV with  $\sigma_S = 3.1$  MeV, and  $\sigma_L = 40$  MeV. This result, shown in figure 2.2.1, reveals a correlation of more than 97%. The same correlation was obtained two years later by Möller et al. (2012) with a microscopic finite-range droplet model optimized to nuclear masses.

Apart from constraining saturation parameters, measurements of the binding energies of nuclei are also useful for nucleosynthesis simulations, to find the right location of the drip lines (Erler et al., 2012) and for calculations of the EOS of the outer crust of NS (Baym et al., 1971; Kreim et al., 2013; Wolf et al., 2013).

### 2.2.2 *Nuclear Resonances*

Nuclear resonances contain important information about the nucleon-nucleon interaction and they can help constraining the saturation properties of nuclear matter. The identification of isoscalar giant monopole (ISGMR) and isovector giant dipole resonances (IVGDR) have been accomplished for many nuclei such as  $^{70}\text{Zr}$ ,  $^{116}\text{Sn}$  and  $^{208}\text{Pb}$  accompanied by theoretical analyses of the data developed both in non-relativistic and relativistic field frameworks.

First of all, ISGMR offer the possibility to constrain the incompressibility parameter  $K$ : Piekarewicz (2004), employing a relativistic mean field model, found  $K = 248 \pm 8$  MeV and a similar result was obtained two years later by Shlomo et al. (2006),  $K = 240 \pm 20$  MeV. The uncertainty of about 20 MeV is mainly caused by the density dependence of the symmetry energy around  $n_0$ .

Moreover, since the data are actually linked to the density dependent incompressibility at  $0.1\text{fm}^{-3}$ , the result for  $K$  is also function of the chosen skewness parameter  $Q$  (Khan & Margueron, 2013).

Another subsequent reanalysis of the ISGMR data was realized by Stone et al. (2014) using

the liquid drop model: they found the range 250 - 315 MeV for K: the significantly higher value is due to different surface contributions with respect to mean field models approaches.

In the second instance, IVGDR provide a measure of the symmetry energy: the hydrodynamical model from [Lipparini & Stringari \(1989\)](#) showed that the giant dipole centroid energy is closely connected to liquid droplet parameters and gives a correlation between S and L.

Employing different Skyrme functions, [Trippa et al. \(2008\)](#) showed that fitting the centroid energy in  $^{208}\text{Pb}$  is approximately equal to evaluating  $E_{sym}(n)$  at the sub-nuclear density  $0.1\text{fm}^{-3}$ , obtaining the small range  $23.3\text{ MeV} < E_{sym}(0.1) < 24.9\text{ MeV}$ . Using different models to describe the relation between  $E_{sym}(0.1)$ , S and L [Lattimer & Lim \(2013\)](#) found the constraints shown in figure [2.2.1](#).

A different approach was followed by [Danielewicz & Lee \(2014\)](#) who proposed isobaric analog states to constrain symmetry parameters deriving values of  $E_{sym}$  at densities from 0.04 to  $0.16\text{ fm}^{-3}$ . In particular, the accuracy of the result is maximum around  $0.1\text{fm}^{-3}$ , becoming progressively worse at the increase of the density.

Combining their results with measurements of skin thicknesses, [Danielewicz & Lee \(2014\)](#) could obtain a tight range for S, (30.2 – 33.7) MeV and also an interval for L, (35 – 70) MeV with a central value of  $L \sim 50\text{ MeV}$ .

Last but not the least, IVGDR are also useful to extract the value of the incompressibility: the data point toward lower values of K with respect to the results from ISGMR.

A third approach used to study the symmetry energy is the the measurement of the electric dipole polarizability D of  $^{208}\text{Pb}$ , since it is correlated to the neutron skin thickness and thus with L ([Lipparini & Stringari, 1989](#); [Reinhard & Nazarewicz, 2010](#)). The first measurement was reported by [Tamii et al. \(2011\)](#) and their data were subsequently re-analyzed by means of different methods ([Piekarowicz et al., 2012](#); [Roca-Maza et al., 2013](#); [Tamii et al., 2014](#); [Lattimer & Steiner, 2014](#); [Zhang & Chen, 2015](#)): the final result is shown in the figure [2.2.1](#).

Finally [Paar et al. \(2014\)](#) analysed together the data from nuclear masses, charge radii, the anti-analog giant dipole resonance, the isovector giant quadrupole resonance, the pygmy dipole resonance transition strength in  $^{68}\text{Ni}$  and the dipole polarizability of  $^{208}\text{Pb}$ : they were able to obtain a very tight constraint both for S,  $S = 32.5 \pm 0.5\text{ MeV}$  and for L,  $L = 49.9 \pm 4.7\text{ MeV}$ .

### 2.2.3 Neutron skin thickness

Another method to probe neutron-rich matter consists in measuring the neutron skin thickness of heavy nuclei which is defined as the difference between their neutron and proton

root-mean-squared radii:

$$\Delta r_{np} = \sqrt{\langle r_n^2 \rangle} - \sqrt{\langle r_p^2 \rangle} \quad (2.2.1)$$

Proton distributions are very well determined (Angeli et al., 2009; Angeli & Marinova, 2013), while neutron radii and thus the skin thicknesses remain more uncertain.

To shed light on the problem, the usual approach consists in studying the neutron distribution from an analysis of proton scattering on heavy nuclei (Ray, 1979; Ray & Hodgson, 1979; Klos et al., 2007; Terashima et al., 2008; Zenihiro et al., 2010): in particular, Clark et al. (2003) found an interval of  $0.07 < \Delta r_{pn} < 0.16 fm$  from scattering on  $^{208}Pb$ .

A tighter constraint was derived by Trzcinska et al. (2001) from the study of antiprotonic atoms: he found that the larger diffuseness parameter for the neutrons with respect to the protons results in a skin thickness of  $\Delta r_{pn} = 0.15 \pm 0.02 fm$  (see also Jastrzebski et al. (2004) and Brown et al. (2007)).

Moreover, the neutron skin thickness has been measured by the Lead Radius Experiment (PREX) through the parity-violating electro-weak asymmetry in the elastic scattering of polarized electrons from  $^{208}Pb$  (Horowitz et al., 2001; Abrahamyan et al., 2012): because the interaction is mediated by a vector meson coupled preferentially to neutrons, this experiments provides a measurement of the neutron form factor and a value of  $0.302 \pm 0.206$  for  $\Delta r_{pn}$  with a large errorbar.

A result of  $0.015_{-0.06}^{+0.04}$ , more consistent with the previous from proton scattering was, finally, found at the MAMI facility with a coherent pion photo-production experiment (Tarbert et al., 2014).

Typel & Brown (2001) have noted that  $\Delta r_{pn}$  of  $^{208}Pb$  is strongly correlated with with the derivative  $\left. \frac{dE(n,\delta)}{dn} \right|_{\delta=1}$ , and thus to the slope parameter L of pure neutron matter at a density below  $n_0$ , characteristic of the average density in the nuclear surface ( $\sim 0.1 fm^{-3}$ ). Many similar studies, fuelled by this first discovery, found similar correlations (Furnstahl, 2002; Warda et al., 2009; Centelles et al., 2009; Chen et al., 2010; Roca-Maza et al., 2011; Gaidarov et al., 2012, 2015; Tsang et al., 2012).

As a consequence, the neutron skin thickness has become an important parameter since, as evident from Eq. 2.1.12 the pressure of NS matter above  $n_0$  depends on L. In particular Horowitz & Piekarewicz (2001) have underlined that models which yield smaller  $\Delta r_{pn}$  in heavy nuclei tend to yield also smaller NS radii (see also Horowitz & Piekarewicz (2002); Steiner et al. (2005); Todd-Rutel & Piekarewicz (2005); Avancini et al. (2007)).

In addition, Chen et al. (2010), fitting the neutron skin thicknesses of tin isotopes, found again a correlation between S and L: this correlation is shown in Figure 2.2.1 and one can note that is basically orthogonal to the one obtained by fitting nuclear masses.

The measurements obtained from antiprotonic atoms are consistent, leading to L in the range (25 – 70) MeV (Centelles et al., 2009).

### 2.2.4 Heavy ions collisions

More indirect experimental constraints on the EOS are given by heavy-ions collisions (HIC). The extrapolation to NS conditions come with large uncertainties: indeed matter in HIC is hot, contains a net charge and it is not necessarily either in thermal or in chemical equilibrium (Tsang et al., 2009).

HIC allow to probe different physical conditions; high energies ( $\sim 1$  GeV), high densities up to  $\sim 4n_0$  and high temperatures (40-50 MeV) characterize the early phase of the collision (Blatttel et al., 1993) while low energies, intermediate temperatures (10-20 MeV) and subsaturation densities are found in the following stages.

To analyze HIC's data, a comparison with theoretical simulations is required (see e.g. Danielewicz (1984a,b); Bertsch & Das Gupta (1988); Buss et al. (2012); Aichelin (1991); Ono et al. (1992); Hartnack et al. (1998); Colonna et al. (2014) for different approaches). In particular the dependence of the interaction on the momentum is important and it influences the distribution of particles and fragments (Chen et al., 2014; Xu et al., 2015). The early phase of the collision can be described quite reliably through hydrodynamic descriptions (Welke et al., 1988; Gale et al., 1990; Huovinen & Ruuskanen, 2006; Gale et al., 2013). At later times when the fragments are formed, the system reaches subsaturation densities and it is mechanically and/or chemically unstable. Those instabilities are the cause of the multifragmentation and of the so called "isospin fractionation" and they are directly connected to the value of symmetry energy at densities below saturation (Li & Ko, 1997; Xu et al., 2000; Tsang et al., 2001; Ono et al., 2003).

On the other hand, there are many observables in HICs that depend on the in-medium interactions that constrain the EOS at high densities (Fuchs & Wolter, 2006; Russotto et al., 2014): in particular the observation of nucleons, mesons, such as pions or kaons, but also light nuclei, such as  $^2\text{H}$ ,  $^3\text{H}$ ,  $^3\text{He}$ , and  $^4\text{He}$  (Chajeccki et al., 2014). For example from the collective flow of nucleons, comparing laboratory experiments with simulations, one can deduce a value for the symmetric matter compression modulus of  $\sim 220 - 240$  MeV (Welke et al., 1988; Reisdorf et al., 2012; Le Fèvre et al., 2016), as suggested also by the analysis of ISGMR data (see e.g. Danielewicz et al. (2002)) as well as from the observation of kaons (Fuchs et al., 2001; Sturm et al., 2001; Hartnack et al., 2006).

The low value of the compression modulus deduced from HIC has consequence on the stiffness of the the NS EOS (see e.g. Sagert et al. (2012); Aichelin & Schaffner-Bielich (2010)).

In addition, the properties of asymmetric matter can be explored by studying isospin dynamics and diffusion (Li, 2002; Baran et al., 2005; Li et al., 2008; Di Toro et al., 2009; Wolter et al., 2009; Cozma et al., 2013; Ademard et al., 2014; De Filippo & Pagano, 2014;

Kohley & Yennello, 2014).

This is the process of neutron and proton exchange between nuclei caused by symmetry energy: after the collision, the isospin content of the fragment, i.e. the yield ratios of particle pairs with the same mass but different isospin, have been measured (see e.g. Yong et al. (2009); Xiao et al. (2014)).

Figure 2.2.1 shows the constraints on the symmetry energy derived from the isospin diffusion in the collision of  $^{112}\text{Sn}/^{124}\text{Sn}$  (Tsang et al., 2004, 2009, 2012).

Starting from the expansion of the symmetry energy near  $n_0$  as in Eq. 2.1.8 information from multifragmentation (Shetty et al., 2004) and isospin diffusion (Chen et al., 2005) observables together result in the constraint  $S \sim 31\text{-}33$  MeV.

Finally, from the two nucleon interaction one can obtain a lower limit to the NS pressure,  $p = 7.56 \text{ MeV fm}^{-3}$  at  $n = 1.85n_0$  (Özel et al., 2016).

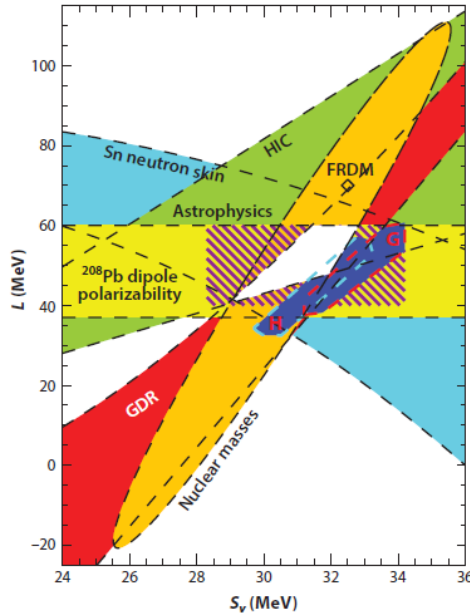


**Figure 2.2.1:** from Özel & Freire (2016) adapted from the original in Lattimer & Steiner (2014). Joint constraints on  $S$  and  $L$  from laboratory experiments. Republished with permission of Annual Reviews, Inc., permission conveyed through Copyright Clearance Center, Inc..

In conclusion, the joint results from laboratory experiments allow to constrain the saturation parameters which have a deep impact on the structure of NS.

In particular, the confidence region for the incompressibility parameter  $K$  can be set in the

range:

$$K \sim (200 - 300) \text{ MeV} \tag{2.2.2}$$

Concerning  $E_{sym}$  from the superposition white area of figure 2.2.1 one can deduce (Lattimer & Steiner, 2014):

$$\begin{aligned} S &\sim (29.0 - 32.7) \text{ MeV} \\ L &\sim (44 - 66) \text{ MeV} \end{aligned} \tag{2.2.3}$$

## 2.3 Astrophysical constraints

### 2.3.1 Mass measurements

Radio observations of pulsars are the most fruitful method to obtain precise mass measurements. Among the vast set of known pulsars (Manchester et al., 2005) some are also observed in X-rays or  $\gamma$ -rays (Abdo et al., 2013; Caraveo, 2014). Moreover, about 10% of the total are part of a binary system and thus their masses can be estimated, thanks to the study of their orbital motion.

The most interesting systems are the ones composed by two compact objects, such as binary neutron stars (BNS) and millisecond pulsar–white dwarf (MSP-WD) systems.

#### *Pulsar timing*

Pulsar timing represent the most accurate method for pulsar mass determination.

Five Keplerian parameters are fundamental in Newtonian gravity to describe the orbital motion: the binary period  $P$ , the orbital eccentricity  $e$ , the projection of the pulsar’s semimajor axis  $a_p$  onto the line of sight  $x_p = a_p \sin i$  (where  $i$  is the orbit’s inclination angle), the time  $T_0$  and the longitude  $\omega$  of periastron.

Two of these observables provide the mass function:

$$f_p = \left(\frac{2\pi}{P}\right) \frac{(a_p \sin i)^3}{G} = \frac{(M_c \sin i)^3}{M^2} \tag{2.3.1}$$

where  $M = M_p + M_c$  is the total mass,  $M_p$  is the pulsar mass, and  $M_c$  is the companion mass.

This equation contains three variables,  $i$ ,  $M_p$ , and  $M_c$ , and thus it cannot alone allow the calculation of the individual masses,  $M_p$  and  $M_c$ .

Luckily, since the binary is composed of compact objects, small relativistic effects can be measured. These are expressed in terms of five post-Keplerian parameters, which are link to  $P$ ,  $x_p$  and  $e$  (Stairs, 2003):

- the rate of advance of periastron  $\dot{\omega}$  that can be usually measured in eccentric orbits.
- the so called Einstein delay,  $\gamma$ . In GR, this is due the combined effects of the variations of the transverse Doppler shift and of the gravitational redshift in an eccentric orbit, an effect called time dilation.
- the orbital period decay  $\dot{P}$  caused by the emission of gravitational waves.
- the Shapiro time delay (Shapiro, 1964), i.e. a delay in the reception of the radio pulses caused by the propagation of the signal through the gravitational field of the pulsar companion. Constraints on the parameters  $i$ ,  $\omega$  and  $e$  come from both the amplitude and the shape of the Shapiro delay.

To constrain the inclination angle of the individual masses at least two of these parameters must be measurable. Exceptions are the cases for which the companion is also a detectable pulsar or an object with an observable spectrum: either via timing or via optical spectroscopy its orbit projected semimajor axis  $x_c$  can be measured providing an extra equation  $q = \frac{M_p}{M_c} = \frac{x_c}{x_p}$ .

### ***Type of sources***

It is useful to divide the sources in three distinct categories, which are characterized by a quite different distributions of measured masses: BNS, recycled pulsars and slow pulsars.

#### *BNS*

The first binary pulsar ever discovered and with a reliable measurement of the mass was a BNS system, PSR B1913+16 (Hulse & Taylor, 1975). This observation has been followed by others and despite those systems represent only about the 5% of the known binary pulsars, there is a hope to get more information about BNS in the near future. Indeed in 2017 the LIGO-VIRGO collaboration (LVC) has announced the first detection of a gravitational wave signal from a BNS merger and the analysis of the data has provided an estimate of the masses of the components of the system (see chapter 4).

#### *Recycled pulsars (ms pulsars)*

The name "recycled" refers to NS that have undergone a process of relevant mass transfer from the companion in a moment during their evolution. Apart from increasing the pulsar mass and deeply reducing the pulsar magnetic field, the major effect of the recycling process is to significantly increase its spin frequency (see e.g. Hessels et al. (2006)). If the new period is the range  $1.39 < P < 20$  ms the NS are called "millisecond pulsars" (MSPs). Most of the MSPs are in a NS-WD binary system with a very low orbital eccentricity; the first observation, a MSP named B1937+21, was performed with the Arecibo telescope in 1982 (Backer et al., 1982).

Because of the fast rotation and the long-term rotational stability of recycled pulsars, their orbital motion can be measured very precisely through timing.

However, an issue on the mass determination can derive from the low orbital eccentricity; this problem can be overcome if:

- the MSP is found in globular clusters (GCs) (in this case the orbit can gain eccentricity thanks to the gravitational interaction with the nearby stars in the GC),
- the Shapiro delay can be measured or
- the companion is optically bright.

*Slow pulsars:*

This category includes the low frequency pulsars and NS in X-ray binaries with high-mass companions, for which the mass is estimated thanks to observations of signals in the X-ray and optical wavelengths. These NS are also named "eclipsing X-ray pulsars" because the X-ray signal is blocked by the companions for part of the orbit.

The mass measurements obtained for this kind of systems are not as precise as the ones from pulsar timing, and moreover they can be subjected to systematic uncertainties (Ozel et al., 2012b; Falanga et al., 2015).

A last set of systems is represented by NS in X-ray binaries with a low mass companion: also in this case the mass determination is less accurate with respect to recycled pulsars, but for this sources a simultaneous mass radius measurements can be obtained (as will be discussed in the next section).

***The maximum mass***

The most interesting mass determination concerns the estimate of the maximum mass of NS, since this is directly related to the EOS.

The first measurement of a very massive NS was reported by Demorest et al. (2010) for PSR J1614-2230, a NS in a NS-WD system. Using the Shapiro delay method, they calculated the mass as  $1.97 \pm 0.04 M_{\odot}$ : this value was then revised by Fonseca et al. (2016) lowering it to  $1.928 \pm 0.017 M_{\odot}$ , then reanalyzed to  $1.908 \pm 0.016 M_{\odot}$  by Arzoumanian et al. (2018).

In 2013, Antoniadis et al. (2013), studying the orbital data of J0348+0432, reported a mass of  $2.01 \pm 0.04 M_{\odot}$ . Thanks to its accuracy and reliability, this mass has been the standard accepted value for the lower bound of the NS maximum mass for many years.

However, recently an even more massive object has come into the picture: again using the Shapiro delay, Cromartie et al. (2019) have measured the mass of the MSP J0740+6620 to be  $2.14^{+0.10}_{-0.09} M_{\odot}$ .

In addition, for a class of objects called black widow and redback systems, even larger masses have been suggested (van Kerkwijk et al., 2011; Romani et al., 2012; Kaplan et al., 2013).

However, the analysis of these systems can present systematics and it is strongly model dependent and therefore cannot be considered as reliable as the aforementioned results (Roberts et al., 2015).

The same considerations are valid also for the eclipsing X-ray binary Vela X-1 for which the mass was estimated as  $2.12 \pm 0.16M_{\odot}$  (Falanga et al., 2015).

The maximum mass of NS can rule out all the EOSs that cannot reach that value and it is primarily determined by the behavior of the EOS at very high densities (Lattimer & Prakash, 2004; Ozel & Psaltis, 2009; Read et al., 2009; Hebeler et al., 2013). In particular the softening above the saturation density due to the appearance of new degrees of freedom can be difficult to reconcile with observations: hence the name "hyperons puzzle" (see chapter 3.2 for a more extensive discussion).

Also the hypothesis that high density matter could contain Bose-Einstein condensate of kaons (Kaplan & Nelson, 1986; Brown et al., 2006) would lead to a maximum mass below  $2M_{\odot}$ . Finally models with deconfined quark matter appearing in the core that are able to fulfil the  $2M_{\odot}$  constraint exist, but they require a careful fine-tuning of parameters, such as for example the sound velocity at the phase transition (Alford et al., 2005; Benic et al., 2015).

### ***The minimum mass***

The evidence for the existence of small NS is interesting because it help to constrain NS hystory and formation mechanisms.

Relevant examples are SMC X-1 and 4U 1538-52, firstly studied by Rawls et al. (2011) and subsequently reanalyzed by Ozel et al. (2012b): they reported masses of  $0.93 \pm 0.12M_{\odot}$  and  $1.18 \pm 0.25M_{\odot}$ , respectively.

If ones considers the collapse of a progenitor star with O-Ne-Mg core and if the loss of matter during the process of formation is negligible, the lowest-gravitational-mass neutron star could be of the order of  $1.15M_{\odot}$ . Moreover, all the models of core-collapse supernovae (CCSN) present a minimum gravitational mass for the proto-NS which depends on the entropy profile within the star (Strobel et al., 1999) and which is in the range  $0.9 - 1.2M_{\odot}$ . Below this limit, dynamical instabilities would forbid the formation a stable NS. The constraint, considering the experimental error, is compatible with currently observed minimum mass.

### ***2.3.2 Radii measurements***

The tightest constraint on the EOS of NS would be provided by a simultaneous measurements of mass and radius of the same compact object (Ozel & Psaltis, 2009; Read et al., 2009; Ozel et al., 2010; Steiner et al., 2013b).

In the last 15 years many techniques for radius determination have been applied and significant progresses have been achieved. However, since the radius measurements are more

indirect with respect to the ones for mass, the result remains more model dependent and less accurate.

Almost all the methods employed are based on the study of thermal emission from the NS surface in order to estimate the angular size of the star or to quantify the GR effects on the signal. The type and the significance of the uncertainties affecting these techniques depend on the kind of object observed (Miller, 2013; Potekhin, 2014).

These approaches can be split into two main categories: spectroscopic measurements and pulse profile modelling.

### *Spectroscopic measurements*

The NS thermal emission can be described, in first approximation, as a blackbody. From the measurements of the integrated flux  $F$ , the effective temperature  $T_{eff}$  through the modelling of the spectrum, and the distance  $D$ , one can estimate their angular diameter:

$$\frac{R_{obs}}{D} = \left( \frac{F_{bol}}{\sigma_B T_{eff}} \right)^{\frac{1}{2}} \quad (2.3.2)$$

where  $\sigma_B$  is the Stefan-Boltzmann constant. However, spectroscopic radius determinations are complicated by different effects which must be taken into account:

- the surface emission is distorted by gravitational lensing and red-shift. Because of that the observed radius is not the geometric one, but the so called "radiation radius". To link it to the physical radius, a mass-dependent correction need to be introduced (Pechenick et al., 1983; Psaltis et al., 2000):

$$R_{obs} = \left( 1 - \frac{2GM}{Rc^2} \right)^{-\frac{1}{2}} R \quad (2.3.3)$$

An additional spin-dependent correction is needed when the spin velocity of the NS is so high to cause a further distortion of the spacetime that, thus, can no longer be represented with the Schwarzschild metric (Baubock et al., 2015).

- the emission is modulated by the atmosphere of the star: the radius estimate thus is influenced by the choice of the model for the composition of the atmosphere which is not always unambiguous.
- NS magnetic field strength and distribution can play a decisive role causing temperature inhomogeneities on the surface.
- the distance is not always well determined
- part of the emitted radiation is absorbed before reaching the observer by means of interstellar hydrogen: to correctly infer the emission, modelling the magnitude of this absorption is important.

Accurate modelling of GR effects on the emission, a farsighted selection of the sources and a combination of many different observations help to overcome these problems and reduce the uncertainties.

The spectroscopic method is applied mainly to two class of sources: Quiescent low mass X-ray binaries and thermonuclear bursters.

*Quiescent low mass X-ray binaries (qLMXBs)*

The first group is composed by LMXBs when they are in the quiescent phase which is

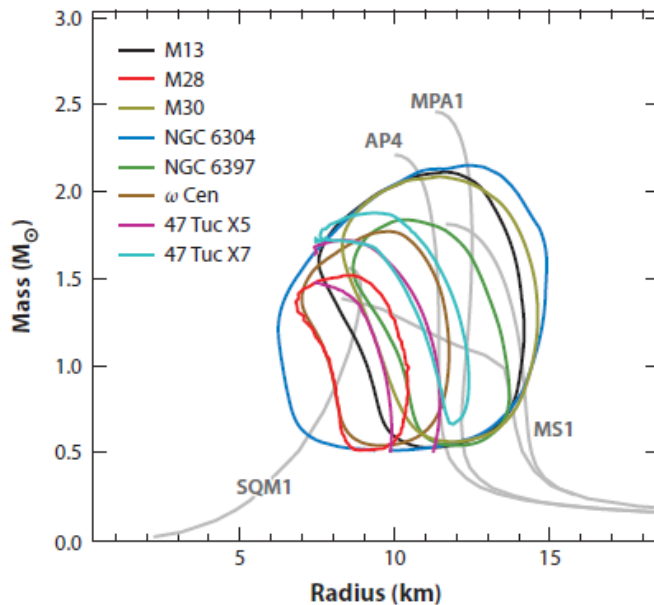


**Figure 2.3.1:** from Özel & Freire (2016). NS mass and radius probability distribution (68% confidence level) obtained in Özel et al. (2016) for qLMXB. Republished with permission of Annual Reviews, Inc., permission conveyed through Copyright Clearance Center, Inc..

characterized by the absence or at least by a strong reduction of the accretion of matter from the companion. Because of this the heat stored in the crust during the accretion can be finally re-radiated (Brown et al., 1998) and the consequent thermal emission observed. Moreover, the atmosphere of this kind of sources is probably composed of light elements such as Hydrogen or Helium and therefore the qLMXB spectrum is quasi-thermal. In addition, the expected magnetic field is very low (Psaltis & Chakrabarty, 1999).

Finally, most of the sources are located in GCs, making it easier to accurately measure their distances. On the other hand, GCs are very dense environments and qLMXBs have very low luminosities. Despite these difficulties, many observations and angular size estimate

have been performed on qLMXBs, thanks to the low background and the high resolution of instruments in the Chandra X-Ray Observatory (Rutledge et al., 2001; Rybicki et al., 2006) and on the X-Ray-Multi-Mirror Mission-Newton (XMM-Newton; Webb & Barret (2007)). The second fundamental ingredient is represented by the developments of radiative models of the NS atmosphere valid under different physical conditions (Zavlin et al., 1996; Rybicki et al., 2006; Özel, 2013).

Starting from slightly diverse assumptions, many analyses to estimate the radii have been performed on qLMXBs in the past 15 years. The results are constraints for 8 qLMXBs in the GCs, M13, M28, M30,  $\omega$ -Cen, NGC 6304, and NGC 6397 (Webb & Barret, 2007; Guillot et al., 2011; Steiner et al., 2013b; Guillot et al., 2013; Guillot & Rutledge, 2014; Lattimer & Steiner, 2014; Heinke et al., 2014; Özel et al., 2016) and 2 in 47 Tuc (Rybicki et al., 2006; Bogdanov et al., 2016).

The mass-radius probability distribution functions (PDFs) obtained by Özel et al. (2016) are shown in Figure 2.3.1.

As previously mentioned, there are many aspects that can lead to systematic uncertainties that need to be considered in the radius inference:

- Atmospheric composition.

The detection of  $H\alpha$  emission from the optical spectra of most of the known qLMXBs reveals that the companions have to possess hydrogen (Heinke et al., 2014). Even though there is not such an evidence for the GC's qLMXBs, it is lawful to assume they have a similar companion. For this reason unmagnetized hydrogen models have mostly been adopted in the spectral analyses to estimate the observed angular sizes. An exception is the source NGC 6397 which has been object of discussion because of its peculiar atmospheric composition. Guillot et al. (2013) and Guillot & Rutledge (2014) favored an hydrogen atmosphere and obtained a very small radius  $\sim 9.5$  Km for a  $1.4M_{\odot}$  NS. On the other hand, Heinke et al. (2014) found an upper limit on the  $H\alpha$  emission and therefore suggested the use of an helium atmosphere which yielded to  $\sim 2$  km larger radius.

- Non-thermal component.

The modelling of the non-thermal component contains assumptions on spectral indices: these choices can affect the resulting radius (Heinke et al., 2014). Since these parameters cannot be precisely measured, the better approach consists in exploring a wide range of values when fitting the data;

- Interstellar extinction.

The spectral analysis is also affected by the uncertainty in the interstellar extinction: in particular the different models employed in various studies (see e.g. Guillot et al. (2013); Lattimer & Steiner (2014)) lead to small difference in the estimated values but large discrepancies in the uncertainties (Heinke et al., 2014).

- Rotational deformation.  
qLMXBs are likely to spin very fast introducing a non-negligible rotational deformation: this can affect the estimate of the radius up to roughly 10% (Poutanen et al., 2014; Baubock et al., 2015).

The analysis performed by Özel et al. (2016) whose results are shown in Figure 2.3.1 took all these effects into account.

*Thermonuclear burster TBs*

The second class of sources analyzed by means of spectroscopic measurements are the burster found in LMXBs, characterized by a helium flare in accreted material. This event is called thermonuclear X-ray burst and causes an increase of the luminosity for the timescale of about 1 s needed to diffuse out to the surface. After this first phase, the phenomenon can evolve in two different ways: one possibility is that the energy is spread out giving birth to the so called cooling tails lasting for a timescale of  $\sim 15 - 50$  s. The second case is realized when the luminosity equals the Eddington limit and the radiation forces are strong enough to overcome gravity and expand the photospheric radius (a phenomenon called PRE) causing the temperature to increase a second time (Lewin et al., 1993).

As qLMXBs, also TBs are likely to have low magnetic fields and to be surrounded by

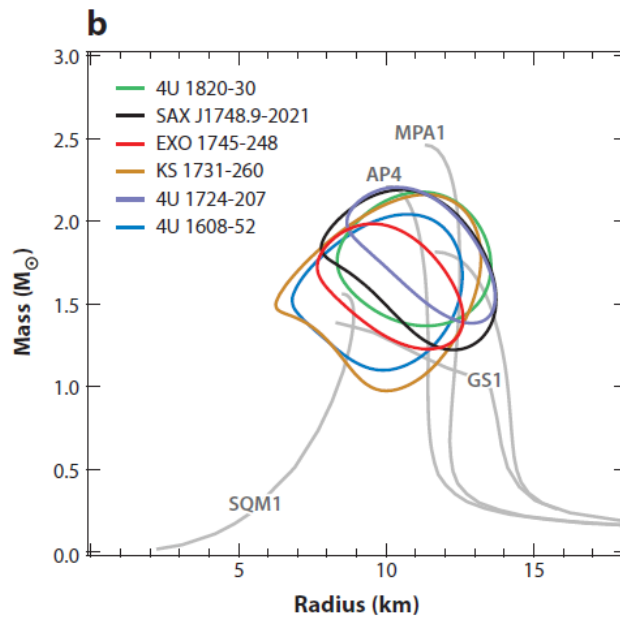


**Figure 2.3.2:** from Özel & Freire (2016). Same as Figure 2.3.1 for TBs. Republished with permission of Annual Reviews, Inc., permission conveyed through Copyright Clearance Center, Inc..

light elements atmospheres. The main debate concerns the modelling of the photospheric burst (Galloway & Lampe, 2012; Ozel et al., 2012a; Guver & Ozel, 2013; Steiner et al., 2013b; Poutanen et al., 2014). Moreover, many different approaches has been developed to infer mass and radius from this burst and in particular to break their degeneracy through spectroscopic measurements (van Paradijs, 1979; Fujimoto & Taam, 1986; Sztajno et al., 1987; Damen et al., 1990; Ozel, 2006). Concerning the modelling of the burst and the atmosphere, many frameworks differing for effective gravities and surface compositions have been explored (London et al., 1986; Madej et al., 2004; Majczyna et al., 2005; Suleimanov et al., 2012). A parameter called color correction factor  $f_c = \frac{T_c}{T_{eff}}$  is also included to calculate the divergence of the atmosphere from a blackbody at the effective temperature.

One possible approach to estimate mass-radius PDFs (sometimes called touchdown method) uses time-resolved spectroscopy to infer the temperature and the Eddington flux; the latter is related to the mass, the radius and the distance of the source. At the same time, it can also be expressed as function of the apparent angular size and thus the combination of these two diverse spectroscopic constraints allows to determine both the mass and the radius.

This method has been implemented for the study of six TBs in LMXB: EXO 1745–248, 4U 1820–30, 4U 1608–52, KS 1731–260, SAX J1748.9–2021, and 4U 1724–207 (Ozel & Psaltis, 2009; Guver et al., 2010a,b; Ozel et al., 2012a; Guver & Ozel, 2013; Özel et al., 2016). In particular, all the sources has been analyzed together with new statistical methods by Özel et al. (2016): the result, suggesting small radii  $\sim 10 - 11$  km, is in agreement with the one

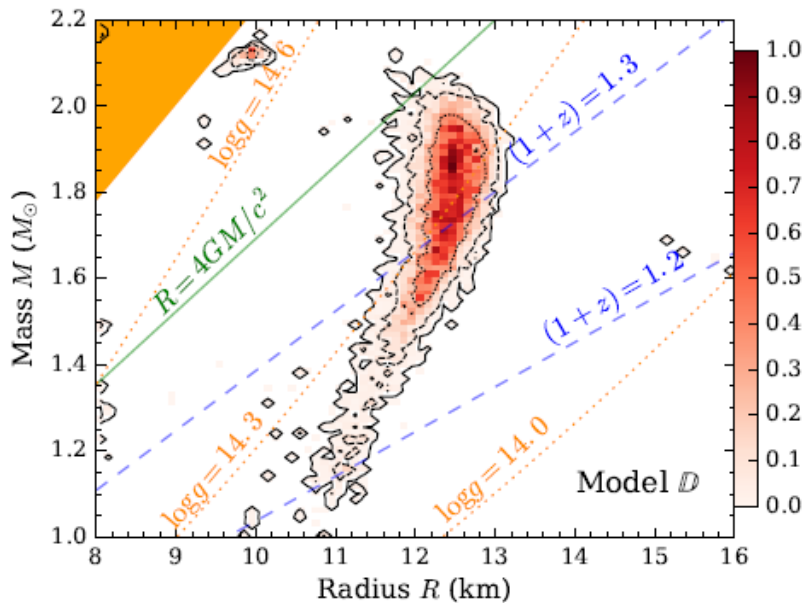


**Figure 2.3.3:** from Nättilä et al. (2017). Mass and radius posteriors for 4U 1702-29. Reproduced with permission © ESO.

obtained for qLMXBs and it is shown in Figure 2.3.2.

An alternative approach, the so called cooling tail method, makes use of the evolution of the color correction factor during the cooling phase to constraint mass and radius (see e.g. Majczyna et al. (2005); Suleimanov et al. (2011); Poutanen et al. (2014); Nättilä et al. (2016)). Finally, Nättilä et al. (2017) used direct simultaneous atmosphere model fits to a set of X-ray burst observations: in particular, they applied this method to data from five bursts of 4U 1702–429, finding  $M = 1.9 \pm 0.3M_{\odot}$  and  $R = 12.4 \pm 0.4$  km (Figure 2.3.3).

Like for qLMXBs, also the measurements of thermonuclear bursts can be affected by systematic uncertainties, such as distances (if the sources are not in GCs), the identification of outliers in the spectroscopic data and the deformation due to spinning.

### ***Pulse profile modelling***

A different method for NS radii measurement is based on the analysis of the periodic oscillation in the thermal emission caused by temperature anisotropies in localized regions on a spinning NS surface. Indeed these regions, called hotspots, generate an observable pulsation in X-rays whose spectrum and flux are periodic due to the spinning. From the detected signal, one can determine the rotational phase evolution of the star and develop a pulse profile.

To reach the observer, the photons propagate through the curved spacetime of the rotating compact star and they are therefore subjected to GR effects (Bogdanov et al., 2019).

First of all, the light bending influences the amplitude of the pulsation and also the delay between photons coming from different points on the surface (Pechenick et al., 1983). Moreover, the gravitational redshift affects the energy-dependent normalisation of the pulse profile. Both these effects are strongly dependent on the compactness of the NS.

Finally, the relativistic beaming, due to the motion of matter on the deformed NS surface, causes the appearance of asymmetry in the pulse profile. It depends on the velocity of the hotspot which is a function of two degenerate parameters: the radius  $R$  and the spin frequency of the NS. Since the latter can be precisely measured, the degeneracy can be broken and the radius can be constrained.

All these effects are considered when mapping the the surface emission of the NS into the pulse profile (Cook et al., 1994; Stergioulas & Friedman, 1995; Miller & Lamb, 1998; Braje et al., 2000; Munro et al., 2002; Poutanen & Gierlinski, 2003; Poutanen & Beloborodov, 2006; Morsink et al., 2007; Bauböck et al., 2013; AlGendy & Morsink, 2014; Psaltis & Özel, 2014; Nättilä & Pihajoki, 2018; Vincent et al., 2018). This profile can be therefore evaluated for a given model of the surface emission, exterior spacetime and instrument.

Using such light-curve models, the properties of the signal oscillations can thus serve as a probe of the stellar space-time and as measurement of its radius and mass (see Watts et al. (2016) for further information).

Three classes of NS, which have different distributions of spin frequencies, are good can-

didates for pulse profile modelling: rotation-powered MSPs, accretion-powered MSPs and thermonuclear X-ray bursters.

*Rotation-powered pulsars*

Among the rotation-powered MSPs, there many sources for which a soft thermal X-ray component has been detected (Grindlay et al., 2002; Zavlin, 2006, 2007).

The interpretation of these data is affected by uncertainties such as the estimate of the non-thermal magnetospheric component that dominates the emission and also the model for the thermal component itself. Despite the complexities, many data recorded by Rontgensatellit (ROSAT), Chandra X-Ray Observatory, and XMM-Newton have been studied; in particular, different analysis have been performed on PSR J0437–4715 (Bogdanov et al., 2007; Verbiest et al., 2008; Bogdanov, 2013) leading finally to the estimate  $M = 1.44_{-0.07}^{+0.07}M_{\odot}$  and  $R = 13.6_{-0.8}^{+0.9}$  Km (Gonzalez-Caniulef et al., 2019).

A major step forward in the application of pulse profile modelling to rotation-powered MSPs is represented by the Neutron Star Interior Composition Explorer (NICER; Gendreau et al. (2016)). NICER, a NASA Mission of Opportunity, is a soft X-ray telescope carrying a soft X-ray timing instrument (XTI), that was installed on the International Space Station (ISS) in 2017.

In 2019 the observation of the MSP PSR J0030+0451 (Lommen et al., 2000; Becker et al., 2000) and the inferred mass-radius were reported (Riley et al., 2019; Miller et al., 2019). Riley et al. (2019) performed a relativistic ray-tracing of thermal emission from hotspots and, since the pulse profile data showed two components, they assumed two hot regions. Among the topologies explored for these hotspots, they preferred the model with both the hot regions located in the same rotational hemisphere (ST+PST). The resulting mass and radius are  $1.34_{-0.15}^{+0.16}M_{\odot}$  and  $12.71_{-1.14}^{+1.19}$  km, respectively (see Figure 2.3.4).

A slightly different but consistent result was reported by Miller et al. (2019) whose independent analysis of the same data yielded  $R = 13.02_{-1.24}^{+1.06}$  km and  $M = 1.44_{-0.15}^{+0.14}M_{\odot}$  (68%).

Finally, a further improvement in the accuracy of the mass-radius estimate for PSR J0030+0451 (and PSR J0437–4715) will be provided by eXTP (the enhanced X-ray Timing and Polarimetry mission; see Watts et al. (2019) for details).

*Accretion-powered pulsars*

In the accretion-powered MSPs the soft x-rays thermal emission comes from the regions at the base of the accretion columns. Once emitted, the photons are Compton scattered in these columns and this influences the amplitude of the observed pulsation (Poutanen & Gierlinski, 2003; Lamb et al., 2009). The model of this thermal emission has been used to analyze various sources (see for example Leahy et al. (2008, 2009, 2011); Morsink & Leahy (2011)).

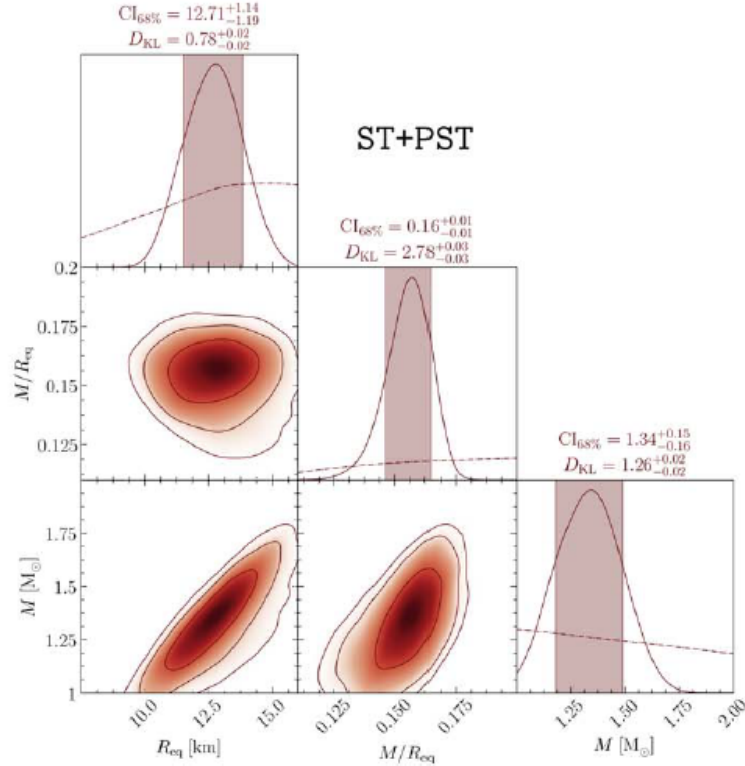


**Figure 2.3.4:** from Riley et al. (2019). One- and two-dimensional marginalized distributions of mass and radius of PSR J0030+0451 for ST+PST. The contours correspond to 15.85%, 68.3% and 84.15% quantiles in posterior mass

### Thermonuclear burst oscillations

During thermonuclear X-ray bursts on accreting NS, hotspots can form giving rise periodic oscillations with large amplitudes, called burst oscillations (Strohmayer et al., 1996; Galloway et al., 2008)

Their origin is to be found in temperature anisotropies on the surface during the nuclear burning (see Watts (2012) for a review).

Again, limits on the compactness can be inferred from the modeling of the pulse profile (Strohmayer et al., 1997; Miller & Lamb, 1998; Weinberg et al., 2001; Munro et al., 2002, 2003) but the results are by now not significantly constraining (Nath et al., 2002; Bhattacharyya et al., 2005b).

However burst oscillation measurement gives possibilities for independent cross-checks by means of complementary constraints (Lo et al., 2013, 2018; Chang et al., 2005) allowing to reduce systematic errors.

In conclusion, the present radius measurements are still affected by uncertainties and dependent on assumptions which make them not as reliable as the mass determination (see [Fortin et al. \(2015\)](#) and [Potekhin \(2014\)](#)). However, combining different radius constraints can provide many clues on the features and the structure of NS. In particular, the radius is strongly sensitive to the pressure at densities of about  $\sim 2n_0$  ([Lattimer & Prakash, 2001](#)). This feature translates in a dependence mainly on the symmetry energy and its derivatives. Moreover, regarding nucleonic EOSs, some studies ([Hebeler & Schwenk, 2010](#); [Gandolfi et al., 2012](#); [Steiner & Gandolfi, 2012](#)) suggest the importance of three-nucleon forces to determine the pressure at these densities; on the other hand the appearance of new degrees of freedom tends to reduce the radius. In addition, [Ozel & Psaltis \(2009\)](#) suggested that the slope of the mass-radius curve is primarily determined by the pressure at  $\sim 4n_0$  and [Sotani et al. \(2014\)](#) demonstrated how the M-R relation for low mass NS can constrain both K and L.

Without any doubt, the tightest constraints can be obtained combining the measurements of the maximum mass with simultaneous mass-radius determinations of the same objects ([Steiner et al., 2010](#); [Özel et al., 2016](#)) In this respect, some of the mass-radius measurements described here will be used in the works presented in chapter [8.4.3](#) and [8](#) of this thesis.

Apart from the aforementioned sources and techniques, other astrophysical phenomenons can give constraints on the radii and other attributes of NS. Just to mention few of them: the observation of the gravitational redshift at the surface, the study of the cooling process, the analysis of quasi-periodic oscillations from accreting stars, the detection of pulsar glitches and neutrino signals from proto-NSs. Since not directly involved in the work reported in this thesis, these additional measurements will not be discuss in details (for further information see the review by [Lattimer & Prakash \(2007\)](#)).

Finally, a completely new era for astrophysical constraint opened few years ago with the observations of BNS merger. This subject will be extensively treated in chapter [4](#).

## *The Equations of State*

### **3.1 Relativistic mean field model**

Firstly introduced by [Duerr \(1956\)](#) and [Walecka \(1974\)](#), the RMF model is a relativistically covariant theory which describes dense hadronic matter including interactions among baryons mediated by meson fields.

The major advantage of the RMFT is that it allows to exploit the constraints from nuclear physics: indeed the parameters of the model are directly connected to the properties of nuclear matter at saturation.

Two coupling constants of the theory can be fixed by using the values of binding energy and particle density.

On the other hand, the charge neutrality condition in NS matter leads to a very asymmetric system with a very high symmetry energy: the RMFT allows to fix the value of  $S$  directly through a coupling constant assuring the reliability of small extrapolation to asymmetric systems. Other constraints on the EOS are represented by the compression modulus  $K$  and the effective mass  $m^*$ . The latter expresses the change of the mass of baryons due to the attractive part of the nuclear force and it is density dependent. The value of the effective mass at saturation density is inferred experimentally from nucleon scattering data (see for example [Jaminon & Mahaux \(1989\)](#) or references in [Margueron et al. \(2018a\)](#)) and the widely accepted range is:

$$\frac{m^*}{m} \simeq 0.7 - 0.8 . \quad (3.1.1)$$

where  $m$  is the usual baryon mass.

These last two parameters guarantee that the extrapolation to higher density is correct near saturation.

This special advantage of the RMFT implies a direct relation between the NS observables which depends on the EOS and the properties of nuclear interaction.

Moreover, in the RMF framework it is relatively easy to include new degrees of freedom, such as the other members of the baryon octet which are supposed to appear at high densities.

### 3.1.1 The $\sigma$ - $\omega$ model

The simplest field model for nuclear matter contains protons and neutrons, which are different isospin states of the nucleon  $\psi$ , a scalar meson  $\sigma$  and a vector meson  $\omega$ .

The Lagrangian for the theory can be written as:

$$L = \bar{\psi}[i\gamma_\mu(\partial^\mu + ig_\omega\omega^\mu) - (m - g_\sigma\sigma)]\psi + \frac{1}{2}(\partial_\mu\sigma\partial^\mu\sigma - m_\sigma^2\sigma^2) - \frac{1}{4}\omega_{\mu\nu}\omega^{\mu\nu} + \frac{1}{2}m_\omega^2\omega_\mu\omega^\mu \quad (3.1.2)$$

Then the relativistic mean-field approximation is introduced (valid for strong source terms) which consists in the substitution of the real meson degrees of freedom with the corresponding expectation values, calculated on the ground state of nuclear matter. The vector field can develop only the zero component, since there is no spatial direction in the problem for a uniform system at rest. So the equations of motion are:

$$m_\sigma^2\langle\sigma\rangle = g_\sigma\langle\bar{\psi}\psi\rangle \quad (3.1.3)$$

$$m_\omega^2\langle\omega_0\rangle = g_\omega\langle\psi^\dagger\psi\rangle \quad (3.1.4)$$

$$[i\gamma_\mu(\partial^\mu + ig_\omega\omega^\mu) - (m - g_\sigma\sigma)]\psi(x) = 0 \quad (3.1.5)$$

Introducing the effective mass  $m^*(\sigma) = m - g_\sigma\sigma$  the eigenvalues of the Dirac equation can be written as:

$$k_0 = g_\omega\omega_0 + \sqrt{\mathbf{k}^2 + m^{*2}} \quad (3.1.6)$$

The next step is to express in a more explicit form the expectation values of the baryon currents; the normalization

$$(\psi^\dagger\psi)_{\mathbf{k}\lambda} = 1 \quad (3.1.7)$$

is used, where  $(\psi^\dagger\psi)_{\mathbf{k}\lambda}$  is the the expectation value in a single-particle state with momentum  $k$  and spin and isospin quantum numbers  $\lambda$ .

So for the baryon density, also called vector density, it is found:

$$n = \langle\psi^\dagger\psi\rangle = 4 \int_0^{k_F} \frac{d\mathbf{k}}{(2\pi)^3} = \frac{2k_F^3}{3\pi^2} \quad (3.1.8)$$

where  $\mathbf{k}_F$  is the Fermi momentum.

For the scalar density the expression is:

$$n_s = \langle \bar{\psi}\psi \rangle = \frac{2}{\pi^2} \int_0^{k_F} k^2 dk \frac{m^*}{\sqrt{k^2 + m^{*2}}} \quad (3.1.9)$$

So, finally, the equations for the meson fields become:

$$g_\sigma \sigma = \left(\frac{g_\sigma}{m_\sigma}\right)^2 \frac{2}{\pi^2} \int_0^{k_F} k^2 dk \frac{m^*}{\sqrt{k^2 + m^{*2}}} \quad (3.1.10)$$

$$g_\omega \omega_0 = \left(\frac{g_\omega}{m_\omega}\right)^2 n \quad (3.1.11)$$

where the first one represents a self-consistency condition for the scalar field. The results of these two equations depends on the ratios  $\frac{g_\sigma}{m_\sigma}$  and  $\frac{g_\omega}{m_\omega}$  which are therefore the two parameters of the model and can be fitted to the experimental values for the saturation density and the binding energy.

A low densities, i.e. for small  $k$ , the right hand side of equations 3.1.10 and 3.1.11 goes to zero and thus one recover the result  $n_s \sim n$  and  $m^* \sim m$ .

On the other hand, in the high density limit, the ratio  $\frac{n_s}{n}$  tends to zero since  $n_s$  itself approaches  $m$  as finite asymptotic value. Thus the scalar meson reduces the effective mass:

$$m^* \sim \frac{m}{1 + \frac{g_\sigma^2 k_F^2}{m_\sigma^2} \pi^2} \quad (3.1.12)$$

which goes to zero at large densities.

It is therefore evident that the scalar meson decreases also the Dirac eigenvalue in 3.1.6. On the contrary, the time component of the vector meson in 3.1.11 increases with  $n$  and thus gives a growing contribution to  $k_0$ . The consequence of the opposite behaviors of the two mediator fields is the existence of a negative minimum at finite density for the binding energy. This means that the medium saturates and this density is the saturation density.

In order to calculate the EOS, the energy momentum tensor can be used because in the rest frame it is diagonal and its elements are the energy density and the pressure. Finally, the expressions are:

$$e = \frac{1}{2} m_\sigma^2 \sigma^2 + \frac{1}{2} m_\omega^2 \omega^2 + \int_0^{k_F} k^2 dk \sqrt{k^2 + m^{*2}} \quad (3.1.13)$$

$$p = -\frac{1}{2} m_\sigma^2 \sigma^2 + \frac{1}{2} m_\omega^2 \omega^2 + \int_0^{k_f} k^2 dk \frac{k^2}{\sqrt{k^2 + m^{*2}}} \quad (3.1.14)$$

An alternative way to calculate pressure from energy density is to use the following

thermodynamical relation, valid at  $T = 0$ :

$$p = n^2 \frac{\partial(\frac{e}{n})}{\partial n} \quad (3.1.15)$$

This is nothing else than the first law of thermodynamics and assures the thermodynamic consistency of the theory.

At low density, after some manipulations of equations 3.1.13 and 3.1.14 one can obtain:

$$p \sim \frac{2k_f^5}{15\pi m}, \quad e \sim \frac{2mk_f^3}{3\pi^2} \quad (3.1.16)$$

thus recovering the typical EOS describing non-interacting fermions  $p \propto e^{\frac{5}{3}}$ . In the opposite limit, both pressure and energy density are dominated by the repulsive vector contribution and therefore  $p \rightarrow e$  and consequently the sound velocity  $v_s \rightarrow c$ .

As previously mentioned, since the theory at this level has two parameters, one can exactly reproduce only the saturation density and the binding energy. The remaining saturation properties are just derived quantities: the calculations lead to a value for the compression modulus  $K \sim 550$  MeV, for the effective mass  $\frac{m^*}{m} \sim 0.5$  and for the symmetry energy  $S \sim 15$  MeV. These results are all in poor agreement with the experimental range and this determines the inability of the model to correctly extrapolate to high density or isospin asymmetry.

### 3.1.2 Extensions of the model

For the purpose of setting the correct values of the experimental constraints on the RMFT, other coupling constants must be inserted in the Lagrangian, meaning new interaction terms.

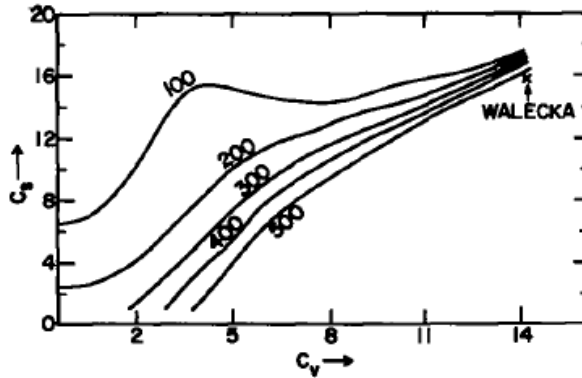


**Figure 3.1.1:** from Boguta & Bodmer (1977). Constant  $K$  contours as functions of  $C_s = \frac{g_\sigma}{m_\sigma}$  and  $C_V = \frac{g_\omega}{m_\omega}$ . Reprinted with permission from Elsevier, Copyright © 1977 Published by Elsevier B.V.

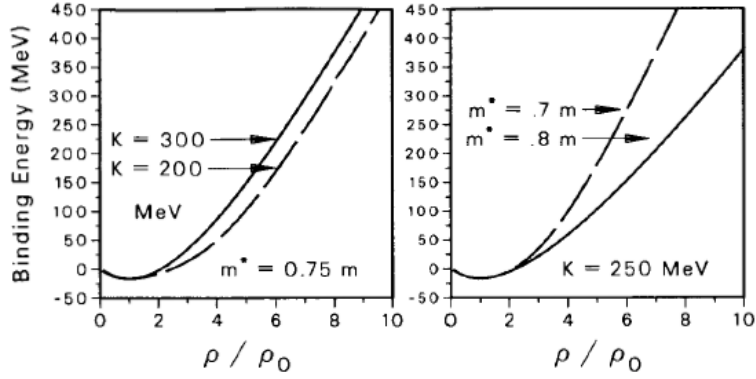


**Figure 3.1.2:** from [Glendenning \(1997\)](#). EOSs for symmetric nuclear matter for different values of  $K$  and  $m^*$  at the edges of the experimental ranges.

One possibility is to consider the self-interactions of the scalar meson which are compatible with the request of renormalizability of the theory.

These terms are in the form:

$$U(\sigma) = \frac{1}{3}bm(g_\sigma\sigma)^3 + \frac{1}{4}c(g_\sigma\sigma)^4 \quad (3.1.17)$$

The equation for the  $\sigma$  meson becomes:

$$g_\sigma\sigma = \left(\frac{g_\sigma}{m_\sigma}\right)^2 \left[ \frac{2}{\pi^2} \int_0^{k_F} k^2 dk \frac{m^*}{\sqrt{\mathbf{k}^2 + m^{*2}}} - bm(g_\sigma\sigma)^2 - c(g_\sigma\sigma)^3 \right] \quad (3.1.18)$$

and to the energy density and to the pressure a contribution  $U(\sigma)$  is added and subtracted, respectively.

The choice of these new interaction terms and the related parameters  $b$  and  $c$  permit to set the values of the effective mass and of the compression modulus through the experimental constraints. For example if  $b$  and  $c$  are fitted to  $n_0$  and  $B$ , then  $K$  and  $m^*$  can be expressed as dependent on the value of  $\frac{g_\sigma}{m_\sigma}$  and  $\frac{g_\omega}{m_\omega}$ , obtaining parametric curves like the ones shown in [Figure 3.1.1](#). The large uncertainties affecting the experimental values of  $K$  and  $m^*$  translate in a variability of the model parameters and thus of the EOS. An example in this regard is provided by [Figure 3.1.2](#).

This first extension of the Walecka model gave the opportunity to obtain reasonable values for four of the saturation properties of nuclear matter. However, if the task of the theory is that of describing NS matter, the Lagrangian must be extended to incorporate an interaction depending on the isospin, that allows to reproduce the experimental value of the

symmetry energy. The job can be fulfilled by the isovector vector  $\rho$  meson:

$$L_{int} = g_\rho \bar{\psi} \gamma^\mu \boldsymbol{\rho}_\mu \cdot \frac{\boldsymbol{\tau}}{2} \psi . \quad (3.1.19)$$

where  $\boldsymbol{\tau} = (\boldsymbol{\tau}_1, \boldsymbol{\tau}_2, \boldsymbol{\tau}_3)$  contains the Pauli isospin matrices.

This interaction adds a field equation for the  $\rho$  meson; considering the fact that only the Lorentz time part and the third isospin component have a mean value on the ground state that is different from zero, one gets:

$$g_\rho \rho_3^0 = \left( \frac{g_\rho}{m_\rho} \right)^2 \frac{1}{2} (n_p - n_n) \quad (3.1.20)$$

where  $n_n$  and  $n_p$  are the neutron and proton number densities. Moreover, the Dirac eigenvalues have an additional term of the form:

$$g_\rho \rho_3^0 I_3 \quad (3.1.21)$$

where  $I_3$  is the isospin of the proton  $\frac{1}{2}$  or neutron  $-\frac{1}{2}$ . This contribution leads to different values of the Fermi momentum for the two nucleons and thus to a dependence of the energy density and of the pressure on the isospin asymmetry through the additional term:

$$\frac{1}{2} m_\rho^2 \rho_{03}^2 \quad (3.1.22)$$

The  $\rho$  meson coupling constant  $\frac{g_\rho}{m_\rho}$  is fixed directly with the experimental value of the symmetry energy.

One of the most remarkable features of the theory at this level is that all the five parameters, i.e. the coupling constants  $\frac{g_\sigma}{m_\sigma}$ ,  $\frac{g_\omega}{m_\omega}$ ,  $\frac{g_\rho}{m_\rho}$ ,  $b$  and  $c$  are linked to the saturation properties  $n_0$ ,  $B$ ,  $K$ ,  $m^*$  and  $S$  through algebraic relations (for the explicit expressions see section 4.8.1 of [Glendenning \(1997\)](#)). This makes particularly easy to explore the variability of the features of the EOS connected with the uncertainties of the empirical parameters. For this reason the Lagrangian of this particular model and these algebraic relations are exploited in the Bayesian analysis presented in chapter [7.5](#).

The major drawback of this simple theory concerns the derivative of the symmetry energy:  $L$  is just a derived quantity calculated directly from the  $E_{sym}$  (see eqn. [2.1.11](#)) and thus it cannot be fitted to its experimental value.

In order to overcome this issue, more parameters need to be added to the model: one possibility consists in introducing density depend couplings ([Typel & Wolter, 1999](#)). For the  $\sigma$  and  $\omega$  mesons this dependence is parametrized like:

$$g_i(n) = g_i(n_0) f_i(x) \quad i = \sigma, \omega \quad (3.1.23)$$

where:

$$f_i(x) = a_i \frac{1 + b_i(x + d_i^2)}{1 + c_i(x + d_i^2)} \quad (3.1.24)$$

and  $x = \frac{n}{n_0}$ .

An exponential dependence is instead chosen for the  $\rho$  meson:

$$g_\rho(n) = g_\rho(n_0) \exp[-a_\rho(x - 1)] \quad (3.1.25)$$

The Lagrangian in this case does not contain the  $\sigma$  self interaction terms and the quantities  $a_i$ ,  $b_i$ ,  $c_i$  and  $d_i$  are not independent; as a consequence the theory contains 7 free parameters. Additional contributions, the so called “rearrangement” terms, coming from the derivatives of the couplings appear both in the self-energies of the Dirac equation and in the expression for the pressure.

A second possibility to fix the value of  $L$  is to add other interaction terms to the Lagrangian like in the case of the SFHo EOS of [Steiner et al. \(2013a\)](#), described in next paragraph.

### 3.1.3 SFHo

SFHo is an EOS based on a statistical approach, able to include accurately the nuclear composition of NS matter, relying both on experimental nuclear masses and theoretical mass models. The interactions among nucleons is described using the framework of the RMF theory. The first version of the EOS, the so called HS, was developed by [Hempel & Schaffner-Bielich \(2010\)](#) using the TMA parameterization ([Toki et al., 1995](#)) and subsequently improved in [Hempel et al. \(2012\)](#). Finally, two new EOSs, SFHo and SFHx based on the same HS model but using a different RMF parametrization with respect to the original one, were reported in [Steiner et al. \(2013a\)](#). These last models were fitted to NS masses and radii constraints (see [Steiner et al. \(2010\)](#)): SFHo is the result of an "optimal" fit while SFHx represent the "extreme" case of a parametrization leading to very small radii. The EOS is provided for a range of densities between  $10^5 - 10^{15} \text{ g cm}^{-3}$  and temperatures from 0.1 MeV to 158.5 MeV ([Hempel, 2011](#)). The EOS for hot and dense matter is not important just for CCSN, but also for other kind of astrophysical phenomena like BNS mergers. In this model matter consists of nuclei, nucleons, electrons, positrons and photons and the weak equilibrium is not imposed. Because of the charge neutrality condition, the different thermodynamical variables are defined as a function of three independent variables: temperature ( $T$ ), baryon number density ( $n$ ) and proton fraction ( $Y_p$ ).

A RMFT is used in order to describe unbound interacting nucleons, while for densities below  $n_{nuc} = 10^{-5} \text{ fm}^{-3}$ , nucleons are treated as non-interacting ideal Dirac particles, because in this regime interactions become negligible. The Lagrangian ([Steiner et al., 2005](#)) contains the isoscalar scalar  $\sigma$  meson, the isoscalar vector  $\omega$  meson and the isovector vector

$\rho$  meson and additional non linear terms:

$$\begin{aligned}
 L = & \bar{\psi}[i\gamma_\mu(\partial^\mu + ig_\omega\omega^\mu) - (m - g_\sigma\sigma) - \frac{1}{2}g_\rho\gamma_\mu\bar{\tau} \cdot \bar{\rho}^\mu - \frac{1}{2}e(1 + \tau_3)\gamma_\mu A^\mu]\psi - \frac{1}{4}F_{\mu\nu}F^{\mu\nu} \\
 & + \frac{1}{2}(\partial_\mu\sigma\partial^\mu\sigma - m_\sigma^2) - \frac{\kappa}{6}(g_\sigma\sigma)^3 - \frac{\lambda}{24}(g_\sigma\sigma)^4 \\
 & - \frac{1}{4}\omega_{\mu\nu}\omega^{\mu\nu} + \frac{1}{2}m_\omega^2\omega_\mu\omega^\mu + \frac{\zeta}{24}g_\omega^4(\omega_\mu\omega^\mu)^2 \\
 & - \frac{1}{4}\bar{B}_{\mu\nu} \cdot \bar{B}^{\mu\nu} + \frac{1}{2}m_\rho^2\bar{\rho}_\mu \cdot \bar{\rho}^\mu + \frac{\xi}{24}g_\rho^4(\bar{\rho}^\mu \cdot \bar{\rho}_\mu)^2 \\
 & + g_\rho^2 f(\sigma, \omega_\mu\omega^\mu)\bar{\rho}^\mu \cdot \bar{\rho}_\mu
 \end{aligned} \tag{3.1.26}$$

where:

$$F_{\mu\nu} = \partial_\mu A_\nu - \partial_\nu A_\mu \tag{3.1.27}$$

$$\omega_{\mu\nu} = \partial_\mu\omega_\nu - \partial_\nu\omega_\mu \tag{3.1.28}$$

$$\bar{B}_{\mu\nu} = \partial_\mu\bar{\rho}_\nu - \partial_\nu\bar{\rho}_\mu \tag{3.1.29}$$

$$f(\sigma, \omega_\mu\omega^\mu) = \sum_{i=1}^6 a_i\sigma_i + \sum_{j=1}^3 b_j(\omega_\mu\omega^\mu)^j \tag{3.1.30}$$

In total this Lagrangian counts 17 parameters: first, the 5 coupling of the non linear Walecka theory described in the previous section  $g_\sigma$ ,  $g_\omega$ ,  $g_\rho$ ,  $\kappa$  and  $\lambda$ ; in addition the mass of the  $\sigma$  meson and the coupling  $\zeta$  and  $\xi$  associated to the fourth order terms in  $\omega$  and  $\rho$ ; finally the coefficients  $a_i$  and  $b_i$  that express the dependence on the density of the symmetry energy. The use of these large amount of parameters allows to reproduce not only the saturation properties on nuclear matter, but also  $^{208}\text{Pb}$  and  $^{90}\text{Zr}$  charge radii and binding energy as well as the NS maximum mass constraint. Moreover, SFHo shows very good agreement with some ab initio theoretical calculations of pure neutron matter, derived, for examples, from Chiral effective field theory (EFT) (Krüger et al. (2013)). The SFHo's resulting saturation properties together with the maximum mass of a NS at zero temperature and the radius for the  $1.4M_\odot$  configuration are shown in Table 3.1.

$n_B^0 [fm^{-3}]$	$B [MeV]$	$K [MeV]$	$m^*/m$	$S [MeV]$	$L [MeV]$	$M_{max} [M_\odot]$	$R_{1.4} [km]$
0.1583	-16.19	245.4	0.7609	31.57	47.10	2.059	11.88

**Table 3.1:** from Steiner et al. (2013a). Properties of nuclear matter and neutron stars of the RMF model SFHo.

The treatment of cluster formation and inhomogeneous matter at low densities is implemented by means of a statistical distribution of different nuclei, whose abundances are calculated using the hypothesis of NSE. These nuclei are treated as Maxwell-Boltzmann

particles while the free nucleons are considered as Fermi-Dirac particles, with interaction modelled through the SFHo RMF parametrization.

For the description of nuclei in this inhomogeneous layer, SFHo is based on the so called AWT table (Audi et al. (2002)), which contains experimental data of masses and, for what concerns nuclei whose masses have not been measured, values are taken from the finite range droplet model of Möller et al. (1995).

The effect of a finite temperature will be to change the number density of certain nuclei because excited states can be populated. This fact is taken into account by means of a semiempirical temperature dependent degeneration function (Fai & Randrup, 1982).

In order to determine the composition, it is also important to take into account the Coulomb energy; in this context nuclei are treated as homogeneous sphere of radius  $R(A) = \left(\frac{3A}{4\pi n_0}\right)^{\frac{1}{3}}$ , distributed as spherical Wigner-Seitz (WS) cells and a uniform distribution of electrons is assumed. The Coulomb energy then vanishes in the region of uniform nuclear matter.

The procedure used to get all the relevant thermodynamical variables, is to write the general expression for the thermodynamic potential assuming the densities  $n_n$ ,  $n_p$ ,  $n_{A,Z}$  and  $n_e$  of neutrons, protons, nuclei and electrons to be known. Only afterwards the true values of this quantities are determined by imposing chemical equilibrium of baryons.

In this description all baryons (free or bound in nuclei) are approximated by hard spheres with a volume of  $\frac{1}{n_0}$ , so the density of nuclei is given by  $\frac{A}{n_0}$ . Then the excluded volume method is implemented: this is based on the principle for which baryons in nuclei can not overlap with any other baryon, so the volume that can be occupied by nuclei is just the one that is not already filled by baryons:

$$\kappa = 1 - \frac{n}{n_0} \tag{3.1.31}$$

For unbound nucleons the constraint imposed is that they cannot lie inside the nuclei; this can be expressed through the so called filling factor of the nucleus:

$$\xi = 1 - \sum_{A,Z} A \frac{n_{A,Z}}{n_0} \tag{3.1.32}$$

In the model, the total energy is written as the sum of separate contributions from electrons, nucleons, nuclei and Coulomb energy, so the total partition function becomes the product of the single partition functions associated to these contributions:

$$Z(T, V(N_i)) = Z_e Z_{nuc} \prod_{A,Z} Z_{A,Z} Z_{Coul} \tag{3.1.33}$$

where  $(N_i)$  is the set of all particle numbers. From this equation the thermodynamical

potential, or Helmotz free energy, can be derived:

$$f = \sum_{A,Z} f_{A,Z}^0(T, n_{A,Z}) + \sum_{A,Z} f_{A,Z}^{Coul} - T \sum_{A,Z} n_{A,Z} \ln(\kappa) + \xi f_{RMFT}^0(T, \frac{n_n}{\xi}, \frac{n_p}{\xi}) \quad (3.1.34)$$

where the first and second terms are the nuclei ideal gas and Coulomb energy respectively. The third addend comes from the excluded volume correction and assures the disappearance of nuclei at the saturation density. Finally the last term represents the nucleons contribution calculated using RMFT but taking into account that the volume available is not the entire volume but the part remaining unoccupied by nuclei.

From the expression 3.1.34 all the thermodynamical variables, such as entropy density, energy density, pressure and chemical potentials can be directly derived in a consistent way. Finally, the values of the densities  $n_n$ ,  $n_p$ ,  $n_{A,Z}$ ,  $n_e$  need to be fixed for a given  $n$  and  $Y_p$ . The electron contribution is constrained by charge neutrality  $n_e = Y_p n$ , while for the baryons the conservation of the baryon number and of the proton fraction are assumed and the chemical equilibrium between nuclei and nucleons is imposed.

### 3.2 The hyperon puzzle and its possible solutions

As discussed in Chapter 1, the identification of the degrees of freedom characterizing the inner core of a NS is the first issue to face in order to build an EOS and it is still unsolved. However, at densities  $> (2 - 3) n_0$  hyperons (Ys) are expected to appear: the neutrons on the Fermi surface can decay to  $\Lambda$ s, the  $\Sigma$  particle can be produced through the reaction  $e^- + n \rightarrow \Sigma^- + \nu_e$  and similar processes can form other hyperons. NS equilibrium conditions make these reactions energetically favoured, mainly because of the fermionic nature of the nucleons (Ns). The proton and neutron chemical potentials increase very rapidly with the baryon density. When the Fermi energy overcomes the eigenvalue of the energy of other baryon species (the mass in a non-interacting system), the conversion of some neutrons and protons to these new baryons lowers the total energy of the system.

To describe the hyperonic matter, one should in principle rely on the underlying YN and YY two-body interactions and on the three-body forces of the type YNN, YYN and YYY. However, because of the small amount of experimental data and the complexities of theoretical calculations, these kind of interactions are poorly constrained. The available data come from the study of hypernuclei and strange particle physics (Hashimoto, 2004; Millener, 2009; Botta et al., 2012; Rappold et al., 2013).

Since the seminal paper of Ambartsumyan & Saakyan (1960), several works studied the effect of hyperons in the NS matter, using both microscopic and phenomenological approaches.

Concerning the first category of models, the extension to include hyperons has been performed mainly in the framework of the Brueckner-Hartree-Fock (BHF) approximation (Schulze et al., 1995, 1998; Baldo et al., 1998, 2000; Vidana et al., 2000b,a; Schulze et al., 2006; Schulze & Rijken, 2011) and the Dirac-Brueckner-Hartree-Fock (DBHF) theory (Sammarruca, 2009; Katayama & Saito, 2014, 2015). On the other hand, among the phenomenological techniques, the most broadly adopted are the ones based on Skyrme forces (Balberg & Gal, 1997; Balberg et al., 1999) and RMF models. The first attempt to include massive baryons into the framework of RMF theory was performed by Garpman et al. (1979) and subsequently by Glendenning (1982a, 1985, 1989). This model is presented in the the following paragraph.

### 3.2.1 Hyperons in RMFT

The theory of Glendenning (1985) is an extension of the RMF model presented in sections 3.1.1 and 3.1.2 to incorporate additional baryon species (identified by the subscript B). In particular the most relevant are the members of the octet of baryons with the lowest masses,  $\Lambda$ ,  $\Sigma$  and  $\Xi$ , whose properties are listed in Figure 3.2.1.

	m (MeV)	J	$I_3$	q	s
N	939	1/2	1/2	1	0
			-1/2	0	0
$\Lambda$	1115		0	0	-1
$\Sigma$	1190		1	1	-1
			0	0	-1
			-1	-1	-1
$\Xi$	1315		1/2	0	-2
			-1/2	-1	-2

**Figure 3.2.1:** from Glendenning (2000). The baryons of the first octet and their features: the spin  $J$ , the isospin projection  $I_3$ , the charge  $q$ , and strangeness  $s$

The new generalized Lagrangian is:

$$\begin{aligned}
 L = & \sum_B \bar{\psi}_B [i\gamma_\mu(\partial^\mu + ig_{\omega B}\omega^\mu) - (m_B - g_{\sigma B}\sigma) - \frac{1}{2}g_{\rho B}\gamma_\mu\boldsymbol{\tau} \cdot \boldsymbol{\rho}^\mu] \psi_B \\
 & + \frac{1}{2}(\partial_\mu\sigma\partial^\mu\sigma - m_\sigma^2\sigma^2) - \frac{1}{4}\omega_{\mu\nu}\omega^{\mu\nu} + \frac{1}{2}m_\omega^2\omega_\mu\omega^\mu - \frac{1}{4}\boldsymbol{\rho}_{\mu\nu} \cdot \boldsymbol{\rho}^{\mu\nu} \\
 & + \frac{1}{2}m_\rho^2\boldsymbol{\rho}_\mu \cdot \boldsymbol{\rho}^\mu - \frac{1}{3}bm_n(g_\sigma\sigma)^3 - \frac{1}{4}c(g_\sigma\sigma)^4
 \end{aligned} \tag{3.2.1}$$

From the Dirac equation for each species B, one can obtain similar eigenvalues as in eqn. 3.1.6 with the additional term 3.1.22. The meson fields eqns. are also similar to 3.1.18, 3.1.11 and 3.1.21 but the contribution of each baryon of the octet must be summed. The final expressions for the energy density and the pressure become:

$$\begin{aligned}
 e = & \frac{1}{3}bm_n(g_\sigma\sigma)^3 + \frac{1}{4}c(g_\sigma\sigma)^4 + \frac{1}{2}m_\sigma^2\sigma^2 + \frac{1}{2}m_\omega^2\omega^2 + \frac{1}{2}m_\rho^2\rho_{03}^2 \\
 & + \frac{1}{3}\sum_B \frac{2J_B + 1}{2\pi^2} \int_0^{k_F} k^2 dk \sqrt{k^2 + m_B^{*2}}
 \end{aligned} \tag{3.2.2}$$

$$\begin{aligned}
 p = & -\frac{1}{3}bm_n(g_\sigma\sigma)^3 - \frac{1}{4}c(g_\sigma\sigma)^4 - \frac{1}{2}m_\sigma^2\sigma^2 + \frac{1}{2}m_\omega^2\omega^2 + \frac{1}{2}m_\rho^2\rho_{03}^2 + \\
 & \frac{1}{3}\sum_B \frac{2J_B + 1}{2\pi^2} \int_0^{k_f} k^2 dk \frac{k^2}{\sqrt{k^2 + m_B^{*2}}}
 \end{aligned} \tag{3.2.3}$$

These equations are supplemented by the expressions for the conserved quantities which characterize the system under consideration, such as the baryon number, the electric charge, and strangeness densities (the latter is not conserved in NS matter):

$$\begin{aligned}
 n &= \sum_B n_B, \quad n_B = (2J_B + 1)b_B \frac{k_B^3}{6\pi^2} \\
 q &= \sum_B Q_B, \quad Q_B = (2J_B + 1)q_B \frac{k_B^3}{6\pi^2} \\
 S &= \sum_B S_B, \quad S_B = (2J_B + 1)s_B \frac{k_B^3}{6\pi^2}
 \end{aligned} \tag{3.2.4}$$

where  $b_B$ ,  $q_B$  and  $s_B$  are the baryon, electric and strangeness charge respectively. Then the composition of the system and thus the Fermi momenta and the meson field strengths can be calculated by imposing the charge neutrality and the chemical equilibrium of the system.

Five of the coupling constants of the Lagrangian can be constrained through the saturation properties of nuclear matter (see section 3.1.2). On the other hand, the hyperons couplings

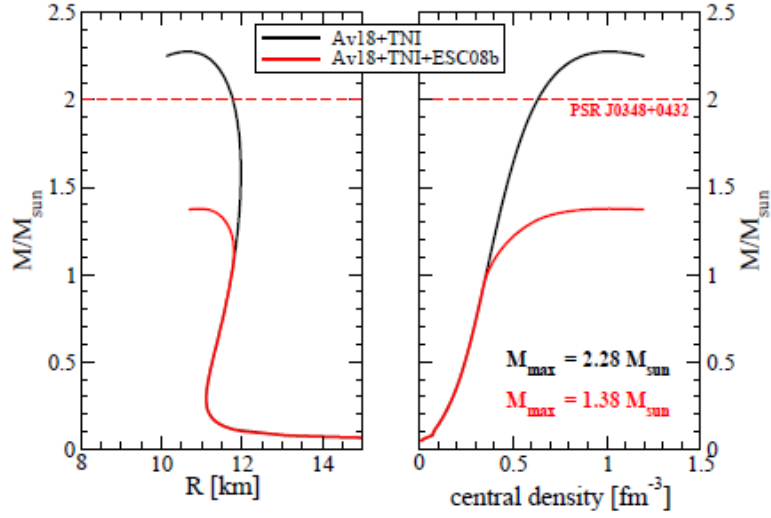


**Figure 3.2.2:** from [Bombaci \(2017a\)](#). Mass as a function of the radius (left) and of the central baryon density (right) in the case of nucleon stars, Av18+TNI ([Wiringa et al., 1988](#); [Baldo et al., 1997](#)) and hyperon stars, Av18+TNI+ESC08b ([Rijken et al., 2010](#)). The curves are obtained with a Brueckner-Hartree-Fock (BHF) calculation ([Bombaci, 2017b](#)). No YY interaction and no three-body interactions have been considered.

are not linked to this ground state and little information about them is gained from their highly uncertain binding energies in hypernuclei (see e.g. [Raduta et al. \(2014\)](#)). A common approach ([Schaffner et al., 1993](#); [Schaffner, 1996](#); [Drago et al., 2014a](#)) consists in choosing the scalar couplings which reproduce the following values of the binding energies in nuclear matter:

$$U_{\Lambda}^{(N)} = -28 \text{ MeV}, \quad U_{\Sigma}^{(N)} = 30 \text{ MeV}, \quad U_{\Xi}^{(N)} = -18 \text{ MeV} \quad (3.2.5)$$

while for the couplings with vector mesons the SU(6) symmetry relations are employed:

$$\frac{1}{3}g_{\omega N} = \frac{1}{2}g_{\omega \Lambda} = \frac{1}{2}g_{\omega \Sigma} = g_{\omega \Xi} \quad (3.2.6)$$

$$g_{\rho N} = \frac{1}{2}g_{\rho \Sigma} = g_{\rho \Xi}, \quad g_{\rho \Lambda} = 0 \quad (3.2.7)$$

### 3.2.2 The hyperon puzzle

The appearance of new degrees of freedom such as hyperons in the inner core of NS has the effect of reducing the pressure. As a consequence, the EOS becomes softer and the maximum mass is lowered.

The majority of RMF theories with hyperons results in maximum masses in the range  $(1.4 - 1.8)M_{\odot}$  (Weber & Weigel, 1989; Glendenning & Moszkowski, 1991; Knorren et al., 1995; Schaffner & Mishustin, 1996; Huber et al., 1999; Pal et al., 1999; Hanauske et al., 2000; Schramm & Zschesche, 2003). Moreover, the reduction of the mass is even larger for models based on microscopic calculations (Baldo et al., 2000; Vidana et al., 2000a; Nishizaki et al., 2001; Li & Schulze, 2008; Djapo et al., 2010; Schulze & Rijken, 2011).

An example of the effect of hyperons on the EOS is shown in Figure 3.2.2: in this case  $M_{max}$  varies from a value significantly bigger than  $2M_{\odot}$  to  $M_{max}$  even smaller than  $1.4M_{\odot}$ . On the other hand, there is an observational evidence of a NS with mass  $2.14_{-0.09}^{+0.10}M_{\odot}$  (Cromartie et al., 2019) and thus an EOS that cannot sustain a configuration of at least  $2.05M_{\odot}$  (the lower bound of 68% CI) is automatically ruled out. It is necessary to point out that most of the works referred in this chapter consider as a lower limit for the maximum mass the value of  $2M_{\odot}$  derived from the older measurement of Antoniadis et al. (2013) (see chapter 2.3.1). Although this constraint needs to be updated in the light of the more recent observation, the problem discussed and the underlined physics remain substantially the same.

The tension between the typical maximum masses obtained for EOS containing hyperons and new observational constraints is at the origin of the so called "hyperon puzzle". Indeed, on one side the appearance of hyperons in NS seems inevitable due to energetic considerations but on the other side the consequence is to make the resulting maximum mass incompatible with observations.

Three possible solutions have been suggested to solve the hyperon puzzle providing an additional repulsion that would reduce the softening of the EOS. These consist in the introduction of:

- a repulsive YY interaction
- repulsive three-body forces including hyperons (YTBF)
- a phase transition to deconfined quark matter which takes place at a density below the threshold for hyperons appearance.

The first approach based on the YY interaction has been mainly developed in the context of RMF models. In this case, the additional repulsion can be obtained through the exchange of a vector meson  $\phi$  and through the introduction of density dependent or higher order couplings in the Lagrangian. Moreover, the SU(6) symmetry breaking in the couplings between the vector meson and the hyperons could amplify the repulsion.

All these prescriptions cause a shift of the hyperons production threshold to larger density and/or a reduction of the hyperons content in  $\beta$ -equilibrated matter allowing, in some cases, to reach a maximum mass  $> 2M_{\odot}$  (Huber et al., 1999; Taurines et al., 2000; Hofmann

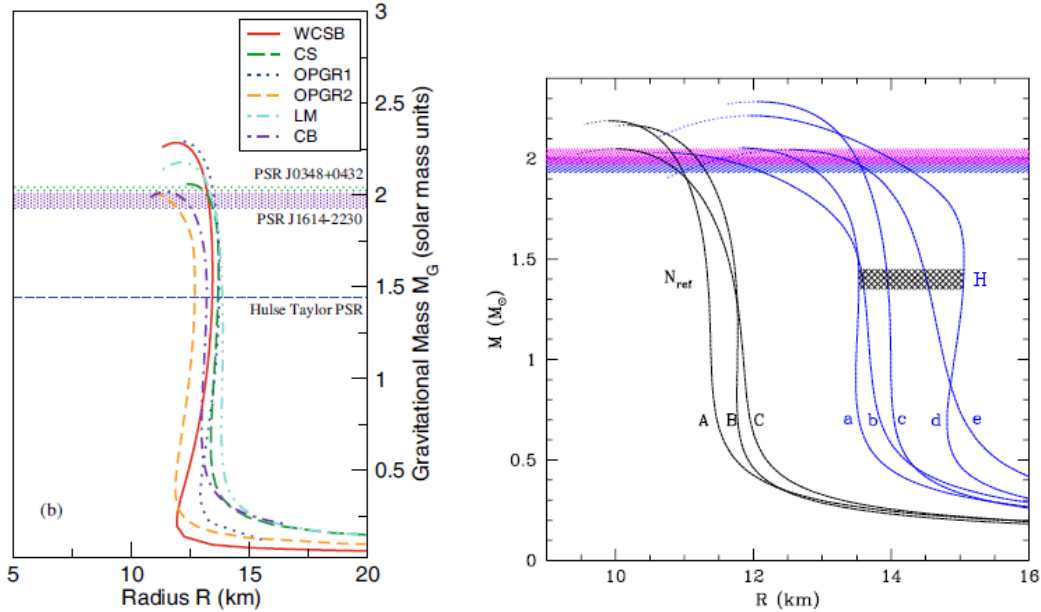


**Figure 3.2.3:** Mass-radius curves for a set of selected EOSs including hyperon-hyperon repulsion satisfying the  $2M_{\odot}$  constraint.

Left (from Chatterjee & Vidaña (2016)): WCSB (Weissenborn et al., 2012a), LM (Lopes & Menezes, 2014), OPGR1 and OPGR2 (Oertel et al., 2015) (note: the OPGR2 is not compatible with the new mass limit), CS (Colucci & Sedrakian, 2013), CB (Char & Banik, 2014). Reprinted by permission from Springer Nature Customer Service Centre GmbH, Copyright © 2016, Springer Nature.

Right (from Fortin et al. (2015)): a (Sulaksono & Agrawal, 2012), b (Bednarek et al., 2012), c (Weissenborn et al., 2012a), d (Uechi & Uechi, 2009), e (Gusakov et al., 2014). Reproduced with permission © ESO.

et al., 2001; Rikovska-Stone et al., 2007; Dhiman et al., 2007; Dexheimer & Schramm, 2008; Bombaci et al., 2008; Miyatsu et al., 2012; Whittenbury et al., 2012; Thomas et al., 2013; Gomes et al., 2015).

In particular, since the short range repulsion of nuclear force is provided by the exchange of  $\omega$  meson, the inclusion of an additional vector meson  $\phi$  could in principle have the same effect proving an increase of this repulsion. At the same time, the requirement of consistency with hypernuclear data forces this new hidden strangeness meson to be coupled only with hyperons, describing an interaction of the type  $YY$ . This possibility has been investigated in many studies (see e.g. Bednarek et al. (2012); Weissenborn et al. (2012a,b, 2014); Agrawal et al. (2012); Lopes & Menezes (2014); Oertel et al. (2015); Maslov et al. (2015)). One of

the main conclusion of these analyses is the need of quartic terms in the  $\phi$  meson in order to obtain an EOS in agreement with observations.

In addition the effect of kaon and antikaon condensation was also considered in [Gupta & Arumugam \(2012\)](#) and [Char & Banik \(2014\)](#). Finally, other approaches such as relativistic energy density functional theory ([Colucci & Sedrakian, 2013](#); [van Dalen et al., 2014](#)) and Skyrme-type models ([Lim et al., 2015](#)) have also been exploited.

In [Figure 3.2.3](#) are shown the mass-radius curves for some selected EOSs containing hyperon-hyperon repulsion.

The drawback of this solution appears to be the need for a fit of a large amount of parameters which are experimentally poorly constrained. For example, [Fortin et al. \(2017\)](#) showed that a wide range of values for the  $\Lambda\phi$  coupling is compatible with both hypernuclear experimental data (here in particular the binding energy  $\Delta B_{\Lambda\Lambda}$  of in double- $\Lambda$  hypernuclei) and the observed mass limit. This means that it is currently still impossible to have a strong experimental proof of the validity of the employed model.

The second suggested possibility to solve the hyperon puzzle is the incorporation of YTBFs in models based on many body calculations. The role of TBFs is important to fit the properties of both nuclei and nuclear matter. In analogy, YTBFs, such as NNY, NYY and YYY, could exist and help to stiffen the high density EOS providing, as the case of YY, additional repulsion.

This kind of interaction was suggested for the first time by [Dalitz \(1960\)](#) and later it was applied to the problem of the NS EOS ([Takatsuka & Yamamoto, 2002](#); [Takatsuka et al., 2008](#)). Since the measurement of the  $2M_{\odot}$  this solution has been the subject of different investigations ([Vidana et al., 2011](#); [Yamamoto et al., 2013, 2014](#); [Lonardonì et al., 2015](#); [Katayama & Saito, 2014, 2015](#); [Yamamoto et al., 2016](#); [Logoteta et al., 2019](#)). However, despite the importance of the YTBF, it is still unclear if their inclusion represent the solution of the hyperon puzzle or if other ingredients are also required.

### 3.2.3 *The small radii problem*

The maximum mass observation is not the only constraint to consider concerning the hyperon puzzle: the radii measurements are also fundamental to test the validity of a theoretical model of the EOS.

Unfortunately, the available radii estimate have quite large errorbars and they are model dependent and thus still object of debate. However, many analyses suggest very small radii, of the order of  $\sim 10 - 11.5$  km for the canonical  $1.4M_{\odot}$  star ([Guillot et al. \(2013\)](#); [Guillot & Rutledge \(2014\)](#); [Özel & Freire \(2016\)](#) and see [chapter 2.3.2](#) for discussion).

The hyperons could in principle help to obtain configurations consistent with this experimental suggestion: indeed the hyperon content of a NS is inversely proportional to its radius ([Providência & Rabhi, 2013](#)). However, as discussed in the previous section, the maximum

masses for these EOSs are very small.

On the other hand, the hyperonic EOSs which are able to fulfill the  $2M_{\odot}$  constraint thanks to both the aforementioned mechanisms (YY repulsion and YTBFs) are characterized by very large radii, as evident in Figure 3.2.3 for few representative solutions (see also table 1 of Chatterjee & Vidaña (2016)). In addition, Fortin et al. (2015), with a systematic study, found a lower limit of 13 km for  $R_{1.4}$  caused by the required stiffening of an EOS containing hyperons to be consistent with the mass limit (see the right panel of Figure 3.2.3 and Figure 5 of Fortin et al. (2015)).

As a consequence, if the "small radii" evidence will be confirmed through more precise and reliable measurements, the hypothesis on the existence of hyperonic stars will be difficult to reconcile with both masses and radii experimental constraints.

A hypothetical way out is represented by the third possible solution to the hyperon puzzle: the appearance of deconfined quark matter in the NS interior (Alford et al., 2008; Weissenborn et al., 2012a; Ozel et al., 2010; Schulze & Rijken, 2011; Schramm et al., 2012; Klähn et al., 2013; Zdunik & Haensel, 2013; Bonanno & Sedrakian, 2012; Lastowiecki et al., 2012; Masuda et al., 2013; Schramm et al., 2013; Fraga et al., 2014).

In this case one needs to investigate whether the repulsion provided by the quark matter suffice to obtain  $> 2M_{\odot}$  configurations and at the same time not too large radii.

The theoretical descriptions of this matter is developed in the framework of different phenomenological models, the most widely used being the MIT bag model (Farhi, 1986) and the Nambu-Jona-Lasinio (NJL) model (Nambu & Jona-Lasinio, 1961); for superconductive quark matter, models are based either on the two-flavor color superconducting (2SC) state or on the color flavor locked (CFL) superconducting one.

Here only the MIT bag model is described because is the one employed in the work presented in chapter 8 and it is at the base of the two families scenario (see section 3.3).

### 3.2.4 *The MIT bag model*

The MIT bag model provides a very simple description of the deconfined quark phase, in terms of the energy density and the pressure of a quark gas: to this the so called "bag constant" is added, which is defined as the difference in energy between the perturbative vacuum and true vacuum.

The baryon and energy density and the pressure can be derived from the thermodynamic potential. At the first order in the strong interaction coupling constant  $\alpha_s$ , the latter is the

sum of different contributions (Haensel et al., 1986):

$$\Omega_f(\mu_f) = -\frac{\mu_f^4}{4\pi^2} \left(1 - \frac{2\alpha_s}{\pi}\right) \quad f = u, d \quad (3.2.8)$$

$$\begin{aligned} \Omega_s(\mu_s) = & -\frac{1}{4\pi^2} \left\{ \mu_s \sqrt{\mu_s^2 - m_s^2} (\mu_s^2 - \frac{5}{3} m_s^2) + \frac{3}{2} m_s^4 \ln \frac{\mu_s + \sqrt{\mu_s^2 - m_s^2}}{m_s} \right. \\ & - \frac{2\alpha_s}{\pi} \left[ 3(\mu_s \sqrt{\mu_s^2 - m_s^2} - m_s^2 \ln \frac{\mu_s + \sqrt{\mu_s^2 - m_s^2}}{m_s})^2 \right. \\ & - 2(\mu_s^2 - m_s^2)^2 - 3m_s^4 \ln \frac{m_s^2}{\mu_s} \\ & \left. \left. + 6 \ln \frac{\sigma}{\mu_s} (\mu_s \sqrt{\mu_s^2 - m_s^2} m_s^2) - m_s^4 \ln \frac{\mu_s + \sqrt{\mu_s^2 - m_s^2}}{m_s} \right] \right\} \quad (3.2.9) \end{aligned}$$

$$\Omega_e(\mu_e) = -\frac{\mu_e^4}{12\pi^2} \quad (3.2.10)$$

Here  $m_f$  and  $\mu_f$  are the mass and the chemical potential of the quark flavor  $f$  and the pre-factor  $\frac{1}{4\pi^2} = -\frac{\gamma_f}{24\pi^2}$  with  $\gamma_f = 6 = 2 \times 3_{color}$  is the degeneracy factor. In this approximation only the strange quark has a mass  $m_s \neq 0$ . Finally,  $\sigma$  is the renormalization scale for the strange quark mass: the standard choice is to renormalize the quark mass "on shell", i.e.  $\sigma = m_s$ . In order to account also the case of low mass strange quark, Farhi (1986) believes that  $\sigma$  should be identified with a mass scale typical of the problem ( $\sim 300$  MeV).

The number densities are obtained directly from the thermodynamic potential as:

$$n_i(\mu_i) = -\frac{\delta\Omega_i}{\delta\mu_i} \quad (3.2.11)$$

and thus the separate contributions are:

$$n_f = \frac{\mu_f^3}{\pi^2} \left(1 - \frac{2\alpha_s}{\pi}\right) \quad f = u, d \quad (3.2.12)$$

$$n_s = \frac{\mu_s^2 - m_s^2}{\pi^2} \left\{ \sqrt{\mu_s^2 - m_s^2} - \frac{2\alpha_s}{\pi} \left[ \mu_s - \frac{3m_s^2}{\sqrt{\mu_s^2 - m_s^2}} \ln \frac{\mu_s + \sqrt{\mu_s^2 - m_s^2}}{\sigma} \right] \right\} \quad (3.2.13)$$

$$n_e = \frac{\mu_e^3}{3\pi^2} \quad (3.2.14)$$

The relationships between the quark chemical potentials are determined again by imposing the conservation of the electric and the baryon charge (the strangeness is not conserved and thus the respective chemical potential is zero):

$$\mu_d = \mu_u + \mu_e \quad , \quad \mu_s = \mu_d \quad (3.2.15)$$

and the condition of charge neutrality:

$$\frac{2}{3}n_u(\mu_u) = \frac{1}{3}[n_d(\mu_d) + n_s(\mu_s)] + n_e(\mu_e) \quad (3.2.16)$$

These equations allow to write all the chemical potentials as function of just one of them, which is indicated as  $\mu$ . The pressure can then be expressed in terms of this independent chemical potential and of the bag constant  $B$  which represents the vacuum pressure:

$$P(\mu) = - \sum_i \Omega_i(\mu) - B \quad (3.2.17)$$

Also the energy density has a contribution from  $B$  as the energy per unit volume carried by the vacuum. The expression is:

$$e = \sum_i (\Omega_i + \mu_i n_i) + B \quad (3.2.18)$$

while the baryon number density is just the average of the values for the different quark flavours:

$$n = \frac{1}{3}(n_u + n_d + n_s) \quad (3.2.19)$$

The equilibrium configuration of the system is the one in which the vacuum pressure is balanced by the Fermi pressure, i.e.:

$$\frac{\delta}{\delta\mu} \left( \frac{e}{n} \right) = 0 \quad (3.2.20)$$

or equivalently:

$$\sum_i \Omega_i = -B \quad (3.2.21)$$

This additional equation allows to determine  $\mu$  once  $B$  and  $m_s$  are specified.

Let us consider now an approximation of the bag model obtained by ignoring one gluon exchange and thus by setting  $\alpha_s = 0$ . In addition the contribution from the electrons is neglected and the system is treated just as a non-interacting Fermi gas of quarks. Equations 3.2.8 and 3.2.9 reduce to:

$$\Omega_f(\mu_f) = - \frac{\mu_f^4}{4\pi^2} \quad f = u, d \quad (3.2.22)$$

$$\Omega_s(\mu_s) = - \frac{1}{4\pi^2} \left\{ \mu_s \sqrt{\mu_s^2 - m_s^2} (\mu_s^2 - \frac{5}{3}\mu_s^2) + \frac{3}{2}m_s^4 \ln \frac{\mu_s + \sqrt{\mu_s^2 - m_s^2}}{m_s} \right\} \quad (3.2.23)$$

and eqns 3.2.24 and 3.2.34 become simply:

$$n_f = \frac{\mu_f^3}{\pi^2} \quad f = u, d \quad (3.2.24)$$

$$n_s = \frac{\mu_s^2 - m_s^2}{\pi^2} \left\{ \sqrt{\mu_s^2 - m_s^2} \right\} \quad (3.2.25)$$

Finally the pressure and energy density are explicitly:

$$p = \frac{\mu_u^4}{4\pi^2} + \frac{\mu_d^4}{4\pi^2} + \frac{1}{4\pi^2} \left\{ \mu_s \sqrt{\mu_s^2 - m_s^2} (\mu_s^2 - \frac{5}{3} m_s^2) + \frac{3}{2} m_s^4 \ln \frac{\mu_s + \sqrt{\mu_s^2 - m_s^2}}{m_s} \right\} - B \quad (3.2.26)$$

$$e = \frac{3}{4\pi} \mu_d^4 + \frac{3}{4\pi} \mu_u^4 + \frac{3}{4\pi} \left[ \mu_s \sqrt{\mu_s^2 - m_s^2} (\mu_s^2 - \frac{1}{2} m_s^2) - \frac{1}{2} m_s^4 \ln \frac{\mu_s + \sqrt{\mu_s^2 - m_s^2}}{m_s} \right] + B \quad (3.2.27)$$

Using the massless quark approximation (also the mass of the s quark is neglected) this expressions lead to the simple EOS:

$$p = \frac{3\mu^4}{4\pi^2} - B \quad (3.2.28)$$

$$e = \frac{9\mu^4}{4\pi^2} + B \quad (3.2.29)$$

$$e = 3p + 4B \quad (3.2.30)$$

The thermodynamical potential in the MIT bag model can also be parametrized as in (Alford et al., 2005):

$$\Omega_{QM} = -\frac{3}{4\pi^2} a_4 \mu^4 + \frac{3}{4\pi^2} a_2 \mu^2 + B_{eff} \quad (3.2.31)$$

with  $a_4 \equiv 1 - c$ . The coefficient  $c$  account for the QCD correction: in the non-interacting quark approximation  $c = 0$  and thus  $a_4 = 1$ . Fraga et al. (2001) demonstrated that a good estimate for  $c$  is  $\sim 0.3$ , meaning that the QCD contribution is not negligible.

As evident from eqn 3.2.23, the  $\mu^2$  term appear because of the strange quark mass, increasing the free energy. On the other hand a similar but negative contribution can arise also from color superconductivity and it is written in terms of the pairing energy  $\Delta$ . Here the color superconductive quark matter is not considered and the interested reader is reminded to references Alford et al. (2005) and Weissenborn et al. (2011). Therefore here  $a_2 \sim m_s^2$ .

In this parametrization  $B_{eff}$ , the effective bag constant, gathers all the parts of the free energy which does not depend on  $\mu$ .

The QCD correction  $c$  has no effect on the expression of the EOS,  $e(p)$  for quark matter. Indeed, with  $a_2 = 0$ , i.e. considering massless  $s$  quark, one obtains:

$$p = (1 - c) \frac{3\mu^4}{4\pi^2} - B_{eff} \quad (3.2.32)$$

$$e = 3(1 - c) \frac{3\mu^4}{4\pi^2} + B_{eff} \quad (3.2.33)$$

$$e = 3p + 4B_{eff} \quad (3.2.34)$$

recovering eqn. 3.2.30. However,  $c$  influences the dependence of the pressure on the chemical potential, strongly effecting the position of an eventual phase transition from normal to quark matter. At the same time, if the transition density  $n_c$  or the Witten density (see next paragraph) is kept fixed, then changing  $c$  modifies the value of the effective bag constant  $B_{eff}$ .

Finally, this model can also be described by the so called constant speed of sound (CSS) parametrization (Drago et al., 2019):

$$e = \frac{p - p_0}{c_s^2} + e_0 \quad (3.2.35)$$

$$p = \frac{c_s^2 e_0}{c_s^2 - 1} \left[ \left( \frac{n}{n_0} \right)^{c_s^2 + 1} - 1 \right] \quad (3.2.36)$$

where  $n_0$ ,  $p_0$  and  $e_0$  are the baryon density, the pressure and the energy density at the "beginning" of the quark EOS. With  $e_0 = 4B$  and  $c_s^2 = \frac{1}{3}$  equation 3.2.35 is identical to eqn. 3.2.30.

### 3.2.5 Hybrid stars (HyS)

The first possibility for stars containing quark matter are the so called hybrid stars (HyS): they are characterized by a core composed by quark matter and an envelope of hadronic matter. The two phases are connected through a phase transition described using a Maxwell or a Gibbs constructions.

In this case the EOS is written as (Alford & Han, 2014):

$$e(p) = \begin{cases} e_{NM}(p) & p < p_{trans} \\ e_{NM}(p_{trans}) + \Delta e + \frac{p - p_{trans}}{c_s^2} & p > p_{trans} \end{cases} \quad (3.2.37)$$

which is 3.2.35 for  $p_0$  equal to the transition pressure and  $e_0$  given by the sum of the pressure of the nuclear matter (NM) EOS and the energy density discontinuity at the transition  $\Delta e$ .

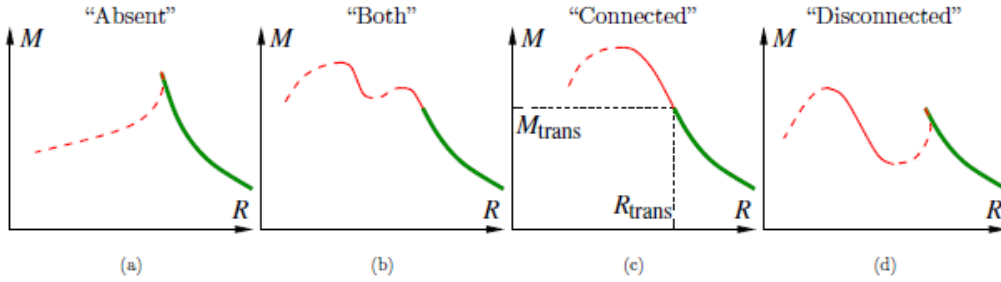


**Figure 3.2.4:** from Alford & Han (2014). Possible topologies of HyS’ mass-radius relation. The green line is the hadronic branch, the solid red lines are stable HyS and the dashed red lines are unstable HyS. (a): the hybrid branch is absent, (c): there is a connected branch, (d): there is a disconnected branch, (b): there are both types of branch.

As described in section 1.4, the stability condition for a compact object states that the mass needs to increase with the central pressure  $p_c$ . Thus, if for  $p_c = p_{trans}$  this criteria is fulfilled the stable HyS branch will be connected to the hadronic one (c). In the case of small quark matter core, the existence of such a branch is almost independent from the slope ( $c_s^{-2}$ ) of  $e(p)$  and it is entirely determined by the discontinuity in energy density  $\Delta e$  at the transition (Seidov, 1971; Schaeffer et al., 1983; Zdunik et al., 1987; Migdal et al., 1979; Kämpfer, 1981; Lindblom, 1998). In particular, the connected HyS branch is found if  $\Delta e$  is smaller than a threshold value  $\Delta e_{crit}$  expressed by:

$$\frac{\Delta e_{crit}}{e_{trans}} = \frac{1}{2} + \frac{3 p_{trans}}{2 e_{trans}} \quad (3.2.38)$$

Figure 3.2.4 contains the different possible hybrid branches which are displayed in 3.2.5 in a schematic phase diagram as a function of  $\Delta e$  and  $p_{trans}$ .

The most interesting feature of the phase diagram is that disconnected branches can occur for a low transition density and a high energy density discontinuity (regions B and D). The appearance of such a solution becomes more likely with the increase of the sound speed of quark matter  $c_s$  (Macher & Schaffner-Bielich, 2005).

In the case of a small quark core, its large density determine an increase of the gravitational pressure which needs to be counteracted by the core pressure; if  $\Delta e < \Delta e_{crit}$  this condition is realized leading to stable configuration such as C and B. On the contrary, if the jump in energy density is too big, i.e.  $\Delta e > \Delta e_{crit}$ , the star is unstable in correspondence to the appearance of quark matter (regions A and D). However, if  $c_s^2 = \frac{dp}{de}$  is big, the pressure increases rapidly with the energy density and a sufficiently large core could be able to sustain a stable configuration (D, Schaeffer et al. (1983)). The disconnected branch is commonly

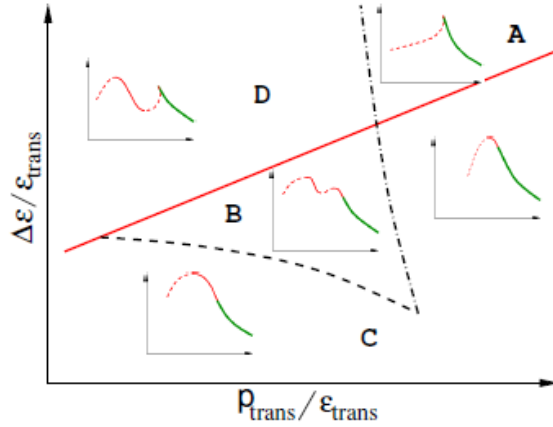


**Figure 3.2.5:** from [Alford et al. \(2015\)](#). Schematic phase diagram containing the same possible topologies of [Figure 3.2.4](#).  $c_s^2 = 1$  and the red line correspond to  $\Delta e_{crit}$ . Reprinted with permission, © 2015 American Physical Society.

defined as the “third family” of compact stars in addition to neutron stars and white dwarfs. Moreover the hadronic and the hybrid branches contain configurations with the same mass but different radii which are for this reason called "twin stars".

Many different kinds of phase transition and twin star models have been explored ([Gerlach, 1968](#); [Kampfer, 1981](#); [Thorsson et al., 1994](#); [Glendenning & Kettner, 2000](#); [Schertler et al., 2000](#); [Schaffner-Bielich et al., 2002](#); [Fraga et al., 2001](#); [Banik & Bandyopadhyay, 2003](#); [Mishustin et al., 2003](#); [Bhattacharyya et al., 2005a](#); [Banik et al., 2004, 2005](#); [Alvarez-Castillo & Blaschke, 2015](#); [Dexheimer et al., 2015](#); [Benic et al., 2015](#); [Blaschke & Alvarez-Castillo, 2016](#); [Zacchi et al., 2016](#); [Alvarez-Castillo et al., 2016](#); [Zacchi et al., 2017](#); [Alvarez-Castillo & Blaschke, 2017](#)).

The values of  $p_{trans}$  and  $\Delta e$  allow also to distinguish different kinds of twin star solutions. In particular, the transition pressure influences the location of the first maximum while the energy gap affect the second one. Based on the position of these two maxima a further categorization of twin stars can be built (see [Christian et al. \(2018a\)](#) for details).

[Alford et al. \(2015\)](#) have studied how the mass and radius measurements can be translated into constraints on the parameters of eqn. [3.2.37](#) for HySs.

The results of their analysis are summarized in [Figure 3.2.6](#) which shows the allowed solutions as functions of  $\frac{p_{trans}}{e_{trans}}$  and  $\frac{\Delta e}{e_{trans}}$  for fixed  $c_s^2$ .

A lower limit  $n_{trans} = n_0$  and an upper limit depending on the hadronic EOS delimit the admitted range for the transition density. A further restriction of the parameter space is imposed by the mass limit: the gray shaded area contains the configurations with a

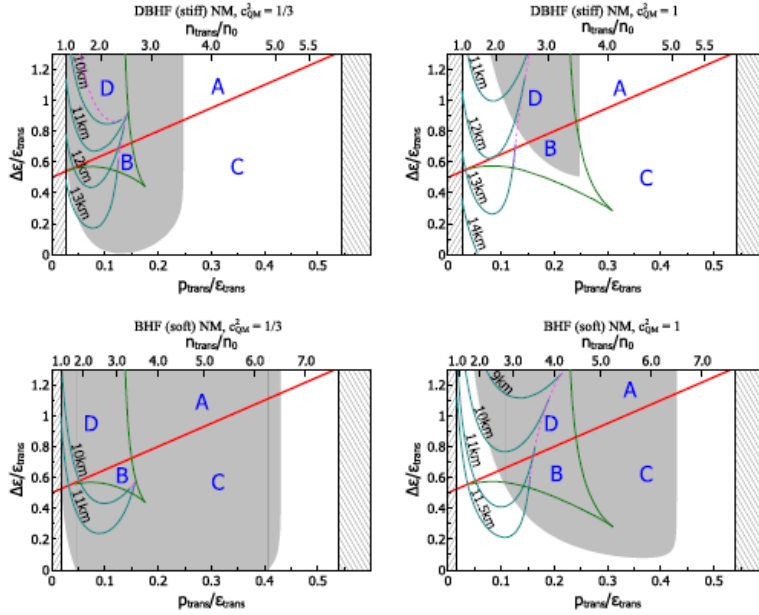


**Figure 3.2.6:** from Alford et al. (2015). Contour plots showing  $R_{1.4}$  of a HyS as a function of the CSS parameters. Reprinted with permission, © 2015 American Physical Society.

maximum mass below  $2M_{\odot}$  and it is therefore excluded (note again that this region should now be enlarged to account for at least  $2.05M_{\odot}$ ).

The upper panels are for DBHF (stiff, Gross-Boelting et al. (1999)) and the lower for BHF (soft, Taranto et al. (2013)) as hadronic EOS.

The contours represent the  $R_{1.4}$  for the HySs: in the allowed region, keeping  $\frac{\Delta e}{\epsilon_{trans}}$  fixed, the radius decreases with the increase of the transition density. The same is found for high  $n_{trans}$  for which the configuration with a mass of  $1.4M_{\odot}$  is completely hadronic.

One can note that with  $c_s^2 = 1$  the excluded region is not too big and a relevant part of the parameter space is allowed by the mass observations (right panels). For this reason, many models of hybrid stars adopt an high value of the sound speed (Lastowiecki et al., 2012; Kojo et al., 2015; Benic et al., 2015; Benic, 2014). On the other hand, conformal symmetry requires a value for  $c_s^2$  close to  $\frac{1}{3}$  and in addition Bedaque & Steiner (2015) suggested the existence of a limit of the type  $c_s^2 < \frac{1}{3}$ . However, with this choice the permitted area is sensibly narrowed (Alford & Han, 2014; Heinimann et al., 2016) and it is composed by two distinct regions: the low pressure transition and the high pressure transition.

In the first case  $n_{trans} \leq 2 n_0$  and the hybrid branch is connected. In this scenario, the minimum radius  $R_{1.4}$  is found in the range  $12.5 - 13$  km depending on the hadronic EOS and it corresponds to configurations at the border of the parameter space for  $n_{trans} \sim n_0$ .

This result seems to be incompatible with the experimental suggestion for small radii and thus either the sound velocity is higher or the transition occurs at high density. In the latter scenario the hybrid branch is again connected but very small and thus the masses and radii are basically the ones characterizing the selected hadronic EOS.

The second possibility consists in selecting a higher value of  $c_s^2$  up to the causal limit  $c_s^2 = 1$ . In this case disconnected branches exist for low transition pressure ( $n_{trans} \leq 2n_0$ ) and large energy gap ( $\frac{\Delta e}{e_{trans}} \sim 1$ ). These configurations can reach a very small value of  $R_{1.4} < 11$  km for  $n_{trans} \sim 2 n_0$ .

In conclusion, the evidence for small radii leaves two scenarios:

- the transition at very high density and a quite soft nucleonic EOS. This solution is allowed also for value of  $c_s^2$  in agreement with the conformal limit. However, it is commonly believed that the threshold for the appearance of hyperons is  $\sim (2 - 3)n_0$  and thus this fact needs to be taken into account.
- a disconnected branch with low density transition and very high  $c_s^2$  and a disconnected branch. In order to obtain small radii the transition density cannot be too small. A recent study (Christian & Schaffner-Bielich, 2020) has put a lower limit  $> 1.7n_0$  for the twin stars solution using the data from NICER (see chapter 2.3.1).

### 3.2.6 Strange quark stars (QSs)

The second class of compact objects containing quark matter are the so called strange quark stars (QSs) made entirely by deconfined strange matter (Alcock et al., 1986; Haensel et al., 1986). Weak interactions are responsible for the flavour equilibrium and thus the strange matter is composed by roughly equal number of  $u$ ,  $d$  and  $s$  quarks.

The existence of QSs is based on the Witten hypothesis according to which strange matter is absolutely stable and it represents the true ground state of matter (Bodmer, 1971; Witten, 1984).

The evidence of quark confinement inside of nuclei suggests that the energy per baryon of two flavour (non-strange) quark matter must be higher than the one of nuclei. However once the Fermi energy of the non-strange gas reaches the value of the  $s$  quark mass, the Pauli principle makes it energetically convenient to convert  $u$  and  $d$  into  $s$ . This process will proceed until all the flavours have the same Fermi energy. In the case for which the energy per baryon  $(\frac{E}{A})_2$  of the two flavour matter is just above the nuclei threshold, then there is a possibility that strange matter has  $(\frac{E}{A})_3$  which is below 939 MeV: this is Witten's conjecture.

More precisely, for an energy per baryon in the range between 930 and 939 MeV the decay of strange matter in nuclei would be possible together with weak interactions. Therefore the real requirement is  $(\frac{E}{A})_3 < 930$  MeV.

If this condition is fulfilled a nucleus could reach this lower energetic level by converting some

$u$  and  $d$  quarks to  $s$  quarks but the necessary processes are higher order weak interactions, i.e. the reaction rate is basically identical to zero. Therefore the existence of nuclei is not in contradiction with the absolute stability of strange matter.

At the same time, as mentioned before, the energy per baryon of two flavour matter must

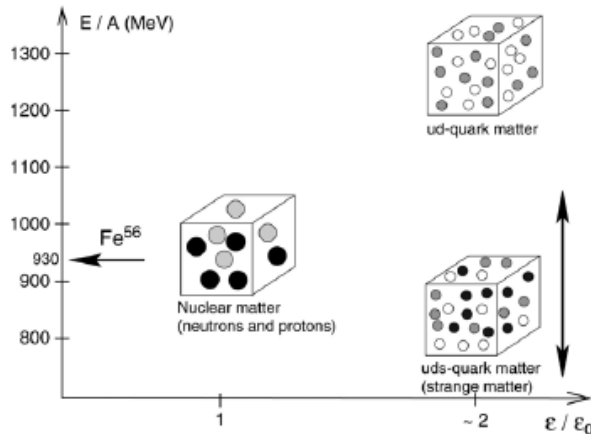


**Figure 3.2.7:** from [Weber \(2005\)](#). Comparison of the energy per baryon of  $^{56}\text{Fe}$ , nuclear matter with the energy per baryon of strange and non-strange quark matter. Reprinted with permission from Elsevier, Copyright © 2004 Elsevier Ltd.

be larger than 930 MeV which characterize iron and it is the lowest in nuclei. Actually, also in this case, the condition is more stringent: there is an extra energy  $b$  to add,  $b$  being the gap in  $\frac{E}{A}$  of non-strange quark matter for  $A \rightarrow \infty$  and for  $A=250$ . [Farhi \(1986\)](#) estimated this gap to be 4 MeV. Finally, the condition for non strange matter is  $(\frac{E}{A})_2 > 934$  MeV. This limit can be translated in term of three flavour matter as  $\sim (\frac{E}{A})_3 > 830$  MeV [Figure 3.2.7](#) gives a schematic illustration of these features.

[Weissenborn et al. \(2011\)](#) have studied the properties of Qs through a systematic exploration of strange quark matter EOS parameter space. They have employed the modified bag model of eqn. [3.2.31 \(Alford et al., 2005\)](#) with  $m_s = 100$  MeV ([Amsler et al., 2008](#)).

[Figure 3.2.8](#) shows the results obtained by changing the QCD correction parameter  $a_4$  from 0 (strong) to 1 (absent) and the effective bag constant  $B_{eff}$ . The curves denominated “3-flavor line” and “2-flavor line” represent the aforementioned conditions on the energy per baryon of strange and non-strange quark matter respectively. These requirements determine the existence of an upper limit of  $M = 3.36M_\odot$  and lower limit for the maximum mass of Qs. Indeed the latter and also the radius are linked to the value of the bag constant through  $M_{max} \propto B_{eff}^{-\frac{1}{2}}$  ([Witten, 1984](#)) and  $R_{max} \propto B_{eff}^{-\frac{1}{2}}$  ([Alcock et al., 1986](#)).

In addition, curves with constant maximum mass are displayed together with the mass limit from Demorest et al. (2010) and the rotational frequency constraint from Hessels et al. (2006).

The green region is the allowed region of parameters for the quark EOS.

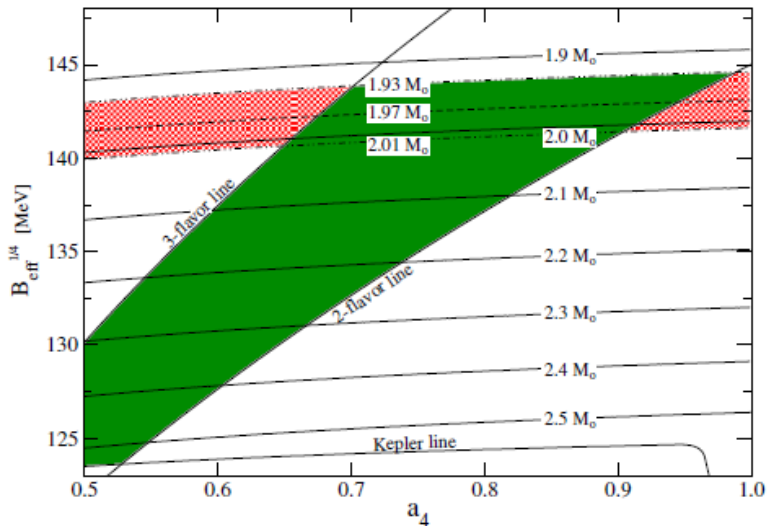


Figure 3.2.8: from Weissenborn et al. (2011). Maximum masses of QSs as a function of  $a_4$  and  $B_{eff}$ .

The equation for strange quark matter can be expressed also using the CSS parametrization of eqns. 3.2.35 and 3.2.36. In this case,  $p_0 = 0$  and  $n_0$  and  $e_0$  are respectively the baryon and energy density at  $p = 0$ ;  $n_0$  is often defined as the Witten density. For the discussion on the allowed space of parameters which characterize this EOS the reader is reminded to our work presented in chapter 8.

### 3.3 The two families scenario

A different possible solution to reconcile large masses and small radii measurements is provided by the so called two families scenario (Drago et al., 2014a,b, 2016b): this is based on the coexistence of two classes of compact objects (CSs). The first one is composed by very compact hadronic stars (HSs) with a soft EOS and the second one by massive QSs with a stiff EOS.

The existence of this QSs branch rely on the validity of the Witten hypothesis (see previous section).

QSs can fulfill the mass constraint but they are at the same time incompatible with the

observational data regarding quasi-periodic oscillations (Watts & Reddy, 2007) and glitches (Madsen, 1988). This evidence prevents the possibility to interpret all the CSs as QSs and suggests the parallel existence of a class of HSs containing hyperons and  $\Delta$ s. Moreover, the appearance of new degrees of freedom soften the EOS and therefore allows to explain the small radii data in terms of this HSs branch.

The stability of HSs constitute an important issue: the production of hyperons in the stellar interior could easily trigger the transition to QSs since the latter are by hypothesis more stable. Therefore a mechanism is required to shift the threshold for the appearance of strange particle to higher densities: in the two families model, this is guaranteed by the formation of  $\Delta$  resonances in the core of the stars.

Although the importance of  $\Delta$  particles at high densities has been pointed out in many heavy-ion collisions experiments (Hofmann et al., 1995; Bass et al., 1999; Zabrodin et al., 2009; Lavagno, 2010), they were initially believed to play a minor role in CSs because of the result of Glendenning (1985) suggesting a late appearance threshold. However, this outcome is model dependent and actually the critical density  $n_{crit}$  for  $\Delta$ s formation depends on the values of the coupling constants (in RMFT) and it is highly correlated with the the derivative of the symmetry energy  $L$ . For this reason, many works underlined the relevance of  $\Delta$ s also in the astrophysical context (Huber et al., 1999; Xiang & Hua, 2003; Chen et al., 2007, 2010; Schürhoff et al., 2010).

Since the softening effect induced by  $\Delta$ s resembles the one caused by hyperons, their early appearance in HSs would open a similar " $\Delta$ s puzzle".

### 3.3.1 The hadronic and the quark EOSs

The hadronic EOS of the two families scenario is built using two different RMF parametrization, the GM3 model Glendenning & Moszkowski (1991) (chapter 3.2.1) and the SFHo (chapter 3.1.3) with the additional inclusion of the remaining baryons of the lightest octet and the  $\Delta(1232)$  isobar resonances.

The expression for the GM3 is given in eqn. 3.2.1 and the coupling constants are selected as previously explained in section 3.2.1. The  $\Delta$  isobar is then incorporated with an additional part in the Lagrangian density similar to the one for nucleons (Boguta, 1982; Li et al., 1997; Kosov et al., 1998):

$$L_{\Delta} = \bar{\psi}_{\Delta\nu} [i\gamma_{\mu}\delta^{m\nu} - (m_{\Delta} - g_{\sigma\Delta}\sigma) - g_{\omega\Delta}\gamma_{\mu}\omega^{\mu} - g_{\rho\Delta}\gamma_{\mu}I_3\rho_3^{\mu}] \psi_{\Delta}^{\nu} \quad (3.3.1)$$

where  $\psi_{\Delta}^{\nu}$  is the Rarita-Schwinger spinor for the  $\Delta$  isobars composed by  $(\Delta^{++}, \Delta^{+}, \Delta^0, \Delta^{-})$  and  $I_3 = \text{diag}(\frac{3}{2}, \frac{1}{2}, \frac{1}{2}, \frac{3}{2})$  the isospin matrix of the  $\Delta$ s.

Conventionally, the coupling constants of the  $\Delta$  and hyperons (labelled with  $i$ ) are expressed

through the ratios:

$$x_{\sigma i} = \frac{g_{\sigma i}}{g_{\sigma N}}, \quad x_{\omega i} = \frac{g_{\omega i}}{g_{\omega N}}, \quad x_{\rho i} = \frac{g_{\rho i}}{g_{\rho N}} \quad (3.3.2)$$

If the SU(6) symmetry holds exactly, then the  $\Delta$ -meson coupling are just  $x_{\sigma\Delta} = x_{\omega\Delta} = 1$ . The threshold for the appearance of the baryon of species  $i$  is given by:

$$\mu_i \geq m_i - g_{\sigma i}\sigma + g_{\omega i}\omega + t_{3i}g_{\rho i}\rho \quad (3.3.3)$$

where  $\mu_i$  is the chemical potential and  $t_{3i}$  is the isospin charge of the baryon  $i$ .

Since the  $\Delta^-$  has the same charge of the neutron-electron couple, it is the first to be formed among  $\Delta$ s. However, being isospin unfavored, its appearance threshold is located at very high densities unless the couplings  $g_{\rho i}$  for all the baryons is set to zero and thus the symmetry energy to an unphysically small value (Glendenning, 1985).

However, as discussed in section 3.1.2, the GM3 model allows to fix the coupling  $g_{\rho N}$  using the a value of  $S = 32.5$  MeV (inside the experimental range) but it does not contain any information on its derivative  $L$ . The latter indeed is automatically determined from the symmetry energy and its value,  $L \sim 80$  MeV, is above the allowed range suggested by data (see chapter 2.2).

In addition, information can be also gathered by many body calculations (Oset & Salcedo, 1987) and phenomenological analysis on electron-nucleus (Koch & Ohtsuka, 1985; Wehrberger et al., 1989; O'Connell & Sealock, 1990), photo-absorption (Alberico et al., 1994) and pion-nucleus scattering (Horikawa et al., 1980; Nakamura et al., 2010) data: the results seem to indicate that the interaction of the  $\Delta$  in the nuclear medium is more attractive with respect to the one of the nucleons (Drago et al., 2014b; Cai et al., 2015). This is an indication that  $x_{\sigma\Delta}$  may be  $> 1$  and similar to the  $\Delta$ -N mass ratio. Therefore the SU(6) symmetry is not exact: this is also suggested by the results from QCD finite-density sum rule which imply  $x_{\omega\Delta} < 1$ .

Assuming  $x_{\sigma\Delta} = 1.25$ ,  $x_{\omega\Delta} = 1$  and  $x_{\rho\Delta} = 0$ , the  $\Delta^-$  is formed just above  $n_0$  and, as a consequence, the onset of hyperons is shifted to  $\sim 5n_0$  (Drago et al., 2014a). This outcome is due to the larger attractive interaction which has been introduced.

A second approach to study the behavior of  $n_{crit}$  consists in keeping the universal couplings from the SU(6) symmetry but incorporate in the model the experimental knowledge about  $L$ . For this purpose, one of the possible methods (as discussed in section 3.1.2) is to introduce a density dependent coupling for the  $\rho$  meson

$$g_{\rho i} = g_{\rho i}(n_0) \exp \left[ a \left( \frac{n}{n_0} - 1 \right) \right] \quad (3.3.4)$$

where the parameter  $a$  depends only on the value of  $L$ .

The result is shown in figure 3.3.1: the threshold density of the  $\Delta^-$  becomes larger with an increasing value of  $L$  while  $n_{crit}$  for the hyperons behaves in the opposite way. In particular,

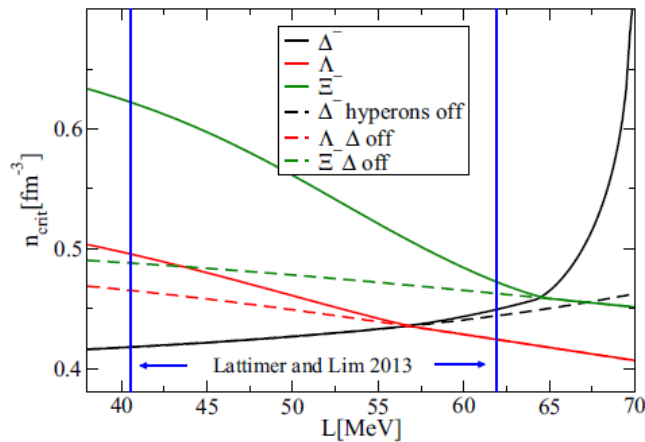


**Figure 3.3.1:** from *Drago et al. (2014b)*. Critical densities of  $\Delta^-$ ,  $\Lambda$  and  $\Xi$  as functions of the  $L$  parameter within the modified GM3 model. Reprinted with permission, © 2014 American Physical Society

if  $L > 65$  MeV, such as in the case of the original GM3 model, the onset of  $\Delta^-$ s is shifted after the one for  $\Xi$  and thus their role is completely negligible (like in [Glendenning \(1985\)](#)). On the other hand, if  $L < 56$  MeV then the isobars appear before the hyperons and the thresholds for  $\Lambda$  and  $\Xi$  are pushed to larger densities.

If the experimental range of  $L$  suggested by [Lattimer & Lim \(2013\)](#) is considered, the outcomes of this analysis imply that for  $n \sim 3n_0$  both  $\Delta^-$ s and hyperons play a relevant role and must therefore be included in the EOS. In addition, if  $L$  is not too large, the isobars appear first and moreover, if less conservative values for the coupling constants are adopted, this could be true for the entire allowed range of  $L$ .

The second parametrization which has been adopted to build the hadronic EOS is the SFHo with  $S = 32$  MeV. The Lagrangian of SFHo given in eqn. [3.1.26](#) already include the possibility of fitting to a selected value of  $L$ , here  $L = 47$  MeV. On the other hand, terms for hyperons and  $\Delta$  resonances are added. Figure [3.3.2](#) shows the resulting particle fractions in the case in which only hyperons are included (panel (a)) and when also  $\Delta$ s are considered (panel (b)). In the first situation, both the  $\Lambda$  and the  $\Xi^-$  are formed at a density of about  $0.5 fm^{-3}$ . In the second case, due to the low value of  $L$ , the  $\Delta^-$ s appear before hyperons for  $n \sim 0.4 fm^{-3}$  and shift the threshold for  $\Lambda$  and  $\Xi$ . This result is in agreement with the analysis performed within the modified GM3 model. Moreover these conclusions hold even for the untoward choice of  $x_{\omega\Lambda} = 1.1$  (green dashed line).

Concerning the quark EOS, the selected description is the one based on the modified bag

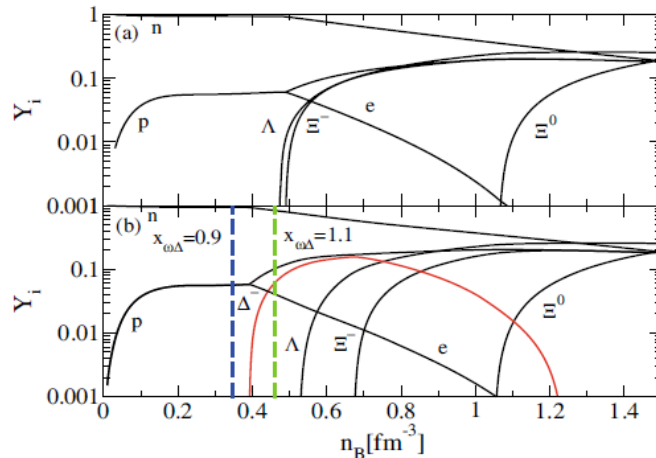


**Figure 3.3.2:** from [Drago et al. \(2016b\)](#). Particles fractions as functions of  $n$  for the SFHo parametrization with the  $SU(6)$  symmetry: panel (a) contains only hyperons while in panel (b) also  $\Delta$ s are included. The dashed lines shows the onset of the  $\Delta^-$  for different value of  $x_{\omega\Lambda}$ . Reprinted by permission from Springer Nature Customer Service Centre GmbH, Copyright © 2016, Springer Nature.

model of eqn. 3.2.31 already described in section 3.2.4. The  $u$  and  $d$  quarks are considered massless while the mass of the strange quark is set to 100 MeV. The parameters  $B_{eff}$  and  $a_4$  must be selected in order to be consistent with the Witten hypothesis (see section 3.2.6). Let us define as an example two allowed sets, i.e. set 1 with  $B_{eff}^{\frac{1}{4}} = 142$  MeV and  $a_4 = 0.9$  and set 2 with  $B_{eff}^{\frac{1}{4}} = 127$  MeV and  $a_4 = 0.6$ .

Another possibility, again in the framework of the MIT bag model, is the CSS parametrization of eqn. 3.2.35 and 3.2.36. This EOS will be further discussed in chapter 8.

A second parametrization adopted for the quark EOS is the one of the pQCD calculations at finite chemical potential. This model depends on only one parameter  $X$ , i.e. the renormalization scale divided by the baryon chemical potential, and its allowed range is  $[1 - 4]$ . This model is not discussed here and for further information the reader is referred to [Fraga et al. \(2014\)](#).

### 3.3.2 The mass radius relation for the two families

Figure 3.3.3 display the mass-radius relations for the two families of HSs and Qs: here for the hadronic EOS the SFHo underlined model is adopted while the quark EOS is build with pQCD parametrization.

First of all, one can note how the inclusion of the  $\Delta$ s isobars leads to a relevant reduction of the maximum mass with respect to the original SFHo and the EOS is no longer compatible

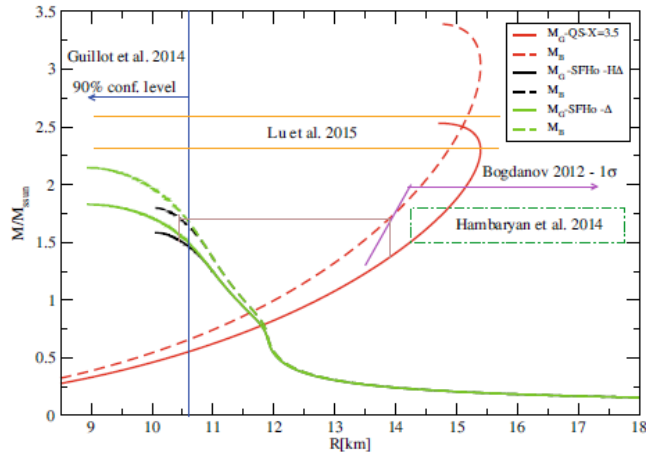


**Figure 3.3.3:** from *Drago et al. (2016b)*. Mass-radius relations for HSs and QSs using SFHo and pQCD parametrizations respectively. The solid lines are for the gravitational mass while the dashed lines are for the baryonic mass. In addition, constraint from *Bogdanov (2013)*; *Hambaryan et al. (2014)*; *Guillot & Rutledge (2014)*; *Lü et al. (2015)* are also shown. Reprinted by permission from Springer Nature Customer Service Centre GmbH, Copyright © 2016, Springer Nature

with the experimental lower bound. On the other side, the  $\Delta$ s allow to obtain very compact configurations with a  $R_{1.4}$  of the order of [10.5 – 11] km (solid green line).

The formation of hyperons implies an additional softening of the hadronic EOS and the maximum mass is further reduced by  $0.1 - 0.2M_{\odot}$  (solid black line) being finally of the order of  $1.5M_{\odot}$ .

On the contrary, the observational limit can be fulfilled by the QSs branch: for example for set 1  $M_{max} = 2M_{\odot}$  (now to be enlarged to 2.05) while set 2 can provide the higher  $2.4M_{\odot}$ . The same for the red solid line in figure 3.3.3 which correspond to  $X = 3.5$  and gives a maximum mass as large as  $2.53M_{\odot}$ .

An important issue concerns the formation of QSs from HSs. In particular one must specify the precise conditions, the probabilities, the type of processes and the typical timescale of the conversion. However, first of all looking at figure 3.3.4 one can already appreciate how this transformation is energetically convenient.

The configuration labeled with B is the first HS in which hyperons start to appear in the inner core and starting from this point the hyperon content increases with the mass up the maximum A. The dots D and C on the black curve represent the QSs configuration with the same baryon mass of B and A (dashed line), but their gravitational mass is about  $0.1M_{\odot}$  lower. Thus, in principle, for all the configurations between B and A a transition would be energetically favoured with a release of an energy of about  $10^{53}$  ergs (*Berezhiani et al., 2003*;

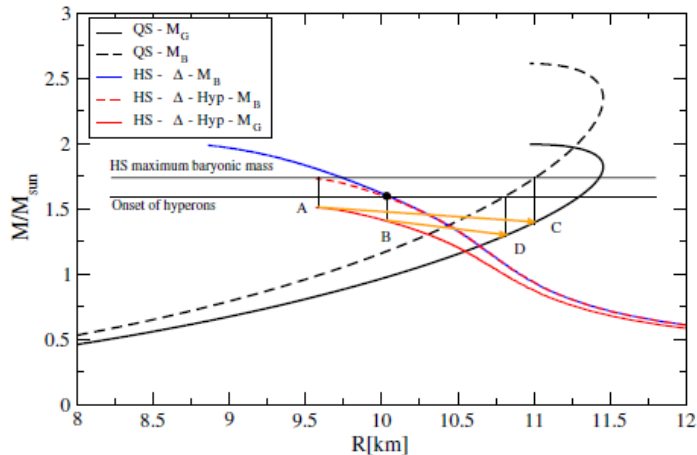


**Figure 3.3.4:** from *Drago et al. (2014a)*. Examples of gravitational and baryonic mass–radius for HSs and QSs (set 1). A represents the maximum mass of the HS; B is the gravitational mass of the first HS containing hyperons and the black dot on the dashed red curve is its corresponding baryonic mass. D and C are the QSs which have the same baryonic masses of B and A. Reprinted with permission, © 2014 American Physical Society.

Bombaci et al., 2004; Drago et al., 2004; Bombaci et al., 2007). Note that the formation of (enough) hyperons is crucial to form the first droplet of strange quark matter which can trigger the conversion. This also imply the existence of a minimum mass for the QSs branch and the existence of configurations with the same gravitational mass but different radius belonging to the two different classes.

In conclusion, within the two families scenario stars with small radii  $R_{1.4} < 11$  km are interpreted as HSs with hyperons and  $\Delta$  resonances and with a maximum mass of the order of  $1.5 - 1.6M_{\odot}$ . On the other hand, massive stars belong to the QSs branch and they have radii larger than 11 km.

### 3.3.3 QSs formation and astrophysical implications

The formation of a QS can take place in three different situations:

- through the mass accretion or through the slowing down of a pulsar which rotates rapidly and which has a mass slightly below the critical one. An example could be represented by LMXBs.
- after the explosion of a SN with a massive progenitor. The delay between the explosion and the start of the deconfinement process can be attributed to the slow down or the

mass accretion of the NS.

- After the mergers of BNS. The possible outcomes of the merger into the context of the two families scenario will be further discussed in chapter 5.

The process of quark deconfinement in a star can be roughly divided in three main steps:

1. **the formation of the first droplet** of quark matter: this can happen through quantum fluctuation, in the case of low temperature system, or through thermal fluctuation in the opposite case of high temperature (Iida & Sato, 1998; Berezhiani et al., 2003; Bombaci et al., 2004; Drago et al., 2004; Bombaci et al., 2007).

The main question concerns the conditions for the creation of a droplet which is stable at its formation pressure. Finding those conditions is a complicated problem to address and it has been explored in few works (Bombaci et al., 2009; Mintz et al., 2010; Bombaci et al., 2011; Lugones, 2016; Bombaci et al., 2016). In the context of the two families scenario, the key idea is that, because of the Witten hypothesis, the strangeness is fundamental to assure the stability and thus a critical density of strange quarks exists for the deconfinement process to start. An approximate estimate of this critical strangeness fraction will be discussed in chapter 5.2.1.

After the formation, the droplet expands until it reaches a macroscopic size.

2. **a turbulent regime** which characterize the further expansion of the bubble of quark matter. In this phase, the deconfinement becomes very rapid and it is described as a combustion process through a standard hydrodynamical approach (Lugones et al., 1994; Drago et al., 2007; Horvath, 2010; Niebergal et al., 2010; Drago & Pagliara, 2015). Since the combustion area is very thin it is approximated as a surface of discontinuity called flame front (Coll, 1976; Anile, 2005). The latter is accelerated by the development of hydrodynamical instabilities, such as the Rayleigh-Taylor, which significantly increase the efficiency of the burning (Drago et al., 2007; Herzog & Ropke, 2011; Pagliara et al., 2013). This allows a rapid conversion of the bulk of the star, with timescales of the order of ms.

This fast burning finally stops at a density where the “condition for exothermic combustion”, the so called Coll condition, is no longer satisfied. This requirement is applied to the process of conversion of fluid 1, the fuel, into fluid 2, the ash:

$$e_1(p, X) > e_2(p, X) \tag{3.3.5}$$

where  $e_i$  is the energy density,  $p_i$  is the pressure and  $X_i = \frac{e_i + p_i}{n_i}$  is the dynamical volume of fluid i.

3. **a diffusive regime** during which the burning proceeds very slowly. This regime has been investigated both analytically in Drago & Pagliara (2015) and through numerical

simulations in [Herzog & Ropke \(2011\)](#) and [Pagliara et al. \(2013\)](#).

The dynamics is described with two differential equations: the first one to model the flame front propagation and the second one to outline the thermal evolution taking into account the neutrino cooling. One of the main results is the quasi plateau characterizing the neutrino luminosity of this phase, related to the constant speed of burning reached almost immediately in this regime.

The process of deconfinement proceeds until the whole object is converted and it has become a QS. The typical timescale is of about few tens of seconds, but it could be reduced by a factor of the order of 3 – 4, because of gravity which pushes the external layers on the conversion front.

The process of formation of QSs has many astrophysical implications (see [Char et al. \(2019\)](#)). First of all, the deconfinement could help SN explosions ([Gentile et al., 1993](#); [Drago & Tambini, 1999](#)): indeed during the collapse of a very massive progenitor a soft mixed phase of quarks and hadrons can be formed and crossed by the collapsing center. The latter then hits the pure quark matter phase whose hardness causes a bounce which triggers the explosion ([Sagert et al., 2009](#); [Fischer et al., 2018](#)). In the context of the two families scenario, the mechanism is different and rely on the rapid combustion of the inner part of the star. Being strongly exothermic, this process results in the emission of neutrinos with a very large luminosity and which could revitalize the SN explosion.

In the second instance the deconfinement could be linked to long Gamma Ray Bursts (GRBs, duration of more then 2s, [Bombaci & Datta \(2000\)](#)). A signature of this connection could be the time delay between the SN explosion and the conversion process which could in principle explain the delay observed in the EM signals of GRBs.

Finally, short GRBs which are emitted after a BNS merger could also be connected to the formation of a QS (see chapter [5.3.2](#)).

## *Binary neutron star mergers*

BNSs are one of the most fascinating objects in astrophysics: not only they are valuable probe of General relativity (GR) with applications in relativistic hydrodynamics and magnetohydrodynamics, but they also provide many constraints about the stellar composition and evolution.

The first discovery of a BNS was PSR B1913+16, a radio pulsar orbiting in the vicinity of another NS, was followed by many other observations in a range of total mass of  $2.65 - 2.85 M_{\odot}$ . The measured decay rates of the orbits correspond to the prediction of GR: the fate of these couples of NS, with a time scale of about  $10^6 - 10^7 \text{ yr}$ , is to spiral down and finally to merge, because of the energy dissipation due to the emission of gravitational waves (GWs).

The GW signal lasts for the entirety of the coalescing phase, dropping only in correspondence of an eventual collapse to a black hole (BH). When the distance is of the order of few NS radii, the luminosity is of the order of  $10^{53} \text{ ergs/s}$  and the amplitude of the waves is about  $10^{-23} - 10^{-22}$  for a binary 100  $Mpc$  distant. These values sit inside the range of sensitivity of the GW detectors advanced LIGO ([Aasi et al., 2015](#)) or advanced VIRGO ([Acernese et al., 2015](#)).

### **4.1 *The main observables***

The most relevant physical phenomena concerning BNS mergers are:

- *tidal forces*

They take place just before the merger, perturbing the system because the space-time metric inside each star is modified by the influence of the companion in a way that is different in the various regions of the star. This determines a breaking of the spherical

symmetry and thus a deformation of the NS. The consequence is the appearance of an induced quadrupole moment  $Q_{ij}$ :

$$Q_{ij} = -\lambda \varepsilon_{ij} \quad (4.1.1)$$

where  $\varepsilon_{ij}$  is the tidal external field and  $\lambda$  is the deformability parameter that depends on the EOS and provides a quantitative estimate about how easily the star can be deformed. The  $\lambda$  parameter can be expressed in terms of the radius  $R$  and the dimensionless Love number  $k_2$  :

$$\lambda = \frac{2k_2}{3} R^5 \quad (4.1.2)$$

A related quantity which is widely used is the so called dimensionless tidal deformability defined as:

$$\Lambda = \frac{\lambda}{M^5} \quad (4.1.3)$$

where  $M$  is the mass of the NS.

- *gravitational waves*

The detection of GWs from a BNS merger provides crucial information on the EOS in two possible ways (for a review see [Baiotti \(2019\)](#)):

- by studying the GW characterizing the inspiral phase: the aforementioned tidal deformation of the NS produces a distortion of the signal. This effect should be detectable at least during the last cycles of the inspiral.
- by analyzing the GW signal during and after the merger: in this case the strong oscillations can be Fourier decomposed and important physical insights can be inferred from the spectrum.

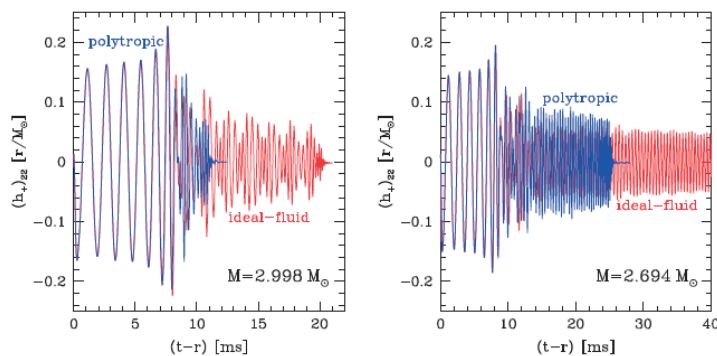


**Figure 4.1.1:** From GW [Rezzolla \(2013\)](#). Amplitudes in the plus polarization,  $l = 2$ ,  $m = 2$  multipoles, for two different EOSs masses of the binary components.

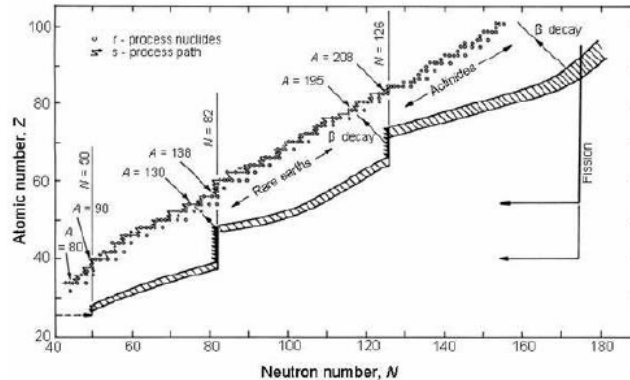


Figure 4.1.2: from Clayton (1983). *r*-processes path

- *short GRBs*

The processes of BNS mergers are also at the origin of short GRBs.

GRBs are very bright flashes of radiations which peak in the  $\gamma$ -rays band and they are divided into two classes depending on the duration of the  $\gamma$ -ray emission (D'Avanzo (2015)): for long GRBs this phase lasts more than 2 s while for the short one the duration is less than 2 s. Moreover the latter are characterized by a harder spectrum and they show a negligible spectral lag, i.e. the time difference between the arrival of high energy and low energy photons. However, these properties resemble the first 1 – 2s of the emission of long GRBs and moreover the evolution of the spectrum is the same.

In addition, short GRBs are less energetic by a factor similar to the ratio of the duration characterizing the two species.

- *ejected mass and r-processes*

The mass ejected during and after the merger is believed to be the seed of the *r*-processes which (together with the *s*-processes) are at the origin of the abundances of trans-iron elements. Beside the *s*-peaks located in correspondence of the neutron magic numbers ( $N = 50, 82, 126$ ), the distribution of heavy elements is characterized by three peaks at  $N = 46, 76, 116$  corresponding to  $A = 80, 130, 195$  which are due to *r*-processes. The latter involves neutron captures which convert a nucleus ( $Z, A$ ) into a heavier isotope ( $Z, A + 1$ ). The chain will proceed until a nucleus that is unstable with respect to  $\beta$ -reactions is finally reached. However, in the case of *r*-processes  $\tau_{n\gamma} \ll \tau_{\beta}$ , i.e. the nucleus lifetime with respect to neutron capture is smaller than the one with respect to  $\beta$ -decay. Therefore before the  $\beta$  reaction could take place, another neutron capture occurs and this proceeds until the bound energy of neutrons is so low that adding more of them becomes extremely unlikely. At this point the nucleus can finally decay via  $\beta$  reaction. The neutron number is reduced by one unit which is gained by

atomic number and thus a different nucleus is obtained.

The r-processes are able to synthesize very neutron-rich isotopes and their path wanders along the neutron drip line (see figure 4.1.2)

The radioactive decay of the r-process elements gives birth to an electromagnetic (EM) signal called Kilonova, a multiband transient with a lifetime of the order of weeks.

In 2017, the first GW observation of a BNS merger, GW170817 (Abbott et al., 2017a) has been announced. The event has further underlined the strong connection between microphysics and the so called "multimessenger astronomy" observations (for a review see Gandolfi et al. (2019)). The basic picture explained above was confirmed by GW170817, which has been detected in coincidence with a short GRB (GRB170817A) with the same sky location (Abbott et al., 2017b). Subsequent followup observations with telescopes spanning the whole EM spectrum revealed also a Kilonova (Abbott et al., 2017c).

## ***4.2 The Merger of Two Compact Stars: A Tool for Dense Matter Nuclear Physics***

The main features explained in the previous section and their connection with the EOS for dense matter are summarized in the review paper Drago et al. (2018a) (from Alessandro Drago, Giuseppe Pagliara, Sergei B. Popov, Silvia Traversi and Grzegorz Wiktorowicz) whose content is reported in the following. The paper represents a contribution written for the Special Issue of Universe (ISSN 2218-1997) "Compact Stars in the QCD Phase Diagram" (Blaschke et al., 2018).

A very similar review, Drago et al. (2018b) written as contribution to THESEUS Workshop 2017 (Amati et al., 2018) (from Alessandro Drago, Giuseppe Pagliara and Silvia Traversi) can be found at the link [2018MmSAI..89..236D.pdf](#).

### ***4.2.1 Introduction***

In this section, we discuss the GW and EM signals emitted during a BNS merger. In particular, we concentrate on the constraints provided by those signals on the high density EOS. Indeed, the composition and stiffness of the EOS of the compact stars composing the binary, strongly influence e.g. the lifetime of the remnant formed in the post-merger phase and its GW signal, the emission of the sGRB, the amount and the features of ejected mass and the resulting Kilonova.

As mentioned above, the first observation, in August 2017, of the merger of two compact objects with masses in the NS range has signed the beginning of the era of the "multimessenger astronomy" (Abbott et al., 2017d). Indeed, the detection by the LVC of a GW

signal (GW170817) from the event has allowed the localization of the binary within a sky region of  $31\text{deg}^2$  and a distance of a  $40_{-8}^{+8}$  Mpc. By virtue of this precise localization, Fermi Gamma-ray Burst Monitor has detected a sGRB event (GRB170817A) having a delay of 1.7 s with respect to the time of the merger (Abbott et al., 2017b). Moreover, in the following weeks, several observations have revealed the existence of EM counterparts of the GW event spreading over the entire EM bands, with signals in the X, UV, optical, IR and radio frequencies.

The study of these different signals allows to gain physical insides concerning many open issues in astrophysics and theoretical physics, which have been for a long time objects of simulations and speculations. Specifically, the analysis of the Kilonova AT2017gfo has finally confirmed NS mergers to be the host of the r-processes through which the most heavy nuclei are synthesized. In addition, it has given information on the amount and features of the matter ejected, which can finally provide constraints on the relevance of the different ejection mechanisms and, thus, on the properties of the progenitors (Abbott et al., 2017e,a).

After giving a description of the main information gained on the EOS from these observations, we give a tentative interpretation of this event within the two families scenario (see chapter 3.3) as due to a HS-QS merger (further details in section 5.6).

#### 4.2.2 State of the art before 17 August 2017

##### *Expectations from the GW signal*

The merger of two compact objects constitutes one of the strongest sources of GWs (Shibata & Uryu, 2002). Three main stages exist which characterize the evolution of the merger process: the inspiral phase before the impact, the coalescence phase during the merger and finally the post merger phase; each one of these stages is distinguishable through its own specific waveform that is strongly dependent on physical observables such as the orbital parameters, the total mass of the binary, the spin of the two stars, the mass asymmetry ( $q$ ) and the EOS of the stars. The GW signal typical of the inspiral phase is mainly determined by the chirp mass  $M_{chirp} = \frac{(m_1 m_2)^{3/5}}{(m_1 + m_2)^{1/5}}$  where  $m_1$  and  $m_2$  are the masses of the biggest and smallest star of the system, respectively. Therefore, a detection of this signal provides a measurement of  $M_{chirp}$  and, indirectly, of the total mass of the binary  $M_{tot} = m_1 + m_2$ . The reason is that, using astrophysical observations and the results of supernovae numerical simulations, one can safely assume that  $m_2 \geq 1.1M_\odot$  and  $q = m_2/m_1 \gtrsim 0.6$ . For the major part of the inspiral phase the two stars can be approximated to point like sources but, when they reach a distance similar to their radius, their finite size must be taken into account. The latter can change in a relevant way the gravitational waveform. Indeed, a fraction of the potential energy of the system is used to perturb the structure of the stars and thus to accelerate the dynamics of the inspiral with respect to the case of point-like sources or a BH-BH merger. The larger the consequent deviation of the GW signal, the bigger is

the tidal deformability  $\Lambda$  and, at fixed masses, the radius of the components of the binary (Flanagan & Hinderer (2008), see section 4.1). Therefore, a precise measurement of the GW from the final milliseconds of the inspiral phase can provide tight constraints on the radii of the merging stars.

Finally, let us consider the possible outcomes of the merger process and the related GW signal. One case is the prompt collapse to BH, i.e. within 1 ms from the collision, which leads to a complete suppression of the GW emission. Several numerical simulations have been performed to investigate the condition for a prompt collapse to occur (Baiotti et al., 2008; Hotokezaka et al., 2013a; Bauswein et al., 2013a; Bauswein & Stergioulas, 2017). A shared conclusion is that the EOS of strong matter deeply affect the value of  $M_{tot}$  above which the remnant immediately collapses to a BH, the so called "threshold mass",  $M_{threshold}$ . In particular, Bauswein et al. (2013a); Bauswein & Stergioulas (2017) found that the compactness  $C_{max}$  of the maximum mass configuration for a cold and non-rotating star  $M_{TOV}$  is directly proportional to the ratio between  $M_{threshold}$  and  $M_{TOV}$ . Thus a eventual detection of a GW signal (or other signals) after the merger, implying that a prompt collapse did not occur, would allow to put a lower limit on  $M_{threshold}$  and consequently also on  $M_{TOV}$ . This information will represent an important clue on the nature of the high density EOS. When the remnant does not immediately collapse, it becomes an hypermassive star, a configuration whose stability is granted by differential rotation. When the latter is completely dissipated, depending on  $M_{tot}$ , the remnant can collapse to BH or turn into a supramassive star, stable because of its uniform rotation. Again, when this rotation is lost, either a BH or, if the mass is sufficiently low, a stable star is formed. In all these situations, during the so called ring-down phase, the remnant emits a strong GW signal, characterized by a very different spectrum with respect to the one proper of the inspiral phase. The features of such spectrum have been investigated in Bauswein & Janka (2012); Bauswein et al. (2012); Takami et al. (2014); Maione et al. (2017). The authors, by performing numerical simulations, found the dominant frequencies of the post-merger signal and proved their strong dependency on the EOS: potentially, the detection of at least one of these modes would allow to constrain the radius  $R_{1.6}$  of the stars within a few hundreds meters (Bauswein et al., 2016). However, unfortunately the ring-down signal has a frequency above the kHz where the sensitivity of LIGO and VIRGO is lower.

### ***Mechanisms describing the prompt emission of short GRB and the Extended Emission***

The difficulties in finding the sGRBs inner engine are related to the necessity to overcome two issues: first, launching a jet with a large Lorentz factor requires a clean environment and thus one needs to individuate a mechanism responsible of reducing the baryonic pollution; second, a fraction of the sGRBs has an Extended Emission (EE), which is comparable to the quasi-plateau emission typical of long GRBs and lasts up to  $\sim 10^4$  s, indicating that the

inner engine is not totally switched off after the prompt emission.

Two ways have been suggested to decrease the baryonic pollution: one is the collapse to BH of the merger remnant, which therefore stops ablating baryons from the surface (Rezzolla et al., 2011); the other is the formation of a QS that again prevents the baryonic pollution once the stars is deconfined up to the surface (Drago et al., 2016a).

For what concerns the origin of the EE, again two solutions can be found in the literature. The first one relies on the formation of a proto-magnetar and the EE is described similarly to a pulsar emission (Lyons et al., 2010; Dall’Osso et al., 2011; Rowlinson et al., 2013). This explanation requires the remnant to become either a supramassive star or a stable star in order to delay the eventual collapse to BH of a time equal at least to the duration of the EE. The major goal of this mechanism is the ability to reproduce the light curves of the EE in an extremely accurate way by using only two parameters: the magnetic field strength, assumed to be of about  $10^{15} - 10^{16}$  G, and the rotation period, which is asked to be of the order of a few milliseconds. The second solutions, suggested in van Putten et al. (2014), consists in the formation of an accretion disk around the BH: despite this possibility cannot be excluded, it has the main drawback of being unable to model the light curves of the EE. Since the EE is present only in a few cases, one can assume that most of the sGRBs are due to the formation, in less than a second, of a BH and that, in those cases, the accretion disk do not produce an EE. The few cases presenting an extended emission are thus explained through the protomagnetar model, in two ways. In the first case, the prompt emission is assumed to be generated again by the formation of a BH and thus one needs the so called "time-reversal" mechanism so that the EE produced before the collapse can actually be observed after the prompt signal (Rezzolla & Kumar, 2015; Ciolfi & Siegel, 2015). The time-reversal is due to the thick cocoon surrounding the protomagnetar, responsible of delaying the propagation of the soft EE signal. On the other hand, the prompt emission can leak out of the cocoon immediately along the rotation axis. In the second case, the formation of a QS powers both the prompt and the EE: the first one is generated when the deconfinement process reaches the surface, while the second is again due to the mechanism of the protomagnetar, which here is a QS (Drago et al., 2016a).

It is relevant to note that the two solutions for the EE can be discriminated through observations. Within the "time-reversal" mechanism, the prompt emission takes place in the moment of the BH formation and therefore the time delay between the GW signal from the merger and the  $\gamma$ -rays from the prompt emission is equal to the lifetime of the supramassive star, i.e.  $\gtrsim 10^3 - 10^4$  s. On the contrary, within the QS mechanism, the time delay of the prompt emission with respect to the merger is of the order of a few seconds, equal to the time needed for the deconfinement to reach the surface. This an important example of the multimessenger analysis contained in many proposals such as the "THESEUS" mission (Stratta et al., 2017).

### ***Ejected mass from NS mergers, r-processes and EM signal***

Understanding the astrophysical event responsible of hosting the r-process nucleosynthesis has been one sensitive topic in astrophysics during the last years. As first hypothesis, the mechanism of CCSN was indicated as the ideal environment for the r-processes to take place (Burbidge et al., 1957). However, recently, detailed calculations and simulations have shown that CCSN are unable to create the right conditions to synthesize the most neutron-rich nuclei (Hoffman et al., 2008; Fischer et al., 2010; Arcones et al., 2007; Roberts et al., 2010). In particular, it seems to be especially difficult for CCSN to produce the "third-peak" of the heavy nuclei abundance curve. These results have revealed the need for other astrophysical sources which could provide a sufficient matter ejection in the right conditions for the r-processes to happen. In the following we discuss the possibility of the r-process chains taking place after a BNS merger.

#### *Ejection mechanism and features of the outgoing fluid*

BNS mergers can result in the ejection of very neutron-rich matter through several processes. A classification of the different components of the ejected mass was at first presented in Hotokezaka & Piran (2015): the main sources are a dynamical ejection during and soon after the collision and a later ejection of part of the disk formed around the remnant due to neutrino and viscous heating.

Two different physical mechanisms can cause the dynamical ejection. The first one is due to the gravitational field of the NS, which leads to a tidal deformation of their internal structure; as a consequence the matter gains angular momentum and is ejected mostly in the equatorial plane. This process begins before the merger and can continue up to about 10 ms after the collision (Hotokezaka et al., 2013b). The material has a very low electron fraction,  $Y_e < 0.1$  (Palenzuela et al., 2015; Radice et al., 2016) that can eventually be increased through weak reactions taking place in a few milliseconds after the merger (Sekiguchi et al., 2015a).

The second mechanism is the shock that is generated at the NS interfaces, which can spread the material in the crusts. In addition, a shock can also be produced in the envelope of the remnant by radial oscillations which give to a fraction of the mass enough energy to become unbound. The shock component can be the dominant one for equal-mass binaries and it is emitted also in the polar direction. The electron fraction is predicted to be in the range  $0.2 < Y_e < 0.4$ , thus larger with respect to the tidal ejecta (Palenzuela et al., 2015; Radice et al., 2016; Sekiguchi et al., 2015a). The main reason for this difference is the higher neutrino flux characterizing the polar axis with respect to the equatorial plane: indeed electron, positron and electron (anti)neutrino captures can deeply affect the evolution of the electron fraction of the emitted mass (Goriely et al., 2015). Finally, the velocities characterizing the dynamically ejected matter are rather high, with values of the order of

$\beta = v/c \sim 0.2 - 0.3$ .

In the post-merger phase, some ashes of the NS surround the remnant forming a disk with a mass in the range  $10^{-3}M_{\odot} < M_{disk} < 0.3M_{\odot}$  (Shibata & Taniguchi, 2006; Rezzolla et al., 2010a; Hotokezaka et al., 2013a). A fraction of this disk can produce an outflow because of neutrino or viscous heating, whose features depend on the type of remnant and on its lifetime. In addition, a role can also be played by the strong magnetic fields existing at this stage. The amount of ejected matter is estimated to be from 5 up to 30% of the total mass of the disk and it is usually characterized by lower speeds with respect to the dynamical component, with a maximum value of the order of  $0.1c$  (Siegel & Metzger, 2017). The electron fraction of the disk ejecta, originally rather low ( $\sim 0.1$ ), can be substantially modified by neutrinos, finally spanning in the interval  $0.05 - 0.5$  with a distribution depending on the employed EOS (Palenzuela et al., 2015).

Several GR hydrodynamical simulations of the merger process have been performed with the aim of evaluating the total amount and describing the features of these different types of ejecta and of studying their dependence on the properties of the binary and on the EOS describing the NS.

The tidal component clearly depends on the tidal deformability  $\Lambda$ : the stiffer the EOS, the larger the value of  $\Lambda$  and thus the amount of tidally ejected matter. On the other hand, the shock produced during and after the merger and the consequent amount of ejecta are influenced by the compactness of the stars: soft EOSs lead to larger impact velocities and therefore to a more powerful shock which can spread more material (Bauswein et al., 2013b). Concerning the disk component, its amount is limited by the total mass of the disk that in turn is linked to the lifetime of the hypermassive star. As a consequence, a large disk ejecta can be plausibly associated to stiff EOSs producing a long-living remnant (Perego et al., 2017).

Finally, the amount of ejected mass is strongly affected by the degree of asymmetry of the binary  $q$ , being larger for more asymmetric binaries with respect to symmetric ones. This result can be interpreted in terms of the stronger effect of the tidal force that induces a deformation of the lighter star to a drop-like object, which is stretched after the merger leading to the development of a pronounced tidal tail. The degree of asymmetry influences also the average electron fraction, which is lower for larger  $q$  and this effect is relevant in particular for the soft EOSs (Sekiguchi et al., 2016a).

Eventual future observations of Kilonovae will help in disentangling the different components, providing crucial constraints for nuclear physics (Stratta et al., 2017).

### *R-processes*

After the ejection, the mass is reprocessed by the r-processes, which can, in principle, produce the known heavy nuclei distributions. The question was whether the BNS mergers

eject enough matter to explain the observed abundances. Many simulations have been performed in order to clarify this issue by reproducing the r-process nucleosynthesis path: nuclear species from the stability valley to the neutron drip line are included in the reaction network and reactions, such as neutron capture, photodisintegration together with fission and  $\beta$ -decay, are considered (Goriely et al., 2011; Korobkin et al., 2012; Goriely et al., 2013; Bauswein et al., 2013b; Just et al., 2015; Siegel & Metzger, 2018). Here the merger rate for galaxy is set in a range  $10^{-5} - 10^{-4} \text{ yr}^{-1}$  and the amount of ejected mass is of about  $10^{-3} - 10^{-2} M_{\odot}$ . The comparison between the results of these simulations and the abundances shows a good agreement for mass numbers in the regime  $A > 120 - 140$ , i.e. the region where the second and the third peak are located.

The ability of the simulated chain to reproduce the abundances of the nuclei lying between the first and the second peak is dependent on the distribution of the electron fraction obtained for the ejected mass and on the inclusion of the whole network of plausible weak interactions. Indeed, the simulations of Goriely et al. (2011); Korobkin et al. (2012); Bauswein et al. (2013b), which considered only the dynamical ejecta and of Siegel & Metzger (2018), that studied also the material from the disk, failed to reproduce the abundances for  $A < 120$  because of the low electron fraction assigned to ejected matter as a result of neglecting the neutrino absorption processes. Goriely et al. (2015) included also the weak interaction of free neutrons obtaining a relevant fraction of mass with  $Y_e = 0.3 - 0.4$  and thus being able to mimic the real abundances of nuclei in the range  $A = 90 - 140$ .

### *EM counterpart*

A probe for the ejection of matter and the realization of r-processes in BNS mergers is the analysis of the EM signal predicted to be associated to these phenomena (Metzger et al., 2010). The peak in luminosity is reached when the density of the expanding ejecta is reduced enough to allow the photons to escape. The typical timescale for this maximum is of the order of 1 day while the luminosity is about  $10^{42} \text{ erg s}^{-1}$ , three orders of magnitude larger than the Eddington luminosity for a  $1M_{\odot}$  star: a feature that earned these EM signals the name Kilonovae. The spectral peak spans in the IR/optical/near-UV wavelengths. The luminosity  $L_{peak}$ , the effective temperature  $T_{peak}$  and the timescale  $t_{peak}$  of the Kilonova depend on the amount  $M_{ej}$ , the velocity  $v$  and the opacity  $k$  of the ejected matter (Metzger et al., 2010):

$$t_{peak} \propto \left( \frac{kM_{ej}}{v} \right)^{\frac{1}{2}}, \quad L_{peak} \propto \left( \frac{vM_{ej}}{k} \right)^{\frac{1}{2}}, \quad T_{peak} \propto \left( vM_{ej} \right)^{-\frac{1}{8}} k^{-\frac{3}{8}}$$

In turn, the properties of the ejecta are linked to the EOS: for instance, an EOS that produces more ejected mass will lead to a brighter optical counterpart, with a peak at longer wavelengths and timescales (Bauswein et al., 2013b).

### 4.2.3 GW170817-GRB170817A-AT2017gfo

#### *Analysis of the GW signal*

The GW signal detected by the LVC (Abbott et al., 2017c) matches the emission from the inspiral phase of a binary with a chirp mass  $M = 1.188^{+0.004}_{-0.002} M_{\odot}$  that implies, assuming a low spin typical of BNS, a total mass  $M = 2.74^{+0.04}_{-0.02} M_{\odot}$ . The masses of the components are therefore in the interval  $1.17 - 1.6 M_{\odot}$ , firmly indicating that the merger involved two NS. Despite the proximity of the source, 40 Mpc, no GW signal has been detected during the merger and the ring-down phase. However, an interesting upper limit on the tidal parameter  $\tilde{\Lambda}$  (a combination of the tidal deformabilities and the masses of the two stars, see section 4.3) has been found: in the low spin case,  $\tilde{\Lambda} < 800$  at the 90% level. This constraint is essentially model independent and it rules out a few very stiff EOSs such as MS1 and MS1b which are based on RMF calculations (Mueller & Serot, 1996).

The outcome of the merger is still not completely clear. Although not fully excluded, the possibility of a prompt collapse seems to be extremely unlikely because of the difficulties that would arise in explaining the origin of the observed electromagnetic counterparts. Actually, one can deduce that, most probably, the post-merger remnant was a hypermassive star: indeed, a supramassive star or a stable star would inject a fraction of its extremely large rotational kinetic energy into the Kilonova or into the GRB on a long timescale and no evidence of this phenomenon has been found in the observed signals (Margalit & Metzger, 2017). This suggests that the total energy of the system, estimated to be  $\sim 95\% M_{tot}$  (assuming  $\sim 5\% M_{tot}$  to be the gravitational binding energy) is larger than  $M_{supra}$ , the maximum mass of the supramassive configuration. The latter has been calculated to be  $\sim 1.2 M_{TOV}$  by different numerical simulations on rotating compact stars (Lasota et al., 1996). Combining these factors one can deduce an upper limit on the maximum non-rotating configuration  $M_{TOV} < 2.2 M_{\odot}$ . This simple result is in agreement with the findings of Margalit & Metzger (2017); Ruiz et al. (2018); Rezzolla et al. (2018) and again it disfavors very stiff EOS with maximum masses above  $2.2 M_{\odot}$ .

In the same way, in order to interpret the remnant as a hypermassive star, one has to impose that the total energy of the system is lower than  $M_{threshold}$ . Bauswein et al. (2017) performed this analysis and concluded that extremely soft EOSs are ruled out, i.e. the radius of the  $1.6 M_{\odot}$  configuration needs to be larger than about 10.7 km.

In summary, few EOSs have already been excluded by the first detection of GWs from a BNS merger. Specifically, very stiff EOSs containing only nucleonic degrees of freedom seem to be disfavoured. In section 4.2.4 (and then again in deep in chapter 5) a different hypothesis, based on the two families scenario (section 3.3), will be discussed in relation with the phenomenology of GW170817.

### ***The weak gamma emission of GRB170817A: was it a standard short GRB?***

The gamma-ray counterpart of GW170817 was delayed by 1.7 s with respect to the moment of the merger and the detected signal was considerably weaker than the one of a typical sGRB. Moreover, no extended emission was observed, which probably suggests that the remnant was not a supramassive star. There are two possible interpretations of this peculiar emission. The first one supposes that the emission was quasi-isotropic and intrinsically sub-luminous (Gottlieb et al., 2018; Kasliwal et al., 2017), while the second one interprets the signal as a standard sGRB, but observed off-axis (Lazzati et al., 2018). The latter is currently the most accredited solution.

Independently from the specific features of the signal, the production of a strong emission in X-rays and  $\gamma$ -rays clearly suggests that the merger did not result in a prompt collapse. Indeed, explicit simulations indicate that, in order to power a jet, the remnant requires a lifetime of at least a few tens of milliseconds (Ruiz & Shapiro, 2017). The same conclusion can be inferred also from the analysis of the Kilonova signal since a relevant amount of matter needs to be ejected in the post-merger phase, as discussed in the next section.

### ***Electromagnetic signal and mass ejection***

#### *Analysis of the optical transient*

On 2017 August 17 there has been the detection of the first electromagnetic counterpart to a GW event attributed to a BNS merger. The data in near-IR (NIR), optical and UV bands extend in a range of time starting at about 0.47 and ending at 18.5 days after the merger and they are consistent with a Kilonova signal predicted to be related to a BNS merger.

The EM spectrum is dominated by a blue component in the earliest phase and in the next few days it shows a faster evolution to redder wavelengths: at 1.5 days the peak is located in the optical band around 5000 Å and already at 2.5 days it is shifted to 7000 Å, evolving to  $\sim 7800$  Å at 4.5 days and slipping finally out of the optical regime in the range between 4.5 and 7.5 days after the collision. By 10 days the peak reaches a wavelength  $> 15000$  Å. (Nicholl et al., 2017). Consistently, the rate of the decline is different depending on the band: while it appears to be very rapid in the ug band (blue) with a rate of about  $\sim 2$  mag/day, the rizY (red) and the HKs (NIR) bands are characterized by smoother decay. For this reason the spectrum at late time becomes dominated by red (Cowperthwaite et al., 2017). The short timescale ( $\sim 1$  day) and the initial luminosities ( $\sim 5 \cdot 10^{41}$  erg s $^{-1}$  at 0.6 days and  $\sim 2 \cdot 10^{41}$  erg s $^{-1}$  at 1.5 days) are compatible with the so called Blue Kilonova: this model for the signal was firstly proposed by Metzger et al. (2010) and later developed in association with the r-processes and the different ejection mechanisms taking place after a BNS merger. For instance, Roberts et al. (2011) studied the tidal tails forming during the

merger while Metzger & Fernández (2014) presented an analysis of the outflow expected from the remnant in the case of a delayed ( $> 100\text{ms}$ ) collapse to BH. All the results have in common the considerably low opacity attributed to the ejecta with values in an interval from  $k = 0.1$  to  $k = 1 \text{ cm}^2\text{s}^{-1}$ , typical of matter containing Fe-group or light r-process nuclei having  $A < 140$ . Therefore, the Blue Kilonova is likely to be connected to r-processes responsible of the synthesis of nuclei, which lies between the first and the second peak.

On the contrary, the late emission which is dominant at timescales of the order of a week, presents a lower luminosity  $\sim 10^{40} - 10^{41} \text{ erg s}^{-1}$  and fits well a second model, called Red Kilonova (Cowperthwaite et al., 2017). Barnes & Kasen (2013); Kasen et al. (2013); Tanaka & Hotokezaka (2013); Tanaka et al. (2018) have presented the analysis of the effect on the resulting EM signal of higher opacity ejected mass. This large value of the opacity, up to about  $10 \text{ cm}^2\text{s}^{-1}$ , is attributed to the presence of heavy nuclei with  $A > 140$ , the Lanthanides: as a consequence, one can interpret the Red Kilonova as the outcome of a nucleosynthesis chain able to fill the third peak of r-processes.

This piece of observational evidence indicates the existence of ejected matter not having a unique value of the opacity and thus a different Lanthanides content. Although a single component ejecta characterized by a power-law speed distribution and a time-dependent opacity (investigated by Waxman et al. (2018) with an analytical model) can not be ruled out, the most accredited hypothesis suggests the existence of at least two different components of the ejected mass, a Lanthanide poor one to explain the Blue Kilonova and a Lanthanide rich one to power the Red Kilonova (Metzger & Fernández, 2014; Wollaeger et al., 2018). This conclusion is also confirmed by the evidence for the blue component not being obscured by the red one, that indicates distinct regions and emission angles for the components of the ejecta characterized by different value of the opacity. This also gives a clue to interpret these two components as the results of distinct ejection sources (Cowperthwaite et al., 2017).

The effective temperature and the duration of the Kilonova signal have been investigated with models outlined in Kasen et al. (2013) and Villar et al. (2017) where the mass, the velocity and the opacity of the ejected matter are treated as fitting parameters. The result of these studies is that the emission is compatible with a two component model, consisting of: a Blue component having  $M_{ej}^B \sim 0.01$ –few  $0.01 M_{\odot}$ , velocity  $v_{ej}^B = 0.27 - 0.3c$  and opacity  $k^B = 0.5 \text{ cm}^2\text{s}^{-1}$  which requires a Lanthanide fraction of  $\sim 10^{-4}$  to  $10^{-5}$  in the outermost part of the ejecta (Cowperthwaite et al., 2017; Nicholl et al., 2017); a Red component having  $M_{ej}^R \sim 0.04 M_{\odot}$ , velocity  $v_{ej}^R = 0.12c$  and opacity  $k^R = 3.3 \text{ cm}^2\text{s}^{-1}$ , which needs a Lanthanide fraction of  $\sim 10^{-2}$  (Cowperthwaite et al., 2017; Chornock et al., 2017). A further possibility to explain the data is a three component model: a Blue one having  $M_{ej}^B \sim 0.01 M_{\odot}$ , velocity  $v_{ej}^B = 0.27c$  and opacity  $k^B = 0.5 \text{ cm}^2\text{s}^{-1}$ ; a Red one with  $M_{ej}^R \sim 0.01 M_{\odot}$ , velocity  $v_{ej}^R = 0.16c$  and opacity  $k^R = 10 \text{ cm}^2\text{s}^{-1}$  and a Purple one having  $M_{ej}^P \sim 0.03 M_{\odot}$ , velocity  $v_{ej}^P = 0.11c$  and an intermediate value for the opacity,  $k^P = 3 \text{ cm}^2\text{s}^{-1}$  (Cowperthwaite et al., 2017).

*Role of different ejection mechanisms*

The distinct values of the opacity, and thus of the Lanthanides fraction, required to explain the Red and Blue (and eventually Purple) Kilonovae, can be directly linked to the electron fraction of the ejected mass,  $Y_e$ : a lower electron fraction results in the ability to synthesize heavier nuclei, thus to a larger concentration of Lanthanides and to a greater opacity. In turn, the  $Y_e$  characterizing the ejected matter depends on the direction and on the mechanism causing the ejection (Wollaeger et al., 2018).

The Blue component, having a very low opacity, requires a Lanthanide-poor matter characterized by an electron fraction  $> 0.25 - 0.3$ : this type of material can be ejected dynamically because of the shock produced at the collision in the NS interfaces (Palenzuela et al., 2015; Sekiguchi et al., 2015a; Goriely et al., 2015; Bauswein et al., 2013b); this kind of ejecta is most likely found within an angle in the range  $30^\circ$  and  $45^\circ$  (Sekiguchi et al., 2016a; Radice et al., 2016), with respect to the polar axis. Since here the flux of neutrinos is more intense, the absorption reactions take place and they play a central role in raising the material electron fraction to  $Y_e \gtrsim 0.25$  (Kasen et al., 2013; Perego et al., 2017). In addition, if the remnant becomes an HMNS, it will be surrounded by a disk, that reaches a stable configuration after few tens of milliseconds and where a neutrino-driven wind is produced at a timescale of about 10 ms (Perego et al., 2014). The latter causes the ejection of about the 5% of the disk mass, mainly in the polar direction. Again, the large neutrino flux present along the polar axis increases the electron fraction up to a distribution, peaking at  $Y_e = 0.3 - 0.4$ , and thus also the wind mechanism finally produces a low-opacity ejecta (Perego et al., 2014; Fernández & Metzger, 2013). The two different sources, the shock and the wind, can be distinguished by means of the resulting velocities of correspondent masses, being of about  $0.2-0.3 c$  for the dynamical ejecta while  $v < 0.1c$  for the neutrino-driven wind ejecta (Siegel & Metzger, 2017; Perego et al., 2014; Fernández & Metzger, 2013).

The very high speed attributed to the Blue component,  $0.27 - 0.3 c$ , constitutes a relevant proof of its dynamical origin. However, while some authors claim the shock representing the exclusive mechanism to power the low opacity component (Cowperthwaite et al., 2017; Nicholl et al., 2017), others interpret it as the result of a combination of both the dynamical and the wind ejecta (Perego et al., 2017). In the first case, the needed amount of ejected mass,  $\sim 10^{-2} M_\odot$  implies a soft EOS allowing to reach a very high impact velocity: this sets an upper limit on the radius of the stars at a value of maximum 12 km (Nicholl et al., 2017). The second hypothesis, on the contrary, does not require an equally tight limit on the NS radius.

Concerning the higher opacity and Lanthanide richer Red component, the widely accepted interpretation suggests, as source, the dynamical tidal ejection which takes place mostly in the equatorial plane (within an angle in the interval  $45^\circ - 60^\circ$ ). The resulting material has

indeed a very low electron fraction  $< 0.1$  (Hotokezaka et al., 2013b; Palenzuela et al., 2015; Radice et al., 2016) and therefore it results in a Red-NIR spectrum characterized by a longer timescale (Kasen et al., 2013; Barnes & Kasen, 2013). The large amount of matter deduced from the data could be an indication of a binary having a very high degree of asymmetry (Cowperthwaite et al., 2017). However, to fully explain the component with  $k \sim 3 \text{ cm}^2\text{s}^{-1}$  and a very large mass, which can be interpreted as part of the Red Kilonova or a distinct Purple Kilonova, one must take into account also the outflow from the disk.

First of all, the matter ejected by the wind at angles  $> 30^\circ$  is less affected by neutrinos and can therefore keep the electron fraction  $Y_e \sim 0.25-0.3$  required to fit the intermediate opacity component (Tanaka et al., 2018; Perego et al., 2014; Kasen et al., 2015). In parallel, a contribution can also be provided by the secular ejecta which is present at the whole solid angle, but it is equatorial dominated: this viscous-driven mechanism can result in the ejection of up to 30% of the disk with a  $Y_e$  depending on the lifetime of the HMNS in comparison with the one of the disk ( $\sim$  ten of ms). For a long-lived HMNS the electron fraction distributes in the range between 0.2 - 0.5 and presents a peak at  $\sim 0.3 - 0.4$ ; on the other hand, if the remnant collapse earlier,  $Y_e < 0.3 - 0.4$  (Fujibayashi et al., 2018).

Perego et al. (2017), using a three component model, and Cowperthwaite et al. (2017) indicate, indeed, this intermediate opacity component as originating from the early viscosity-driven secular ejection: this conclusion implies both a short-lived remnant ( $\sim 30$  ms) and a large mass of the disk  $\sim 0.08 M_\odot$ . These two features point to different directions for what concerns the properties of the EOS: on one hand a soft EOS can prevent the remnant to form a long-lived HMNS, but on the other hand, the larger value of the tidal deformability proper of a stiffer EOS can lead to the formation of more pronounced tidal tails and therefore a more massive disk surrounding the remnant. However, the upper limit set on the tidal deformability by the GW measurement (discussed in section 4.2.3) and the absence of a direct collapse to BH rule out extremely stiff or extremely soft EOS respectively, suggesting therefore an EOS with an intermediate softness.

In summary, the mechanisms able to provide the observed Kilonova (and the GRB) are still not fully understood but more detections in the future will shed light on this problem.

#### 4.2.4 A different hypothesis: a hadronic star - quark star merger

In this section, we will shortly discuss the possible explanations of the features of the GW signal seen in August 2017 and its EM counterpart within the two families scenario and assuming that the corresponding binary was composed by a HS and a QS. The aim here is only to provide few hints correlated with the above discussion, but this subject (and also the reason for the choice of this binary) will then be described in details in chapter 5.

First, the GW signal has definitely suggested that extremely stiff EOSs are excluded: the limit set on  $\tilde{\Lambda}$  is satisfied only for stars having radii  $\lesssim 13.4$  km (Annala et al., 2018). Both HSs and QSs fulfill this constraint (see chapter 3.3 and Hinderer et al. (2010)).

Second, GRB170817A, since it comes without an EE, is likely launched through the BH mechanism of Rezzolla et al. (2011); Ruiz et al. (2016), explained in section 4.2.2. Within the two families scenario, the remnant is a HM hybrid star in which the deconfinement process to convert hadronic into quark matter is taking place and that will collapse as soon as the differential rotation is dissipated.

Let us finally describe how to fit the features of the observed Kilonova. Perego et al. (2017) proposes an effective two components model where the secular ejecta is predicted to be characterized by a very low opacity ( $\sim 1 \text{ cm}^2\text{s}^{-1}$ ), comparable to the one of the neutrino-driven wind component. This hypothesis leads to two main consequences: firstly, the lifetime of the remnant needs to be long enough to allow weak reactions to increase the electron fraction to  $> 0.3$  and, secondly, the tidal ejecta has to provide a very significant contribution.

Both these demands can be satisfied by a HS-QS merger; indeed the aforementioned HM hybrid star formed after the merger can survive for a timescale of the order of hundreds of milliseconds. In addition, if the binary is very asymmetric with  $q$  of about  $0.75 - 0.8$ , the tidal deformability of the lightest star (HS) can reach value of  $\sim 500$  (Wiktorowicz et al., 2018). This rather high value of  $\Lambda$  together with the assumed large asymmetry of the binary can result in a significant amount of tidal ejecta, which allows to explain both the third peak of r-processes and the Red Kilonova without the necessity of a high opacity secular ejecta.

### 4.3 from $\tilde{\Lambda}$ to radii constraints

As explained in the previous section, the GW signal characterizing the last cycles of the inspiral phase is "deformed" by the effect of tidal forces. Because of that, GW170817 allowed to put some constraints on the so called dimensionless tidal deformability  $\tilde{\Lambda}$  defined as:

$$\tilde{\Lambda} = \frac{16}{13} \frac{(m_1 + 12m_2)m_1^4\Lambda_1 + (m_2 + 12m_1)m_2^4\Lambda_2}{(m_1 + m_2)^5} \quad (4.3.1)$$

The upper limit is  $\tilde{\Lambda} < 800$  at 90% confidence level, assuming low-spin priors. This requirement ruled out some very stiff EOSs (Abbott et al., 2017c).

At the same time, extremely soft EOSs are also disfavoured. Indeed, the detection of post-merger EM signals, such as the GRB and the KN, excludes the prompt collapse scenario suggesting the formation of a hypermassive NS (HMNS) configuration. This is possible only if  $M_{thr} > M_{tot}$ : Bauswein et al. (2017) translate this phenomenological evidence into a lower limit for the radius  $R_{1.6} > 10.7 \text{ km}$ . A second argument from Radice et al. (2018b) states that the amount of mass required to explain the Kilonova signal allows to infer a lower limit

on the tidal deformability  $\tilde{\Lambda} > 400$  (see also Alexander et al. (2017), Pian et al. (2017) and Coulter et al. (2017)).

Burgio et al. (2018), by using a set of several EOSs studied the relation between the aforementioned constraints on  $\tilde{\Lambda}$  and the radius for the  $1.5M_{\odot}$  configuration  $R_{1.5}$ . In particular, they evaluated  $\tilde{\Lambda}$  and the minimum  $R_{1.5}$  of the binary for the allowed values of masses, given the measured chirp mass and a range of asymmetries  $q = [0.7 - 1]$ .

In the case of one-family scenario, i.e. a single EOS describing both the NS, they found a strong correlation among the two variables which leads to a lower limit  $R_{1.5} > 11.8$  km. On the contrary, if a second branch of CSs containing quark matter is introduced, the relation among  $\tilde{\Lambda}$  and  $R_{1.5}$  is violated. In particular, within the twin star scenario,  $R_{1.5} = 11.6$  km was obtained with  $c_s^2 = \frac{2}{3}$ , lowered to  $R_{1.5} = 10.7$  assuming  $c_s^2 = 1$ . On the other hand, within the two families scenario, both the parametrizations employed for the hadronic EOS result in even smaller radii,  $\sim 10.6$  km and  $\sim 11.2$  km.

In conclusion, the lower limit on the radius found for one-family EOSs is not valid in the case of EOSs assuming two branches, one of which containing quark matter. In these two families types of solutions, the radius can be considerably smaller than 12 km allowing, once again, to reconcile apparently contradictory experimental data.

#### 4.4 GW190425

A second detection of a GW signal from a binary whose mass parameters are consistent with two NS has been announced on 2019 April 25 (Abbott et al., 2020a). The observation of GW190425 was performed with the LIGO Livingston detector, while Virgo did not participate to the detection but its data gave a contribution in the parameter estimation. The 90% credible intervals for the source properties are shown in Table 4.1 for the low-spin prior ( $< 0.05$ ) and the high-spin prior ( $< 0.89$ ) cases.

This event is particularly interesting because of the estimated total mass, which is relevantly

	low-spin prior	high-spin prior
primary mass $m_1$	$1.60 - 1.87M_{\odot}$	$1.61 - 2.52M_{\odot}$
secondary mass $m_2$	$1.46 - 1.69M_{\odot}$	$1.12 - 1.68M_{\odot}$
chirp mass $M_{chirp}$	$1.44^{+0.02}_{-0.02}M_{\odot}$	$1.44^{+0.02}_{-0.02}M_{\odot}$
mass ratio $\frac{m_2}{m_1}$	$0.8 - 1.0$	$0.4 - 1.0$
total mass $m_{tot}$	$3.3^{+0.1}_{-0.1}M_{\odot}$	$3.4^{+0.3}_{-0.1}M_{\odot}$
dimensionless tidal deformability $\tilde{\Lambda}$	$\leq 600$	$\leq 1100$

**Table 4.1**

larger than those of any previously known BNS system. This opens the possibility for the

GW analysis to investigate extreme states of nuclear matter up to several time  $n_0$  where phase transitions can occur.

However, unfortunately the signal-to-noise ratio for GW190425 is quite low (12.9) compared to GW170817 thus the inferred limits of the tidal deformability and the radius are consistent but less constraining with respect to the one obtained from the first BNS detection. In particular,  $\tilde{\Lambda} < 1100$  and  $R < 15$  km using the EOS insensitive relation (Yagi & Yunes, 2016, 2017).

Finally, Abbott et al. (2020a) claim no evidence for a post-merger signal in GW (with the method from Chatziioannou et al. (2017) and Abbott et al. (2019)), neither of a related EM emission. The lack of a GRB or a Kilonova suggests a prompt collapse to BH: the probability for this scenario was estimated (following Agathos et al. (2020)) to be 97% with the high-spin prior and 96% assuming the low-spin prior.

# 5

## *Merger of Compact Stars in the Two-families Scenario*

This chapter is dedicated to the description of our work in [De Pietri et al. \(2019\)](#) where the outcome of the merger process is studied in the context of the two families scenario (© AAS. Reproduced with permission).

In particular, a comparison is made between the results obtained using as EOSs SFHo containing only nucleons (chapter [3.1.3](#)) and SFHo-HD, the hadronic branch of the two families scenario including also hyperons and  $\Delta$ s (chapter [3.3.1](#)).

For this purpose, we performed hydrodynamical simulations of the merger using two open source software based on numerical relativity, LORENE ([lorene.obspm.fr](#), [Bonazzola et al. \(1998\)](#)) and the Einstein Toolkit (ET, [einsteintoolkit.org](#), [Loffler et al. \(2012\)](#), for the last version see [Brandt et al. \(2020\)](#)). The first one provides the initial conditions for the process, while the last one deals with the dynamics of the merger. A brief description of the ET main modules and the equations to be solved is provided in [Appendix A](#).

### **5.1 Introduction**

The first detection of GW from the merger of two compact stars in 2017 ([Abbott et al., 2017c](#)) determines a relevant step forward for the physics of compact objects and dense nuclear matter (see chapter [4](#) for a detailed discussion). The GW signal associated to the inspiral phase contains information on the average tidal deformability  $\tilde{\Lambda}$  of the binary that depends strongly on the stiffness of the EOS of dense matter. Many recent studies have used the limits on  $\tilde{\Lambda}$ , to infer constraints on the radius of compact stars ([Fattoyev et al., 2018](#); [Most et al., 2018](#); [Lim & Holt, 2018](#); [Abbott et al., 2018](#); [Burgio et al., 2018](#)). The

electromagnetic counterparts, GRB170817A and the Kilonova AT2017gfo, allow to add further limits on the EOS by suggesting that, most probably, the remnant of the merger is a hypermassive compact star and by demanding that the mass ejected and powering the Kilonova signal is of the order of  $0.05M_{\odot}$  (Bauswein et al., 2017; Margalit & Metzger, 2017; Annala et al., 2018; Ruiz et al., 2018; Radice et al., 2018b; Rezzolla et al., 2018). The most relevant conclusion of those analyses can be summarized by affirming that the EOS cannot be very stiff, therefore EOSs leading to a radius larger than approximately 13.5 km are ruled out; in addition, the maximum mass of the static configuration should be smaller than about  $\sim 2.2M_{\odot}$  although this value comes with a large error of the order of  $0.2M_{\odot}$ . This result is interesting: indeed, suggestions of radii larger than  $\sim 13.5\text{km}$  would point to a stiff EOS composed by nucleons only while for smaller radii new non-nucleonic degrees of freedom could be present in compact stars.

The appropriate degrees of freedom composing a compact star can be deduced from the value of the radius of a configuration with mass of  $1.5M_{\odot}$  (see section 3.2 for a detailed discussion). Firstly, in the case of a large radius,  $13\text{ km} \lesssim R_{1.5} \lesssim 13.5\text{ km}$ , the central density is low enough for non-nucleonic degrees of freedom to appear only inside the most massive stars (Lonardoni et al., 2015). Secondly, for  $11.5\text{ km} \lesssim R_{1.5} \lesssim 13\text{ km}$ , hyperons or  $\Delta$  resonances will appear already in stars with a mass of  $\sim 1.5M_{\odot}$  (Maslov et al., 2015). In this case, also deconfined quarks could appear in the core of the star that becomes a hybrid star (Nandi & Char, 2018). Finally, for a radius  $R_{1.5} \ll 11.5\text{km}$  the only possibility is to consider disconnected solutions of the TOV equation (Alford et al., 2013; Burgio et al., 2018). These solutions show a mass window inside which two different configurations exist: the first composed only of hadronic matter and the second made totally or partially of deconfined quark matter. These models correspond either to the twin-stars scenario (see section 3.2.5) or to the two-families scenario (see section 3.3).

A relevant point is that within the two families scenario HSs and Qs coexist. A method to classify compact stars is to check their masses and radii: in some cases the observational evidence allow to discriminate among the two families (Char et al., 2019). Once the star has been identified as a HS or a QS, the model can be tested by checking whether all the remaining properties are consistent or not with that classification.

In this work, we extend a previous study on the predictions of the mergers of HS-HS binaries within the two families scenario (Drago & Pagliara, 2018). After giving overview of the merger phenomenology within this scenario, we present the outcomes of numerical simulations of the merger of two HSs performed using the ET. We employ two EOSs: the first one is soft and contains hyperons and deltas and leads to the HSs family and the second one, for comparison, is a stiffer EOS made purely of nucleonic matter. The main result of the simulations is a quantitative estimate of the threshold mass for the merger of two HSs. Moreover, we provide an estimate of the mass ejected, which is a relevant quantity that influences the phenomenology of Kilonovae. In addition, we discuss quark

matter nucleation and finally the different possible types of merger within the two families scenario by exploiting the population synthesis code `Startrack` (Belczynski et al., 2002, 2008; Wiktorowicz et al., 2017).

## 5.2 Equations of state of hadronic matter and quark matter

To build the EOS we adopt the RMF model SFHo of Steiner et al. (2013a) with the inclusion of hyperons and delta resonances. The EOS, labelled as SFHo-HD has been already investigated in Burgio et al. (2018) and it corresponds to a choice of the coupling of the sigma meson with the delta resonances of  $x_{\sigma\Delta} = 1.15$  (see section 3.3.1).

For the EOS of quark matter we employ a simple bag-like parametrization (Alford et al., 2005; Weissenborn et al., 2011) containing effective bag constant  $B_{\text{eff}}$  and a parameter  $a_4$  that encodes the pQCD corrections. We choose  $B_{\text{eff}}^{1/4} = 137.5$  MeV,  $a_4 = 0.75$  and  $m_s = 100$  MeV for the mass of the strange quark and we find  $M_{\text{TOV}}^Q \sim 2.1M_{\odot}$  (see section 3.3.1).

### 5.2.1 Transition from hadronic matter to quark matter

To describe the formation of quark matter we use a scheme developed in Heiselberg et al. (1993); Iida & Sato (1998); Berezhiani et al. (2003); Bombaci et al. (2004); Niebergal et al. (2010). This model is based on quantum nucleation and the main idea is that the process of creation of the first quark matter droplet conserves the flavor composition and thus it is not possible to nucleate strange quark matter in the case in which kaons or hyperons do not already exist in the hadronic phase. In Figure 5.2.1 the fraction  $Y_i$  of baryons is plotted as a function of the baryon density  $n_b$ . One can notice that, an increase of  $n_b$  corresponds to a larger hyperon content and this makes the conversion to strange quark matter more probable. A way to approximately define a threshold for the process of conversion of hadronic matter into strange quark matter is to ask that the mean distance of  $s$  quarks inside the confined phase,  $d_s$ , is of the order or smaller with respect to the average distance of the nucleons in nuclear matter:  $d_n = n_0^{-1/3}$ , where  $n_0 = 0.16 \text{ fm}^{-3}$  is the saturation density. The reason for this limit is that the  $s$  quarks should be close enough so that they can interact with each other and, in this way, help the formation of a first droplet of deconfined quark matter. This is an intuitive way to define a critical density and can be regarded as a necessary condition (for a more quantitative discussion see the papers cited above). Another important point is that the high temperature reached in the merger could trigger a thermal nucleation and the whole deconfinement process would be significantly faster (Di Toro et al., 2006).

Let us now define the strangeness fraction as  $Y_S = (n_{\Lambda} + 2(n_{\Xi^0} + n_{\Xi^-}))/n_b$ . In the upper panel of Figure 5.2.1, the fraction of the strange and not-strange baryons is shown, together with the  $Y_s$ , at a temperature  $T = 0$ . The aforementioned condition on the strangeness

minimal density is fulfilled above a baryon density of about  $(0.9\text{--}1)\text{ fm}^{-3}$  corresponding to  $Y_S \sim 0.2\text{--}0.3$  and to about  $(6\text{--}7)n_0$  (in the figure see the two points drawn on the dashed line). This density is relevantly larger than the threshold density for formation of hyperons, that is close to  $0.6\text{ fm}^{-3}$  (in agreement with Bombaci et al. (2004, 2009)). We underline that, for  $T = 0$ , the condition for quark nucleation is fulfilled at densities smaller than the ones corresponding to the maximum mass which is mechanically stable,  $M_{\text{TOV}}^H$ . Therefore, following Bombaci et al. (2004), we introduce a different notation  $M_{\text{max}}^H$  for the maximum mass of a HS that is stable with respect to quark nucleation.

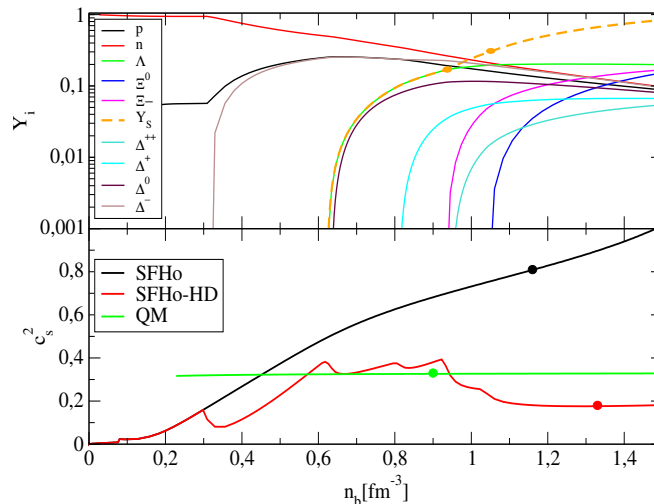


**Figure 5.2.1:** Upper panel: density dependence of the particle fractions  $Y_i$  and strangeness fraction  $Y_S$  for  $\beta$ -stable matter at  $T = 0$ . The orange points specify the range of densities and  $Y_S$  for which the nucleation of strange quark matter can take place:  $0.2 \lesssim Y_S \lesssim 0.3$ . Lower panel: squared speed of sound as a function of the density in the case of SFHo EOS, of its generalization including hyperons and  $\Delta$ s, SFHo-HD, and for the quark matter (QM) EOS. The black and red dots correspond to the central densities and the squared speed of sound of the maximum mass configuration.

A property, specific of the two families scenario and of this mechanism of quark deconfinement, is the chance to form also hybrid stars (HybSs) at finite temperatures as an outcome of the partial turbulent conversion from hadronic matter to quark matter. These HybSs live for approximately 10 s, the time which is needed to hadronic matter to complete the conversion into quark matter, within the diffusive regime. They feature a two-phase structure composed by a hot quark matter core and an initially cooler hadronic matter layer, which are in mechanical equilibrium but not in thermal or chemical equilibrium. By exploiting the Coll’s condition, one can model the EOS for this short-living hybrid configuration (see section 3.3.3 for details). The motivation to study here these transient

configurations (labelled as Coll-hyb) is that, in the case of a HS-HS or of a HS-QS merger, they can be formed in the postmerger remnant while the conversion still proceeds.

In this scenario, the QSs have also a minimum mass  $\sim (1.35 - 1.45)M_{\odot}$  depending on the the maximum mass of HSs (see section 3.3.2).

A further peculiar feature of the two families scenario regards the value of the squared speed of sound  $c_s^2$ : in the hadronic EOS, it remains below  $\sim 0.4$  because of the softening channels related to the appearance of hyperons and  $\Delta$ s (red line of Figure 5.2.1). Concerning the quark EOS, at the increase of the density, it approaches the conformal limit of 1/3 from below (see green line Figure 5.2.1). For a discussion on the speed of sound within the two families scenario see chapter 8.5.

### 5.2.2 *Static and rotating configurations*

The outcome of the merger of two compact objects, in particular the features of the post-merger remnant and of the GW and electromagnetic signals, is determined by two quantities: the threshold mass,  $M_{\text{threshold}}$ , and the maximum mass of the supramassive configuration,  $M_{\text{supra}}$ , which are strongly dependent on the EOS (for details see section 4.2.2). This is true either in the case of a one-family model and in the case of the two families scenario, but, for the latter, the problem is more complex because those quantities have to be calculated for both families (and also for the Coll-hyb configuration).

Firstly, we show the results obtained for the structure of both the static and the rotating stars using the aforementioned EOSs. Several studies have been focused on the investigation of the dependence of the threshold mass on the stiffness of the EOS: Bauswein et al. (2013a, 2016); Bauswein & Stergioulas (2017), using explicit numerical simulations, found that the ratio  $k = M_{\text{threshold}}/M_{\text{TOV}}$  scales linearly with the compactness of the maximum mass configuration,  $M_{\text{TOV}}/R_{\text{TOV}}$ ;  $k$  ranges between 1.3 and 1.6, depending on the EOS. In Section 5.4, a way to estimate  $k$  directly from numerical simulations will be discussed. For what concerns  $M_{\text{supra}}$ , several works have obtained that  $M_{\text{supra}} \sim 1.2M_{\text{TOV}}$  (Lasota et al., 1996; Breu & Rezzolla, 2016) in the case of stars having a crust, such as HSs and HyBs, while for QSs  $M_{\text{supra}} \sim 1.4M_{\text{TOV}}$  (Gourgoulhon et al., 1999; Stergioulas, 2003).

We have calculated both the static and the keplerian configurations with the RNS code of Stergioulas & Friedman (1995). The results are plotted in Figure 5.2.2: in all the cases, the standard relations between  $M_{\text{TOV}}$  and  $M_{\text{supra}}$  previously discussed are confirmed. In particular, for our Coll-hyb, the Kepler configuration has a maximum mass of the order of  $2.6M_{\odot}$ . The stability of this configurations is crucial both for HS-HS and HS-QS mergers. We have not estimated the maximum mass for a Coll-hyb configuration  $M_{\text{threshold}}^{\text{Coll-hyb}}$  with differential rotation through a numerical simulation, but we can safely use the assumption  $M_{\text{threshold}}^{\text{Coll-hyb}} \geq M_{\text{supra}}^{\text{Coll-hyb}}$ .

Now we summarize the resulting values for the masses previously discussed. First of all, we introduce  $M_{\text{tot}}$  as the sum of the gravitational masses of the two stars composing the

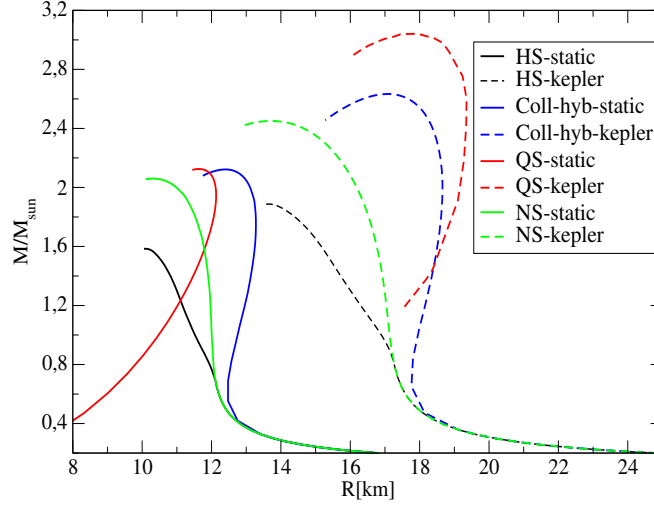


**Figure 5.2.2:** Static and keplerian mass-radius curves for NSs described through the SFHo EoS, HSs, Coll-HybSs and QSs.

binary:

$$M_{\text{tot}} = M_1 + M_2. \quad (5.2.1)$$

This quantity need to be distinguished from the remnant mass  $M_{\text{remnant}}$ , i.e. the gravitational mass which remains after the GW emission and the mass ejection. These two masses are related by the equation:

$$M_{\text{remnant}} = (1 - \alpha)M_{\text{tot}}, \quad (5.2.2)$$

where  $\alpha$  is about a few percent. Plausible values for the aforementioned masses are:

- HSs:

- $M_{\text{TOV}}^H \sim M_{\text{max}}^H \sim 1.6M_{\odot}$
- $M_{\text{supra}}^H \sim 1.9M_{\odot}$
- $M_{\text{threshold}}^H \sim 2.5M_{\odot}$

- Coll-HyBs:

- $M_{\text{TOV}}^{\text{Coll-hyb}} \sim M_{\text{TOV}}^Q \sim 2.1M_{\odot}$
- $M_{\text{supra}}^{\text{Coll-hyb}} \sim 2.6M_{\odot}$
- $M_{\text{remnant}}^{\text{Coll-hyb}} = (1 - \alpha)M_{\text{threshold}}^{\text{Coll-hyb}} \sim 1.5 M_{\text{TOV}}^{\text{Coll-hyb}} \sim 3.1M_{\odot}$

- QSs:

- $M_{\text{TOV}}^Q \sim 2.1M_{\odot}$

- $M_{\text{supra}}^Q \sim 3M_{\odot}$
- $M_{\text{threshold}}^Q \sim M_{\text{supra}}^Q \sim 3M_{\odot}$ <sup>1</sup>

Within the two families scenario, an uncertainty exists on  $M_{\text{TOV}}^H$  (and consequently on  $M_{\text{supra}}^H$  and  $M_{\text{threshold}}^H$ ) and on  $M_{\text{max}}^H$  caused by the difficulty in the estimate of the critical central density at which the deconfinement process is triggered. A reasonable interval of values for  $M_{\text{max}}^H$  is  $(1.5 - 1.6)M_{\odot}$  and slightly higher for  $M_{\text{TOV}}^H$ .

Concerning the QSSs, a large variability remains for  $M_{\text{TOV}}^Q$ , which reflects the large error-bar in the estimate of the maximum mass of a compact star  $(2.2 \pm 0.2)M_{\odot}$  (an analysis of QSSs EOS is presented in chapter 8). This uncertainty translates also into a similar variability on the value of  $M_{\text{TOV}}^{\text{Coll-hyb}}$ : once the latter,  $M_{\text{TOV}}^{\text{Coll-hyb}}$ , is selected, the value for  $M_{\text{supra}}^{\text{Coll-hyb}}$  can be explicitly calculated. On the contrary,  $M_{\text{threshold}}^{\text{Coll-hyb}}$  has only been estimated by exploiting the results in [Weih et al. \(2018\)](#), which indicates that the maximum mass of stars with differential rotation is about  $\sim 1.5$  times larger than  $M_{\text{TOV}}$ .

Lately, [Char et al. \(2019\)](#) performed an analysis of the observational result concerning masses and radii of compact stars within the two families scenario. The authors found that, within this model, all the available constraints can be fulfilled. Moreover, the ranges of the masses of HSs and QSSs is in agreement with the mass distribution of the two sub-populations studied in [Antoniadis et al. \(2016\)](#); [Alsing et al. \(2018\)](#); [Tauris et al. \(2017\)](#) which are centered at  $m_1 = 1.39M_{\odot}$  with  $\sigma_1 = 0.06M_{\odot}$  and at  $m_2 = 1.81M_{\odot}$  with  $\sigma_2 = 0.18M_{\odot}$ , respectively. The values that we find for  $M_{\text{max}}^H$  and for  $M_{\text{min}}^Q$  are very similar to the upper limit for  $m_1$  and the lower limit for  $m_2$ , respectively. A possibility is therefore to identify the first sub-population with HSs and the second with QSSs.

### 5.3 Classification of the mergers

Within our scenario, three different types of binaries exist, HS-HS, HS-QS, QS-QS. The HS-HS is the only possible kind of merger within a one-family model while QS-QS has been studied in some works without an assumption about the number of branches of compact stars ([Haensel et al., 1991](#); [Bauswein et al., 2009, 2010b](#)). On the other hand, HS-QS is a combination which is possible only in the case of the two families scenario. These various possibilities are shown in the diagram of [Figure 5.3.1](#), where the two axes represent the chirp mass  $M_{\text{chirp}}$  and the mass asymmetry  $q = m_2/m_1$ , since these two parameters determine the properties of the binary. As evident from the diagram, the phenomenology of mergers is very rich: for example, inside the small window marked as "All-comb.", all the three type of mergers are possible. On the contrary, there are regions in the diagram where we can

<sup>1</sup>The ratio between  $M_{\text{threshold}}^Q$  and  $M_{\text{TOV}}$ , which are close to the one between  $M_{\text{supra}}$  and  $M_{\text{TOV}}$ , is extracted from [Figure 2 of Bauswein et al. \(2009\)](#).

exactly predict one specific type of merger (for example only HS-HS is possible in the green area). Consequently, for binaries characterized by same  $M_{\text{chirp}}$ , the merger could either result in a prompt collapse in the HS-HS case or lead to a hypermassive or a supramassive configuration in the case of HS-QS (Drago & Pagliara, 2018). Consider that the classification of Figure 5.3.1 is only based on the maximum and minimum masses for the HSs and the QSs and it does not provide information about the outcome of the possible mergers, a problem addressed in section 5.3.2. In addition, the probabilities of the different merger processes will be discussed in section 5.5 by using a code for population synthesis.

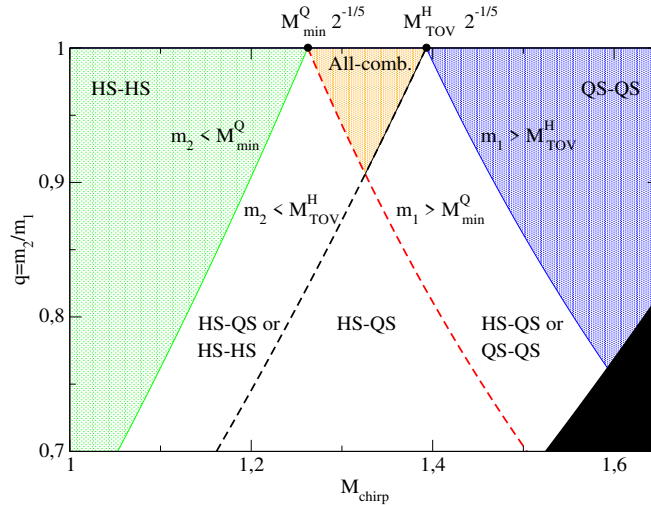


**Figure 5.3.1:** Possible mergers types within the two families scenario, as functions of the binary chirp mass and mass asymmetry. The chosen minimum masses are  $M_{\text{min}}^H = 1M_{\odot}$  and  $M_{\text{min}}^Q = 1.45M_{\odot}$  while the maximum masses are  $M_{\text{max}}^H = 1.6M_{\odot}$ ,  $M_{\text{TOV}}^Q = 2.1M_{\odot}$ . In the black area  $m_1 > M_{\text{TOV}}^Q$  and it is therefore excluded.

### 5.3.1 Quark deconfinement in the merger of compact stars

To gain a better understanding about the importance of the features of the Hyb-Coll configuration to establish the outcome of a merger, one has to consider in which way the quark deconfinement process is triggered and continues inside a compact object. The evolution will be different for the three types of binaries.

- *HS-HS merger.* In this situation, before the merger there is no quark matter in the system. Only when the temperatures and densities increase enough, hyperons are formed in the core and eventually the strangeness fraction reaches the threshold to trigger the deconfinement. These conditions are reached in the first few  $ms$  after the merger (Sekiguchi et al., 2011). Therefore, the values of  $M_{\text{TOV}}^{\text{Coll-hyb}}$ ,  $M_{\text{supra}}^{\text{Coll-hyb}}$  and

$M_{\text{threshold}}^{\text{Coll-hyb}}$  influence the fate of the newly born object after the deconfinement of the central region.

In section 5.4.7 we will study the conditions for quark nucleation by directly employing the results of our merger simulations. <sup>2</sup>

- *HS-QS merger.* Contrarily to the previous case, quark matter is present in the system before the merger. Unfortunately, since the HS-QS merger process involves two distinct EOSs, at present we are not capable to simulate it with the ET. However, we can compare this merger with the HS-HS one, by considering that, in the mixed binary case, the remnant will be already composed in a large fraction by quark matter. If the quark matter does not occupy the entire region that satisfies the Coll's condition, the rapid combustion phase can take place also in this case. Moreover, the quark deconfinement could proceed faster, because the initial post-merger phase is highly turbulent and thus it can mix hadronic and quark matter forming a mixing area which will be much larger than in the laminar case. As before,  $M_{\text{TOV}}^{\text{Coll-hyb}}$ ,  $M_{\text{supra}}^{\text{Coll-hyb}}$  and  $M_{\text{threshold}}^{\text{Coll-hyb}}$  are key ingredients to determine the outcome of the merger.
- *QS-QS merger.* The main interesting property of this process is the possibility to have a "clean" environment, if one assumes that very little or no hadronic matter is ejected in the merger and post-merger phase (Haensel et al., 1991). Thus the system is cleaner from baryon contamination because less matter can be emitted by e.g. neutrino ablation. The reason is that strange quark matter has a much larger binding energy with respect nuclear matter. The phenomenological signatures of this kind of merger will be discussed in the next section. Obviously, since the system is made entirely of deconfined quark matter, the only significant quantities are  $M_{\text{TOV}}^Q$ ,  $M_{\text{supra}}^Q$  and  $M_{\text{threshold}}^Q$ .

### 5.3.2 Possible outcomes of a merger

Now we discuss the different possible outcomes of the merger and the associated phenomenology. A first important issue to consider concerns the way a sGRB can be generated within the two families scenario.

#### *sGRB inner engine*

Two ways to generate a sGRB are possible: the first is based on the formation of a BH (MacFadyen & Woosley, 1999) while the second on the formation of a proto-magnetar

---

<sup>2</sup>Consider that the value of  $M_{\text{TOV}}^{\text{Coll-hyb}}$  is not unique but depends on the pre-merger configuration. The real value can be estimated only with a simulation of the merger including the deconfinement process (Pagliara et al., 2013) but this remains presently a quite challenging task. Therefore the value we are employing is to consider as an approximation of the real one.

(Metzger et al., 2011). For further details on these schemes see section 4.2.2.

In the two families scenario both the mechanisms can play a role: if a BH forms in the post-merger after few tens of ms, a sGRB can be launched because of the energy extracted from the disk, while if the remnant becomes a supramassive star and it is stable at least for a few seconds, the sGRB can be generated within the protomagnetar mechanism. In this second case, the delay of sGRB is connected to the time required to deconfine the stellar surface close to the rotation axis: as long as the nucleons are present on that surface the jet cannot be launched because the baryonic load is too large, while when the whole surface is filled by quarks, the baryonic load quickly drops to zero. Moreover, an extended emission can also be explained considering the time needed for the supramassive configuration to collapse (Rowlinson et al., 2013; Lü et al., 2015).

Let us move now to the discussion on the outcomes of the mergers in the aforementioned cases and adopting for all the critical masses the values described in section 5.2.2.

### *HS-HS merger.*

This is the case studied with the numerical simulations of this work. In the next sections we will estimate the value of  $M_{\text{threshold}}^H$  and we will examine if the conditions for the trigger of the phase conversion are reached. The outcomes of the merger process depends on the value of  $M_{\text{tot}}$  and the possibilities are three:

1)  $M_{\text{tot}} > M_{\text{threshold}}^H$ : this case is a prompt collapse to BH. We have a GW signal during the inspiral phase (with  $\tilde{\Lambda}$  very small because of the small radii of the HSs), no post-merger GW signal, no sGRB <sup>3</sup> and eventually an extremely faint Kilonova produced only by very small amount of the mass ejected by tidal forces before the merger (see section 5.4).

2)  $M_{\text{supra}}^{\text{Coll-hyb}}/(1-\alpha) < M_{\text{tot}} < M_{\text{threshold}}^H$ . This possibility is never realized, within the parameter space discussed in the previous section.

3)  $M_{\text{tot}} < \min[M_{\text{supra}}^{\text{Coll-hyb}}/(1-\alpha), M_{\text{threshold}}^H] = M_{\text{threshold}}^H$ : the remnant becomes initially a hypermassive hadronic star. The deconfinement process takes place as discussed before and it dramatically changes the structure of the star: the differential rotation could be enhanced due to the presence of two different phases and the radius of the remnant increases (Drago & Pagliara, 2015). The spectrum of the GW signal caused by the oscillations of the remnant, at first peaked at high frequencies, should feature a progressive shift towards smaller frequencies during the production of quark matter (Bauswein et al., 2016). At the end of the process, the HS is transformed into a QS and it can be either a supramassive or a stable star, if  $M_{\text{TOV}}^Q$  is very large. An extended X-ray emission after the sGRB and a

---

<sup>3</sup>An exception is the case of highly asymmetric systems ( $q \sim 0.8$ ) for which a sGRB could be launched because a massive torus is formed around the BH ( $\sim$  few  $0.1M_{\odot}$ , see Rezzolla et al. (2010a); Giacomazzo et al. (2013)). However, within the two families scenario, the torus would be significantly lighter because its mass scales linearly with  $M_{\text{TOV}}$ , which is  $\sim 1.6$  for HSs.

Kilonova signal should be present.

*HS-QS merger.*

1)  $M_{\text{tot}} > M_{\text{threshold}}^{\text{Coll-hyb}}$ : this case is basically equal to the analogous one for HS-HS merger, with the only difference being the bigger value of  $\tilde{\Lambda}$  characterizing the inspiral phase, due to larger radii.

2)  $M_{\text{supra}}^{\text{Coll-hyb}}/(1-\alpha) < M_{\text{tot}} < M_{\text{threshold}}^{\text{Coll-hyb}}$ : here the remnant becomes a hypermassive star. Within our model this is the only possible interpretation for GW170817. This will be discussed more deeply in section 5.6.

3)  $M_{\text{tot}} < M_{\text{supra}}^{\text{Coll-hyb}}/(1-\alpha)$ : again this case is close to the (3) of HS-HS merger and an interesting phenomenological feature is the possibility to produce an extended emission following the sGRB.

*QS-QS merger.*

1)  $M_{\text{tot}} > M_{\text{threshold}}^Q \sim M_{\text{supra}}^Q/(1-\alpha)$ : concerning the phenomenology, most probably, this is an irrelevant case because the mass distribution for binary systems has a peak at  $1.33M_{\odot}$  with a  $\sigma \sim 0.11M_{\odot}$  (Kiziltan et al., 2013) while the value of  $M_{\text{supra}}^Q \sim 3M_{\odot}$ . Anyway, the outcome would be similar to the case (1) of the other two types of binary.

2)  $M_{\text{tot}} < M_{\text{threshold}}^Q \sim M_{\text{supra}}^Q/(1-\alpha)$ . This case was already investigated in the past by Haensel et al. (1991) as a plausible mechanism to produce a sGRB. In particular, they pointed out that the merger environment is clean from baryon pollution and thus it is easier to obtain an ejecta with a high Lorentz factor. In their analysis, the source of the sGRB is given by the cooling of the remnant and therefore the spectrum would be close to the black body one, but neither rotation nor magnetic field were taken into account. If the remnant rotates rapidly and has a strong magnetic field, then the protomagnetar mechanism can be applied also to this case, with the possibility of generating an extended emission. The possibility of having a Kilonova signal associated with such an event is still an open issue and it is investigated in the work presented in chapter 6.

## 5.4 Numerical simulations of the merger of HS-HS

We considered the processes of BNS merger exploiting numerical relativity for purely HSs considering two EOSs, namely the SFHo presented in section 3.1.3 and SFHo-HD, described in chapter 3.3.1 and 5.2 and we investigate the behavior of equal mass binaries, as summarized in Table 5.1.

EOS	$M$ ( $M_{\odot}$ )	$R$ (km)	$C$	$\Lambda$	$M_{ADM}$ ( $M_{\odot}$ )	$J_{ADM}$ (CU)	$\Omega_0$ (krad/s)
SFHo-HD	1.18	11.166	0.156	544	2.340	5.783	1.713
SFHo-HD	1.20	11.133	0.159	483	2.379	5.945	1.725
SFHo-HD	1.22	11.100	0.162	429	2.419	6.092	1.736
SFHo-HD	1.24	11.067	0.165	382	2.451	6.257	1.747
SFHo-HD	1.26	11.034	0.169	340	2.490	6.427	1.759
SFHo-HD	1.28	11.002	0.171	303	2.530	6.597	1.770
SFHo-HD	1.30	11.970	0.175	270	2.570	6.771	1.781
SFHo	1.18	11.942	0.145	944	2.332	5.765	1.714
SFHo	1.20	11.939	0.148	856	2.372	5.926	1.725
SFHo	1.22	11.934	0.151	777	2.431	6.174	1.742
SFHo	1.24	11.929	0.153	705	2.450	6.258	1.748
SFHo	1.26	11.925	0.156	641	2.490	6.426	1.759
SFHo	1.28	11.919	0.159	582	2.529	6.597	1.770
SFHo	1.30	11.913	0.161	530	2.569	6.770	1.781
SFHo	1.32	11.907	0.164	482	2.608	6.945	1.791
SFHo	1.34	11.900	0.166	439	2.647	7.121	1.801
SFHo	1.36	11.893	0.169	399	2.687	7.299	1.812
SFHo	1.38	11.885	0.171	364	2.726	7.480	1.822
SFHo	1.40	11.877	0.174	332	2.766	7.663	1.832
SFHo	1.42	11.868	0.177	302	2.805	7.847	1.843

**Table 5.1:** Main properties of the equal mass models employed in this studied, which are labeled by the name of the EOS. Here the gravitational mass ( $M$ ), the radius ( $R$ ), and the compactness ( $C$ ) of the single stars are included. In addition, In the Table we report the total ADM mass ( $M_{ADM}$ ) and angular momentum ( $J_{ADM}$ ), and the angular velocity ( $\Omega_0$ ), at the beginning of the simulations. The initial separation is roughly 44.3 km for all the models.

#### 5.4.1 Numerical methods

In our simulations, we use the same numerical methods as [De Pietri et al. \(2018\)](#); [De Pietri et al. \(2016a\)](#); [Maione et al. \(2017, 2016\)](#). Here, we summarize only the general setup and parameters: in particular, the resolution adopted in this work is  $dx = 0.1875 \text{ CU} = 277 \text{ m}$  (for a discussion on the convergence properties of this code see [De Pietri et al. \(2016a\)](#)).

The simulations are performed through the ET ([Loffler et al., 2012](#)), a modular and open source numerical relativity code based on Cactus (for further information on the code and the formalism employed see [Allen et al. \(2011\)](#) or [Appendix A](#)). The evolved variables are discretized on a Cartesian grid using 6 refinement levels, each characterized by twice

the resolution of its parent level. The external border of the grid is set at  $720M_{\odot}$  (1040 km) from the center. The code solves the BSSN-NOK formulation of Einstein's equations (Nakamura et al., 1987; Shibata & Nakamura, 1995; Baumgarte & Shapiro, 1998; Alcubierre et al., 2000, 2003) implemented in a module named McLachlan (Brown et al., 2009), and the hydrodynamics equations in GR with *high resolution shock capturing methods*, with the open source module GRHydro (Baiotti et al., 2005; Mösta et al., 2014). In particular, we employ a finite-volume approach using the HLLE Riemann solver (Harten et al., 1983; Einfeldt, 1988) and the WENO reconstruction method (Liu et al., 1994; Jiang & Shu, 1996). In De Pietri et al. (2016a), the combination of the BSSN-NOK formulation and the WENO reconstruction algorithm was proved to be the best choice as setup for the ET, even at low resolutions. Concerning the time evolution we select the "method of lines", with fourth-order Runge-Kutta (Runge, 1895; Kutta, 1901). For numerical reasons, the evolution of the system is performed on an external matter atmosphere with a fixed density of  $\rho_{atm} = 6.1 \cdot 10^5 \text{ g/cm}^3$  (as in Lehner et al. (2016)) which is slightly larger than the value employed in Sekiguchi et al. (2015b) and Radice et al. (2018a) but it is still low enough to avoid inertial effects of the atmosphere on the ejecta on a timescale of  $\sim 10$  ms after the merger (Sekiguchi et al., 2015b). The initial data are generated using the LORENE code (Gourgoulhon et al., 2001), as non-rotating binaries within the so called conformal thin sandwich approximation. For both models employed in this work, we choose the initial distance at 44.3 km like in Maione et al. (2016); Feo et al. (2017).

#### 5.4.2 Initial data: EOS approximation

In order to construct the initial conditions for the code, the first step consists in the approximations of the EOS in a form suited to be used as inside the ET. This means to build a table of the cold EOS and to fit it through a piecewise polytropic function. The finite temperature behavior of the EOS is then modelled by adding a thermal part parametrized by a further polytropic index.

The SFHo EOS is given as a table in which the thermodynamical quantities are functions of three independent variables: temperature ( $0.1 \text{ MeV} \lesssim T \lesssim 75.86 \text{ MeV}$ ), baryon number density ( $5.75 \cdot 10^{-8} \text{ fm}^{-3} \lesssim n \lesssim 1.44 \text{ fm}^{-3}$ ) and total proton fraction ( $0.01 \leq Y_p \leq 0.5$ ). This needs to be reduced to a bi-dimensional table by fixing the value of  $Y_p$ , in order to obtain the EOS in the form  $p = p(T, n)$  and  $e = e(T, n)$  for pressure and energy density. This goal is achieved by imposing the  $\beta$ -equilibrium condition. The latter involves the calculation of thermodynamic integrals which can lead to numerical instabilities. The problem arises when temperature becomes low while the density is high, i.e. the ratio between the electron chemical potential  $\mu_e$  and temperature in the exponent of the Boltzmann factor is large. In

order to deal with this issue an approximation is introduced: an integral of the form

$$\int_{m_e}^{\infty} dE \cdot E \sqrt{E^2 - m_e^2} \cdot \left( \frac{1}{1 + \exp \frac{E - \mu_e}{T}} - \frac{1}{1 + \exp \frac{E + \mu_e}{T}} \right) \quad (5.4.1)$$

at low temperature can be approximated as

$$\int_{m_e - \mu}^{m_e + \mu} dx \cdot \frac{(x + \mu) \cdot \sqrt{(x + \mu)^2 - m_e^2}}{1 + \exp(\frac{x}{T})} \quad (5.4.2)$$

if  $\frac{\mu_e}{T} > 20$ . From a practical viewpoint, when using the data from the table,  $\frac{\mu_e}{T} > 20$  is the only relevant condition, independently from the temperature (for details see Appendix B).

Once a cold EOS table is built, the physical information contained in it must be re-written in a form suited for EOS-Omni, the ET modules for the EOS (see Appendix A). The matter is described through the thermodynamical variables (De Pietri et al. (2016b)):

- $\rho$  : the baryon mass density
- $P$  : the pressure
- $\epsilon$  : the specific internal energy which is defined from the energy density as:

$$\epsilon = \frac{e}{n_B m_B} - 1 \quad (5.4.3)$$

The EOS is then expressed as a sum of a "cold" ( $T = 0$ ) part and a thermal part in order to take into account the effects of finite temperatures:

$$P(\rho, \epsilon) = P_{cold}(\rho) + P_{th}(\rho, \epsilon) \quad (5.4.4)$$

The cold piece is described through a piecewise polytropic approximation (Read et al. (2009)). This means that the density interval is divided in  $n$  different regions for which  $\rho_i \leq \rho \leq \rho_{i+1}$  and the pressure is written as a polytropic equation of the form:

$$P(\rho) = K_i \rho^{\Gamma_i} \quad (5.4.5)$$

The energy density satisfies the general equation:

$$d \frac{e}{\rho} = -P d \frac{1}{\rho} \quad (5.4.6)$$

Thus, for  $\Gamma_i \neq 1$ :

$$e(\rho) = (1 + a_i) \rho + \frac{K_i}{\Gamma_i - 1} \rho^{\Gamma_i} \quad (5.4.7)$$

where

$$a_i = \frac{e(\rho_i)}{\rho_i} - 1 - \frac{K_i}{\Gamma_i - 1} \rho_i^{\Gamma_i - 1} \quad (5.4.8)$$

As a consequence, the internal energy becomes:

$$\epsilon(\rho) = a_i + \frac{K_i}{\Gamma_i - 1} \rho^{\Gamma_i - 1} \quad (5.4.9)$$

and the sound velocity is expressed as:

$$v_s(\rho) = \sqrt{\frac{dP}{de}} = \sqrt{\frac{\Gamma_i P}{e + P}}. \quad (5.4.10)$$

Each piece of the EOS is parametrized by the constant  $K_i$ , the adiabatic index  $\Gamma_i$  and the initial density. However, because of the continuity of the function at the transition densities, one is left with only two independent variables. Indeed the parameter  $K_i$  can be written as:

$$K_i = \frac{P(\rho_{i-1})}{\rho_{i-1}^{\Gamma_i}} \quad (5.4.11)$$

To be implemented in the ET, the EOS variables must be evaluated in the so called gravitational units, i.e.  $G = c = k_B = 1$ , where  $k_B$  is the Boltzmann constant. The value of the baryonic mass is chosen as the minimum of  $\frac{e}{n}$  required to have the internal energy always positive.

The relations linking the mass density and the pressure (or energy density) in gravitational unit to  $n$  and  $P$  in the usual "nuclear physics" units are given by:

$$\rho = n_B \cdot 2.7 \cdot 10^{-3} M_\odot^{-2} \quad (5.4.12)$$

$$p(M_\odot^{-2}) = p(\text{MeV fm}^{-3}) \cdot 2.9 \cdot 10^{-6} \quad (5.4.13)$$

Using the equations for the pressure expressed in gravitational units and the continuity condition, we performed a fit of both the EOSs with a 10 pieces piecewise polytropic function. The relative error for  $P$  introduced by this approximation is on average of the order of 5% and it is smaller for densities above the neutron drip line.

Up to this point, the approximation for the "cold" part of the EOS has been described. However, finite temperatures are reached during the merger and post-merger phase, and therefore the thermal effect must be included in the EOS.

As the pressure in equation 5.4.4, also the internal energy can be split in two contributions

(Bauswein et al. (2010a)):

$$\epsilon = \epsilon_{cold} + \epsilon_{th} \quad (5.4.14)$$

Assuming an "ideal gas" behavior, the pressure can be defined as function of the thermal part of the internal energy as:

$$P_{th} = (\Gamma_{th} - 1)e_{th} = (\Gamma_{th} - 1)\rho\epsilon_{th} \quad (5.4.15)$$

where  $\Gamma_{th}$  is the so called thermal adiabatic coefficient. A common approximation, employed also in our work, is to assume a constant value for  $\Gamma_{th}$ , but in principle this parameter changes with density and temperature. For this reason, an analysis of the trend of thermal adiabatic coefficient is essential.

Inverting equation 5.4.15 one obtains an expression for  $\Gamma_{th}$ :

$$\Gamma_{th}(\rho, T) = \frac{P_{th}}{\rho\epsilon_{th}} + 1 = \frac{P - P_{cold}}{\rho(\epsilon - \epsilon_{cold})} + 1 \quad (5.4.16)$$

which can be rewritten in terms of the more familiar energy density  $e$ :

$$\Gamma_{th} = \frac{P - P_{cold}}{e - e_{cold}} + 1 \quad (5.4.17)$$

Thus the thermal coefficient can be evaluated for a chosen temperature  $T$  once the EOS

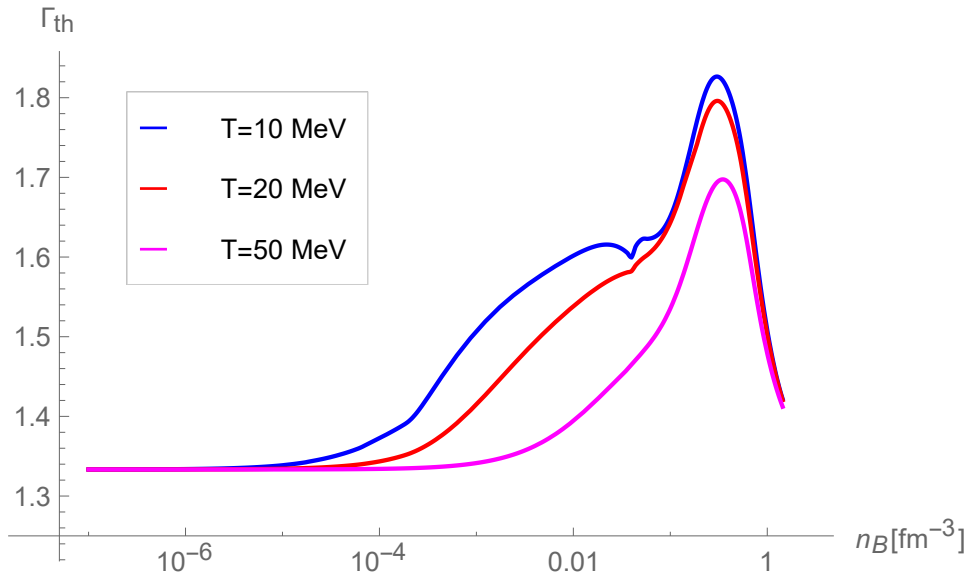


**Figure 5.4.1:** Comparison among the thermal adiabatic index  $\Gamma_{th}$  for fixed temperatures of 10, 20 and 50 MeV.  $\Gamma_{th}$  is shown as a function of baryon density.

table corresponding to that  $T$ , together with the "cold" one, is provided. The results for some selected "samples" of temperatures, 10 MeV, 20 MeV and 50 MeV, are shown in Figure 5.4.1.

Observing the plots, the strong dependence of  $\Gamma_{th}$  on the baryon density is immediately evident. The thermal index is characterized by a peak just above the saturation point and it progressively decreases moving to lower densities, finally reaching the limit value  $\Gamma_{th} = 4/3$ . For  $T = 10$  MeV and  $T = 20$  MeV the peak is located at  $\sim 1.8$ . A dependence from the temperature becomes evident comparing the results for  $T = 20$  MeV and  $T = 50$  MeV: while the asymptotic behavior does not change, the value of the peak at higher temperatures is reduced and shifted to larger densities. For  $T = 50$  MeV the maximum is found at  $\Gamma_{th} = 1.7$ . However, the dependence on temperatures is quite weak and the trend of  $\Gamma_{th}$  is mainly influenced by the baryon density.

Since in the post-merger phase, the temperatures are mostly (even if not always) of the order of 10 – 20 MeV (see Figure 4 of De Pietri et al. (2019)), we selected as constant value of  $\Gamma_{th}$  in our simulations, the peak of the corresponding curves,  $\Gamma_{th} = 1.8$ .

### 5.4.3 GW extraction

During the simulations, the GW signal is extracted with the module `WeylScalar4` using the so called Newman-Penrose scalar  $\Psi_4$  (Newman & Penrose, 1962; Baker et al., 2002). The latter is connected to the GW strain by the following equation, valid only at spatial infinity:

$$\Psi_4 = \ddot{h}_+ - i\ddot{h}_\times \quad (5.4.18)$$

Here  $h_+$  and  $h_\times$  are the two polarizations of the GW strain  $h$ . Then, the signal is decomposed into multipoles by means of the spin-weighted spherical harmonics of weight  $(-2)$  (Thorne, 1980). The module responsible for this procedure is `MULTIPOLE` that uses the relation

$$\psi_4(t, r, \theta, \phi) = \sum_{l=2}^{\infty} \sum_{m=-l}^l \psi_4^{lm}(t, r) {}_{-2}Y_{lm}(\theta, \phi). \quad (5.4.19)$$

In this work, we concentrate only on the main  $l = m = 2$  mode and therefore we label  $h_{2,2}$  simply as  $h$ . In order to minimize the errors in the extraction of the GW strain from  $\Psi_4$ , the signal extracted during the simulation at finite distance from the source, need to be extrapolated to infinity to be used in equation 5.4.18.  $\Psi_4$  is then integrated twice in time (for details see Maione et al. (2016)): to this aim, we use the second order perturbative

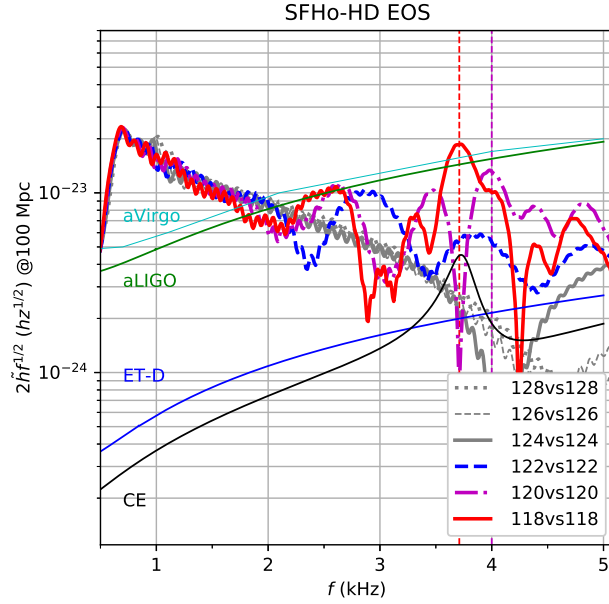


**Figure 5.4.2:** Spectrum of the GW signal for the different binaries and the SFHo-HD EOS. The models for which the remnant survives for  $\geq 1$  ms after the merger are characterized by a reduced  $f_2$  peak, that is, on the contrary, fully suppressed for models that show a prompt collapse to BH ( $M_{\text{tot}} \geq 2.48M_{\odot}$ ).

correction of Nakano et al. (2015),

$$\begin{aligned}
 R\psi_4^{lm}(t_{\text{ret}})|_{r=\infty} = & \left(1 - \frac{2M}{R}\right) \left( r\ddot{\bar{h}}^{lm}(t_{\text{ret}}) \right. \\
 & - \frac{(l-1)(l+2)}{2R} \dot{\bar{h}}^{lm}(t_{\text{ret}}) \\
 & \left. + \frac{(l-1)(l+2)(l^2+l-4)}{8R^2} \bar{h}^{lm}(t_{\text{ret}}) \right), \tag{5.4.20}
 \end{aligned}$$

where the GW strain ( $\bar{h}^{lm}$ ) at finite coordinate radius (here  $R = 1033$  km) is calculated by integrating  $\Psi_4$  twice in time using a simple trapezoid rule. We start from coordinate time zero and we fix only the two integration constants with a physical meaning,  $Q_0$  and  $Q_1$ , by subtracting to the signal its own linear fit,

$$\bar{h}_{lm}^{(0)} = \int_0^t dt' \int_0^{t'} dt'' \psi_4^{lm}(t'', r), \tag{5.4.21}$$

$$\bar{h}_{lm} = \bar{h}_{lm}^{(0)} - Q_1 t - Q_0 \tag{5.4.22}$$

After the integration, a digital high-pass Butterworth filter is applied: this filter is designed to have a maximum amplitude reduction of 0.01 dB at the initial GW frequency  $f_{t_0}$  (equal to 2 times the initial orbital angular velocity) and an amplitude reduction of 80 dB at  $0.1f_{t_0}$ . All the information related to the GW is reported as a function of  $t_{ret}$ , the retarded time defined as:

$$t_{ret} = t - R^* \quad (5.4.23)$$

$$R^* = R + 2M_{ADM} \log\left(\frac{R}{2M_{ADM}} - 1\right) \quad (5.4.24)$$

In this work, we focus on the observable  $|\tilde{h}(f)|f^{1/2}$ , the GW amplitude spectral density, which is obtained from the GW strain:

$$|\tilde{h}(f)| = \sqrt{\frac{|\tilde{h}_+(f)|^2 + |\tilde{h}_\times|^2}{2}}, \quad (5.4.25)$$

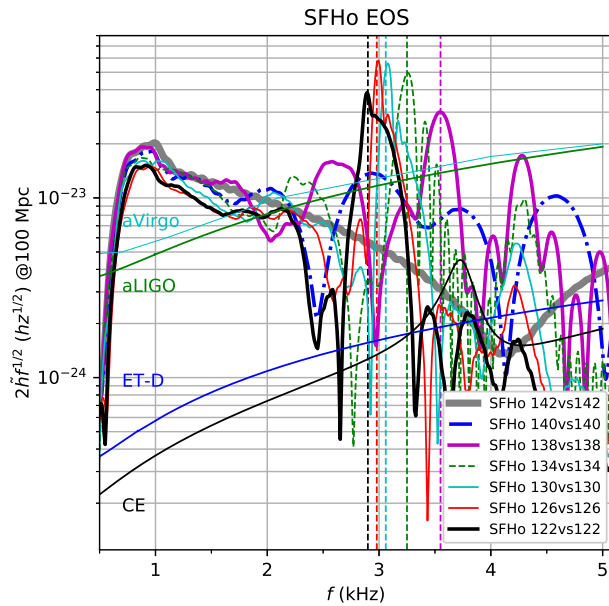


**Figure 5.4.3:** Spectrum of the GW signal for the different binaries and the SFHo EOS. Note that the binary with total mass  $2.84 M_\odot$  shows no post-merger peak while the one with total mass  $2.80 M_\odot$  has just a marginal dominant  $f_2$  peak. All the other, less massive model, are characterized on the contrary a distinct main  $f_2$  peak and two side peaks with lower amplitudes which become less important as the total mass of the binary decrease.

Here  $\tilde{h}(f)$  is the Fourier transform of the complex GW strain,

$$\tilde{h}(f) = \int_{t_i}^{t_f} h(t) e^{-2\pi i f t} dt \quad (5.4.26)$$

and the associated GW energy in the interval ranging from 1 ms up to 15 ms after the time of the merger. The latter is defined as the time at which the  $l = 2, m = 2$  GW strain  $h^{lm}$  has a maximum and it is fixed at  $t = 0$ .

#### 5.4.4 Estimate of the ejected mass and disk mass

One of the main goals of our work consists in the estimation of the amount of matter dynamically ejected during and after the merger. For this purpose, a condition must be established in order to determine whether a fluid element is able to escape to infinity (Rezzolla et al., 2010a; Kastaun & Galeazzi, 2015).

A stationary spacetime is assumed, i.e. the  $\partial_t$  is a Killing vector and it is associated to the conservation law

$$K_\mu \frac{dx^\mu}{d\tau} = \text{constant} \quad (5.4.27)$$

while  $\partial_\mu$  can be expressed as:

$$K^\mu = (\partial_t)^\mu = (1, 0, 0, 0) \quad (5.4.28)$$

The corresponding contravariant vector is obtained performing a contraction with the metric:

$$K_\mu = g_{\mu\nu} K^\nu \quad (5.4.29)$$

and the time-component remains the only non-null element:

$$K_t = g_{tt} K^t = g_{tt} \quad (5.4.30)$$

Therefore from equation 5.4.27:

$$K_t \frac{dx^t}{d\tau} = g_{tt} u^t = u_t = \text{constant} \quad (5.4.31)$$

where  $u_t$  is the contravariant time-component of the four-velocity.

At infinity  $u_t = -W$ , with  $W$  being Lorentz factor: the latter is equal to one for a particle that reaches infinity with zero three velocity.

Thus an element of fluid is able to get to  $\infty$  only if  $-u_t$  is at least equal to one and the condition for unbound matter reads:

$$-u_t > 1 \quad (5.4.32)$$

The total amount of ejected mass is then the integral of the unbound matter density over the whole computational domain (not considering the part that corresponds to the atmosphere). This is the method we employ in our work. We calculate the integral at each simulation time and then we assume, as a measure of the total ejected mass, the maximum of such values found in the whole simulation time, which we denoted as  $M_{\text{ej}}$ . This criterion, however, represents a necessary but not always sufficient condition: this problem could lead to an underestimation of the mass ejected.

For this reason, we repeated the estimate also by directly computing the flow of unbound (again  $u_t < -1$ ) matter leaving spherical surfaces located at a given radius (using the module `Outflow`). Using this approach we determined the flow of unbound material for a set of different radii from  $65 \text{ CU} \simeq 96 \text{ km}$  up to  $700 \text{ CU} \simeq 1034 \text{ km}$ , the latter being the border of our computational domain.

In addition, we have estimated the mass of the disk  $M_{\text{disk}}$  (reported in Table 5.2) as the total mass present in the domain having a density  $\rho \leq 3.3 \cdot 10^{11} \text{ g/cm}^3$  and which is bound (i.e., having  $u_t > -1$ ) 20 ms after the merger. This method of estimating  $M_{\text{disk}}$  allows to quantify the mass surrounding the remnant that has not been dynamically ejected. In a later phase, part of this matter can become unbound due to viscous or neutrino heating.

#### **5.4.5 Results of the numerical simulations**

As discuss before, in this study we simulate symmetric binary systems for HS-HS and NS-NS configurations starting from about four orbits before merger and up to about 20 ms after merger.

All our employed models are characterized by a very similar behaviour. The main properties of the evolution are shown as snapshots for the example model SFHo-HD 118vs118 in Figure 5.4.4 and in Figure 5.4.5. In particular, in Figure 5.4.4, the densities of the ejected matter and the temperatures are plotted at different times, while Figure 5.4.5 contains the velocities of the fluid and the localization of the unbound mass. In addition, the computed GW signal from our simulation is displayed in Figure 5.4.2 and Figure 5.4.3, where we show the power spectrum that is extracted by means of a detector at  $R = 1034 \text{ km}$  for the models SFHo-HD and SFHo, respectively. In Table 5.2 we report the values of  $M_{\text{ej}}$  and of  $M_{\text{disk}}$  associated to each simulation. The same values are also displayed in Figure 5.4.10 as a function of  $M_{\text{tot}}$ . A noticeable feature of the GW spectrum is that the post merger  $f_2$  peak is not present in models with  $M_{\text{tot}} \geq 2.48$  and  $M_{\text{tot}} \geq 2.84$ , for SFHo-HD and SFHo respectively. This is due to the fact that, for these binaries, we have a prompt collapse to BH. This fact is clear if one looks at the plots 5.4.6 and 5.4.7 showing the maximum density as a function of time for the two models. In the opposite cases in which there is no prompt collapse, the main properties of the spectrum are the same as the ones described in Takami et al. (2015); Bauswein & Stergioulas (2015); Maione et al. (2017). In particular, the post merger spectrum shows a main  $f_2$  peak whose frequency is strongly dependent on the EOS. Moreover, this frequency

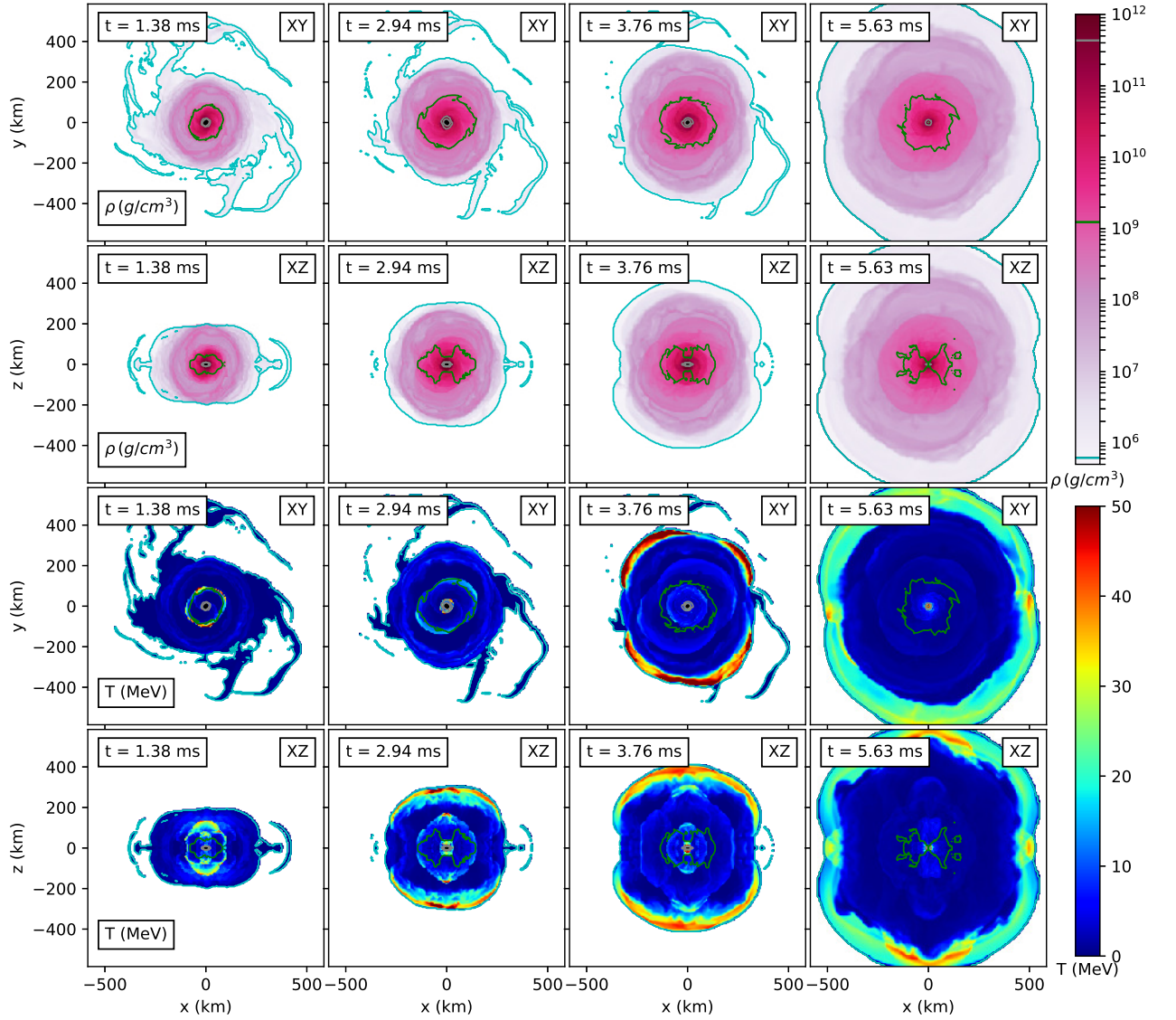


**Figure 5.4.4:** Snapshots of the projections on the XY and XZ plans of the time component of the density ( $\rho$ ) and of the temperature ( $T$ ) for the SFHo-HD 118vs118 model. The white region outside the solid cyan line is the atmosphere, while the colored lines represent the density contour corresponding to the densities chosen for the polytropic approximation described in section 5.4.2.

is proportional to the mass of the star because its tidal parameter decreases. Moreover, also secondary peaks are present in the spectrum but their relative importance decreases with a reduction of the total mass of the binary. The existence of a well defined dominant

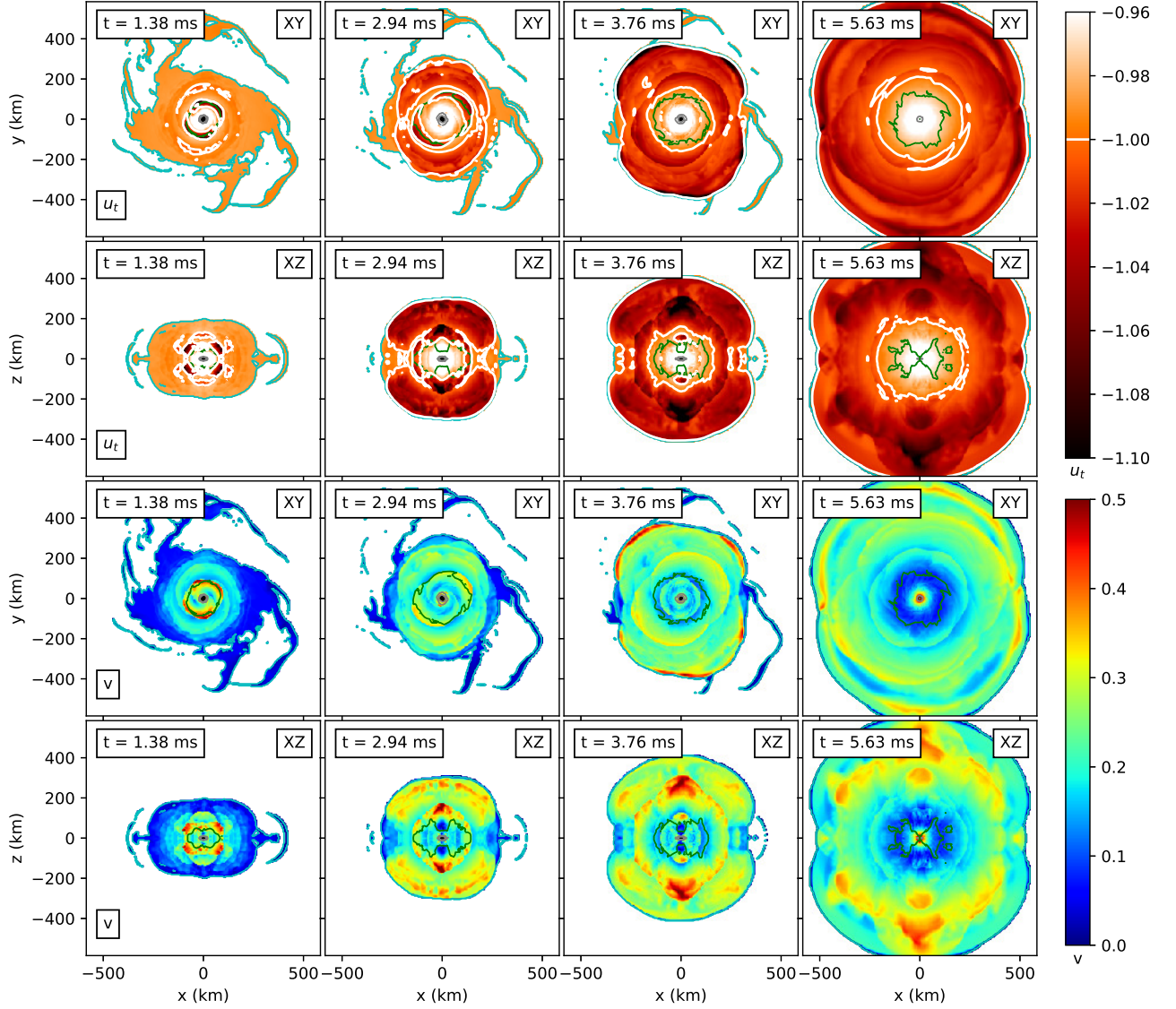


**Figure 5.4.5:** Snapshots of the projections on the XY and XZ plans of the fluid velocity ( $u_t$ ), and the matter velocity ( $v$ ), for the SFHo-HD 118vs118 model. The white region outside the solid cyan line is the atmosphere while the colored lines represent the density contour corresponding to the densities chosen for the polytropic approximation described in section 5.4.2. In the first two rows, the solid white line refers to the  $u_t = -1$  condition, that separates bound and unbound matter, as discussed in section 5.4.4. The times  $t$  is calculated with respect to the merger time for this model.

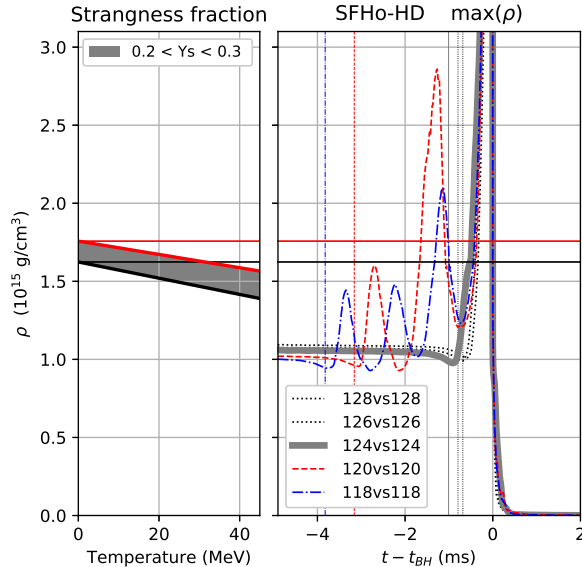


**Figure 5.4.6:** Left panel: density corresponding to a strangeness fraction  $Y_s = 0.2$  (Black line) and  $Y_s = 0.3$  (Red line) as a function of the temperature (MeV). Right panel: maximum mass density in the computational grid as a function of time for the SFHo-HD models.

peak and its frequency  $f_2$  could allow a clear determination of the type of merger and of the features of the EOS. Indeed, firstly, that would be a clear signature that the binary did not promptly collapse to a BH and secondly its spectrum contains information on the stiffness of dense matter. For example, in the case of the 1.18-1.18  $M_\odot$  models, a main peak at frequency  $f_2 = 3.71$  kHz or  $f_2 = 2.88$  kHz are found for SFHo-HD or SFHo, respectively. Consider that [Bauswein et al. \(2016\)](#) have demonstrated that the value of  $f_2$  is strictly connected to the value of  $R_{1.6}$ . Unfortunately, the amount of GW energy available for the mode detection is maximum of the order of 0.1  $M_\odot$  (see [Table 5.2](#)) and thus it is unlikely that the  $f_2$  peak will be detected using the present generation of GW detectors but it will probably be observed with the third generation detectors.

Now the results concerning the ejected matter and the mass of the disk are discussed. In [Figure 5.4.8](#) we display an example of the outflow, in this case for the SFHo-HD 118vs118. We can estimate the ejecta at each radius by integrating the flow of unbound matter on time. In this case, the obtained flows at coordinate radius 96, 220, 443 and 590 km are: (5.0, 10.7, 11.24, 11.45)  $mM_\odot$ , respectively. As evident, this method to compute the total ejected matter is very sensitive to the extraction radius and this property is common to all the employed models. In addition, we compared the results found by using this approach with those estimated by considering the maximum of total unbound mass inside the whole computational grid, at a given time. We underline that the difference between the results of

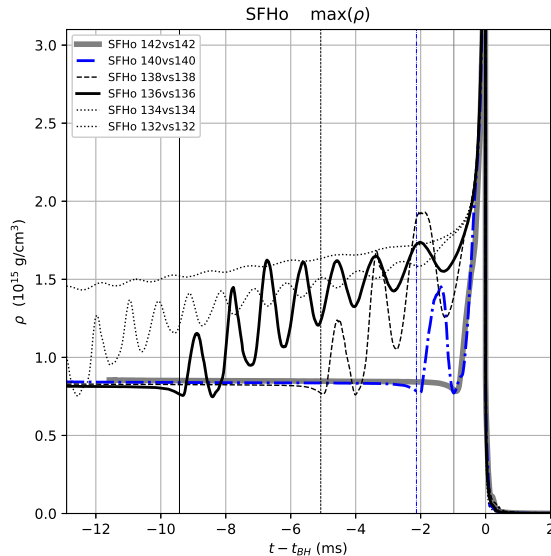


**Figure 5.4.7:** maximum mass density in the computational grid as a function of time for the SFHo models. Note that the first model with a total mass of  $2.84 M_{\odot}$  shows no bouncing.

the two approaches for  $M_{\text{ej}}$  is always lower than about 20% and the two estimates get closer as we increase the extraction radius.

In the lower panel of Figure 5.4.8, one can see that the majority of the mass dynamically ejected is created between 100 km and 200 km from the center of the grid where the remnant is located. Moreover, it is connected to three main outbursts of ejected mass associated to the three bounces of the maximum density. This fact is even more evident in Figure 5.4.9, where we show the radial density profile of the unbound matter as a function of the coordinate radius, at different times. Here, one can notice that three shocks are generated within a radius of 100 km for  $t=0.14\text{ms}$ ,  $t=1.15\text{ms}$  and  $t=2.15\text{ms}$  (the first has a lower amplitude). Then the shocks move out, amplify and spread during the evolution of the system. This is very similar to what is observed for the flux of ejecta at different radii in the upper panel of Figure 5.4.8, where one can observe three clearly separated peaks at  $R = 100$  km that subsequently join and spread as the unbound mass flows outside the computational grid.

A similar overall dynamics is connected to the ejection of mass for all the employed models (except the ones that collapse promptly to BH for which the matter ejection is suppressed). The results for  $M_{\text{ej}}$  and  $M_{\text{disk}}$  for all the models as a function of  $M_{\text{tot}}$  are displayed in the lower and upper panel, respectively, of Figure 5.4.10. The corresponding values are also listed in Table 5.2. A noticeable feature regarding the ejected mass is the existence of a maximum located at a value of  $M_{\text{tot}}$  slightly smaller than  $M_{\text{threshold}}$ . This is one of the most

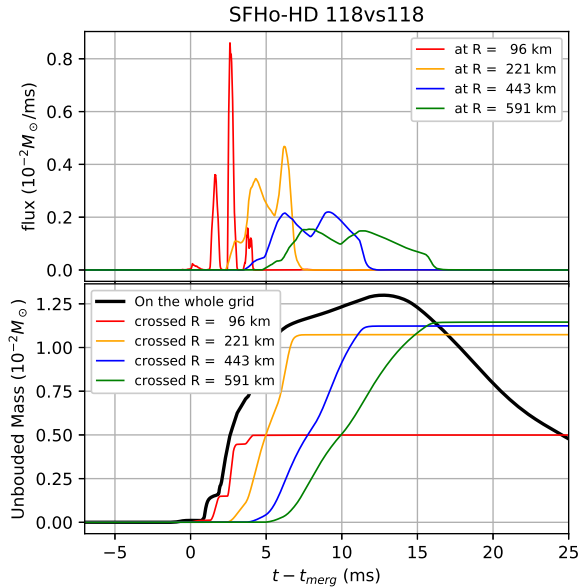


**Figure 5.4.8:** Upper panel: results for the unbound mass estimated from the flow crossing spherical surfaces with a different coordinate radius. At the closest surface, one can note the presence of three peaks, which are related to the "rebounds" of the hypermassive NS formed in the post-merger. Those peaks become broader when crossing the farther surfaces because of the different velocities characterizing the ejected material. Lower panel: time integrated fluxes at the different crossing radii. The total unbound mass on the whole computation domain for each time is shown as a black line.

important results of the present study. In particular, this maximum is of about  $\simeq 16 \text{ m}M_{\odot}$  and it is found at  $2.72M_{\odot}$  for the SFHo EOS. In the case of SFHo-HD, the maximum of the ejected mass is located below or close to  $\sim 2.36M_{\odot}$ , which is lowest among the simulated  $M_{\text{tot}}$ . For this value, we found an ejected mass of about  $\simeq 13 \text{ m}M_{\odot}$ , very similar to the peak for the SFHo EOS. The ejected matter features a very steep decay as  $M_{\text{tot}}$  increases and finally the ejection is almost totally suppressed for models characterized by a prompt collapse.

A further distinctive feature between the two EOSs concerns the value of  $M_{\text{disk}}$ : for SFHo-HD it is always  $\lesssim 0.01M_{\odot}$  while in the case of SFHo it can be even an order of magnitude larger. These properties are potentially very relevant for the phenomenology of the Kilonova signal. Indeed, as discussed in sections 4.2.2 and 4.2.3, the luminosity of the three components of the Kilonova, red, blue and purple, (Perego et al., 2017) are strongly dependent on the ejection mechanisms. An important fraction of the ejecta can, in principle, come from the remnant disk and thus a very small value of  $M_{\text{disk}}$  suggests a strong suppression of specific

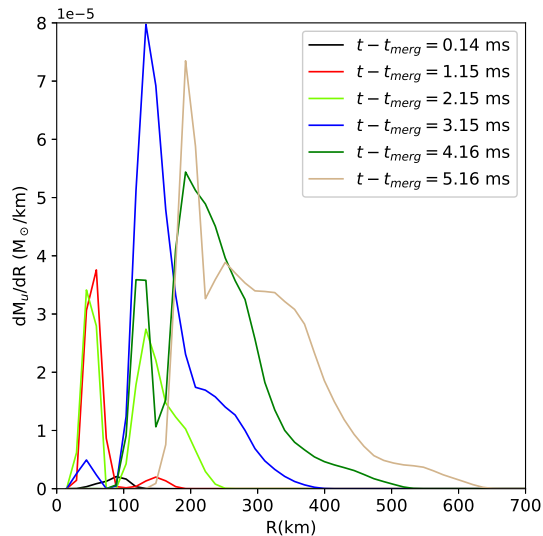


**Figure 5.4.9:** Snapshots at given times of the radial density of the unbound mass as a function of the radius in the case of the SFHo-HD 118vs118 model. The presence of various peaks at a given radius and for different times is related to the shocks generated by the oscillations of the remnant shown in Figure 5.4.6.

components of the Kilonova signal.

We can now compare our results with the ones found in the literature and obtained through similar numerical simulations: few simulations employ the SFHo EOS and masses close to our SFHo 136vs136 model. The outflow dynamics in this case is plotted in Figure 5.4.11. Our results are in general agreement with the ones obtained in Sekiguchi et al. (2015b, 2016b) for this EOS. The authors found an ejected mass of the order of  $10 m_{\odot}$  for a  $1.35\text{-}1.35 M_{\odot}$  binary and a similar value also in the case of an asymmetric binary of approximately the same total mass (Shibata et al., 2017). Moreover, they found, for the same systems, a disk mass in a range from  $50 m_{\odot}$  up to  $120 m_{\odot}$  and thus the order of magnitude is the same as we obtained in the present work. Estimates of the ejecta for SFHo are also subject of other papers, such as Bauswein et al. (2013b) using SPH dynamics, Lehner et al. (2016) and Bovard et al. (2017) and Radice et al. (2018a) using `WhiskyTHC` code. The last work presents also a comparison among all the previously mentioned numerical results in Table 3, showing how the variability among the different estimates is quite large. Concerning our results, a few potentially not negligible effects have not been incorporated, i.e. a treatment of the neutrino transport, a completely consistent description concerning the thermal component of the EOS and, in addition, we exploit a piece-wise polytropic approximation. Despite these shortcomings, our results are still in a very good agreement

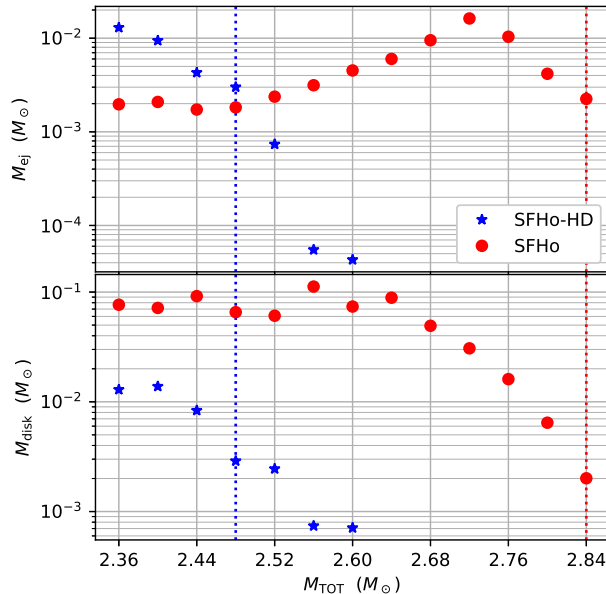


**Figure 5.4.10:** Ejected mass and mass of the disk mass as listed in Table 5.2 as a function of the total mass of the binary. The blue dots correspond to the SFHo-HD models, while the red dots correspond to the SFHo ones. The dotted vertical lines are located at the values of  $M_{\text{threshold}}$  for both EOS.

with the work of Sekiguchi et al. (2015b), where the authors considered full beta equilibrium, the thermal evolution and also approximated neutrino cooling and absorption.

Another relevant variable which can affect  $M_{\text{ej}}$  and  $M_{\text{disk}}$  is the mass asymmetry  $q$ . This problem has been discussed in Rezzolla et al. (2010b); Giacomazzo et al. (2013) and lately again in Kiuchi et al. (2019). The mass of the disk is expected to be always larger for asymmetric binaries due to the more efficient angular momentum transfer and tidal interactions during the merger. However, this conclusion can not be generalized to the  $M_{\text{ej}}$  and further investigations are needed, in particular when one considers models close to the threshold mass, because the outcome of merger may rapidly change from a prompt collapse to a short lived remnant (Kiuchi et al., 2019).

#### 5.4.6 Estimate of the Threshold mass

A preliminary estimate of the threshold mass for the SFHo and SFHo-HD EOSs can be found by means of the empirical formulae suggested in Bauswein et al. (2013a, 2016); Bauswein & Stergioulas (2017). The ratio  $k = M_{\text{threshold}}/M_{\text{TOV}}$  scales linearly with  $C_{\text{max}}$ , i.e. the compactness of the maximum mass configuration,  $k = 2.43 - 3.38C_{\text{max}}$ . For SFHo

Model	$M_{\text{ej}}$ ( $mM_{\odot}$ )	$M_{\text{disk}}$ ( $mM_{\odot}$ )	$E_{\text{gw}}^{\text{POST}}$ ( $mM_{\odot}$ )	$f_2$ (kHz)	$t_{\text{BH}}$ (ms)
SFHo-HD 118vs118	12.993	12.92	25.42	3.71	3.82
SFHo-HD 120vs120	9.435	13.81	22.42	4.00	3.16
SFHo-HD 122vs122	4.290	8.34	6.06	—	1.91
SFHo-HD 124vs124	3.011	2.89	0.66	—	1.00
SFHo-HD 126vs126	0.737	2.45	0.20	—	0.79
SFHo-HD 128vs128	0.055	0.74	0.04	—	0.70
SFHo-HD 130vs130	0.043	0.71	0.01	—	0.59
SFHo 118vs118	1.968	76.66	42.16	2.88	---
SFHo 120vs120	2.085	71.72	43.87	2.90	---
SFHo 122vs122	1.730	91.81	42.00	2.90	---
SFHo 124vs124	1.824	65.58	52.98	2.96	---
SFHo 126vs126	2.375	60.86	58.33	2.98	---
SFHo 128vs128	3.145	112.24	50.33	3.05	---
SFHo 130vs130	4.523	73.82	59.33	3.06	---
SFHo 132vs132	6.007	88.87	67.29	3.18	25.75
SFHo 134vs134	9.511	49.27	65.09	3.25	13.55
SFHo 136vs136	16.244	30.71	58.76	3.40	9.42
SFHo 138vs138	10.367	16.09	46.06	3.55	5.06
SFHo 140vs140	4.170	6.45	22.39	—	2.13
SFHo 142vs142	2.247	2.01	2.02	—	0.98

**Table 5.2:** Values of ejected mass,  $M_{\text{ej}}$ , and of the mass of the disk,  $M_{\text{disk}}$ , energy emitted in GW in the post-merger phase,  $E_{\text{gw}}^{\text{POST}}$ , frequency of the dominant peak of the GW signal,  $f_2$ , and time of the collapse to BH,  $t_{\text{BH}}$ , for all the employed models.

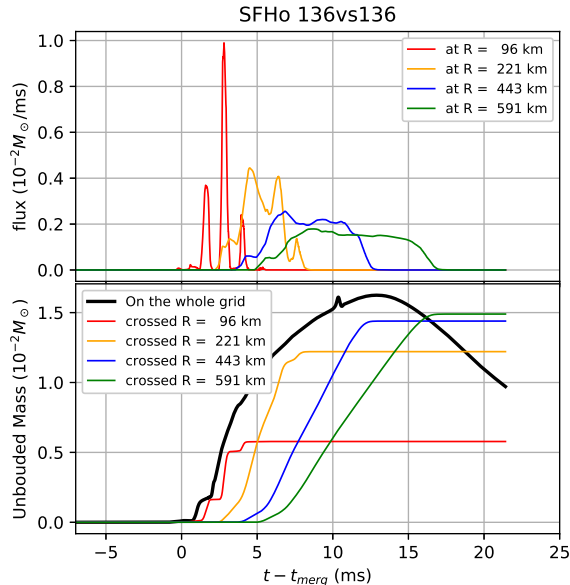


**Figure 5.4.11:** Upper panel: results for the unbound mass estimated from the flow crossing spherical surfaces with a different coordinate radius. At the closest surface, one can note the presence of three peaks, which are related to the "rebounds" of the hypermassive NS formed in the post-merger. Those peaks become broader when crossing the farther surfaces because of the different velocities characterizing the ejected material. Lower panel: time integrated fluxes at the different crossing radii. The total unbound mass on the whole computation domain for each time is shown as a black line.

$C_{max} = 0.3$  leading to  $M_{\text{threshold}} = 2.94M_{\odot}$  while for SFHo-HD,  $C_{max} = 0.23$  giving a  $M_{\text{threshold}} = 2.61M_{\odot}$ . Then we want to compare these results with the ones inferred from our numerical simulations. Concerning SFHo-HD, from the Table 5.2 one notes that for  $M_{\text{tot}} > 2.48M_{\odot}$  the collapse takes place in less than 1ms and  $M_{\text{ej}}$  drops below  $mM_{\odot}$ . In addition, almost no GW energy is present in the post-merger phase. Therefore, from our numerical simulations, we deduce a  $M_{\text{threshold}} \sim 2.5M_{\odot}$  for SFHo-HD, slightly smaller than the value of the empirical formula. In the case of SFHo, our largest  $M_{\text{tot}}$  value is  $2.84M_{\odot}$  and it leads to a direct collapse to a BH. Therefore it represents a good estimate of  $M_{\text{threshold}}$  for the SFHo EOS, again a few percent smaller than the naive estimate. A more recent analysis performed in full general relativity suggests a non-linear formula to fit the relation between  $M_{\text{threshold}}/M_{\text{TOV}}$  and  $C_{max}$  (Köppel et al., 2019). By exploiting this new relation, we find  $M_{\text{threshold}} = 2.86M_{\odot}$  and  $M_{\text{threshold}} = 2.52M_{\odot}$  for SFHo and SFHo-HD respectively, therefore in excellent agreement with our results.

Finally, this fitting formula can also be used to estimate the value of  $M_{\text{threshold}}$  for other hadronic EOSs or for different parameter sets. In particular, one can investigate how much the threshold density for the formation of hyperons (that determines  $M_{\text{max}}^H$ ), influences  $M_{\text{threshold}}$ . Interestingly, we found that, if we artificially switch off hyperons keeping only nucleons and  $\Delta$  resonances,  $M_{\text{threshold}} \sim 2.5M_{\odot}$ , therefore very similar to the value in presence of hyperons.

#### 5.4.7 Trigger of the phase conversion

The two families scenario predicts, For  $M_{\text{tot}} < M_{\text{threshold}}^H$ , that the phase conversion from hadronic to quark matter certainly occurs. As previously discussed, an explicit simulation of the conversion process in the context of the merger is presently impossible, but one can still estimate when the conversion should be triggered. This happens only when a relevant amount of strangeness, i.e.  $Y_S \gtrsim 0.2$ , is produced while the remnant evolves.

In the left panel of Figure 5.4.6, we show the stripe found in the mass density-temperature plot for which the value of  $Y_S$  is large enough to trigger the phase conversion. In the

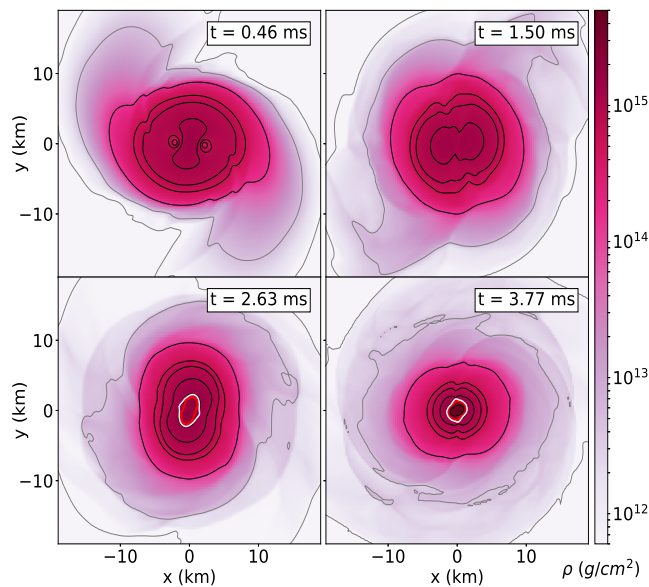


**Figure 5.4.12:** Projection in the  $XY$  plane of the density of the remnant at the time at which the baryon density has a maximum, for the SFHo-HD  $1.18M_{\odot} - 1.18M_{\odot}$  model. The thin black and gray contours correspond to the densities of the polytropic approximation of the EOS. The thick red and white lines mark the region of the remnant in which the quark nucleation can start (same region of the stripe displayed in Figure 5.4.6).

right panel we also display the temporal evolution of the maximum baryon density for the different  $M_{tot}$  in the SFHo-HD case. Considering the model 118vs118, one can notice that the condition for quark matter nucleation is fulfilled after the first two oscillations of the remnant. In addition, Figures 5.4.12 and 5.4.13 give a better visualization of the regions inside the remnant where the condition for the beginning of the deconfinement process is reached. After the trigger, the evolution of the conversion changes dramatically the structure of the remnant: a big part of the star is already converted into quark matter within a few ms and, as a consequence, the radius increases by a few km and the released heat increases the temperature of the remnant. Moreover, the fast change of the total moment of inertia of the remnant causes the development of a relevant amount of differential rotation (Pili et al., 2016). Last but not least, the stiffening of the EOS is capable to stabilize the remnant against collapse. A very similar evolution characterizes also the SFHo-HD 120vs120 model, but in this case the conditions for the deconfinement to start are fulfilled with the second bounce instead of the third one.

In the light of the above, we need to comment on the results for the ejected mass in these

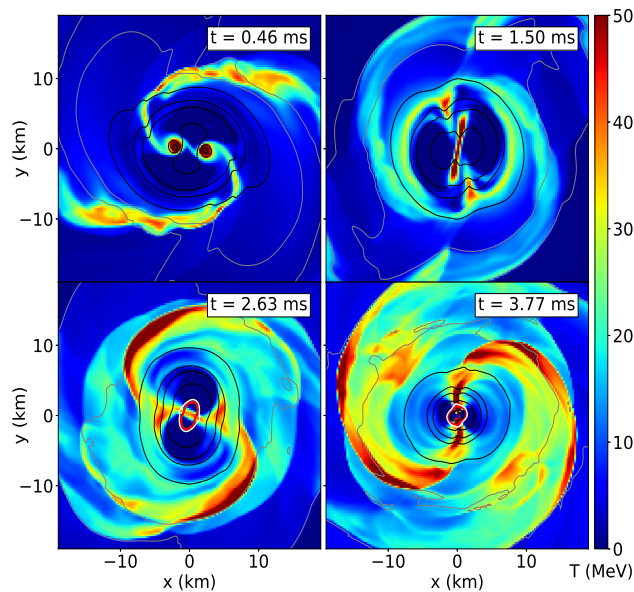


**Figure 5.4.13:** Projection in the  $XY$  plane of the temperature of the neutron star in the post-merger phase at the time of the peaks in the maximum baryon density. The model considered in this figure is the SFHo-HD with mass combination of  $1.18M_{\odot} - 1.18M_{\odot}$ . The thin black and gray contour lines correspond to the densities of the polytropic approximation used in this work. Thick red and white lines as in Fig. 5.4.12.

cases. The oscillations of the maximum density are linked to the shock waves that cause the emission of most of the dynamical ejecta. Therefore, even without an explicit simulation, one can assume in first approximation that our results before the trigger of the phase transition (i.e., as example, in the SFHo-HD 118vs118 model before the third peak) are rather reliable. Finally, let us consider the cases with larger masses. For example, in the SFHo-HD 124vs124 model, characterized by prompt collapse, the condition for nucleation is fulfilled only when the collapse has already started and thus the appearance of the quark phase is not enough to prevent it. On the other hand, in SFHo-HD 122vs122, the threshold for nucleation is reached during a first oscillation of the maximum density, but a second one causes already the collapse of the remnant. In this situation it is possible that a relevant part of the remnant is converted to quark matter but it is quite probable that the related stiffening of the EOS is not sufficient to avoid the collapse.

## 5.5 *Rates of the mergers from population synthesis analysis*

In the following we discuss the rate of merger events expected for the different types of binaries. For this task, we investigated the evolution towards mergers of compact objects in binaries in the context of the two families scenario. In particular, we used a population synthesis code called `Startrack` (Belczynski et al., 2002, 2008; Wiktorowicz et al., 2017). Since we are mainly interested in GW170817, we focused on systems having parameters close to the observed ones and we adapted the simulation parameters to mimic an environment similar to the host galaxy (NGC4993).

As in Wiktorowicz et al. (2017), we employed the two families scenario with the assumption that a HS is transformed into a QS when its gravitational mass reaches a maximum value,  $M_{\text{max,ns}} = M_{\text{max}}^{\text{H}}$ .

Here we do not report the details of the population synthesis analysis, but only a summary of the results. The interested reader is asked to refer to the full text of the paper at: [full text link: iopscience](#).

The estimated merger rates are reported in Table 5.3. For the two families scenario, two models have been adopted with the deconfinement taking place at a mass of the HS of  $1.5M_{\odot} = M_{\text{max},1}$  and  $1.6M_{\odot} = M_{\text{max},2}$ . A third model with only one family is provided for reference: in this case all compact stars are HSs and the deconfinement never takes place. We assumed that all compact objects, formed before the merger, having a mass above  $M > 2.5M_{\odot}$ , collapse to a BH and are therefore not included in the simulation.

In our study, we compare the merger rates calculated for all the possible kinds of systems and the ones which correspond to events similar to GW170817. The latter are characterized by a chirp mass in the interval  $M_{\text{chirp}} = (1.188 \pm 0.1)M_{\odot}$  (the  $\pm 0.1M_{\odot}$  was selected arbitrarily,

Model	all mergers			GW170817-like					
				0.7 < q < 1.0			0.7 < q < 0.85		
	HS-HS	HS-QS	QS-QS	HS-HS	HS-QS	QS-QS	HS-HS	HS-QS	QS-QS
$M_{\max}^H = 1.5 M_{\odot}$	9.1	3.1	0.2	6.4	0.4	0.01	0.03	0.2	–
$M_{\max}^H = 1.6 M_{\odot}$	9.2	3.2	0.02	6.5	0.3	–	0.1	0.2	–
one-family	12.8	–	–	6.6	–	–	0.3	–	–

**Table 5.3:** Merger rates [ $\times 10^{-3} \text{yr}^{-1}$ ] from population synthesis. For the two families scenario we have selected two possible values for  $M_{\max}^H$  and we list the results for all the possible merger combinations: HS-HS, HS-QS and QS-QS. Results in the case of one family scenario are also listed for comparison. Notice that for  $q \lesssim 0.85$ , a HS-QS merger is more likely than a HS-HS merger.

but this choice has a negligible effect on our conclusions) and by a mass ratio of  $q > 0.7$ . First of all, in the case of "all mergers" we found that the rate of HS-QS represent roughly one fourth of the total rate and it is therefore not strongly suppressed with respect to the rate of HS-HS.

Concerning the GW170817-like events, the results depend on the value of the mass ratio  $q$  of the binary. In Table 5.3, we compare the values for merger rates when considering the entire range of acceptable mass ratios ( $q > 0.7$ ) and, separately, the results when a lower mass ratio ( $0.7 < q < 0.85$ ) is assumed. This choice was motivated by the study of the GW170817 event (Abbott et al., 2018) according to which a mass ratio  $q \sim 0.85$  is highly consistent with the data. The results we obtained for the two ranges of  $q$  are quite different. The first one ( $q > 0.7$ ) is dominated by systems with a high mass ratio that are mostly HS-HS, because for  $M_{\text{chirp}} \approx 1.188$  and  $q \approx 1$  the masses of the components of the binary can barely touch the QS mass range  $M_{\min,1}^Q > 1.37M_{\odot}$ , or  $M_{\min,2}^Q > 1.46M_{\odot}$ . On the contrary, for  $0.7 < q < 0.85$  one of the stars usually is more massive than  $M_{\min}^Q$  and therefore it becomes a QS. As a consequence, despite the mergers within the entire range of asymmetry prefer the HS-HS mergers, the ones characterized by a lower mass ratio ( $0.7 < q < 0.85$ ) are most probably HS-QS mergers. However, for the former case the obtained merger rates are much higher ( $\sim 6.8 \text{ kyr}^{-1}$ ) than for the latter case ( $\sim 0.2\text{--}0.3 \text{ kyr}^{-1}$ ).

Another important conclusion of our analysis is that the rates of QS-QS mergers are in all the situations very much suppressed and they reach at most a few percent of the entire number of expected events which involve at least one QS, in agreement with the results of Wiktorowicz et al. (2017). Specifically, the probability that GW170817 was connected to a QS-QS merger is completely negligible.

Finally, we underline that all the merger rates found from population analyses are remarkably below the one estimated from GW170817. Now, let us discuss the interpretations of

GW170817 within the two families scenario in terms of the possible types of merger and their likelihood.

- *HS-HS binary*: This is the most probable type of merger for GW170817, considering the complete range of mass ratio values ( $q > 0.7$ ). Indeed, despite from the observational values of the chirp mass and of mass ratio the limits on the mass of the primary is  $(1.37\text{--}1.64)M_{\odot}$  and of the secondary is  $(1.17\text{--}1.37)M_{\odot}$ , the outcome of population synthesis analysis is that  $q \sim 1$  is favoured and thus the components have a mass  $M \sim 1.37M_{\odot}$ . Therefore, the probability that at least one of this is a QS is quite low.
- *HS-QS binary*: This is the preferred binary to interpret GW170817, in the low mass ratio ( $0.7 < q < 0.85$ ) case: indeed the most massive component can reach the QSs mass range. However, for GW170817-like events, the merger rate for low mass ratios ( $\sim 0.2\text{--}0.3 \text{ kyr}^{-1}$ ) is notably smaller with respect to the wider range (i.e.  $q > 0.7$ ;  $\sim 6.8 \text{ kyr}^{-1}$ ).
- *QS-QS binary*: This is a negligible case. In particular, as one can infer from Figure 5.3.1, GW170817 cannot be a QS-QS. For what concerns GW170817-like mergers, there is a very marginal probability that they can be due to QS-QS for  $q \sim 1$  corresponding the "all-comb" region of Figure 5.3.1.

## 5.6 GW170817 and its interpretation as a HS-QS merger

The binary system of GW170817 is characterized by a total mass of  $M_{\text{tot}}^{170817} = 2.74_{-0.01}^{+0.04}M_{\odot}$  and, within the two families scenario, it can be identified only as HS-QS. Indeed  $M_{\text{threshold}}^H < M_{\text{tot}}^{170817}$  and thus a HS-HS merger would result in a prompt collapse to a BH. At the same time, this possibility is ruled out by the observation of both a sGRB  $\sim 2$  sec after the merger and later of a Kilonova signal. Moreover, as commented in the previous section, GW170817 cannot also be identified as a QS-QS merger.

From a phenomenological point of view, it is hard to establish whether in our scenario and with the interpretation in terms of a HS-QS, we can explain the whole features that concerns GW170817 because of the lack of an explicit simulation. However, we can check if our model fulfills the lower and upper limits on  $\tilde{\Lambda}$ . In particular, the first one empirically suggested by Radice et al. (2018b), represents a requirement to describe the Kilonova signal AT2017gfo (although Kiuchi et al. (2019) recently criticized this constraint). In Figure 5.6.1, we display the tidal deformabilities of the two stars in the binary and  $\tilde{\Lambda}$ , assuming the same chirp mass as GW170817, for the one family model and for all the combinations in the two families scenario (HS-HS, HS-QS and QS-QS) <sup>4</sup>. One can notice that both the upper limit on  $\tilde{\Lambda}$ , as

---

<sup>4</sup>The QS-QS case is included just for comparison but it is not realistic

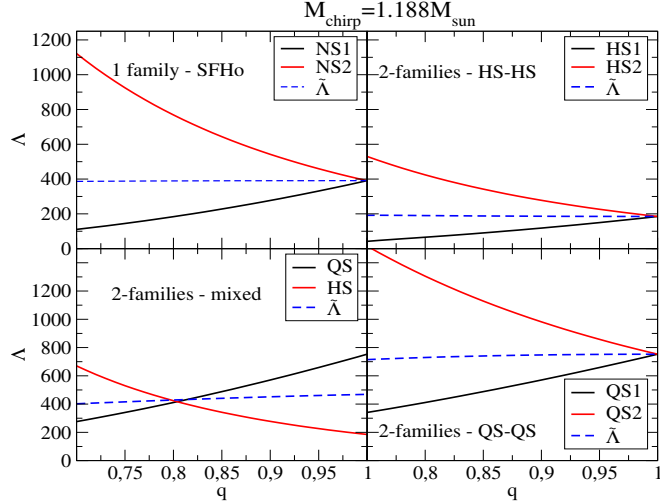


**Figure 5.6.1:** Tidal deformabilities for the stars in a binary system assuming the same chirp mass as GW170817 for the one family model and for all the combinations in the two families scenario (HS-HS, HS-QS and QS-QS). The employed EOSs are the one described in section 5.2.

inferred from the GW signal, and the lower limit, coming from the analysis of the Kilonova (Radice et al., 2018b), can be satisfied within the two families scenario for a HS-QS system (for further details see also Burgio et al. (2018)). Here, the reason for the small value of  $\Lambda$  which characterizes the HS component is mainly the softening due to the appearance of  $\Delta$  resonances. On the other hand, a HS-HS binary is not compatible with the observational constraints because the value obtained for  $\tilde{\Lambda}$  is too small (Radice et al., 2018b; Kiuchi et al., 2019). This result provide a further proof that the interpretation of GW170817 as an HS-HS merger is excluded.

A further aspect to be discussed is the possibility to explain the electromagnetic counterparts of GW170817 within the two families scenario. For what concerns GRB170817A, there is no evidence for the presence of an extended emission following the prompt signal. Therefore, as explained in section 5.3.2, this sGRB can be lunched by the disk accreting onto the BH. On the other hand, the possibility of obtaining a Kilonova signal depends on whether or not the quark matter ejected during a merger involving a QS is able to evaporate into nucleons. This will be the subject of chapter 6. If this is the case, the Kilonova produced because of a HS-QS or QS-QS merger would not be significantly different with respect to the one produced in a HS-HS merger. Moreover, the ejection of matter can be very efficient and it allows to explain AT2017gfo as a HS-QS merger: indeed, in this case the radii of the two compact stars are both rather small, the threshold mass is large and the system is asymmetric. These are the requirements proposed in Kiuchi et al. (2019) to explain the amount of mass needed for AT2017gfo and they cannot be satisfied at the same time within

a one family model.

## 5.7 Discussions and Conclusions

The motivation of this work is to study the phenomenological implications and signatures of the two families scenario in the context of the merger of compact stars.

In this model, three different types of binaries exist, HS-HS, HS-QS, QS-QS. These possibilities are analyzed as functions of the chirp mass  $M_{chirp}$  and the mass asymmetry  $q = \frac{m_2}{m_1}$ . Once the kind of binary is specified, its fate in the post-merger phase and the properties of the connected signals are determined by the threshold mass,  $M_{threshold}$ , and the supramassive maximum mass  $M_{supra}$ . An estimate of these quantities is provided for the possible compact objects (at the moment or soon after the merger), HS, QS and Coll-Hyb, the latter being a hybrid configuration which is formed during the eventual deconfinement process. In the light of the above, the possible outcomes of a merger and the connected phenomenology are discussed.

The case of HS-HS is then studied in detail performing numerical relativity simulations of the merger through the ET software. We employed two EOSs, i.e. SFHo and SFHo-HD and we consider symmetric binaries with total masses in the range  $2.36 - 2.84M_{\odot}$ . The cold EOSs are written as piecewise polytropic functions and the thermal part is approximated through a constant thermal adiabatic index  $\Gamma_{th} = 1.8$ .

The analysis of the results of the simulations allows to find many signatures of the two families scenario. The first one is the value of the threshold mass which can be inferred through the study of the evolution of both the maximum density in the computational grid and the GW signal: we found  $2.84M_{\odot}$  for SFHo, and  $\sim 2.48M_{\odot}$  in the case of SFHo-HD and thus significantly smaller than the total mass for GW170817 (see section 5.4.6). This suggests the possibility, in the two families scenario, of a prompt collapse to a BH for binaries with a total mass in the interval  $(2.48 - 2.74)M_{\odot}$ , between  $M_{threshold}^H$  and the mass of the binary associated to GW170817. Such an event would be recognizable through the lack of significant electromagnetic counterpart and would be interpreted as a HS-HS merger.

On the other hand, for binaries with low  $M_{tot}$ , many observable properties allow to distinguish between the one family and two family scenario. The most immediate one would be the value of  $\tilde{\Lambda}$  which is appreciably smaller for SFHo-HD with respect to SFHo, because of the softening due to the formation of  $\Delta$  resonances at about twice the saturation density. Therefore, if future precise measurements of the GW signal from the inspiral phase can put upper limits on  $\tilde{\Lambda}$ , the possibility of merger of very compact stars (i.e. HSs in the two families scenario) will be tested.

A second signature of the two families scenario may also be provided by an eventual future

observation of the postmerger signal. Indeed, if the outcome is not a prompt collapse, the post merger spectrum shows a main  $f_2$  peak in frequency which, for a given total mass, is larger for softer EOSs. Therefore, during the first milliseconds of the life of the remnant, the frequency  $f_2$ , for SFHo-HD is about 1kHz larger than one found for a typical NS-NS merger. Moreover, if  $M_{tot}^H < M_{thr}^H$ , a phase conversion of hadronic matter to quark matter can occur. However the deconfinement process is triggered only when  $Y_S \sim 0.2$ , i.e. the HS contains a relevant amount of strangeness. We studied the possibility for this condition to be fulfilled by means of the strong oscillations of the remnant. In the two families scenario the newly born QS is characterized by a stiffer EOS, and thus the conversion would cause a shift of  $f_2$  to a smaller value (see [Bauswein et al. \(2016\)](#) for a preliminary study of this signature). Note that this result is the opposite of what found in recent works discussing the occurrence, in the post-merger, of a phase transition to quark matter: in these cases, since the EOS containing quark matter is softer, the transition reduces the lifetime of the remnant and shift  $f_2$  to larger frequencies ([Most et al., 2019](#); [Bauswein et al., 2019](#)).

The second relevant feature of the merger is the ejection of matter: we estimated both the dynamically ejected mass and the mass of the disk (part of which can become unbound in a later phase). The dynamical ejecta is mostly due to the shock waves generated by the bouncing of the maximum density at a distance in the range 100 – 200 km from the center of the remnant. Comparing different binary masses, we found for both the EOSs a maximum for the dynamical ejecta larger then  $10^{-2}M_\odot$  in correspondence of a  $M_{tot}$  slightly smaller than the respective  $M_{threshold}$ . A feature which allows to distinguish among the two EOSs is  $M_{disk}$ , being up to an order of magnitude larger in the case of SFHo. This result has consequences on the expected Kilonova signal: a small value of  $M_{disk}$  determines a suppression of the purple component with respect to the ones linked to the dynamically ejected mass, in particular the blue one believed to be associated to the shocked material ([Perego et al., 2017](#)).

Finally, a population synthesis analysis reveals that the amount of QS-QS binaries is negligible while, for intermediate values of  $M_{tot}$  and  $q$ , a mixed binary of the type HS-QS is very likely. These results, together with the phenomenology previously described, lead to the interpretation of GW170817 as a HS-QS merger. In addition, we underline again that the two families scenario was suggested to explain the observations of stars with large masses and the possible existence of compact stars with small radii. This is the same problem born again when trying to model AT2017gfo: [Siegel \(2019\)](#) suggested that the presence of a dominant shock-heated component in the ejecta favors radii smaller than (11-12)km. The latter can be easily accommodated within the two families scenario but are basically excluded within the one-family scenario.

# 6

## *The fate of quark matter: strangelets evaporation*

As discussed in the previous sections, the two families scenario predicts a relevant number of binaries which contain at least one QS: when those systems merge, quark matter can be ejected in the form of strangelets. The latter are self-bound lumps of strange matter composed of up, down, and strange quarks in chemical equilibrium and electrons which guarantee charge neutrality.

A nugget with baryon number  $A$  contains  $3A$  quarks in a quark matter phase which is absolutely stable in the conditions of zero temperature and external pressure. This is valid for a range of baryon numbers  $10^2 < A < 2.5 - 3 \cdot 10^{57}$  (i.e. from a size of few fermis to  $\sim 10$  km). For  $A$  lower than  $10^2$ , the energy per baryon is raised to  $> 930$  MeV by means of shell effects and thus the quark matter can decay. The maximum  $A$  corresponds to a QS and it is set by the stability condition against a gravitational collapse into a BH.

In this chapter, the fate of this quark matter is investigated, analyzing its possible evaporation into nucleons.

The evaporation of the ejected quark nuggets would result in the formation of normal nuclear matter around the remnant, such as in a common NS-NS merger: this would allow to explain the Kilonova signal AT2017gfo, which in the two families scenario is connected to a HS-QS merger.

## 6.1 Criticisms to QSs existence

Besides the Kilonova issue, other criticisms on the existence of QSs and strangelets must be investigated.

First of all, if the strangelets are stable, they could, in principle, be detected in experiments, but, up to the present time, no observations have been reported. The absence of strangelets detected in Earth and Lunar experiments puts some limits on the flux which are summarized in Price et al. (1984); de Rujula & Glashow (1984); Perillo Isaac et al. (1998); Weber (2005); Han et al. (2009) while, concerning the search for strange quark matter in cosmic rays, the resulting upper limit from the PAMELA space spectrometer are described in Adriani et al. (2015) and displayed as blue lines in Figure 6.1.1.

A further constraint comes from astrophysics: Madsen (1988), assuming a large strangelets pollution, argued that the existence of QSs would imply that all the compact stars are QSs. Indeed every star whose fate is to become a NS, captures at least one nugget of quark matter which is able to trigger the deconfinement process. At the same time, pulsars exhibiting the glitches are believed to be ordinary NS, since the thin crust of a QS has a moment of inertia too small to explain this physical phenomenon. Therefore, either strangelets (and QSs) do not exist, or the flux is not large enough for a lump to hit each NS or its progenitor. This argument results in a further extension of the limits on the strangelets flux already

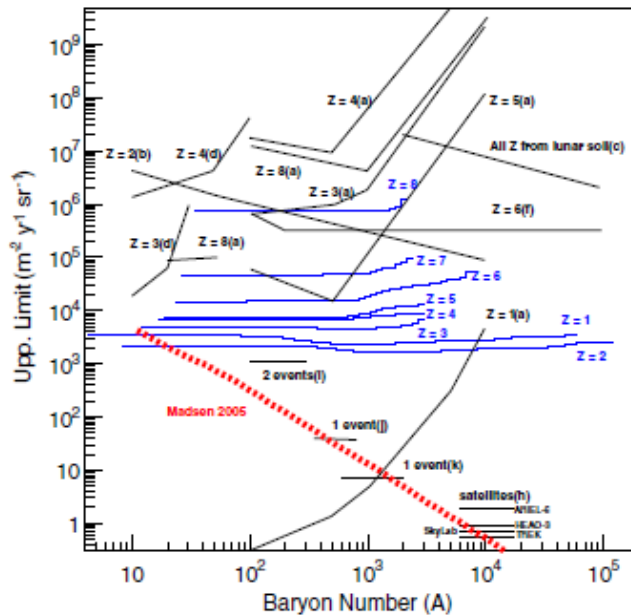
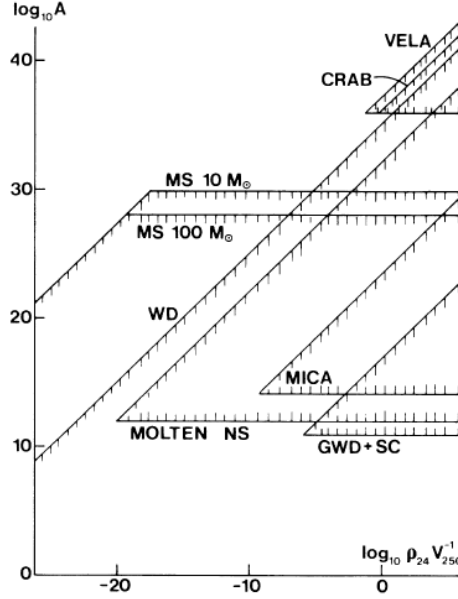


Figure 6.1.1: from Adriani et al. (2015). Limits on the strangelets flux as measured by PAMELA for particles with charge  $1 \leq Z \leq 8$  (blue lines) compared with previous results.



**Figure 6.1.2:** from [Madsen \(1988\)](#). Limits on the strangelets flux from experiments and astrophysics. See text for details. Reprinted with permission, © 1988 American Physical Society.

determined through experiments. Figure 6.1.2 summarizes all these constraints: the nuggets baryon number  $A$  is displayed as a function of the contribution to the galactic halo density, written in terms of  $v_{250} = \frac{v_\infty}{250} \text{ km s}^{-1}$  and  $\rho_{24} = \frac{\rho_\infty}{10^{-24}} \text{ g cm}^{-3}$ . Here,  $v_\infty$  and  $\rho_\infty$  are the lump speed and contribution to the galactic halo density far from the star.

The excluded regions are the ones on the hatched side of lines representing the different "probes"; Earth-based limits come from track-etch experiments with mica (MICA), scintillator experiments (SC; [Nakamura et al. \(1985\)](#); [Barish et al. \(1987\)](#)) and a GW detector search (GWD; [Liu & Barish \(1988\)](#)). The other lines indicate nugget capture from different objects, such as main-sequence stars (MS) and the Crab and Vela pulsars. Moreover, giant stars with a central region resembling a "white dwarf" (WD), and molten neutron stars (MOLTEN NS) are also considered. The first one is a phase present after the stars leaves the main sequence, immediately before a type-II supernova explosion, while the second one can last for the first few months after the NS is born.

Looking at figure 6.1.2 one can see how the limits imposed by the possibility of captures from NS and their progenitors are much more constraining than the ones coming from Earth-based experiments.

In order to test a model based on the existence of stable quark matter with the aforementioned restrictions, an estimate of both the size and the flux of strangelets is required.

Two are the known astrophysical settings for quark lumps production: the quark-hadron phase transition at the time of primordial baryogenesis ( $\sim 10$  s after the big-bang) or the partial fragmentation of a QS during the merger.

In the next paragraph the main results from [Alcock & Farhi \(1985\)](#) and [Madsen et al. \(1986\)](#) are reported: they studied the strangelets in the early universe as a possible dark matter candidate. The formalism developed by [Alcock & Farhi \(1985\)](#) is the one we have also adopted in our analysis.

## 6.2 *Strangelets in cosmological context vs stranglets from the merger*

According to Witten, the production of strangelets took place when the cooling Universe reached a critical temperature  $T_c$ , of the order of 100 MeV. This temperature represents the threshold between the two phases of quark matter, the confined and deconfined phase.

Because of confinement, a single quark can never be separated from the original strangelet and thus the only way to change its baryon number is the "evaporation" of the nugget, through the emission of neutrons or protons. The strange matter has an energy per baryon ( $\frac{E}{A}$ ) between 830 and 930 MeV (see section 3.2.6). Therefore, the ionization energy, i.e. the energy required to emit one neutron, is  $I < 100$  MeV. As a consequence, when the Universe is at temperature  $\sim I$ , the evaporation is unavoidable:

$$(A + 1) + I \rightarrow A + n \tag{6.2.1}$$

However, the Universe cools down to 1 MeV with a timescale of 1 s and thus large enough nuggets could evaporate only partially. The question then arises about the maximum baryon number of a nugget which completely evaporate in the early Universe phase.

[Alcock & Farhi \(1985\)](#) calculated the evaporation rate of strange nuggets after the QCD phase transition. At the corresponding temperature,  $\simeq 100$  MeV, the environment is a sea of photons, electrons, neutrinos, and their antiparticles. Two problems have to be examined: the cooling of strangelets due to the evaporation itself and the possible re-absorption of the emitted neutrons. Neutrinos play a fundamental role concerning the first issue, since they represent the only source of re-heating of the evaporating nuggets. On the other hand, the rate of absorption of neutrons by the strangelets depends strongly on the density in their vicinity which, in this "cosmological" context, is determined only by the evaporated baryons. Moreover, the evaporation determines an excess of  $s$  quarks at the surface of the nuggets and, in order for the process to proceed, weak reactions need to re-equilibrate the flavour content. Taking all those problems under consideration, [Alcock & Farhi \(1985\)](#) concluded that the minimum baryon number of a lump that can survive is  $10^{52}$ , i.e. an object with a

mass similar to a planet.

Madsen et al. (1986) pointed out some criticisms in this results, specially concerning the weak reaction rate estimated to be  $\sim 3$  orders of magnitude lower then the simple one calculated in Alcock & Farhi (1985). This reduced the limit for the surviving strangelets to  $A < 10^{46}$ .

Therefore small cosmological nuggets evaporate completely and do not play a role in the calculation of the flux: only very big lumps remain. The latter, as evident from Figure 6.1.2, are basically undetectable. As a consequence, the flux of strangelets that could be seen, directly or indirectly, through experiments, is mainly due to mergers. Therefore the estimate of the rate of mergers involving a QS, the baryon number of fragments and the possibility of evaporation must be investigated and the resulting flux compared with the limits in figures 6.1.1 and 6.1.2.

The first attempt in this regard was performed by Wiktorowicz et al. (2017) which, through a population synthesis simulation, calculated the rate of QS mergers in our Galaxy being about  $12 \text{ Gyr}^{-1}$ . Since a fraction of binaries shows a prompt collapse to BH, this number is considered as a upper limit. Assuming an ejected mass of about  $10^{-2} M_{\odot}$  for each event and a velocity  $v_{250} = 1 \text{ km s}^{-1}$  for the small size nuggets, they provided an estimate of the flux which depends only on the baryon number  $A$ .

They found a result in agreement with the limits coming from Earth and Lunar experiments and from the PAMELA detector (Adriani et al., 2015). On the other hand, the ability to fulfill the astrophysical limits depends, first of all, on the typical size of the fragments: according to Madsen (1988), only strangelets with  $A \lesssim 10^{30}$  can trigger a phase conversion. Already in 2002, it was claimed for the first time that the strangelets dynamically ejected during the merger have a baryon number  $\gtrsim 10^{38}$  (Madsen, 2002): if this is the case the probability of capture of a strangelet by a star is negligible.

Second, the nuggets ejected in the merger process can evaporate soon after their emission or even after the capture by a star at the moment of the CCS. This depends strongly on the temperatures reached by the nuggets.

In the light of these considerations, it appears evident how the conditions of density and temperature reached during the mergers are fundamental ingredients to disentangle the strange matter issue. In our work, we study the fragmentation and the evaporation process in a more quantitative way using exactly these conditions as estimated through hydrodynamic simulations.

A further, even more direct, open problem concerns the possibility of a Kilonova associated with a merger containing at least one QS and the features of the signal. Paulucci et al. (2017) claimed that the evaporation and the consequent r-processes actually take place, but the chain is unable to synthesize the lanthanides. This would lead to Kilonova dominated by the blue component. However, given the complexity of the subject and the multitude of variables in the picture, further studies are needed to completely clarify this issue.

### 6.3 QS-QS merger simulations

Up to the present day, the only simulations of QS-QS mergers have been performed by [Bauswein et al. \(2009, 2010b\)](#).

The authors employed the MIT bag model (see chapter [3.2.4](#)) to describe the QSs, with a mass of the strange quark  $m_s = 100$  MeV. The simulations were run for various combinations of masses and using two different values for the bag constant:  $B = 60$  MeV fm<sup>-3</sup> leading to a stiffer EOS (MIT60) and  $B = 80$  MeV fm<sup>-3</sup> corresponding to a softer EOS (MIT80).

The purpose of the aforementioned works was to estimate the Galactic production rate of strange matter nuggets ([Bauswein et al., 2009](#)) and to study the characteristic features of the GW signal from a QS-QS merger which allows to distinguish such an event from a canonical NS-NS merger ([Bauswein et al., 2010b](#)). For the detailed description of the results the reader is reminded to the original papers (some of the quantitative estimate depends on the specific choice of the model which is incompatible with the recent maximum mass limit). However, in the following the most general physical insights suggested by the simulations are listed (see also section [6.5.1](#)):

- the ejecta depends on the bag constant and on the asymmetry  $q$ , and it is larger for less compact models and more asymmetric binaries because of the more pronounced tidal effects. The matter is ejected from the extremity of rapidly rotating spiral arms which are formed after a few ms from the moment of the merger (Fig. 4 of [Bauswein et al. \(2010b\)](#));
- for some combinations of the parameters of the EOS and of the binary, the total amount of ejected mass can reach a value of the order of  $10^{-2}M_\odot$ ;
- the temperatures are slightly lower with respect to the ones found during the canonical NS-NS merger, but they are still of the order of tens of MeV.

The simulations are performed with a code combining a three dimensional relativistic smoothed particle hydrodynamics approach (SPH) with an approximate treatment of GR. The latter makes use of the conformal flatness condition with additional methods for the description of the GW signal. The details of this scheme and of the code are provided in [Oechslin et al. \(2007\)](#).

The main advantage of this approach is that it allows to follow the trajectories of the nuggets of quark matter and thus gives information not only on the location of the lumps, but also on the evolution of their temperature. As mentioned before, this is a fundamental ingredient to understand if the particles evaporate. In this regard, we will study the data of the simulation with masses of  $1.2M_\odot$  and  $1.35M_\odot$  and the MIT60 EOS, concerning the maximum temperatures reached by the nuggets.

Moreover, it is also relevant to investigate how long this temperature is kept by the each lump and compare it with the timescale for the evaporation corresponding to that temperature.

This information allows to determine the percentage of the ejected nuggets which can evaporate.

## **6.4 Abstract**

In this work, we considered the case of binaries which contain two Qs: when those systems merge, quark matter can be ejected in the form of strangelets.

We studied the partial fragmentation of a QS into strangelets during the process of the merger and we investigated the fate of this quark matter, analyzing its possible evaporation into nucleons. For this purpose, we took into account the thermodynamic conditions of the post-merger phase, both in terms of densities and temperatures. These variables, together with the typical size of the ejected fragments, are fundamental to estimate the timescale of the evaporation. We showed that the 93% of the quark matter ejected during and after the merger evaporate into nucleons. Only a small amount of mostly large size nuggets, which eventually become unbound after the merger, can survive. As a consequence, the probability that strangelets can either affect the evolution of stars or be detected directly is negligible. Moreover, the evaporation of the ejected quark nuggets would result in the formation of normal nuclear matter around the remnant and would give birth to a Kilonova signal as in the case of BNS merger.

## **6.5 Formation and evaporation of strangelets during the merger of two compact stars**

In this work, we make use of the formalism developed by [Alcock & Farhi \(1985\)](#) and we consider the criticisms of [Madsen et al. \(1986\)](#), but applied to the production of strangelets from the merger of two compact stars. Usually, this problem is studied in association with a double QS merger ([Bauswein et al., 2009, 2010b](#); [Paulucci & Horvath, 2014](#))<sup>1</sup>, but, since within the two families scenario NSs (HSs) and QSs can coexist, one must also take into account the possibility of a merger HS-QS. Moreover, as discussed in section 5.6, GW170817-GRB170817A-AT2017gfo could represent an example of this type of event ([Drago & Pagliara, 2018](#); [Burgio et al., 2018](#); [De Pietri et al., 2019](#)).

Here, by exploiting the theory of fragmentation and the outcomes of merger simulations, we studied both the distribution in size (or baryon number) of the ejected droplets and the fraction of their mass which can evaporate in the first few milliseconds after the merger.

---

<sup>1</sup>The merger QS-BH was investigated by [Kluźniak & Lee \(2002\)](#), where no ejected matter was found.

### **6.5.1 Ejection of quark matter**

A relevant amount of quark matter can be, in principle, ejected during a merger involving at least one QS, similar in order of magnitude to the one obtained in a standard NS merger (for a description of the ejection mechanisms see section 4.2.2).

Presently, the only available simulations of a QS-QS merger have been performed by [Bauswein et al. \(2009, 2010b\)](#): the methods and the main outcomes have been briefly described in section 6.3. Here we use the results of these simulations in our calculations. On the contrary, there were no existing simulations for a HS-QS merger and therefore, with the aim of understanding the mass ejection in this case, we have performed the first one. In this case, almost all the ejected mass comes from the HS and only a negligible amounts of unbound quark matter is present at the end of the simulation. The reason for this is the high binding energy characterizing the QS, which thus completely disrupts the HS in the collision. The eventual ejection of quark matter in a later phase is prevented by the hadronic matter surrounding the QS. Since the strangelets production for a HS-QS binary is inefficient, we will not further discuss this case here and we will focus on the QS-QS merger. Anyhow the thermodynamical conditions proper of the two types of event are very similar.

Although the secular evolution of the remnant from QS-QS and HS-QS merger has not been explicitly simulated, one can safely hypothesize that no quark matter is emitted from this system beyond the dynamical timescales. Droplets of quark matter having a macroscopic size orbit around the remnant (see Figure 4 of [Bauswein et al. \(2010b\)](#)) and they behave similarly to test-particles, conversely to the hydrodynamical evolution and viscous processes taking place in the tori formed after a NS-NS merger. Therefore it seems very improbable that secular processes could be able to unbind fragments made of quark matter. The evaporation process can affect also gravitationally bound droplets but this is irrelevant from the point of strangelet production.

### **6.5.2 Fragmentation of quark matter**

As described in section 6.3, after a QS-QS merger the matter is ejected by means of the fragmentation of the spiral arms, in a way similar to droplets foaming from sea waves or the water drops from a rotating sprinkler. The final size of the strangelets before the evaporation process, is the results of two different mechanisms: first the fragmentation of the QS and next the rescattering of the resulting initial fragments. Let us begin by studying the size of the droplets emitted in turbulent flows ([Kolmogorov, 1949](#); [Hinze, 1955](#); [Frohn & Roth, 2000](#); [Lefebvre, 1988](#)), such as the initial ones ejected after a QS-QS merger. In this case, the turbulence is driven by forces acting on large scales and the turbulent fragmentation is due to the cascade of turbulence to smaller scales. Two quantities regulate this process. The first one is the Kolmogorov scale, which separates the turbulent from the visco-dissipative regime and it is defined in terms of the shear viscosity of quark matter  $\mu$  ([Heiselberg & Pethick,](#)

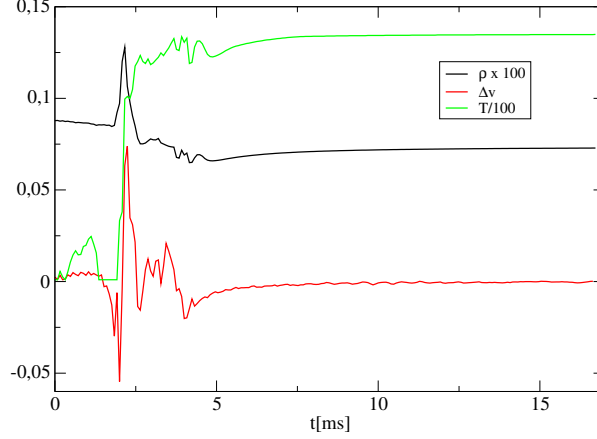


**Figure 6.5.1:** Density ( $M_{\odot}^{-2}$ ), temperature (MeV) and changes in the scalar velocity (units of  $c$ ) for an example ejected particle.

1993), the density  $\rho$  and the energy dissipation rate  $\epsilon$ , as  $l_K = (\mu^3/\rho^3\epsilon)^{1/4}$ . The second one is the Weber number, which is size dependent and it is calculated as the ratio between the turbulent kinetic energy and surface tension  $\sigma$ ,  $We(d) = (\rho/\sigma)v(d)^2d$ , where  $v(d)$  is the turbulent velocity evaluated at the scale  $d$ . One of the conditions for the turbulent fragmentation in the inertial regime to take place is  $We(d) \gtrsim O(1)$ . The minimum  $d$  for which this limit is fulfilled is the so called Hinze scale  $l_H$  and defines the smallest size of droplets that can be formed. In addition, a further requirement is  $d > l_K$ . In our case, the turbulent speed on the larger scale, i.e.  $\sim$  the size of a QS, is estimated to be  $v(R) \sim (0.02 - 0.05)c$  from the QS-QS simulations in Bauswein et al. (2009, 2010b). This value is used also to calculate  $\epsilon \sim v(R)^3/R$  (Davidson, 2015). The surface tension is set to  $\sigma \sim 10\text{MeV}/\text{fm}^2$  and the viscosity is evaluated through the relation:

$$\frac{\mu}{\text{g cm}^{-1} \text{s}^{-1}} = 1.7 \times 10^{18} \left(\frac{0.1}{\alpha_s}\right)^{5/3} \rho_{15}^{14/9} T_9^{-5/3} \quad (6.5.1)$$

where  $\rho_{15} = \rho/10^{15} \text{g cm}^{-3}$  and  $T_9 = T/(10^9 \text{K})$  (Heiselberg & Pethick, 1993). Adopting the values  $\alpha_s = 0.1$ ,  $\rho = 5 \times 10^{14} \text{g cm}^{-3}$  and  $T = 10^{11} \text{K}$  and imposing  $We \gtrsim 4$ , the resulting Kolmogorov scale is  $l_K \sim 5 \times 10^{-6} \text{cm}$  and the Hinze scale is  $l_H \sim 10^{-4} \text{cm}$ . Thus the turbulent fragmentation proceeds down to the a size of  $10^{-4} \text{cm}$  corresponding to  $A_H \approx 10^{27}$ . After the ejection, since the mean free path is rather short  $\sim 10^{-3} \text{cm}^2$ , the droplets are rescattered many times and therefore they fragment to smaller sizes. The Weber number regulates

<sup>2</sup>assuming a spherical shell of radius 10 km and width 1 km

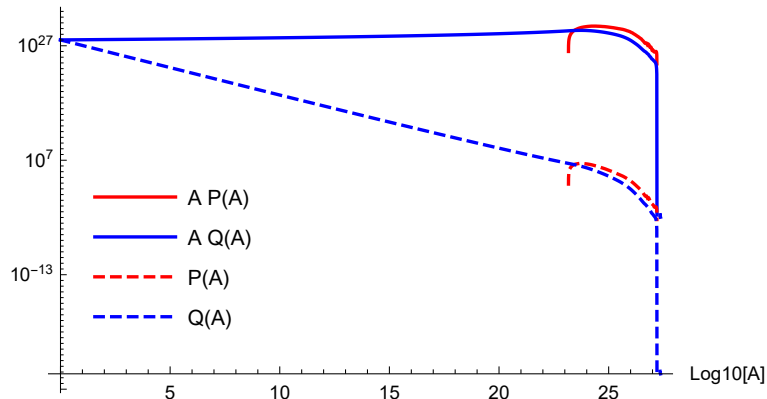


**Figure 6.5.2:** Number density of fragments before,  $P(A)$ , and after evaporation,  $Q(A)$ , as a function of  $\text{Log}_{10} A$ . Also shown are the corresponding distributions of the baryonic mass of the fragments. As discussed in the text, the normalization is chosen to be  $A_{\text{tot}} = \int_1^{\infty} dA A P(A) = 10^{56}$ .

also this process together with the size dependent Ohnesorge number,  $Oh = \mu/(\rho\sigma d)^{1/2}$ . If  $Oh \gtrsim 1$  the scattering of two strangelets is dominated by viscosity which prevents the formation of smaller fragments (see e.g. Lefebvre (1988) and Figure 1 of Hsiang & Faeth (1995)). In the QS-QS simulations we found that the majority of the ejected droplets undergoes through a shock which increases their temperatures up to about 15 MeV or even larger (see Figure 6.5.4). Under those conditions the role played by the viscosity is marginal and in principle the fragmentation caused by rescattering could continue down to strangelets with  $A \lesssim 10^{10}$ . However, this is prevented by the Weber number, that again is responsible to limit the smaller possible size of the fragments.

In Figure 6.5.1, we provide an example of the trajectory (with the evolution of the associated thermodynamical variables) of a fluid element which will be finally ejected, as found in numerical simulations. The occurrence of shock, at  $t = 2$  ms when the two QSs firstly touch, is evident in the plot from the large change of the scalar velocity and by a rapid increase of the temperature. Moreover, in several cases, the density decreases immediately after the shock, suggesting a decompression of the material. The change of velocities, on timescales shorter than a millisecond, and the density fluctuations, lasting for few milliseconds, suggest the occurrence of violent collisions among the droplets, which thus are fragmented into smaller pieces (see Appendix C for further details). Furthermore, favourable conditions for the fragmentation process are created, during this phase, by the densities reached which are below the equilibrium one and imply therefore a vanishing pressure. As shown in the Appendix C, we have performed a Monte Carlo simulation of the re-scattering process, including the information about the changes of velocity derived from the statistical analysis of the trajectories. The velocities found at the scale of the "particles", the pieces of about 1 km followed in the simulations, are assumed to follow the Kolmogorov scaling until the

minimum size allowed by the Weber number is finally reached. Using this method, we were able to obtain the distribution of the sizes (and thus baryon numbers) of the strangelets due to the initial fragmentation and to the re-scattering process. This distribution, displayed in Figure 6.5.2, shows that the resulting fragments are relevantly smaller than the initial ones, but still significantly larger than the limit imposed by the Ohnesorge number. We notice also the existence of a sharp lower limit on  $P(A)$ , which is related to the fact that the maximum energy available for the fragmentation is not large enough to produce considerably smaller droplets. In addition, we underline that the smallest fragments obtained in our simulation, still have a size comparable with the  $l_K$ , and thus our use of the Kolmogorov scaling is justified.

### 6.5.3 Evaporation of strangelets

The evaporation consists in the emission of a baryon, usually a neutron, that leaves a strangelet having a baryon number  $A - 1$ . This process is endothermic and the amount of energy required is at least equal to the ionization (or binding) energy  $I$ . In our analysis we assume  $I$  to be in the range  $I \sim 50 - 70$  MeV, because these are the typical values needed to obtain a stable QS with a mass about  $2 M_\odot$  (Drago et al., 2019). A first equation for the evaporation rate is derived directly from the detailed balance principle and it is written as (Alcock & Farhi, 1985):

$$\frac{dA}{dt} = \frac{1}{2\pi^2} m_n T^2 e^{-\frac{I}{T}} (f_n + f_p) \sigma_0 A^{\frac{2}{3}} \quad (6.5.2)$$

where  $m_n$  is the mass of the nucleon,  $T$  is the temperature and  $f_{n,p}$  are absorption efficiencies (in the case of neutrons and protons), i.e. correction factors to the geometric cross section  $\sigma_0 A^{\frac{2}{3}}$ .

The simple estimate of Equation 6.5.2 must be modified to take into account two physical processes: the eventual (re-)absorption of neutrons from the environment and the cooling of the strangelet caused by the evaporation itself. As discussed in section 6.2, the physical conditions that we need to consider here are different from the ones found by Alcock & Farhi (1985); Madsen et al. (1986) during the cosmological baryogenesis. In that context, the temperature evolution depends on the universe expansion rate while, during the merger, it is affected by the expansion and the cooling of the ejecta as estimated through simulations. On the other hand, similarly to the cosmological case, for a QS-QS merger the density of nucleons near the evaporating strangelets is provided by the evaporation process itself. Differently, when considering the evaporation after a HS-QS merger, the density of nucleons already present in the environment (because of the HS) must be taken into account.

Since the evaporation requires energy, the temperature of the strangelet  $T_s$  becomes smaller than the temperature of the environment  $T_u$ , but, in order to obtain a relevant evaporation rate,  $T_s$  has to remain comparable to the ionization energy  $I$ . For this reason, it is essential

to have a re-heating mechanism for the strangelets. In the context of the merger, the latter can be provided by neutrinos:  $T_s$  can therefore be estimated by imposing an equilibrium condition between the energy lost by the strangelet, due to both the evaporation and the neutrino emission, and the one gained by the strangelet because of neutrino absorption (see Equations (15,22) of [Alcock & Farhi \(1985\)](#)):

$$4\pi r_s^2 \left[ \frac{7\pi^2}{160} \right] [T_u^4 p(r_s, T_u) - T_s^4 p(r_s, T_s)] = \frac{dA}{dt} (I + 2T_s) \quad (6.5.3)$$

where  $r_s$  is the strangelets radius and  $p(r_s, T)$  is the probability of interaction between the strangelet and the neutrino. Finally, the net evaporation rate  $dA/dt$  will be calculated as

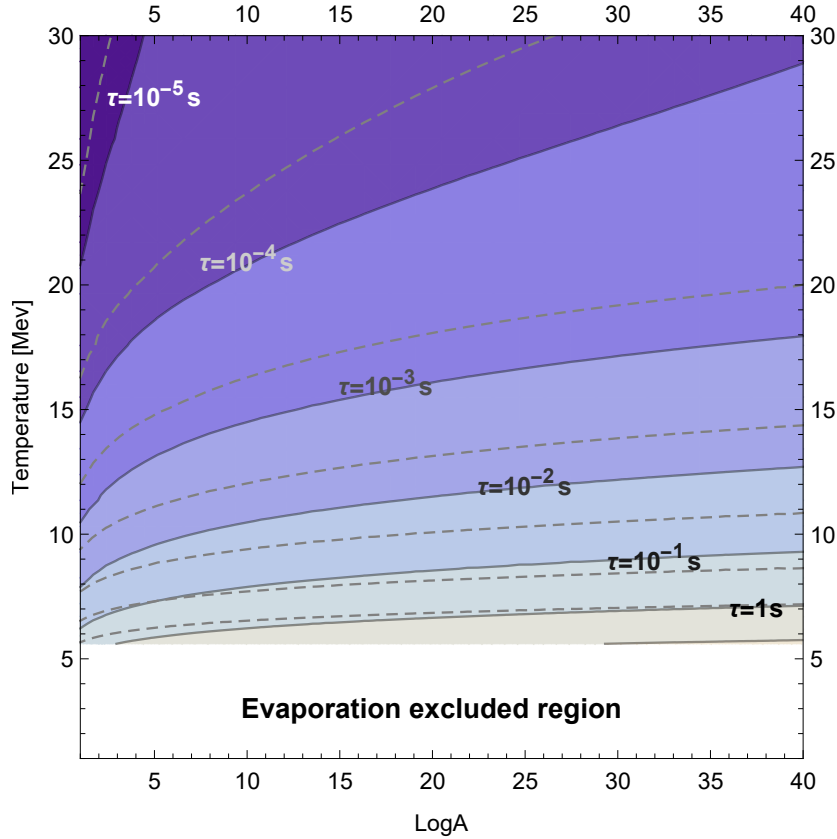


**Figure 6.5.3:** Evaporation timescale computed by assuming neutrino absorption as re-heating mechanism and a the nucleon density determined by the evaporated nucleons. Solid lines and color shading refer to  $I = 50 \text{ MeV}$ , the dashed lines correspond to  $I = 70 \text{ MeV}$ .

the difference between the evaporation and absorption rates:

$$\frac{dA}{dt} = \left[ \frac{m_n T_s^2}{2\pi^2} e^{-\frac{1}{T_s}} - N_n \left( \frac{T_s}{2\pi m_n} \right)^{\frac{1}{2}} \right] (f_n + f_p) \sigma_0 A^{\frac{2}{3}} \quad (6.5.4)$$

where  $N_n$  is the density of nucleons. By solving the Equations 6.5.3 and 6.5.4 one can evaluate the evaporation timescale of a strangelet with baryon number  $A$  as a function of the temperature and the density of the environment.

Here, we focus only on the QS-QS merger case, where  $N_n$  is given only by the nucleons ejected because of evaporation and it can be calculated using the condition for mechanical equilibrium between the components of the system: on one side the pressures due to photons and electrons and on the other side the ones due to the emitted neutrons and protons (Alcock & Farhi, 1985). The resulting density is  $N_n(T_s) = 11\pi^2(T_u^4 - T_s^4)/(360T_s)$ .

In Figure 6.5.3, we show the evaporation timescales as functions of the baryon number and of the temperature. For  $T \lesssim 5.6$  MeV, indicated in the plot with a white area, the evaporation process never takes place since the re-absorption rate always overcomes the evaporation rate. One can demonstrate that, under the aforementioned conditions, the evaporation timescale behaves as:

$$\tau_A \propto \text{Log}A. \quad (6.5.5)$$

As described in Madsen et al. (1986), the fast evaporation of the strangelets into nucleons results in an increase of the strangeness fraction near its surface and this can make the process no longer energetically convenient unless weak reactions have the time to re-equilibrate the

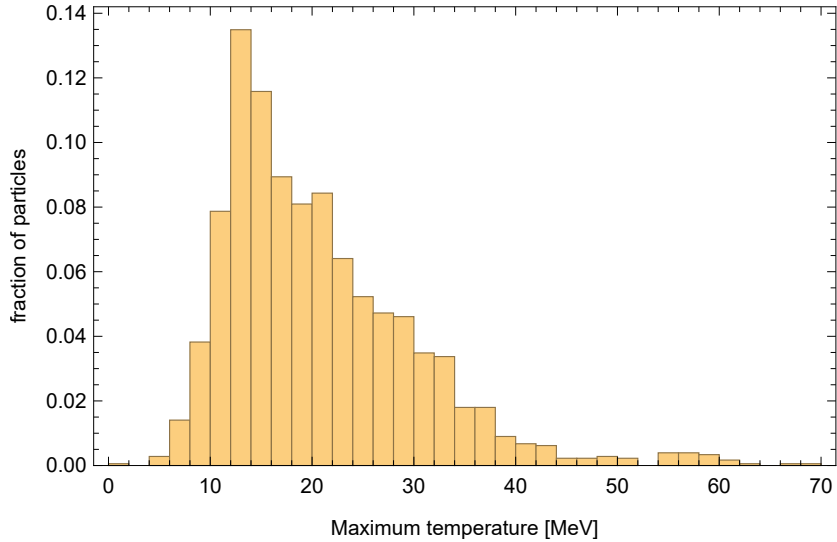


**Figure 6.5.4:** Maximum temperatures reached by each of the ejected particles.

	100 % evaporated	99.9 % evaporated	99 % evaporated
A=10 <sup>10</sup>	0.68	0.78	0.81
A=10 <sup>35</sup>	0.57	0.78	0.81

**Table 6.1:** Probability of total or partial evaporation of a strangelet with a baryon number either of 10<sup>10</sup> or of 10<sup>35</sup> and assuming a binding energy of  $I = 70$  MeV. The temperatures characterizing ejected particles are taken from the QS-QS simulation of [Bauswein et al. \(2010b\)](#), using the EOS MIT60 with masses 1.2 and 1.35 $M_{\odot}$ .

system. This implies the existence of an upper limit on the evaporation rate. As in [Alcock & Farhi \(1985\)](#); [Madsen \(1988\)](#), we include this constraint, also considering the temperature dependence and the Pauli blocking ([Heiselberg et al., 1986](#)), which lower the weak reaction rates by 3-4 orders of magnitude with respect to the simple estimate of [Alcock & Farhi \(1985\)](#). Finally the limit reads:  $dA/dt \lesssim K_{PB} G_F^2 \mu_q^5 \sin^2 \theta_c A$ , where  $\mu_q$  is the chemical potential of the s quarks and  $K_{PB} \sim 10^{-3} - 10^{-4}$ . This implies, in turn, a lower limit on the evaporation timescale which turns out to be only weakly dependent on  $A$  and translates into the fact that the evaporation, even for light fragments, cannot be completed in less than  $\sim (10^{-6} - 10^{-5})$ s. Since we are taking into account evaporation timescales of the order of at least  $10^{-4}$ s, this limit does not influence our results.

In order to study at least the partial evaporation of the ejected fragments, we examine the temperatures characterizing the particles while they move along their trajectories. Figure [6.5.4](#) displays the histogram containing the maximum temperatures: the majority of the particles reaches temperatures larger than 10 MeV and, as a consequence, a relevant fraction of the strangelets evaporates into nucleons. The percentage of evaporated quark matter can be calculated through Equation [6.5.5](#) and by comparing the resulting timescale of evaporation with the time that each particle passes above a given temperature. With this procedure, one can find the distribution of the baryon numbers of the remaining strangelets after evaporation, plotted in Figure [6.5.2](#), and the amount of evaporated mass, listed in Table [6.1](#). Here, one can see that the result depends on  $A$  only through the limit on the maximum amount of mass which can evaporate, clearly corresponding to  $A$ . This is a direct consequence of Equation [6.5.5](#). Further details on the way we computed the fraction of evaporated mass are given in the Appendix [C](#).

### 6.5.4 Phenomenological implications

In section [6.1](#) and [6.2](#) we discussed the experimental limits on the strangelets flux and the phenomenological implications depending on whether or not the evaporation takes place after

a merger involving a QS. Now we can discuss our results in relation with those constraints. First of all, let us define  $A_{\text{tot}} = \int_1^\infty dA A P(A)$  as the total amount of quark matter ejected. Because of the evaporation, the remaining quark matter is then reduced to  $\int_1^\infty dA A Q(A) = 0.07 A_{\text{tot}}$ , suggesting that about 93% of the mass emitted in the form of strangelets evaporated into nucleons. Moreover, we underline that our result for the evaporation concerns the duration of the simulation which is of about 15 ms after the merger. This means that the neutrons required for the r-process chain to take place are emitted very soon and rather close to the center of the merger, re-creating the similar conditions to the standard NS-NS merger which allow to power a Kilonova.

In the second place, let us discuss the astrophysical limits on the strangelets flux. For that, we assume the rate of QS-QS merger in our galaxy to be  $\sim 10$  per billion years, as in [Wiktorowicz et al. \(2017\)](#), and the average amount of ejecta per merger to be  $\sim 0.01 M_\odot$ . This corresponds to a total number of ejected baryons of about  $A_{\text{tot}}^{\text{gal}} = 10^{56}$ . The total number of non-evaporated strangelets in the Galaxy is estimated by integrating the final distribution  $Q(A)$ , i.e.  $N_{\text{tot}}^{\text{gal}} = \int_1^\infty dA Q(A) = 5 \times 10^{30}$ , which is roughly the half of  $\int_1^\infty dA P(A)$  because the other half has completely evaporate. Now, we can check if the flux of strangelets is large enough that at least one of them is captured by a star turning it into a QS. As in [Madsen \(1988\)](#), we write the impact rate of strangelets with a  $A$  in the range between  $A_1$  and  $A_2$  onto a star with mass  $M$  and radius  $R$ :

$$\begin{aligned} F &= (1.39 \times 10^{30} \text{s}^{-1})(m_p / (10^{-24} \text{g/cm}^3)) \\ &\quad \times (N(A_1, A_2) / V_{\text{gal}})(M / M_\odot)(R / R_\odot) v_{250}^{-1} \\ &= (3.3 \times 10^{-36} \text{s}^{-1}) N(A_1, A_2)(M / M_\odot)(R / R_\odot) v_{250}^{-1} \end{aligned} \quad (6.5.6)$$

where  $m_p$  is the proton mass,  $V_{\text{gal}}$  is the volume of the galaxy and  $N(A_1, A_2) = \int_{A_1}^{A_2} dA Q(A)$ . The most relevant case is that of the MOLTEN NS (see section 6.1): this phase lasts for a time  $\tau_{\text{melt}}$  of few months after the NS is born and it is characterized by the absence of a solid crust. This allows the strangelets to penetrate the NS and trigger the phase transition to quark matter ([Madsen, 1988](#)). From Figure 6.1.2, one can see that only nuggets with  $A > 10^{12}$  do reach the MOLTEN NS ([Madsen, 1988](#)). The corresponding flux of strangelets turns out to be:  $F \tau_{\text{melt}} \sim 2 \times 10^{-3} v_{250}^{-1} \ll 1$  and thus the likelihood of this mechanism is absolutely negligible.

Using Equation 6.5.6 in the case of MS stars, one finds a rate of capture of about one strangelet per year, but this would probably evaporate because of the high temperatures reached in the pre-supernova collapse, as suggested by the results plotted in Figure 6.5.3. Moreover, if  $v_{250} \gg 1$  the droplets would spread on a volume significantly larger than  $V_{\text{gal}}$  and both these modifications would lower the capture rate estimated with equation 6.5.6. Finally, let us consider the limits derived from experiments ([Madsen, 1988](#); [Adriani et al., 2015, 2017](#)). Assuming again a speed of the strangelets close to the one of the galactic halo,

i.e.  $v_s \sim 250$  km/s, the total flux in the galaxy is:

$$dj_s/d\Omega = v_s N_{\text{tot}}^{\text{gal}} / (4\pi V_{\text{gal}}) \sim 1.4 \times 10^{-30} \text{cm}^{-2} \text{s}^{-1} \text{sr}^{-1}, \quad (6.5.7)$$

meaning smaller of  $\sim 18$  orders of magnitude with respect to the limit imposed by experiments. This outcome is caused by the fact that we have not assumed, in our estimate, a density of strangelets such as  $\delta(A - \bar{A})/A$  as usually done, but we have taken into account an explicit model both for the fragmentation and the evaporation process. In conclusion, the results we found indicate that both a direct detection of strangelets, through experiments, and an indirect one, through their effect on the stellar evolution, are extremely unlikely. Last but not the least, the possibility to have at least a part of dark matter made of strangelets generated at the baryogenesis time and having  $A \sim 10^{46}$  (Witten, 1984; Burdin et al., 2015; Jacobs et al., 2015) cannot be excluded: the existence of cosmological strangelets would probably suggest the existence of QSs, but we have demonstrated that the existence of the latter is not ruled out by the present data on the strangelets abundance.

# Bayesian analysis of RMF models

This chapter is dedicated to the description of our work in [Traversi et al. \(2020\)](#) where we performed a Bayesian analysis to infer the EOS of NS described through a RMF model, using astrophysical measurements (© AAS. Reproduced with permission). The formalism adopted in our study is described in the following.

## 7.1 Bayes theorem and sampling methods

The Bayesian inference is a method of statistical inference in which the probability for a hypothesis is updated through the Bayes theorem.

First of all, the inference is defined as the process of deducing from one statement considered as true, another whose truth is believed to be a consequence of the former. In particular, a statistical inference quantifies via probabilities the strength of inductive inferences from data (D) and models to hypotheses concerning the phenomena that produce the data.

The Bayesian recipe evaluates hypotheses through their probabilities  $p(H_i|\dots)$  conditional on given information using the rules of probability theory:

- product rule:

$$p(A, B|I) = p(A|I)P(B|A, I) = p(B|I)p(A|B, I) \quad (7.1.1)$$

where  $P(A, B|I)$  is the probability for both the propositions A and B being true assuming that I is true.

- sum rule:

$$p(A + B|I) = p(A|I) + p(B|I) - p(A, B|I) \quad (7.1.2)$$

where  $p(A + B|I)$  is the probability that either proposition A or B is true assuming

that I is true.

- normalization:

$$p(A|I) + p(\bar{A}|I) = 1 \tag{7.1.3}$$

where  $\bar{A}$  represents the proposition that A is false.

The Bayes theorem is directly derived from the product rule:

$$p(A|B, I) = \frac{p(B|A, I)p(A|I)}{p(B|I)} \tag{7.1.4}$$

Replacing A and B by hypothesis (H) and data (D), one finally gets:

$$p(H|D, I) = \frac{p(D|H, I)p(H|I)}{p(D|I)} \tag{7.1.5}$$

The Bayes theorem relates the probability that the hypothesis is true given the data to the probability that one would observe the measured data if the hypothesis is true. Explicitly, the terms in equation 7.1.5 are:

- the prior probability,  $p(H|I)$ . It represents the knowledge about the hypothesis before analyzing the current data.
- the likelihood function  $p(D|H, I)$ , is the probability of observing  $D$  given  $H$ . As a function of D with H fixed, it specifies the compatibility of the data with the given hypothesis.
- The denominator  $p(D|I)$  is the so called evidence. It is independent from the hypothesis and can be considered as a normalization constant.
- The left hand side is the posterior probability,  $p(H|D, I)$ , and it is a function of  $H$ . It represents the knowledge about the truth of the hypothesis updated using the data.

The presence of the prior turns out to be very useful in the cases where multiple types of measurements are combined to constrain a model, because it allows the inclusion of additional information into the computation. However, the choice of the prior is sometimes controversial and can hide subtleties. One of the most commonly used recipe is a non-informative prior, such as the flat or the uniform prior.

Despite the simple formulation of the theorem, applying the Bayesian approach is not always straightforward. In case of a one parameter model, i.e.  $H \equiv \theta$  it is sufficient to calculate the distribution  $p(\theta|D, I)$  as a function of  $\theta$ . However, as the dimension of the problem grows,  $\boldsymbol{\theta} = [\theta_1, \theta_2, \dots, \theta_n]$ , this direct method becomes increasingly complex. For this reason, the Bayesian approaches often depend on sampling methods which allow to generate

a chain of points which resembles the posterior distribution function (PDF), i.e. to obtain a set of  $X$  values  $\{X(1), X(2), X(3), \dots\}$  that follow this distribution. This statement means that the probability to obtain a particular  $X(i)$  is equivalent to  $p(X(i))$  and the histogram drawn from the set of  $X(i)$ s, apart from a scaling factor, looks like  $p(X)$ .

The commonly used method is called Markov chain Monte Carlo (MCMC). The simplest and most widely adopted MCMC algorithm is the Metropolis–Hastings (M–H) method (Mackay, 2003; Gregory, 2005; Press et al., 2007; Hogg et al., 2010). The iterative procedure is the following (Foreman-Mackey et al., 2013):

1. Given a position  $X(t)$ , a proposal new value  $Y$  is sampled from the so called transition distribution  $Q(Y; X(t))$ , which is usually an easy function of  $Y$  given an  $X(t)$ . A common choice for  $Q(Y; X(t))$  is a multivariate Gaussian distribution centered on the current  $X(t)$ .
2. This proposal is then accepted with a probability:

$$\min \left( 1, \frac{p(Y|D) Q(X(t); Y)}{p(X(t)|D) Q(Y; X(t))} \right) \quad (7.1.6)$$

In this case  $X(t+1) = Y$  ; on the contrary, if the proposal is rejected, the new value is set to the previous one  $X(t+1) = X(t)$ , which is thus repeated in the chain.

After a sufficiently high number of iterations, the M–H algorithm converges to a stationary chain of samples from the distribution. The convergence rate can be estimated through the autocorrelation time: this quantity represents the number of steps required to the MCMC process in order to draw two subsequent independent samples. The shorter the autocorrelation time, the more efficient is the chain. The values of the set selected before the sampling has equilibrated are called the "burn-in" and must be rejected.

In our Bayesian analysis, we used the `emcee` package (Foreman-Mackey et al. (2013), [emcee.readthedocs.io/en/v3.0.2/](http://emcee.readthedocs.io/en/v3.0.2/)), that employs the sampling algorithm called the "stretch move", firstly proposed by Goodman & Weare (2010). This method relevantly enhances the performance of the MCMC with respect to the standard M-H algorithm.

This "stretch move" approach simultaneously evolves an ensemble of  $K$  walkers  $S = \{X_k\}$ : the proposal distribution for a walker  $k$  is calculated from the current positions of the remaining  $K - 1$  walkers in the complementary ensemble  $S_{[k]} = \{X_j; \forall j \neq k\}$ . In particular, a walker  $X_j$  is selected randomly from  $S_{[k]}$  and the proposal to update  $X_k$  becomes:

$$X_k(t) \rightarrow Y = X_j + Z[X_k(t) - X_j] \quad (7.1.7)$$

Here  $Z$  is a random variable coming from a distribution  $g(Z = z)$  and equation 7.1.7 is symmetric if

$$g(z^{-1}) = zg(z) \quad (7.1.8)$$

If this condition is fulfilled, in order to satisfy the detailed balance, the acceptance probability is set to:

$$q = \min 1, Z^{N-1} \frac{p(Y)}{p(X_k(t))} \quad (7.1.9)$$

$N$  being the dimension of the parameter space. The same procedure is applied to each walker in the ensemble.

The form of  $g(z)$  suggested by [Goodman & Weare \(2010\)](#) is:

$$g(z) \propto \begin{cases} \frac{1}{\sqrt{z}}, & \text{if } z \in \left[\frac{1}{a}, a\right] \\ 0, & \text{otherwise} \end{cases} \quad (7.1.10)$$

with  $a = 2$ .

For further technical details the reader is referred to [Foreman-Mackey et al. \(2013\)](#) while for a complete review on MCMC to [Hogg & Foreman-Mackey \(2018\)](#).

## 7.2 Model selection

In the previous paragraph, the Bayesian inference was described in relation with the problem of parameter estimation given a defined model. However, there exists cases when there is uncertainty on which one among a set of alternative models better describes the data. This issue is usually called model selection or model comparison problem.

A naive approach to choose between the proposed alternatives could be based of how good their fit are to the data. However, this approach would always prefer the model with the larger number of parameters which lacks of any predictive power (the so called "overfitting" problem). To correctly estimate the relative merit of the possible theories, one can rely on different criteria: among these the most used is the Bayes Factor (BF). As an example, let us suppose to have two models, A and B, with adjustable parameters  $\theta$  and  $\lambda$  ([Sivia, 2006](#)). In order to understand which of the model is more suitable for the data, one needs to calculate the posterior probabilities for A and B being correct and evaluate their ratio:

$$posterior\ ratio = \frac{p(A|D, I)}{p(B|D, I)} \quad (7.2.1)$$

If this is significantly greater than one, then A's theory is preferred while if it is significantly less than one, then B's model is selected; finally if it is  $\sim 1$ , then there is no evidence from the current data to prefer a model over the competitor.

Applying the Bayes theorem to both the numerator and the denominator, equation [7.2.1](#)

becomes

$$\frac{p(A|D, I)}{p(B|D, I)} = \frac{p(D|A, I)}{p(D|B, I)} \cdot \frac{p(A|I)}{p(B|I)} \quad (7.2.2)$$

because the term  $p(D|I)$  do not depend on the model and thus cancels out. As in the parameter estimation problems, the answer to the model selection question is also function of the probability that one assigns a priori to each model. The common choice consists in taking the ratio of the prior terms in equation 7.2.2, to be equal to one:

$$BF_{AB} = \frac{p(D|A, I)}{p(D|B, I)} \quad (7.2.3)$$

This equation defines the Bayes factor (BF), which represents a measure of the strength of evidence in favor of one between two competing theories.

To calculate  $p(D|A, I)$  and  $p(D|B, I)$ , one can exploit the marginalization and product rule to write these probabilities in terms of other PDFs which might be easier to calculate. In particular, for  $p(D|B, I)$  (and the same for A):

$$p(D|B, I) = \int p(D, \lambda|B, I)d\lambda = \int p(D|\lambda, B, I)p(\lambda|B, I)d\lambda \quad (7.2.4)$$

The term  $p(D|\lambda, B, I)$  is the likelihood for a given  $\lambda$  while  $p(\lambda|B, I)$  is the prior for  $\lambda$  in the model B.

Moreover, one can compare the model selection formulation with parameter estimation. Assuming the correctness of B's theory, the Bayes theorem allows to infer  $\lambda$  given the data:

$$p(\lambda|D, B, I) = \frac{p(D|\lambda, B, I)p(\lambda|B, I)}{p(D|B, I)} \quad (7.2.5)$$

Thus, from the definition of the BF one understands that the usually neglected evidence plays a crucial role in discovering the merit of B's model relative to an alternative one.

In a first approximation, the parameter estimation consists in locating the point corresponding to the maximum of the likelihood function whereas the model selection requires the evaluation of its average value. This is the main advantage of the model selection based on the BF with respect to the simple "better fit" criterion: in a model with a lot of parameters, many likelihoods gain from a more precise agreement with the data but their contribution is averaged over a larger parameter space.

Unfortunately, often the explicit calculation of the evidence is a complex task. An alternative method for the model selection problems (but in this case based of the maximum likelihood) relies on the Bayesian Information criterion (BIC):

$$\text{BIC} = k \ln(n) - 2 \ln(L_{max}) \quad (7.2.6)$$

where  $k$  is the number of parameters,  $n$  the number of observations and  $L_{max}$  the peak in the likelihood function. The favoured model is the one with the lower BIC and the evidence is relevant if  $\Delta\text{BIC} \gtrsim 2$ .

### 7.3 Previous works

The formalism described in section 7.1 and 7.2 can be adopted to infer the EOS starting from the knowledge provided by laboratory experiments and astrophysical measurements. Following Steiner et al. (2010), Özel et al. (2016) and Raithel et al. (2017), one can write the probability for a model of the EOS given the available data as:

$$p(\text{EOS}|\text{data}) = p(\theta_1, \theta_2, \dots, \theta_n|\text{data}) \quad (7.3.1)$$

where  $\{\theta_1, \theta_2, \dots, \theta_n\}$  is the set of parameter which describes the EOS.

Using the Bayes theorem, one obtains:

$$p(\theta_1, \theta_2, \dots, \theta_n|\text{data}) = C \cdot p(\text{data}|\theta_1, \theta_2, \dots, \theta_n) \cdot p(\theta_1, \theta_2, \dots, \theta_n) \quad (7.3.2)$$

where  $p(\theta_1, \theta_2, \dots, \theta_n)$  is the prior,  $C$  is a normalization constant and  $p(\text{data}|\theta_1, \theta_2, \dots, \theta_n)$  is the probability to obtain the data given a set of EOS parameters. If we consider astrophysical sources, the latter can be expressed explicitly as:

$$p(\text{data}|\theta_1, \theta_2, \dots, \theta_n) = \prod_{i=1}^N p(M_i, R_i|\theta_1, \theta_2, \dots, \theta_n) \quad (7.3.3)$$

where  $(M_i, R_i)$  are the masses and radii (PDFs) of the  $N$  sources (for further details see Özel et al. (2016); Raithel et al. (2017) or in section 7.5.2).

In the light of the above, it is clear that the EOS has to be conveniently parametrized: the most widely employed method consists in matching the low density EOS (considered as known) with the high density EOS expressed through a piecewise polytropic function. In this case the parameters are the adiabatic indices and the density at which the two EOS connect.

The optimal number of pieces and the matching densities that lead to the smallest uncertainties in reproducing the theoretical EOSs, were studied in detail by Read et al. (2009) and Özel & Psaltis (2009). They found that three piecewise polynomials connecting at pressures of 1.85 ( $P_1$ ), 3.7 ( $P_2$ ), and 7.4  $\rho_{sat}$  ( $P_3$ ) represent the most suitable choice. These pressures are constrained by some theoretical conditions. First of all,  $P_3 \geq P_2 \geq P_1 \geq P(\rho_0)$  for the microscopically stability, second  $c_s^2 = \frac{\partial p}{\partial e} \leq c^2$  for causality, and finally the EOS maximum mass must exceed the observational limit. Moreover, the knowledge from laboratory experi-

ments can translate into constraints on  $P_1$ .

Steiner et al. (2013b) and Özel et al. (2016) discussed the sensitivity of the Bayesian analysis on these conditions and on the choice of the priors.

Using the piecewise polytropic parametrization, Steiner et al. (2010, 2013b) and Özel et al. (2016), exploited the data from the observations of thermonuclear bursts and/or LMXBs in quiescence to constraint the EOS. All these works predicted a rather soft EOS, with radii  $R_{1.4} \sim 11 - 12$  km. Recently, with the same method, Jiang et al. (2020) analyzed the data on GW170817, PSR J0030+0451 (NICER) and some nuclear experiments, and obtained  $\Lambda_{1.4} = 390^{+320}_{-140}$ , radius  $R_{1.4} = 12.2^{+1.0}_{-0.9}$  km. In addition, Steiner et al. (2018), employing a piecewise linear parameterization (Steiner et al., 2013b, 2015), found a preference for EOS with a strong phase transition (see also Alvarez-Castillo et al. (2016); Blaschke et al. (2020)). In recent years, the study on the optimal "set up" of the piecewise polytropic parametrization for reproducing the observable properties of NSs for a different set of EOS was revisited by Raithel et al. (2016, 2017): they indicated five segments with matching densities at 1, 1.4, 2.2, 3.3, 4.9, and 7.4  $\rho_0$ .

A similar scheme consisting in characterizing the EOS through the values of the speed of sound at different densities, was introduced by Capano et al. (2020): they constrained the EOS through chiral effective field theory and the data from the multimessenger observations of GW170817 and they obtained  $R_{1.4} = 11.0^{+0.9}_{-0.6}$  km (90% CI).

A comparison between a speed of sound parameterization and the piecewise polytropic one is provided in Greif et al. (2019).

Another possibility is the so called spectral representation of the EOS (Lindblom, 2010; Fasano et al., 2019), i.e. a series expansion of the adiabatic index  $\Gamma(p)$  of the form:

$$\Gamma(p) \simeq \exp \left\{ \sum_{k=0}^3 \gamma_k \left[ \log \left( \frac{p}{p_0} \right) \right]^k \right\} \quad (7.3.4)$$

where  $p_0$  is the pressure at the crust-core interface and  $(\gamma_0, \gamma_1, \gamma_2, \gamma_3)$  are free parameters of the model.

Lately, Margueron et al. (2018a,b) proposed a different approach labelled as "metamodel": he constructed the EOS using Taylor expansions such as equations 2.1.6, 2.1.7 and 2.1.8. This method allows to obtain direct constraints on the saturation properties of nuclear matter and their density dependence. Margueron et al. (2018a) analyzed these properties both through a direct study of the experimental data and through a complementary analysis of the predictions from a set of relativistic and non-relativistic theoretical models. In addition, Margueron et al. (2018b), employing the metamodeling parameterization and considering the present knowledge on the empirical parameters, found a rather large radius for NS, which seems therefore to be only marginally compatible with the astrophysical data.

Finally, non-parametric method for the inference of the EOS was introduced by Landry & Essick (2019); Essick et al. (2020): instead of selecting a priori a functional form for  $e(p)$ ,

they used Gaussian process regression (GPR) to generate a large set of possible realizations of the EOS. Using the data from GW observations, they obtained small tidal deformabilities and radii in the case of an "agnostic" prior, while they found larger values when they imposed an "informed" prior, which has to resemble a set of theoretical EOSs.

## 7.4 *Extended abstract*

We perform a Bayesian analysis to constrain the EOS of NS combining the knowledge about nuclear matter at saturation and the data from 15 astrophysical sources: the thermonuclear bursters and the qLMXBs of Özel et al. (2016) and Nättilä et al. (2017), the recent measurement in Riley et al. (2019), (see section 2.3.2) and the gravitational wave event GW170817 (Abbott et al. (2018), see chapter 4).

Differently from the works described in the previous paragraph, we build the EOS by using a RMF model. In particular we employ the non-linear Walecka model discussed in sections 3.1.1 and 3.1.2. The advantages of this choice are several: first RMFT allow to model the EOS within a wide range of densities, temperatures, and chemical compositions; second, the inclusion of new degrees of freedom, such as hyperons, is relatively easy; last, it allows to directly include in the analysis the constraints on the saturation properties of nuclear matter coming from laboratory experiments. Indeed, the Lagrangian of the model has five parameters, which are the coupling constants  $\frac{g_\sigma}{\sigma}$ ,  $\frac{g_\omega}{\omega}$ ,  $\frac{g_\rho}{\rho}$ ,  $b$ , and  $c$  associated to the mesons interaction terms. As discussed in section 3.1.2, these parameters are linked through algebraic relations to the saturation density  $n_0$ , the binding energy  $B$ , the incompressibility  $K$ , the effective mass  $m^*$  and the symmetry energy  $S$  at saturation. Therefore the latter are the free parameters in our Bayesian inference. We explore different priors, both concerning the types, i.e. uniform and Gaussian, and the ranges of the parameters. In particular, we distinguish among two classes: the informed priors, namely the *baseline* (Lattimer & Lim, 2013), the *Marg\_unif* and *Marg\_gauss* (Margueron et al., 2018a), which take into account the constraints from laboratory experiments and the agnostic priors, *Wide\_unif* and *Wide\_gauss*, where the parameters can span over a larger ranges.

Finally, we extend our model to investigate the effect of including  $\Lambda$  hyperons with fixed coupling constants for the *baseline* and the *Wide\_unif* priors.

Following the approach described in section 7.3, we perform a Bayesian analysis and find the joint PDFs for the nuclear empirical parameters. From the most probable value and the 68% CI of this multidimensional posterior we deduce the preferred range for the NS radii and the maximum mass.

In addition, a posteriori we calculate the slope of the symmetry energy  $L$  and the RMF coupling constants. Finally, through the evaluation of the BIC and the Bayes Factor, we provide a quantitative comparison among the model to infer the most suitable one to describe

the data.

We found that the constraints on the parameter range imposed by nuclear physics prevent the NS radius  $R_{1.4}$  to reach values below  $\sim 12.5$  km. This evidence, strengthened by the fact that, in many cases, the most probable  $M - R$  curve for a certain model sits on the edge of the 68% CI, suggests a tension between the nuclear theory and the astrophysical measurements. For this reason, the preferred prior is the agnostic *Wide\_unif*: the resulting EOS is characterized not only by a smaller radius  $R_{1.4} \sim 12$  km, but also by a strong reduction of the effective mass at densities  $\sim 2 - 3n_0$ . This feature can be interpreted as a signal of a phase transition to a chiral symmetry restored phase.

Finally, when  $\Lambda$ s enter in the model, the radius becomes  $\sim 14$  km, showing how this simple model is unable to consistently reproduce the astrophysical data.

## ***7.5 Bayesian inference of dense matter EOS within RMF models using astrophysical measurements***

In this work, we propose a new scheme for a Bayesian inference of the EOS based on RMF models, in which the exchange of scalar and vector mesons mediates the interactions between baryons (see chapter 3.1). This class of models, that extends the original Walecka model (see 3.1.1), has been widely adopted to calculate the properties of finite nuclei and to model the EOS within a large range of temperatures, densities and chemical compositions. Indeed, these type of EOSs, such as, for example, the TM1 models (Shen et al., 1998), the BHB $\Lambda\phi$  (Banik et al., 2014) and the SFHo (Steiner et al., 2013a) (section 3.1.3), have been employed both in supernova and merger simulations. Moreover, these models have many advantages: first, they can encode the constraints from finite nuclei and symmetry energy, second, they can easily include other baryons such as hyperons and finally one can investigate also the chemical composition and its impact on the cooling. Specifically, the available information coming from the experimental data on hypernuclei can be included in the EOS. Moreover, this class of models has also been tested recently with the GW data (Malik et al., 2018; Nandi et al., 2019; Lourenço et al., 2019). A further aspect regards phase transitions: if the nucleon effective mass is used as an order parameter, the mean field equation for the  $\sigma$  field, being non-linear, can reveal the occurrence of a phase transition. As we will discuss later, a fast drop of the effective mass, represented as a function of the baryon density, can be interpreted as a clue for a partial restoration of chiral symmetry and therefore a probable phase transition to quark matter. In addition, once the EOS has been constrained through NS observations at zero temperature, it can be extended to finite temperatures and tested also for investigations concerning transient phenomena such as supernova and merger events. For what regards the astrophysical data, in our Bayesian analysis we exploit a larger data set

with respect to previous studies. In particular, we have used the data for the five qLMXBs and the six thermonuclear bursters from [Özel et al. \(2016\)](#), one X-ray source from [Nättilä et al. \(2017\)](#), the recent observations of PSR J0030+0451 from the NICER collaboration (see chapter [2.3.2](#)) and both the components of GW170817 ([Abbott et al., 2018](#)) (see chapter [4.2.3](#)).

### 7.5.1 Equation of State

The class of RMF models we employ in this work is the non-linear Walecka model firstly proposed by [Boguta & Bodmer \(1977\)](#) and [Glendenning & Moszkowski \(1991\)](#). This contains a third and a fourth order self-interaction terms for the scalar field  $\sigma$ , which have been included in the Walecka model with the aim of keeping the values of the incompressibility and of the effective mass at the saturation density under control ([Boguta & Bodmer, 1977](#)) (for further details see section [3.1.2](#)). The Lagrangian of our model is written as:

$$\begin{aligned} \mathcal{L}_B = & \sum_B \bar{\Psi}_B (i\gamma_\mu \partial^\mu - m_B + g_\sigma B \sigma - g_\omega B \gamma_\mu \omega^\mu - g_\rho B \gamma_\mu \boldsymbol{\tau} \cdot \boldsymbol{\rho}^\mu) \Psi_B \\ & + \frac{1}{2} \left( \partial_\mu \sigma \partial^\mu \sigma - m_\sigma^2 \sigma^2 \right) - \frac{1}{3} b m_n (g_\sigma \sigma)^3 - \frac{1}{4} c (g_\sigma \sigma)^4 \\ & - \frac{1}{4} \omega_{\mu\nu} \omega^{\mu\nu} + \frac{1}{2} m_\omega^2 \omega_\mu \omega^\mu - \frac{1}{4} \boldsymbol{\rho}_{\mu\nu} \cdot \boldsymbol{\rho}^{\mu\nu} - \frac{1}{2} m_\rho^2 \boldsymbol{\rho}_\mu \cdot \boldsymbol{\rho}^\mu, \end{aligned} \quad (7.5.1)$$

where, the  $\sigma$ ,  $\omega$  and  $\rho$  are the scalar, vector and vector-isovector mesons respectively. The Lagrangian is characterized by five unknown parameters:  $g_\sigma/m_\sigma$ ,  $g_\omega/m_\omega$ ,  $g_\rho/m_\rho$ ,  $b$ ,  $c$ . These variables are connected through algebraic relations to five saturation properties of symmetric nuclear matter: the saturation density ( $n_0$ ), the binding energy per nucleon ( $E_0$ ), the incompressibility ( $K$ ), the effective mass of nucleon ( $m^*$ ) and the symmetry energy ( $S$ ) ([Glendenning, 1997](#)). Therefore, we can actually parametrize our EOS by means of the aforementioned empirical parameters from nuclear physics. The mean field equations and the expressions for the thermodynamical quantities are described in chapter [3.1.1](#) and [3.1.2](#) or in the reference [Glendenning \(1997\)](#). The EOS can be easily extended to include new degrees of freedom such as hyperons (see section [3.2.1](#)). Here, we take into account only the  $\Lambda$  hyperon with a fixed value of  $-28$  MeV for the potential depth ([Glendenning & Moszkowski, 1991](#)) as it is deduced from experiments. The SU(3) symmetry allows to set the value of the coupling with the  $\omega$  meson to  $2/3g_\omega/m_\omega$  ([Weissenborn et al., 2012a](#)) while the coupling with the  $\sigma$  meson can be directly calculated from the potential depth. In our analysis, in the case including hyperons, we keep these parameters fixed as in [Weissenborn et al. \(2012a\)](#), the aim being just to check the effects on the PDF of switching on the  $\Lambda$ 's. The main drawback of our model is that it is not possible to include other saturation

properties like the slope of the symmetry energy  $L$  or higher order derivatives (such as the curvature  $K_{\text{sym}}$  and the skewness  $J_{\text{sym}}$ ) which are proven to be important in Xie & Li (2019) in the range of density up to  $2.5n_0$ . Specifically, within our parametrization  $L$  is derived directly from  $S$  and thus it is highly correlated with it. We say in advance that some of our results will be characterized by a value for  $L$  larger than the typical one found in the literature i.e.  $40 \text{ MeV} \lesssim L \lesssim 60 \text{ MeV}$ , (see Xie & Li (2019), Lattimer & Lim (2013) and chapter 2.2 for details). The limit on the tidal deformability from GW170817 also seems to point towards even smaller values, corresponding to a range of  $L$  going down to 9 MeV (Raithel & Özel, 2019) thus suggesting a relevant tension with the laboratory data on neutron skin thickness (see Fattoyev et al. (2018) and section 2.2.3 for a discussion). In principle, to incorporate the aforementioned quantities one should introduce other interaction terms (such as meson mixing terms as in Steiner et al. (2013a)) or, following Typel & Wolter (1999), density dependent couplings (see section 3.1.2). However, the price in this case would be to lose the direct algebraic expressions which link the parameters of the model to the saturation properties. Another complication comes from the sign of the quartic coupling  $c$ . In many accepted parametrizations  $c$  is negative and therefore leading to the result of the energy unbounded from below when the  $\sigma$  field is large. Concerning this problem, a common point of view is to treat the model as an effective model that cannot be extrapolated to arbitrarily high densities and to verify that the EOS is well-behaved (checking for example the absence of mechanical and chemical instabilities and the causality limit) in the density regime of NS.

### 7.5.2 Bayesian Analysis

Our analysis is based on the Bayes theorem in equation 7.1.5 and described in section 7.1. We mainly follow the methodology developed by Steiner et al. (2010); Özel et al. (2016); Raithel et al. (2017) discussed in chapter 7.3.

In our work, the empirical parameters,  $\{m^*, K, n_0, S, E_0\}$  constitute the parameter set  $\theta$ . In order to evaluate the posterior  $P(\theta)$  by making use of the mass-radius PDFs  $P_i(M, R)$  for the  $N = 15$  sources employed in our analysis (see section 2.3.2), we exploit the relation:

$$P(m^*, K, n_0, S, E_0 | \text{data}) = CP(\text{data} | m^*, K, n_0, S, E_0) \times P(m^*)P(K)P(n_0)P(S)P(E_0), \quad (7.5.2)$$

where  $C$  is a normalization constant;  $P(m^*)$ ,  $P(K)$ ,  $P(n_0)$ ,  $P(S)$ , and  $P(E_0)$  are the priors for the empirical parameters and

$$P(\text{data} | m^*, K, n_0, S, E_0) = \prod_{i=1}^N P_i(M_i, R_i | m^*, K, n_0, S, E_0), \quad (7.5.3)$$

is the likelihood function, expressing the probability to generate  $N$  mass-radius observations provided a particular set of empirical parameters. To calculate the probability that a given EOS leads to the realization of  $(M, R)$  for a particular source, we use the procedure described in Raithel et al. (2017). We select a set of parameters and evaluate the couplings through the algebraic relations. At this point, we can solve the mean field equations to build the EOS. The latter is then used to solve the TOV equations and draw a mass-radius curve up to the maximum mass, the last stable point on the curve. The next step consists in computing the likelihood for each configuration belonging to the curve through a comparison with the M-R distribution of each source. Finally, the maximum probability found for the configurations is assigned to the parameter set as,

$$P_i(M_i, R_i | m^*, K, n_0, S, E_0) = P_{\max}(M_i, R_i | m^*, K, n_0, S, E_0, \rho_c), \quad (7.5.4)$$

Here, for a given EOS, the mass-radius curve is parametrized by the central density ( $\rho_c$ ) of the NS. We perform Markov-Chain Monte Carlo (MCMC) simulations in order to populate the PDF of equation 7.5.2. For that we exploit the python emcee package which makes use of a stretch-move algorithm (Foreman-Mackey et al., 2013) (see chapter 7.1). Finally, with the aim of comparing between different models, we calculate the evidence by performing a Monte Carlo integration over the posterior. In addition, we also evaluate the BIC using the standard definition:  $\text{BIC} \equiv -2 \ln \mathcal{L}_{\max} + k \ln N$ , where  $k$  the number of parameters,  $N$  the number of data points and  $\mathcal{L}_{\max}$  is the maximum likelihood (see section 7.2).

### 7.5.3 Conditions on the priors

The choice of priors is of fundamental importance to interpret the experimental data within the domain of a model. Indeed, the shape of the posteriors can be altered by eventual ambiguities in the priors and, as a consequence, also the predictions of the model would be modified (Steiner et al., 2016). Thus, we study the effects of choosing priors which differs both for the type and the ranges of the parameters. These priors basically contains our assumptions for the model. Therefore, they can be regarded as individual models by themselves and they can be quantitatively compared by computing the BF between every pair of them. We classify our priors into two different categories: informed and agnostic. The first class of priors are based on the available constraints on the nuclear empirical parameters derived from laboratory experiments (see section 2.2). In the case of agnostic priors, those constraints are relaxed and thus the parameters are allowed to be determined predominantly through the requirements of the astrophysical observations. Concerning the type, we use both Gaussian and uniform priors in order to check their effects on the posterior. In particular, we employ five different priors based on many different studies found in literature, such as Lattimer & Lim (2013); Dutra et al. (2014); Oertel et al. (2017); Margueron et al. (2018a).

**Baseline** The prior ranges follows the data from laboratory experiments. The ranges of  $m^*$  and  $K$  are taken from [Glendenning \(1997\)](#) while  $S$  from [Lattimer & Lim \(2013\)](#). In addition, we selected a sensible interval for both  $n_0$  and  $E_0$ .

**Marg\_unif** This uniform prior is based on Table 11 of [Margueron et al. \(2018a\)](#) concerning the RMF models: the boundary of each range is fixed by the minimum and maximum value of the corresponding parameter. The models listed in the reference table were selected among a wider class of RMF models because they are able to provide sensible results for several nuclear properties.

**Marg\_Gauss** We take the mean and standard deviation of the empirical parameters from the aforementioned table of [Margueron et al. \(2018a\)](#) and create a Gaussian prior.

**Wide\_unif** This uniform prior is built using the maximum and minimum values of the parameters among the type 2 EOSs of Table VII of [Dutra et al. \(2014\)](#). We take into account only the type 2 EOSs because those are associated to the RMF model having the same scalar self-interactions of our Lagrangian. We underline that not all the models listed in this table are consistent with modern nuclear physics constraints, in particular for what concerns the symmetry energy.

**Wide\_Gauss** This prior is based again on the type 2 EOSs of Table VII of [Dutra et al. \(2014\)](#), but in this case we parametrize the uncertainties through Gaussian distributions. The resulting standard deviations are larger with respect to the Marg\_Gauss prior.

The ranges of the empirical parameters for the aforementioned priors are summarized in Table 7.1.

Priors	Range	$m^*$	$K$ (MeV)	$n_0$ ( $fm^{-3}$ )	$S$ (MeV)	$B/A$ (MeV)
Baseline	Min	0.7	200	0.14	28	-16.5
	Max	0.8	300	0.16	35	-16.0
Marg_unif	Min	0.64	219	0.145	31.19	-16.35
	Max	0.71	355	0.153	38.71	-16.12
Marg_Gauss	Mean	0.67	268	0.1494	35.11	-16.24
	$\sigma$	0.02	34	0.0025	2.63	0.06
Wide_unif	Min	0.55	172.23	0.145	17.38	-17.03
	Max	0.8	421.02	0.173	50.0	-13.78
Wide_Gauss	Mean	0.708	245.29	0.152	34.11	-16.17
	$\sigma$	0.079	39.30	0.004	4.42	0.36

**Table 7.1:** List of the priors that we employ in this work.

In addition, we accept only EOS fulfilling the following physical constraints and observational requirements:

1. mechanical stability.

2. causality for the range of densities typical of NS.
3. Consistency with observations for what concerns the maximum mass, which must therefore exceed  $2M_{\odot}$ , as in [Güven et al. \(2020\)](#).

### 7.5.4 Observational Data

In this section, we shortly describe the 15 sources employed in our analysis. In [Özel et al. \(2016\)](#), we find the data concerning two different types of sources, the thermonuclear bursters and the qLMXBs. <sup>1</sup> The thermonuclear bursters are 4U 1820–30, SAX J1748.9–2021, EXO 1745–248, KS 1731–260, 4U 1724–207, and 4U 1608–52. The mass-radius PDFs for these sources are estimated through their apparent angular sizes, distances and touchdown fluxes. The qLMXBs that we use here are M13, M30, NGC 6304, NGC 6397, and  $\omega$  Cen. When they are in quiescence, the heat, that was accumulated in the crusts of the NS during accretion, is radiated and crosses a light element atmosphere. The mass-radius PDFs for the qLMXBs are calculated with a spectral analysis of the thermal emission.

Another useful observable is the X-ray burst cooling tail spectra, exploited by [Nättilä et al. \(2017\)](#) to derive the mass  $M = 1.9 \pm 0.3 M_{\odot}$  and the radius  $R = 12.4 \pm 0.4$  km of 4U 1702–429 (for details see chapter 2.3.2). In addition, recently the NICER collaboration has estimated the mass and radius of the millisecond pulsar PSR J0030+0451 through pulse profile modelling: they found  $M = 1.34^{+0.15}_{-0.16} M_{\odot}$ ,  $R = 12.71^{+1.14}_{-1.19}$  km ([Riley et al., 2019](#)) (for details see chapter 2.3.2). As suggested in [Jiang et al. \(2020\)](#), to mimic the mass-radius posteriors of 4U 1702–429 and PSR J0030+0451, we make use of a bivariate Gaussian distribution:

$$P(M, R) = \frac{1}{2\pi\sigma_M\sigma_R\sqrt{1-\rho^2}} \exp\left\{-\frac{1}{2(1-\rho^2)}\left[\frac{(M-\mu_M)^2}{\sigma_M^2} - 2\rho\frac{(M-\mu_M)(R-\mu_R)}{\sigma_M\sigma_R} + \frac{(R-\mu_R)^2}{\sigma_R^2}\right]\right\}, \quad (7.5.5)$$

The values of the means and the standard deviations for PSR J0030+0451 are  $\mu_M = 1.34M_{\odot}$ ,  $\mu_R = 12.71$ km,  $\sigma_M = 0.155M_{\odot}$ ,  $\sigma_R = 1.165$ km. In addition we select  $\rho = 0.9$ , to reproduce the high correlation between mass and radius ([Jiang et al., 2020](#)). In the same way, for 4U 1702–429, we use  $\mu_M = 1.9M_{\odot}$ ,  $\mu_R = 12.4$ km,  $\sigma_M = 0.3M_{\odot}$ ,  $\sigma_R = 0.4$ km, and again  $\rho = 0.9$ .

Finally, we consider the EOS insensitive posterior provided by the LVC for the mass-radius of the two components of GW170817 ([Abbott et al., 2017c, 2018](#)). <sup>2</sup>

---

<sup>1</sup>The M-R PDF of the sources of [Özel et al. \(2016\)](#) are available at <http://xtreme.as.arizona.edu/neutronstars/>.

<sup>2</sup>The data from GW170817 can be found at <https://dcc.ligo.org/LIGO-P1800115/public>.

Models	$m^*$	K (MeV)	$n_0$ (fm $^{-3}$ )	S (MeV)	$E_0$ (MeV)	L (MeV)
Baseline	0.759	204.1	0.160	29.3	-16.32	81.2
Marg_unif	0.710	219.1	0.152	31.3	-16.26	90.9
Marg_Gauss	0.713	163.8	0.150	34.5	-16.23	100.6
Wide_unif	0.760	178.1	0.156	27.0	-16.65	74.7
	0.761	280.2	0.173	19.2	-16.43	49.8
Wide_Gauss	0.760	177.6	0.151	37.6	-16.16	106.9
Wide_unif with $\Lambda$	0.682	319.8	0.170	17.6	-16.72	50.6
Baseline with $\Lambda$	0.704	279.2	0.142	28.7	-16.11	83.2

**Table 7.2:** Most probable empirical parameters from the joint posterior along with the calculated  $L$ . Additionally, for the Wide\_unif the parameters associated to the second mode of the PDF are also listed.

### 7.5.5 Simulation Results

We build the joint five-dimensional PDFs of the empirical parameters  $\{m^*, K, n_0, S, E_0\}$  using the method described above assuming the different priors summarized in Table 7.1 and considering the sources discussed in section 7.5.4. Subsequently, we evaluate, *a posteriori*, the slope of the symmetry energy ( $L$ ) and the PDFs of the RMF coupling constants from the samples of the posterior. In Table 7.2 we list the values of the parameters corresponding to the most probable configurations of the joint PDFs. Here, also the results for the model with hyperons are included, where we employ the baseline and the Wide\_unif priors. Therefore we have seven different analyses for the comparative investigation of the priors and to study the effects of the inclusion of hyperons. A comment concerning the values of  $L$  is required: the most probable values in Table 7.2 are, in several cases, outside the presently accepted range for  $L$  (Xie & Li, 2019; Lattimer & Lim, 2013). The result using the uniform prior is the one characterized by the smallest values of  $L$ , particularly its second mode that has  $L \sim 50$  MeV. As a consequence, we consider the outcomes found within the uniform prior to be more important from a phenomenological point of view. However, concerning the astrophysical observables, such as  $R_{1.4}$ , they are associated not only to  $L$  (Hornick et al., 2018) but also to the higher order terms in the expansion of the symmetry energy, such as  $K_{\text{sym}}$  and  $J_{\text{sym}}$ , which are affected by large uncertainties:  $-400\text{MeV} < K_{\text{sym}} < 100\text{MeV}$  and  $-200\text{MeV} < J_{\text{sym}} < 800$  MeV, (Zhang & Li, 2019), while for updated and tighter limits, see Carson et al. (2019). In the additional material of chapter 7.5.7, we display in Figure 7.5.18 the symmetry energy as a function of the baryon density for the most probable EOSs for each of the priors together with the values of the aforementioned two higher order derivatives. Note that the latter are within the experimental uncertainties.

For the visualization of the one- and two-dimensional projection plots of the posterior samples, we make use of the python corner.py package (Foreman-Mackey, 2016). The

contours in the two-dimensional plots indicate the  $1\sigma$  (39.3%), 68% and 90% confidence intervals (CIs). Then, we show the mass-radius curves which correspond to the samples within 68% CI of the joint 5-dimensional posterior and we highlight the most likely sequences obtained with each of the priors. In Table 7.3 we list the maximum mass and the  $R_{1.4}$  for the most probable EOSs along with the ranges of  $R_{1.4}$  and  $M_{max}$  corresponding to the 68% CI of the joint posterior. Table 7.4 contains the medians of the marginalized distributions of  $R_{1.4}$ . Note that the values for the most likely sequences and the ranges in Table 7.3 are related to the most probable set of empirical parameters and the 68% CI calculated from the joint posterior. These values are not necessarily equal to the ones inferred from distribution of the radii characterizing the EOSs obtained from the posterior samples. Indeed, for example, if several configurations of parameters give equally big radii, the histogram of the radii will be shifted towards larger values. Thus, although those combinations are individually less probable, they lead to a shift of the peak of the distribution of radii away from the value associated to the most likely set.

Finally, we calculate the BIC and the evidence for each model and we compute the BF as the ratio between evidences. These quantities provide a quantitative comparison suggesting the best plausible model among the ones we have considered in this work. The results for the BFs and the  $\Delta$ BICs are reported in Tables 7.5 and 7.6 respectively.

For the sake of clearness the tables contain all the seven cases, but we mainly present and comment on the plots and results for baseline, Wide\_unif, Wide\_Gauss priors and baseline prior with  $\Lambda$ . The results for Marg\_unif, Marg\_Gauss priors and Wide\_unif prior with  $\Lambda$ , together with the RMF coupling constants PDFs are provided in section 7.5.7 as an additional material.

In Figure 7.5.1, we display the marginalized PDFs of the empirical parameters for the baseline prior (the RMF coupling constants corresponding to this PDF are shown in

Models	Baseline	Marg_unif	Marg_Gauss	Wide_unif	Wide_Gauss	Wide_unif with $\Lambda$	Baseline with $\Lambda$
$R_{1.4}$ (Km)	12.58	13.47	12.55	11.70   12.15	12.32	12.80	14.18
$\Delta R_{1.4}$ (Km)	12.48 – 13.30	13.43 – 13.84	11.82 – 13.24	11.16 – 12.78	11.32 – 13.18	12.71 – 13.25	14.13 – 14.24
$M_{max}$ ( $M_{\odot}$ )	2.01	2.29	2.27	2.00   2.00	2.03	2.01	2.00
$\Delta M_{max}$ ( $M_{\odot}$ )	2.00 – 2.24	2.28 – 2.42	2.11 – 2.46	2.00 – 2.39	2.00 – 2.40	2.00 – 2.10	2.00 – 2.03

**Table 7.3:**  $R_{1.4}$  and maximum mass of the most probable configuration of the joint posterior. Ranges of  $R_{1.4}$  and maximum mass corresponding to the samples within 68% CI of the empirical parameters.

Models	Baseline	Marg_unif	Marg_Gauss	Wide_unif	Wide_Gauss	Wide_unif with $\Lambda$	Baseline with $\Lambda$
$R_{1.4}$ (Km)	$12.95^{+0.25}_{-0.20}$	$13.68^{+0.09}_{-0.12}$	$12.56^{+0.37}_{-0.29}$	$12.42^{+0.31}_{-0.33}$	$12.37^{+0.37}_{-0.38}$	$13.00^{+0.22}_{-0.16}$	$14.19^{+0.03}_{-0.03}$

**Table 7.4:** Median of the distribution for  $R_{1.4}$ .

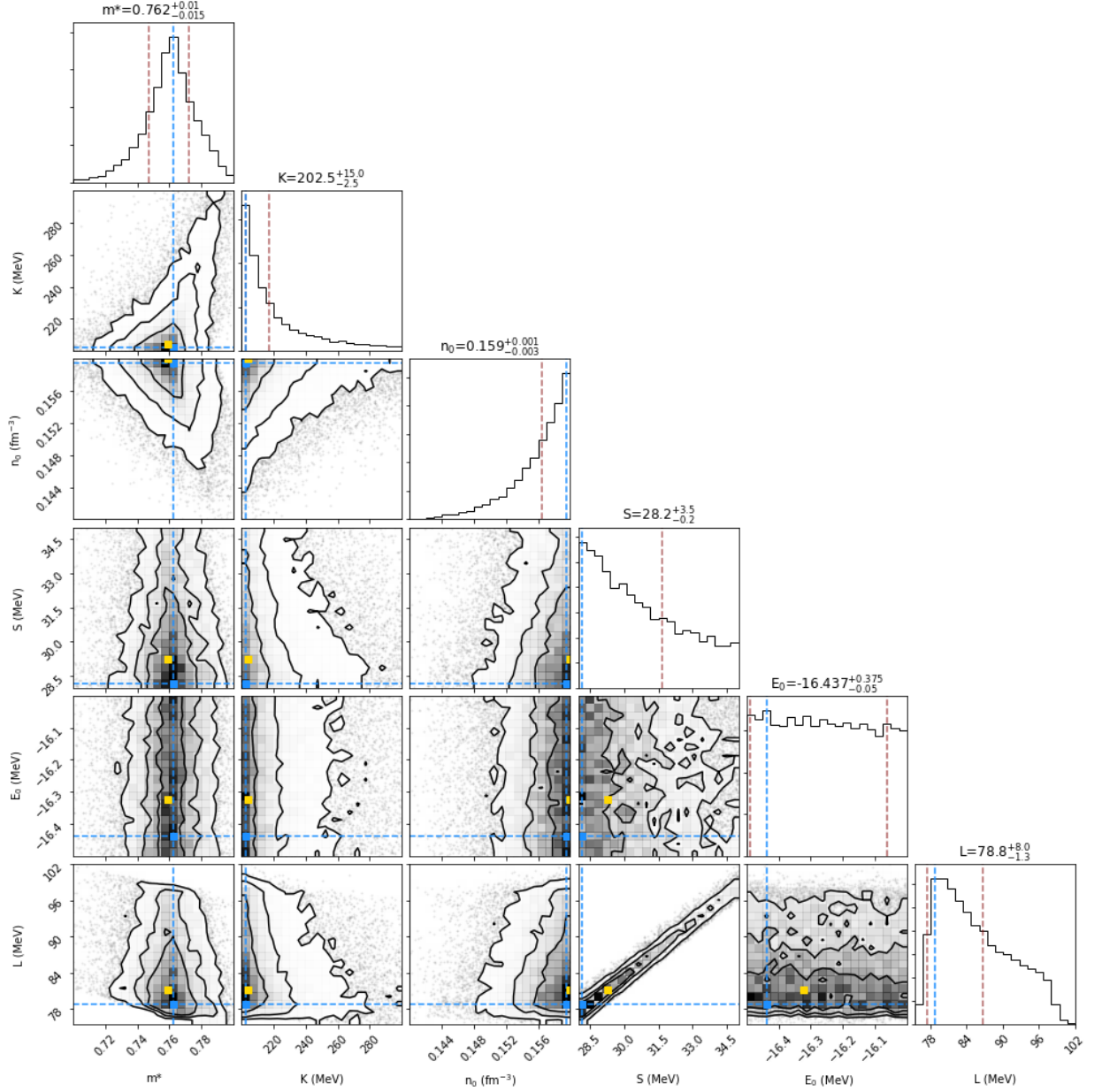


**Figure 7.5.1:** Posterior distributions of the empirical parameters for the baseline prior. In the marginalized one-dimensional plots the blue lines correspond to the mode and the maroon lines the  $1\sigma$  CI. The contours in the two-dimensional PDFs are at  $1\sigma$  (39.3%), 68% and 90% CI respectively. The yellow points represent the most probable values for the joint posterior.

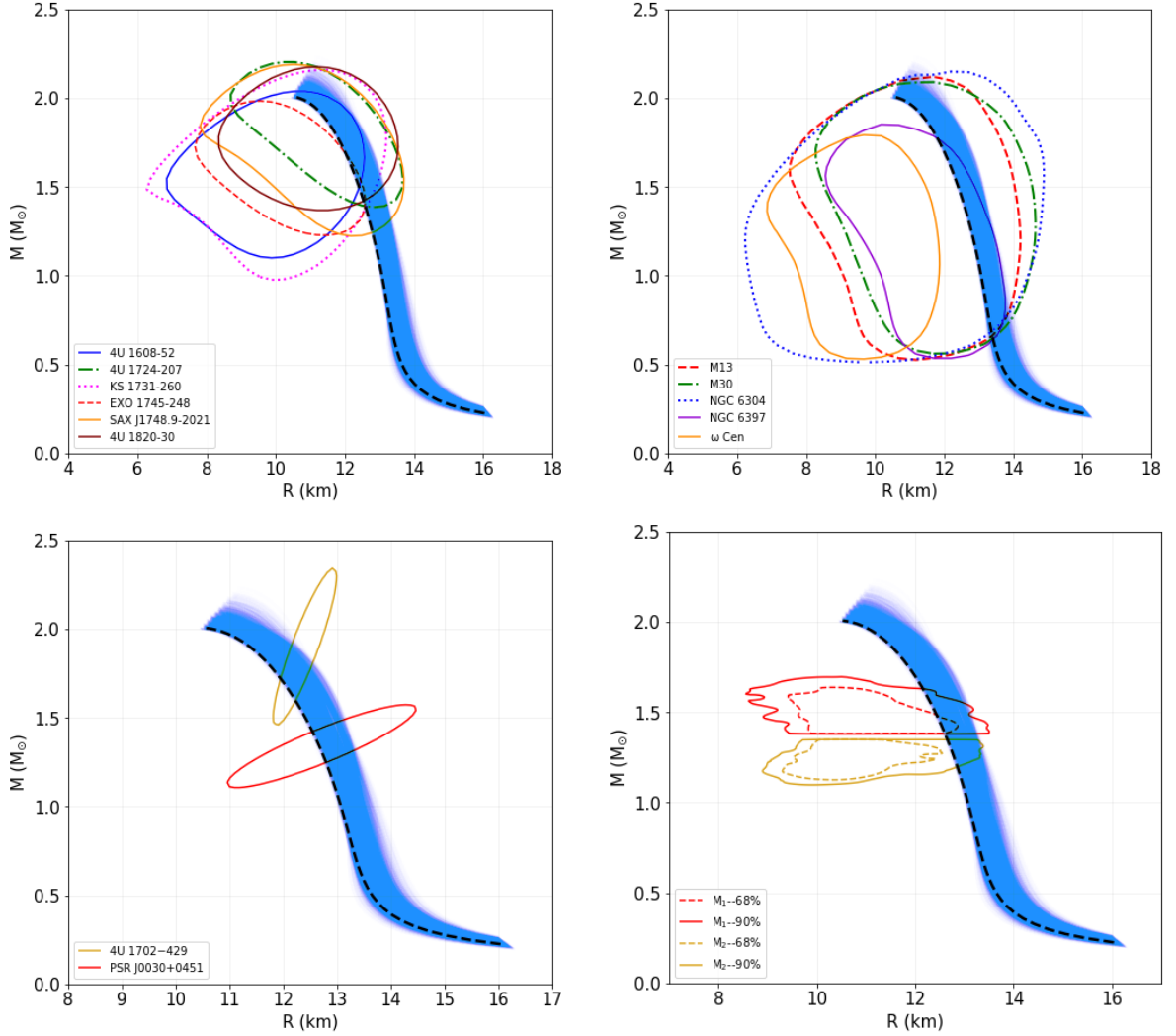


**Figure 7.5.2:** *Inferred mass-radius curves corresponding to the EOS parameters up to 68% CI assuming the baseline prior along with the sources. The bottom right panel corresponds to the event GW170817. The black dashed lines in all the panels represent the most probable EOS parameter set.*

Figure 7.5.17 in the additional material). The most likely parameters of the joint PDF are represented in the marginalized plots as the yellow points. We note a flat distribution for  $E_0$ , a marked peak for  $m^*$ , while  $K$ ,  $n_0$ , and  $S$  are characterized by the most probable configurations located at the edge of the respective prior boundary. The peak of  $m^*$  can be interpreted by taking into account its strong correlation with the maximum mass (Weissenborn et al., 2012b): the smaller the  $m^*$ , the larger the maximum mass. Thus a

not too big value of  $m^*$  helps to reach the  $2M_\odot$  lower limit but, at the same time, since the sources have small radii,  $m^*$  prefers also not too small values. Concerning  $K$ ,  $n_0$ , and  $S$ , they influence the stiffness of the EOS at intermediate densities and thus their values are mainly constrained by the sources radii. This can be seen more clearly looking at the inferred mass-radius sequences plotted in Figure 7.5.2. The most probable curve sits on the edge of the 68% CI of the distribution of inferred EOSs. It is also compatible with the 68% CI for the most of the sources, being  $\omega$ Cen the only one showing a mild inconsistency with the most probable sequence.

In Figure 7.5.3, we display the empirical parameters PDFs resulting from the analysis with the Wide\_unif prior. The  $m^*$  has a peak at a slightly smaller value with respect to the baseline prior. Concerning  $K$ ,  $n_0$ , and  $S$ , they show a similar behavior as before with the most likely values at the boundaries of the parameter space. The joint posterior is characterized by a hint of bimodality that is not evident looking only at the marginalized PDFs. The two modes of the distributions are represented in Figure 7.5.3, as yellow (the absolute maximum) and blue (the second relative maximum) points. We note, from Table 7.2, that the value of  $S$  associated to the second maximum is most probably ruled out by the present nuclear physics experimental data. On the other hand, the parameter set representing the main mode of the posterior is significantly similar to the one of the LS180 supernova EOS, whose empirical parameters have the values  $n_0 = 0.155 fm^{-3}$ ,  $K = 180$  MeV,  $S = 28.6$  MeV and  $L = 73.8$  MeV (Lattimer & Swesty, 1991). It is impressive that the same saturation properties obtained within a medium-dependent liquid-drop model can be reproduced through a RMF model.

In Figure 7.5.4 we present the corresponding M-R sequences, which also show a bimodal behavior following the joint PDF. Two different regions are evident in the M-R plots where the curves are banded together. The two modes are represented through the dashed and the dotted lines, respectively, and they are in good agreement with the observational data. However, as explain before, the dotted line is most probably ruled out <sup>3</sup>. Remarkably, the most probable curve features a bump close to  $\sim 1M_\odot$  and differently from LS180, it fulfills the  $2M_\odot$  limit and it has a radius  $R_{1.4} = 11.7$  km which is 0.5 km smaller than the one of LS180. Therefore, while these two EOSs have very similar saturation properties, they are characterized by different behaviors for  $\beta$ -stable matter at high density. This fact is due to the non-linearity of the RMF parametrization, that will be further discussed in section 7.5.6.

In Figure 7.5.5, we present the results with the Wide\_Gauss prior. The PDFs for all the parameters do not deviate considerably from the prior distribution, with the exception of  $K$ . For this variable, one can notice a significant shift of the peak, that moves about

---

<sup>3</sup>One can note that this M-R sequence is quite similar to the APR EOS (Akmal et al., 1998b), that however is compatible with the present knowledge concerning the nuclear symmetry energy. Again, if we introduce in the Lagrangian additional terms to better describe the symmetry energy we could in principle obtain solutions like the dashed line that are consistent with both nuclear physics data and astrophysical data.

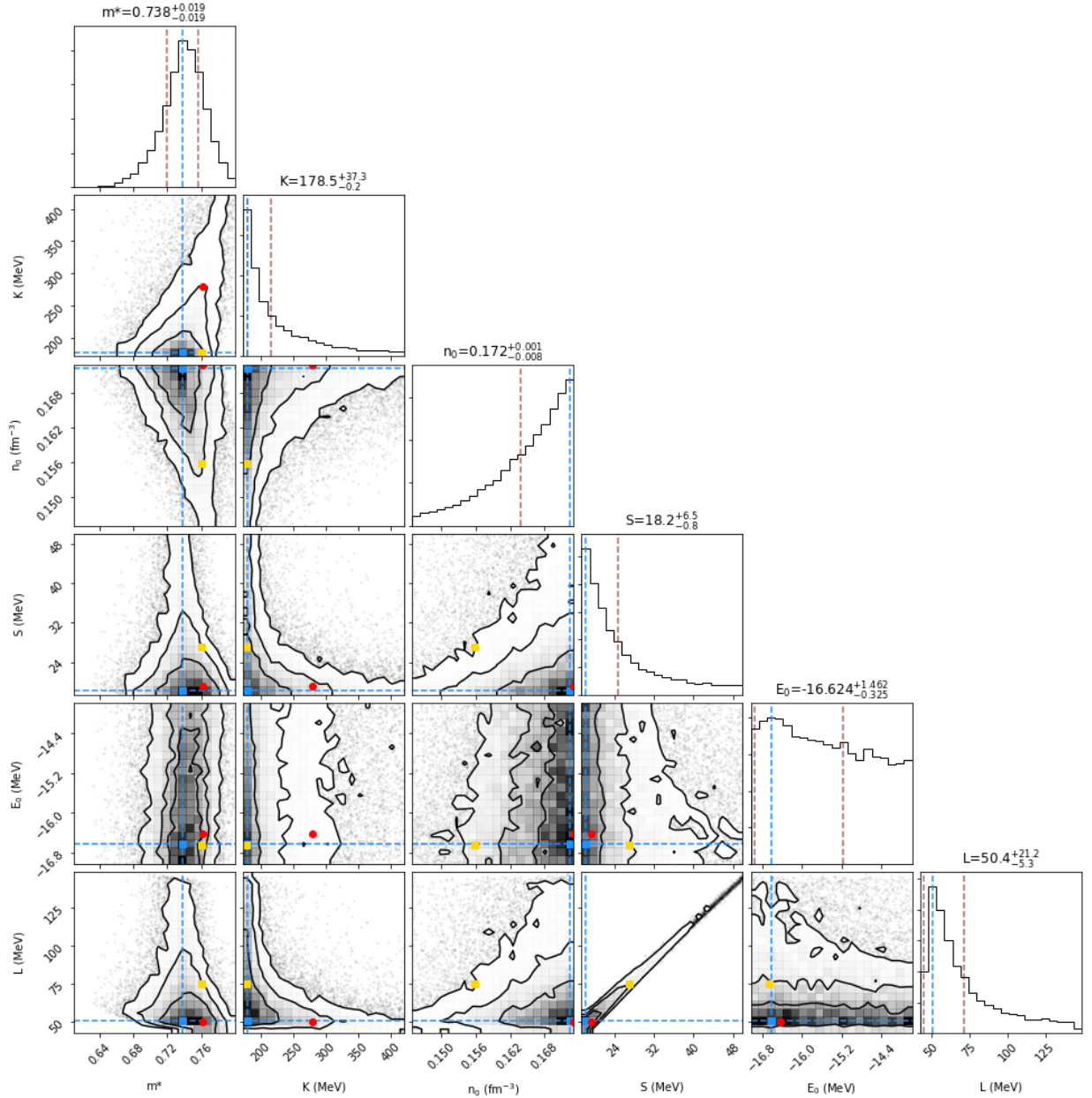


**Figure 7.5.3:** Same as Figure 7.5.1 for the Wide\_unif prior. The red points indicate the second mode of the joint distribution.

$2\sigma$  below the mean of the prior. This suggests that the EOS prefers to be quite soft near saturation and to become stiffer at higher density because of not too high effective mass and high symmetry energy. The small value of  $K$  resulting from this analysis is consistent with the result of the KaoS collaboration studying heavy ions collisions (Sagert et al., 2012).

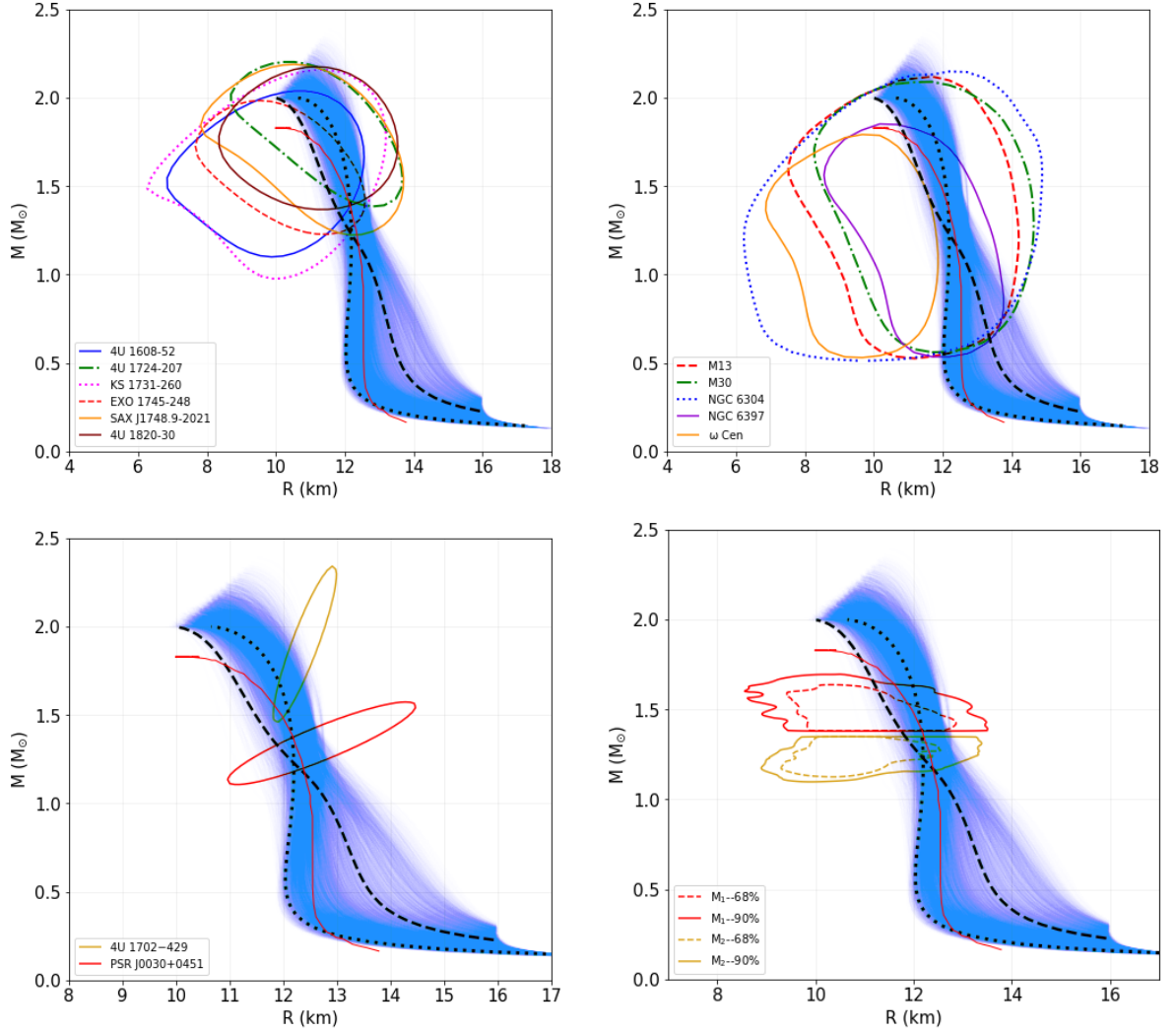


**Figure 7.5.4:** Same as Figure 7.5.2 for the *Wide\_unif* prior. Here the black dotted lines in all the panels represent the curve related to the second mode of the joint distribution for the empirical parameters. The red curve shows *LS180* for comparison.

The bimodality obtained in the previous case is removed by the use of a Gaussian prior but in Figure 7.5.6 one can still appreciate the existence of the bump on the mass-radius sequence of the most probable EOS. Again, we find a value for  $R_{1.4}$  smaller than the one associated to the baseline prior. This is the result of a correlation between  $K$  and the radius of a NS, also noted in Ferreira & Providência (2019).

As last in this section, we study the effect of including the  $\Lambda$  hyperons in the EOS. As expected, the formation of a new degree of freedom in the system has the effect of softening

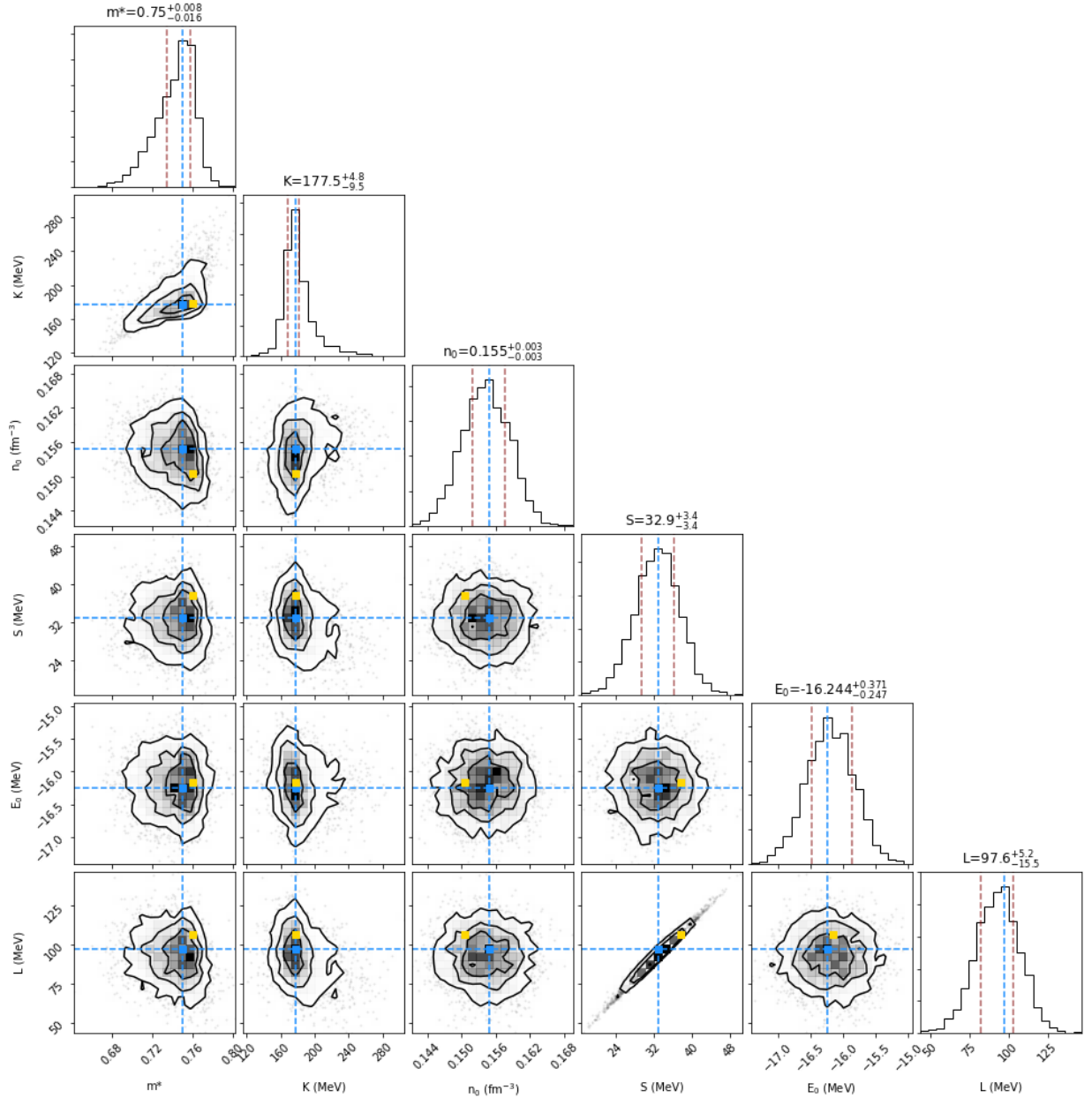


**Figure 7.5.5:** Same as Figure 7.5.1 for the Wide\_Gauss prior

the EOS. As a consequence, a very large region of the parameter space is no longer consistent with the  $2M_{\odot}$  constraint and it is therefore ruled out leading to a severe restriction of the parameter space. The PDFs for the empirical parameters found using the baseline prior and the corresponding M-R curves are plotted in Figures 7.5.7 and 7.5.8 respectively. In the marginalized distributions of  $m^*$  and  $K$ , one can see the qualitative dissimilarities with

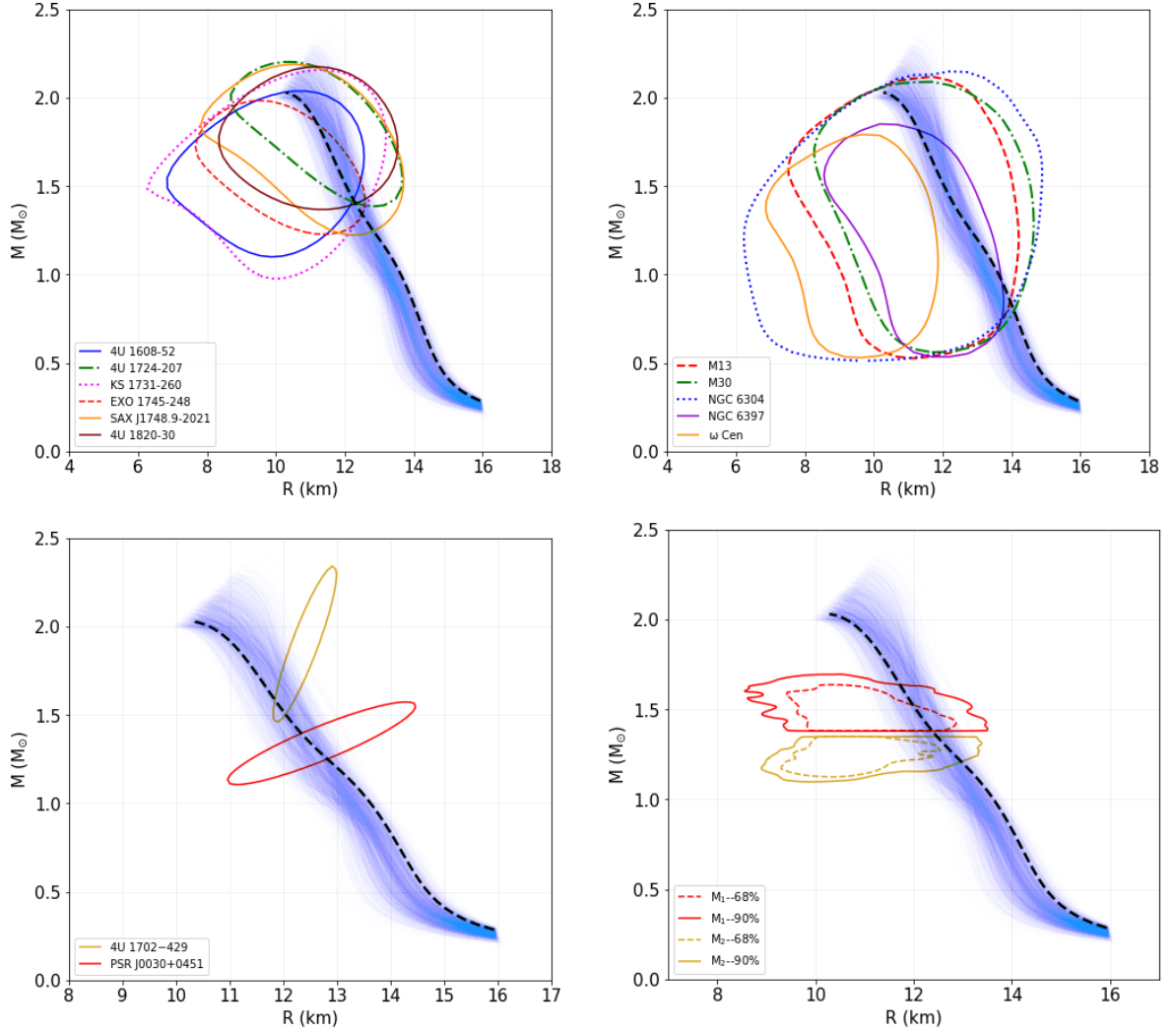


**Figure 7.5.6:** Same as Figure 7.5.2 for the *Wide\_Gauss* prior.

respect to the cases without hyperons. In particular,  $m^*$  does not feature a peak and its PDF tends towards the lower boundary of the range. Moreover, contrary to the previous results,  $K$  prefers the higher edge. These behaviors derived from the necessity to compensate the softening due to hyperons in order to fulfil the  $2M_\odot$  limit. We obtain M-R curves which are outside the 68% CI of the posteriors of the majority of the sources. The most probable EOS is characterized by a value of  $R_{1.4} > 14$  km, relevantly larger than for the other priors. In the *Wide\_unif* prior case with  $\Lambda$ , we find some M-R solutions within the observable constraints but the too small values of symmetry energy rule out these EOSs (See Figures 7.5.15 and 7.5.16 in chapter 7.5.7).

Finally, we compare the employed models using the BIC and the evidence (from which

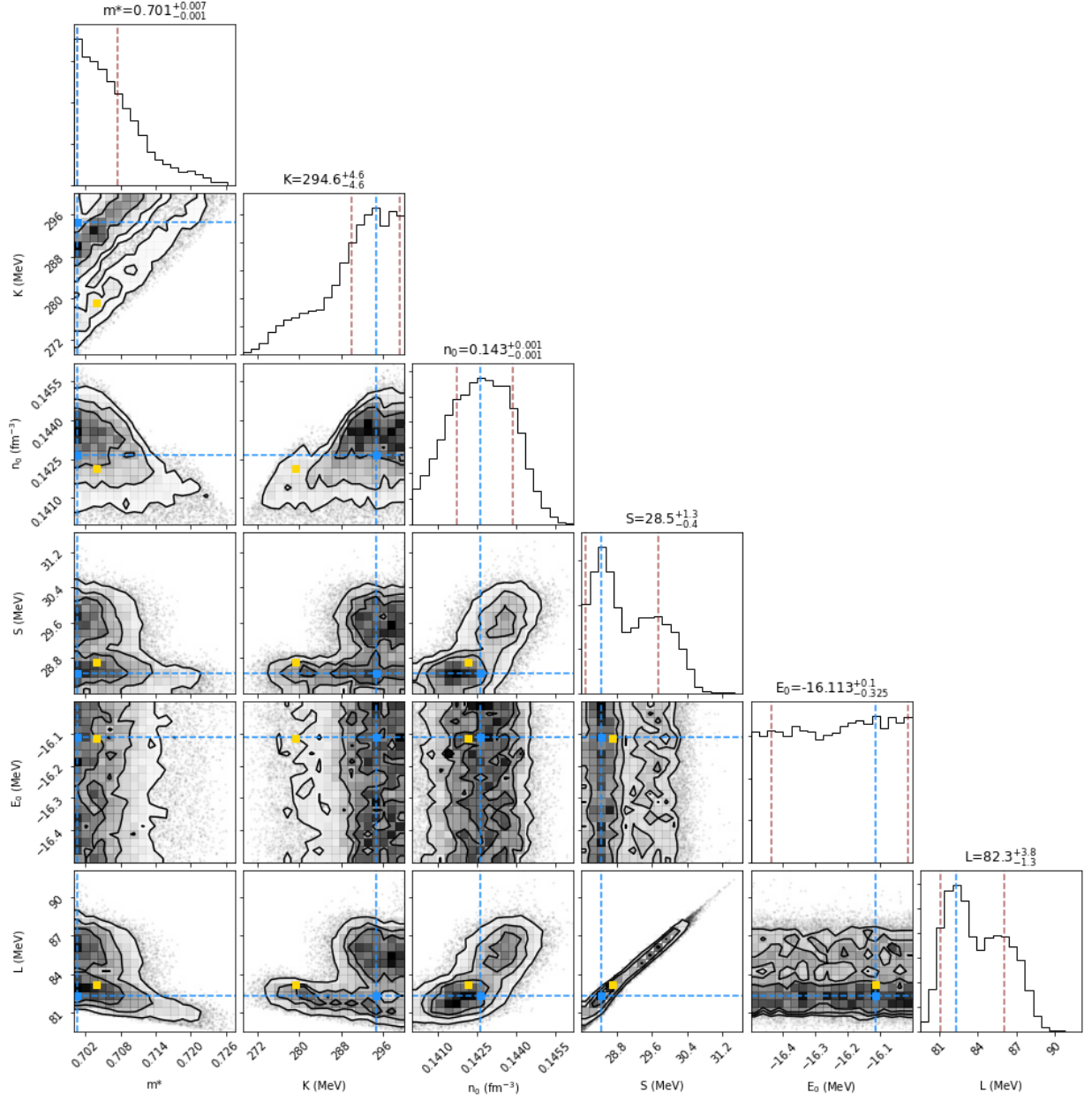
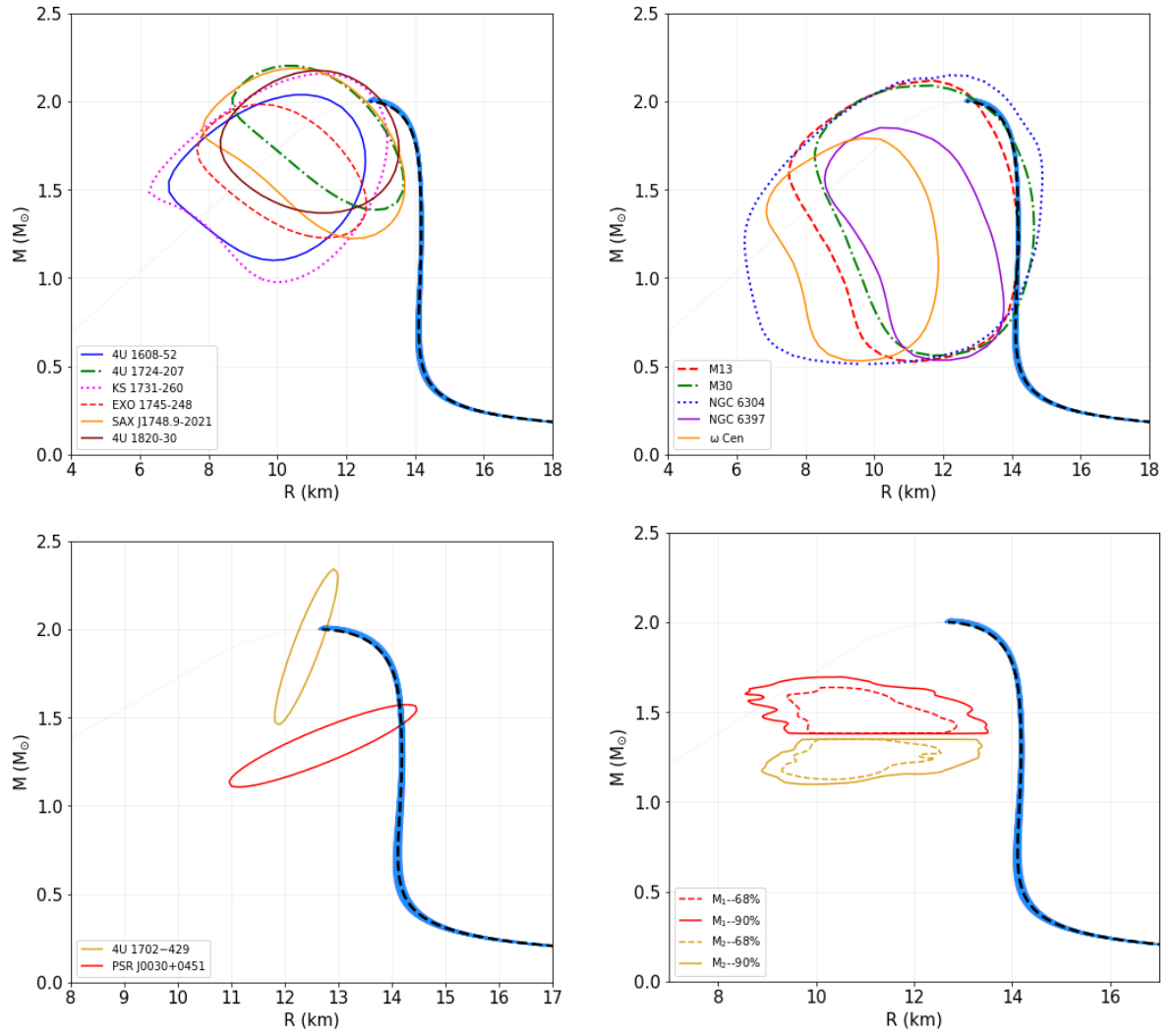


Figure 7.5.7: Same as Figure 7.5.1 for the baseline prior with  $\Lambda$  in the system.



**Figure 7.5.8:** Same as Figure 7.5.2 for the baseline prior range with  $\Lambda$  hyperon in the system.

the BF is derived). From Table 7.5, we see that the largest evidence is associated to the Wide\_Gauss prior, while the smallest to the Marg\_unif prior in the case of nucleonic models. Between the models with hyperons, the Wide\_unif is favoured over the baseline prior and, as expected, in general the nucleonic models are favoured over the hyperonic ones. The same conclusion can be drawn from Table 7.6, showing the values of  $\Delta\text{BIC}$ , the Marg\_Gauss case being the only exception. The reason has to be found in the different ingredients present in the BIC and the BF. The first one takes into account only the the number of prior parameters and the likelihood of the most probable configuration. Instead, the BF includes the full prior distribution. Thus, for Gaussian priors the probabilities which are very distant from the central value are suppressed. As a consequence, two models with similar parameters and maximum likelihood values can result in similar BIC but different BF when having a different type of prior distribution. This is the case of the Marg\_Gauss prior, as the peak of the PDF for  $K$  deviates by more than  $3\sigma$  from the mean of the Gaussian prior.

Now, let us discuss the interpretation of the BFs when comparing the two classes of priors, the informed and the agnostic. For the informed prior, we consider the baseline model while for the agnostic the Wide\_unif model, as an example. If the maximum likelihood set for both of the models is inside the overlap region of the two priors, one would expect a smaller evidence for the Wide\_unif case. This is a consequence of its larger prior volume which penalizes it over the baseline. Therefore, the fact that instead we obtain a larger evidence for the Wide\_unif suggests a tension between nuclear physics encoded in the informed priors and the astrophysical observations, consistent with the results of [Güven et al. \(2020\)](#).

Model 1 \ Model 0	Baseline	Marg_unif	Marg_Gauss	Wide_unif	Wide_Gauss	Wide_unif with $\Lambda$	Baseline with $\Lambda$
Baseline		$4 \cdot 10^{-5}$ n. decisive	0.04 n. strong	6.5 p. moderate	30.2 p. strong	0.03 n. very strong	$1.4 \cdot 10^{-7}$ <b>n. decisive</b>
Marg_unif	$2.4 \cdot 10^4$ p. decisive		951.3 p. decisive	$1.6 \cdot 10^5$ p. decisive	$7.2 \cdot 10^5$ p. decisive	710.4 p. decisive	0.003 n. decisive
Marg_Gauss	25.1 p. strong	0.001 n. decisive		163.7 p. decisive	756.8 p. decisive	0.75 n. weak	$3.6 \cdot 10^{-6}$ n. decisive
Wide_unif	<b>0.15</b> <b>n. moderate</b>	$6.4 \cdot 10^{-6}$ n. decisive	0.006 n. decisive		4.6 p. moderate	<b>0.005</b> <b>n. decisive</b>	$2.2 \cdot 10^{-8}$ n. decisive
Wide_Gauss	0.03 n. strong	$1.4 \cdot 10^{-6}$ n. decisive	0.001 n. decisive	<b>0.21</b> <b>n. moderate</b>		0.001 n. decisive	$4.7 \cdot 10^{-9}$ n. decisive
Wide_unif with $\Lambda$	33.6 p. very strong	0.001 n. decisive	1.34 p. weak	219.2 p. decisive	1013.4 p. decisive		$4.8 \cdot 10^{-6}$ n. decisive
Baseline with $\Lambda$	$7 \cdot 10^6$ p. decisive	293.5 p. decisive	$2.8 \cdot 10^5$ p. decisive	$4.6 \cdot 10^7$ p. decisive	$2.1 \cdot 10^8$ p. decisive	$2.1 \cdot 10^5$ p. decisive	

**Table 7.5:** Bayes factors ( $BF_{01}$ ). We indicate the strength of the preference between the two compared models. Here p. (n.) suggest a positive (negative) preference for model 0 over model 1.

Model 1	Model 0	Baseline	Marg_unif	Marg_Gauss	Wide_unif	Wide_Gauss	Wide_unif with $\Lambda$	Baseline with $\Lambda$
Baseline			17.72 n. decisive	-1.07 p. weak	-2.11 p. moderate	-2.33 p. moderate	2.49 n. moderate	<b>24.00</b> <b>n. decisive</b>
Marg_unif		-17.72 p. decisive		-18.79 p. decisive	-19.83 p. decisive	-20.05 p. decisive	-15.24 p. decisive	6.26 n. strong
Marg_Gauss		1.07 n. weak	18.79 n. decisive		-1.04 p. weak	-1.26 p. weak	3.55 n. moderate	25.05 n. decisive
Wide_unif		<b>2.11</b> <b>n. moderate</b>	19.83 n. decisive	1.04 n. weak		-0.22 p. weak	<b>4.60</b> <b>n. moderate</b>	26.10 n. decisive
Wide_Gauss		2.33 n. moderate	20.05 n. decisive	1.26 n. weak	<b>0.22</b> <b>n. weak</b>		4.81 n. moderate	26.31 n. decisive
Wide_unif with $\Lambda$		-2.49 p. moderate	15.24 n. decisive	-3.55 p. moderate	-4.60 p. moderate	-4.81 p. moderate		21.50 n. decisive
Baseline with $\Lambda$		-24.00 p. decisive	-6.26 p. strong	-25.05 p. decisive	-26.10 p. decisive	-26.31 p. decisive	-21.50 p. decisive	

**Table 7.6:**  $\Delta BIC_{01}$ . We indicate the strength of the preference between the two compared models. Here p. (n.) suggest a positive (negative) preference for model 0 over model 1.

### 7.5.6 Discussion and conclusions

We have seen before that the uniform informed priors lead to M-R relations which are qualitatively very close to the old parameterization of [Glendenning & Moszkowski \(1991\)](#). This finding suggests that, within the present uncertainties on the saturation properties of nuclear matter and by employing uniform priors, it is essentially impossible to set  $R_{1.4}$  smaller than  $\sim 12.5$ km, see [Tables 7.3 and 7.4](#) and [Figure 7.5.2](#). Radii of the order of  $\sim 11$ km can be obtained only for configurations in the vicinity of the maximum mass. This conclusion is obviously dependent on our modelling of the EOS and, in particular, on our choice of RMF model. However, we underline that this outcome is completely in agreement with both the results from the metamodelling analysis of [Margueron et al. \(2018b\)](#) and the independent work by [Most et al. \(2018\)](#). In those papers the EOS is modelled in a different way: in the first case with a Taylor expansion around saturation while in the second case a chiral effective field theory up to to saturation and, for larger densities, a piecewise polytropic parametrization. In addition, the fact that the most likely M-R configuration lies on the left edge of the 68% CI is suggesting the existence of a tension between the values of the nuclear physics empirical parameters and the astrophysical data, as discussed before. That is the main motivation to investigate different priors.

Interestingly, when we are allowed to explore a wider area of the parameters space, as with Wide\_unif, Wide\_Gauss and Marg\_Gauss (see [section 7.5.7](#)), we find a qualitative difference in the M-R curve with a bump appearing for a mass close to  $1M_{\odot}$ . This behaviour resembles the one obtained with the occurrence of a smooth phase transition (such as a Gibbs mixed phase with quark matter). To clarify the origin of this feature, we show in [Figure 7.5.9](#) the density dependence of the effective mass, which, because of the non-linearity

of the sigma potential, can reveal a phase transition. Indeed,  $m^*$  is characterized by a fast drop for the aforementioned three priors at a density of about 2 – 3 times the saturation density and one can also note a change in concavity with respect to the baseline and the Marg\_unif priors. The bump is evident also in Figure 7.5.10, where the gravitational mass is plotted as a function of the central baryon density. This behaviour is evocative of a partial restoration of chiral symmetry and we can interpret it as an explicit indication that astrophysical data suggests the appearance inside NS of new phases of strongly interacting matter. Note that the largest evidence is associated to the prior adopting a wide Gaussian distributions of the empirical parameters: in this situation  $R_{1.4}$  can drop below  $\sim 12$  km and, at the maximum mass configuration, radii as small as  $\sim 10$  km are reached (see Figure 7.5.6).

Other works have led to a similar conclusion following different approaches: hints for a phase transition have been found in Essick et al. (2020) by using the non parametric inference, in Güven et al. (2020) with the metamodeling tools and in Fujimoto et al. (2020) employing a the deep neural network methods and finally in Steiner et al. (2018) with a Bayesian analysis with a tuned parameterization for strong phase transitions.

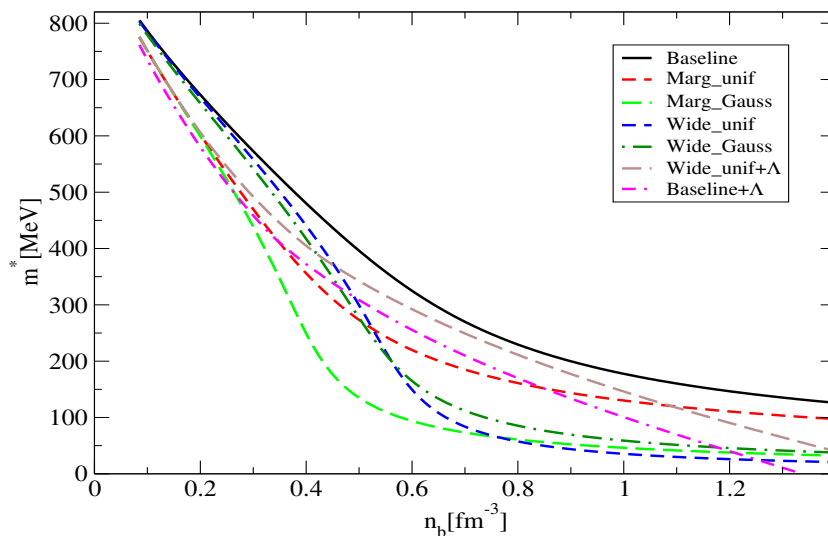


**Figure 7.5.9:** *Effective mass as a function of density for the five priors here adopted. The curves correspond to the most probable parameters for each prior. Also the two cases with the inclusion of  $\Lambda$  are shown.*

Let us consider now the cases in which the  $\Lambda$ s are included in the model. From Figure 7.5.10, we notice that, in all the pure nucleonic cases, the central density corresponding to the  $2M_{\odot}$  configuration is larger than  $\sim 4n_0$ . As a consequence, the approximation of neglecting hyperons in these models needs to be justified by resorting to a possible stiffening mechanism able to shifts the threshold for the formation of hyperons to a larger density:

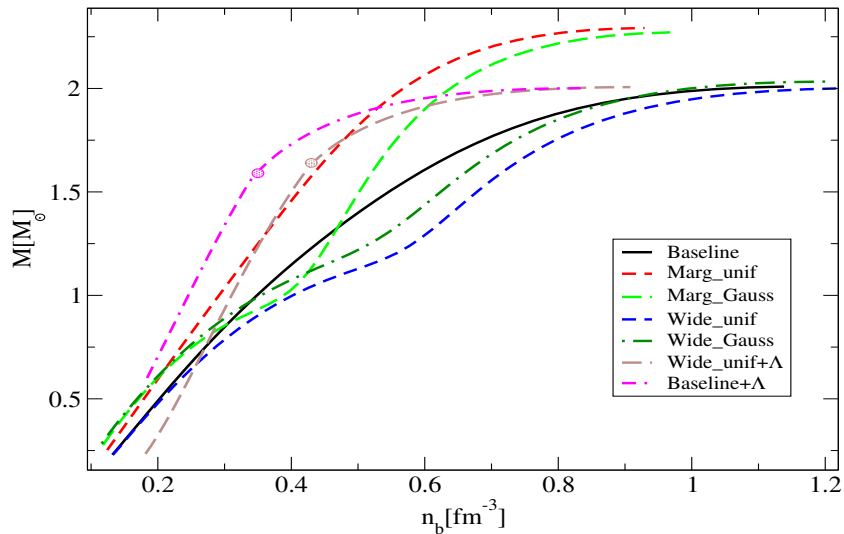


**Figure 7.5.10:** Gravitational mass as a function of the central density as obtained from the same EOSs of Fig.7.5.9. The circles correspond to the onset of  $\Lambda$ 's in the EOSs.

examples are the strong repulsion caused by three body interactions (Lonardonì et al., 2015) or hidden strangeness vector field such as the  $\phi$  meson, as in Weissenborn et al. (2012a) (for details see chapter 3.2.2). On the other hand, in our hyperonic EOSs, the  $\Lambda$ s appear in NS with masses in the range  $1.6 - 2 M_\odot$ . For the Wide\_unif case, the fact that the  $\Lambda$ s are formed and, at the same time, the  $2M_\odot$  limit is fulfilled is due to an unacceptably small value of the symmetry energy (see Tables 7.2 and 7.7) and to a very large value of  $K$ . This EOS must therefore be considered very unlikely. By including  $\Lambda$ s with the baseline prior, the  $2M_\odot$  requirement leads to an early stiffening of the EOS resulting in  $R_{1.4} \gtrsim 14$  km. This outcome is in agreement with previous results presented in Fortin et al. (2015): here the authors suggest that the presence of hyperons systematically shifts the radius of NS to larger value with respect to stars made only of nucleons. As evident in Figure 7.5.8 the predicted mass-radius sequences are incompatible even with the 90% CI provided by GW170817. Therefore, the inclusion of hyperons within our minimal modelling strengthens the tension between nuclear physics and the astrophysical measurements. This conclusion is also supported by the results suggested by the BFs.

A plan for a future work is to further study this issue for instance by adding a repulsive channel for hyperons. Indeed, we can find many examples in the literature where the inclusion of hyperons do not forbid to get values of  $R_{1.4}$  of about 13km and still fulfilling the  $2M_\odot$  constraint (see as examples Logoteta et al. (2019); Weissenborn et al. (2012a); Maslov et al. (2015); Negreiros et al. (2018) and chapter 3.2.2). Moreover, in principle, also  $\Delta$  resonances should be included since their onset is comparable to the one of hyperons (Drago et al. (2014b); Cai et al. (2015); Li et al. (2018), see chapter 3.3.1).

In addition, the indications of a phase transition obtained in this work, can be further investigated by considering a transition to quark matter by means of a Gibbs construction, as in [Weissenborn et al. \(2011\)](#); [Nandi & Char \(2018\)](#).

Finally, a last possibility consists in implementing EOSs characterized by disconnected branches in the M-R plane such as in the twin-stars ([Christian et al. \(2018b\)](#); [Benic et al. \(2015\)](#), see section 3.2.5) or in the two families scenario ([Drago et al. \(2014a, 2016b\)](#); [Burgio et al. \(2018\)](#); [De Pietri et al. \(2019\)](#), see section 3.3). In chapter 8, we will present a Bayesian analysis employing a model for Qs within the two family scenario.

### 7.5.7 Additional material

In this section, we present the results for Marg\_unif, Marg\_Gauss priors and the Wide\_unif with  $\Lambda$ . We also provide in Table 7.8 the most probable values for the RMF coupling constants from the joint PDFs for all the cases. The marginalized distributions are plotted in Figure 7.5.17 for the baseline prior and are available as online contents at the link [iopscience.iop.org/article/10.3847/1538-4357/ab99c1](https://iopscience.iop.org/article/10.3847/1538-4357/ab99c1) for the remaining six priors.

In addition, in Table 7.7, we list the median values of the marginalized PDFs of the empirical parameters for all the priors.

Models	$m^*$	K (MeV)	$n_0$ (fm $^{-3}$ )	S (MeV)	$E_0$ (MeV)	L (MeV)
Baseline	$0.761^{+0.015}_{-0.016}$	$212.7^{+32.0}_{-9.8}$	$0.157^{+0.002}_{-0.004}$	$30.3^{+2.7}_{-1.7}$	$-16.26^{+0.17}_{-0.17}$	$84.4^{+8.3}_{-5.1}$
Marg_unif	$0.705^{+0.004}_{-0.008}$	$226.6^{+13.0}_{-5.7}$	$0.152^{+0.001}_{-0.002}$	$33.4^{+3.0}_{-1.7}$	$-16.24^{+0.08}_{-0.08}$	$97.6^{+8.8}_{-5.0}$
Marg_Gauss	$0.707^{+0.016}_{-0.014}$	$161.1^{+14.0}_{-11.9}$	$0.151^{+0.002}_{-0.002}$	$34.7^{+2.9}_{-2.7}$	$-16.24^{+0.06}_{-0.06}$	$101.7^{+8.6}_{-8.1}$
Wide_unif	$0.740^{+0.023}_{-0.027}$	$203.5^{+82.7}_{-24.9}$	$0.166^{+0.005}_{-0.009}$	$22.7^{+11.7}_{-4.1}$	$-15.57^{+1.17}_{-1.02}$	$62.7^{+35.3}_{-12.4}$
Wide_Gauss	$0.746^{+0.014}_{-0.024}$	$177.3^{+18.1}_{-10.9}$	$0.154^{+0.004}_{-0.004}$	$32.8^{+4.5}_{-4.8}$	$-16.20^{+0.37}_{-0.37}$	$93.3^{+13.6}_{-14.1}$
Wide_unif with $\Lambda$	$0.683^{+0.024}_{-0.029}$	$355.9^{+44.0}_{-58.7}$	$0.169^{+0.003}_{-0.006}$	$18.9^{+2.5}_{-1.0}$	$-15.40^{+1.09}_{-1.14}$	$54.9^{+8.7}_{-4.9}$
Baseline with $\Lambda$	$0.706^{+0.006}_{-0.004}$	$292.1^{+5.4}_{-9.1}$	$0.143^{+0.001}_{-0.001}$	$28.9^{+1.0}_{-0.6}$	$-16.24^{+0.17}_{-0.18}$	$83.6^{+3.0}_{-2.0}$

**Table 7.7:** Median of the marginalized distributions for the empirical parameters.

The results for Marg\_unif prior are shown in Figure 7.5.11. This particular range, usually allows to build EOSs that are stiffer than the ones found with the baseline prior. However, to conform with the astrophysical observations, the most likely parameter set for the Marg\_unif again lies on the edge of the boundary which returns the softest possible EOS. Comparing with the baseline, we note the absence of a peak in the marginalized distribution of  $m^*$ . On the contrary, the latter is characterized by the most probable configuration sitting near the edge of the upper limit that corresponds to the softest EOS. Otherwise, the behaviors of  $K$ ,  $n_0$ , and  $S$  are very similar to those of the baseline prior. In Figure 7.5.12, we display the inferred M-R sequences along with the most likely one. Because of our choice of the prior ranges, the deduced EOSs are stiffer and the M-R curves are outside of the 68% CI of most of the X-ray sources and of the GW data.

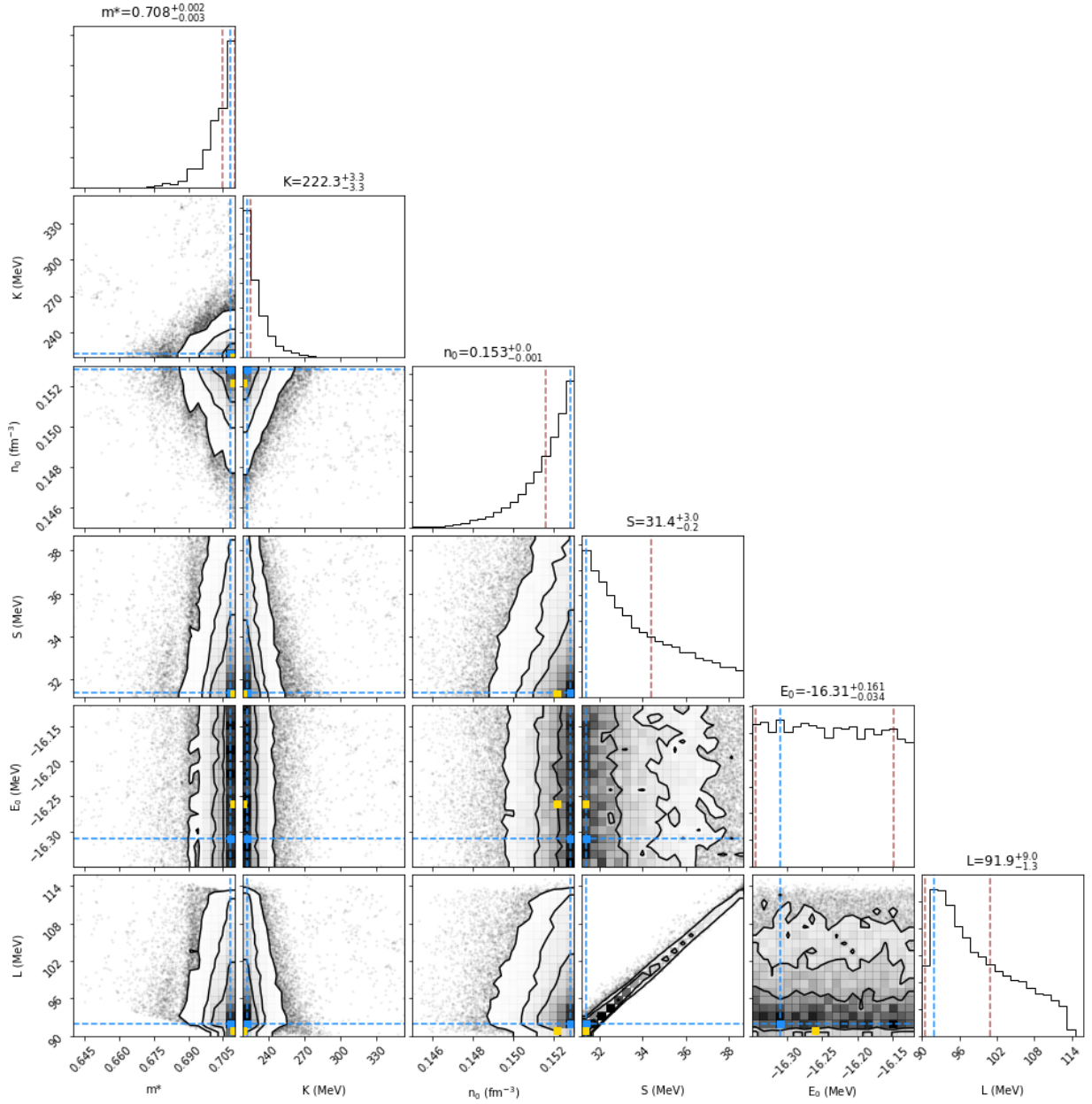
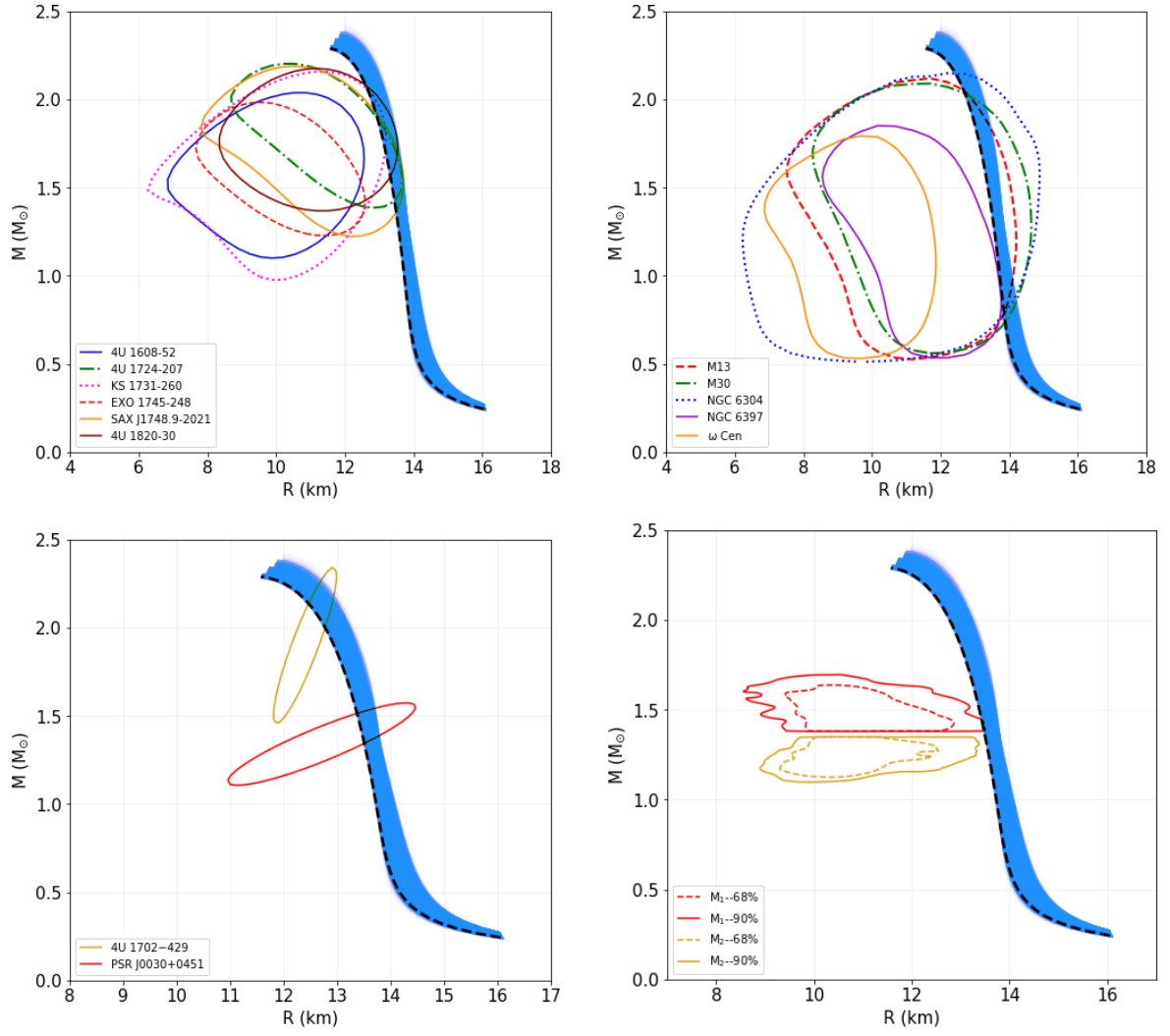


Figure 7.5.11: Same as Figure 7.5.1 for the Marg\_unif prior



**Figure 7.5.12:** Same as Figure 7.5.2 for the Marg\_unif prior.

Models	$g_\sigma/m_\sigma$ (fm)	$g_\omega/m_\omega$ (fm)	$g_\rho/m_\rho$ (fm)	b	c
Baseline	3.252	2.270	1.888	0.00991	-0.01083
Marg_unif	3.505	2.629	2.047	0.00548	-0.00615
Marg_Gauss	3.585	2.628	2.267	0.00713	-0.00985
Wide_unif	3.351	2.296	1.774	0.01148	-0.01510
	3.000	2.153	0.882	0.00596	0.00231
Wide_Gauss	3.381	2.351	2.490	0.01056	-0.01373
Wide_unif with $\Lambda$	3.340	2.609	0.274	0.00279	-0.00129
Baseline with $\Lambda$	3.556	2.768	1.971	0.00319	-0.00180

**Table 7.8:** Most probable RMF coupling constants from the joint PDF.

In Figure 7.5.13, we present the PDFs of the empirical parameters for the Marg\_Gauss prior. The most evident feature is the value of the peak of  $K$ , which is shifted by more than  $3\sigma$  with respect to the peak of the prior. In Figure 7.5.14 we show the corresponding mass-radius sequences which are qualitatively close to the ones obtained with the Wide\_Gauss prior. However, the most probable configuration is characterized by a much larger maximum mass, because the EOS becomes stiffer due to the much lower value of  $m^*$ .

The posterior distributions and the corresponding mass-radius relations for the Wide\_unif with  $\Lambda$  case are shown in Figure 7.5.15 and 7.5.16, respectively. The preferred value for  $K$  is very large to reduce the softening of the EOS due to the formation of hyperons, while  $S$  is very small in order to obtain a very symmetric matter i.e. less neutron rich which helps in suppressing the production of  $\Lambda$ s. However, such small values of  $S$  are excluded by the available experimental knowledge.

The results shown in this section (concerning the Marg\_unif and Marg\_Gauss priors) are commented in more depth in Char et al. (2020), which we do not report here for the sake of brevity. Thus we kindly ask the interested reader to find the content at the link <https://www.mdpi.com/2571-712X/3/3/40>.

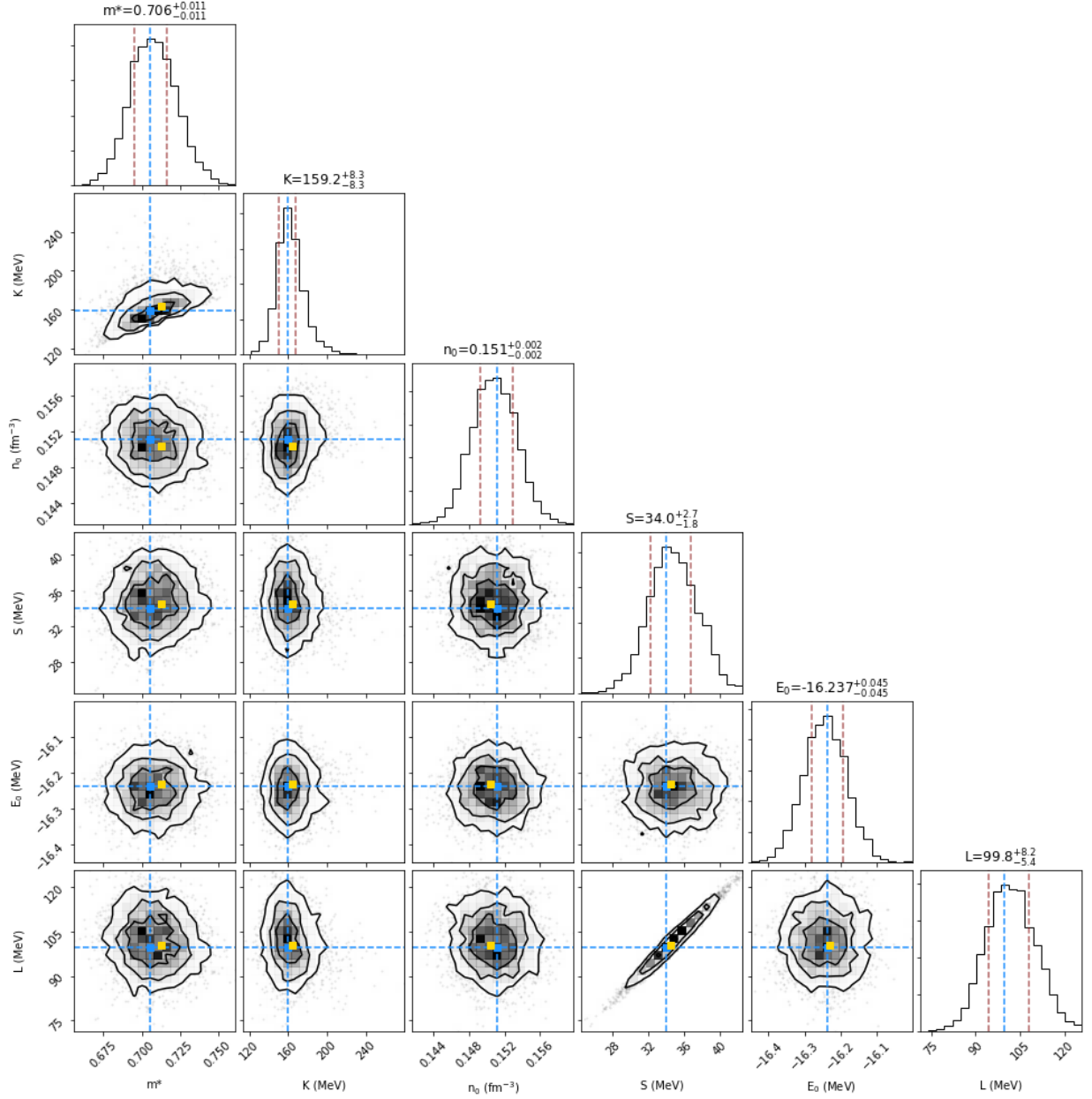


Figure 7.5.13: Same as Figure 7.5.1 for the Marg\_Gauss prior.

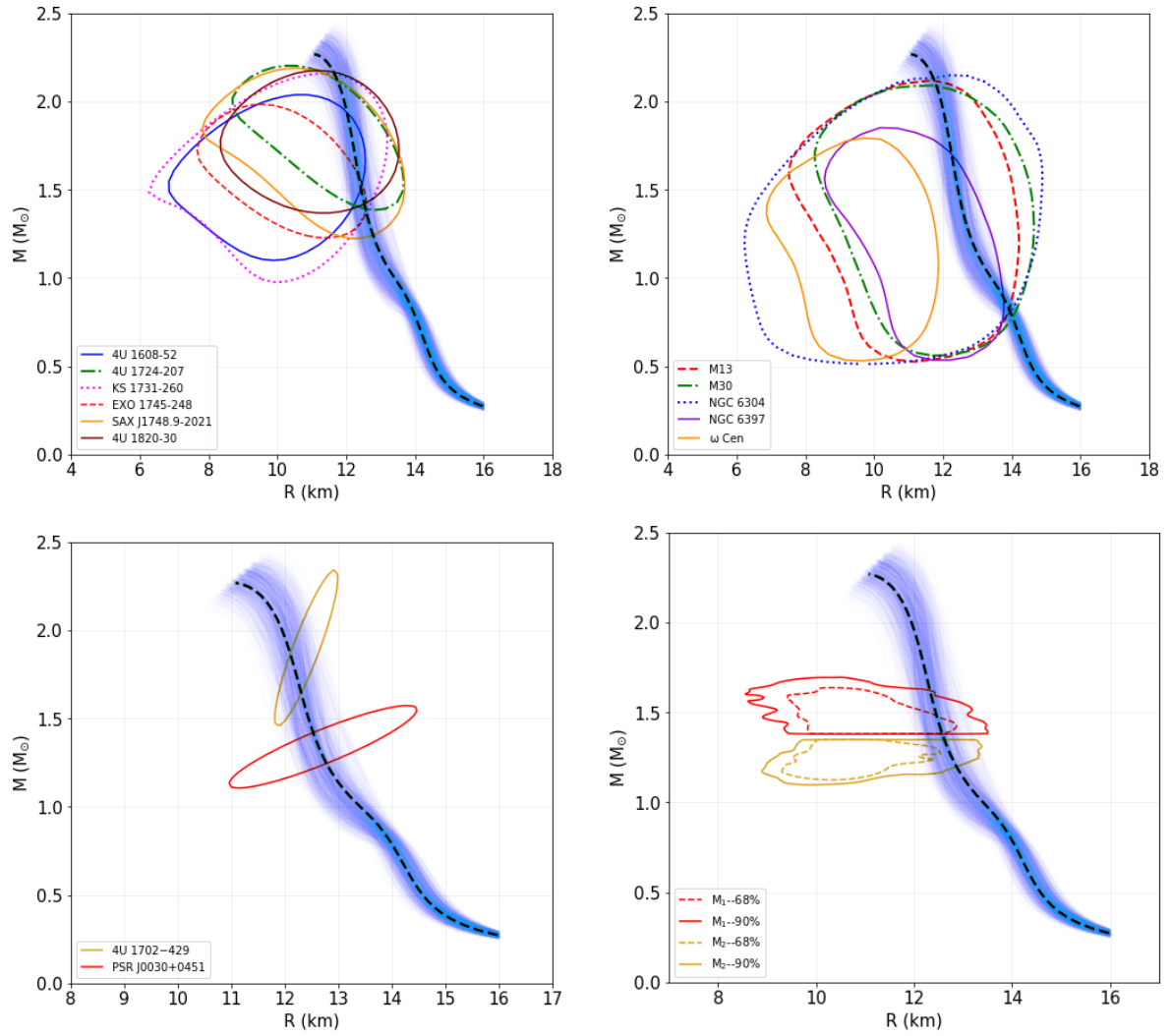


Figure 7.5.14: Same as Figure 7.5.2 for the Marg\_Gauss prior.

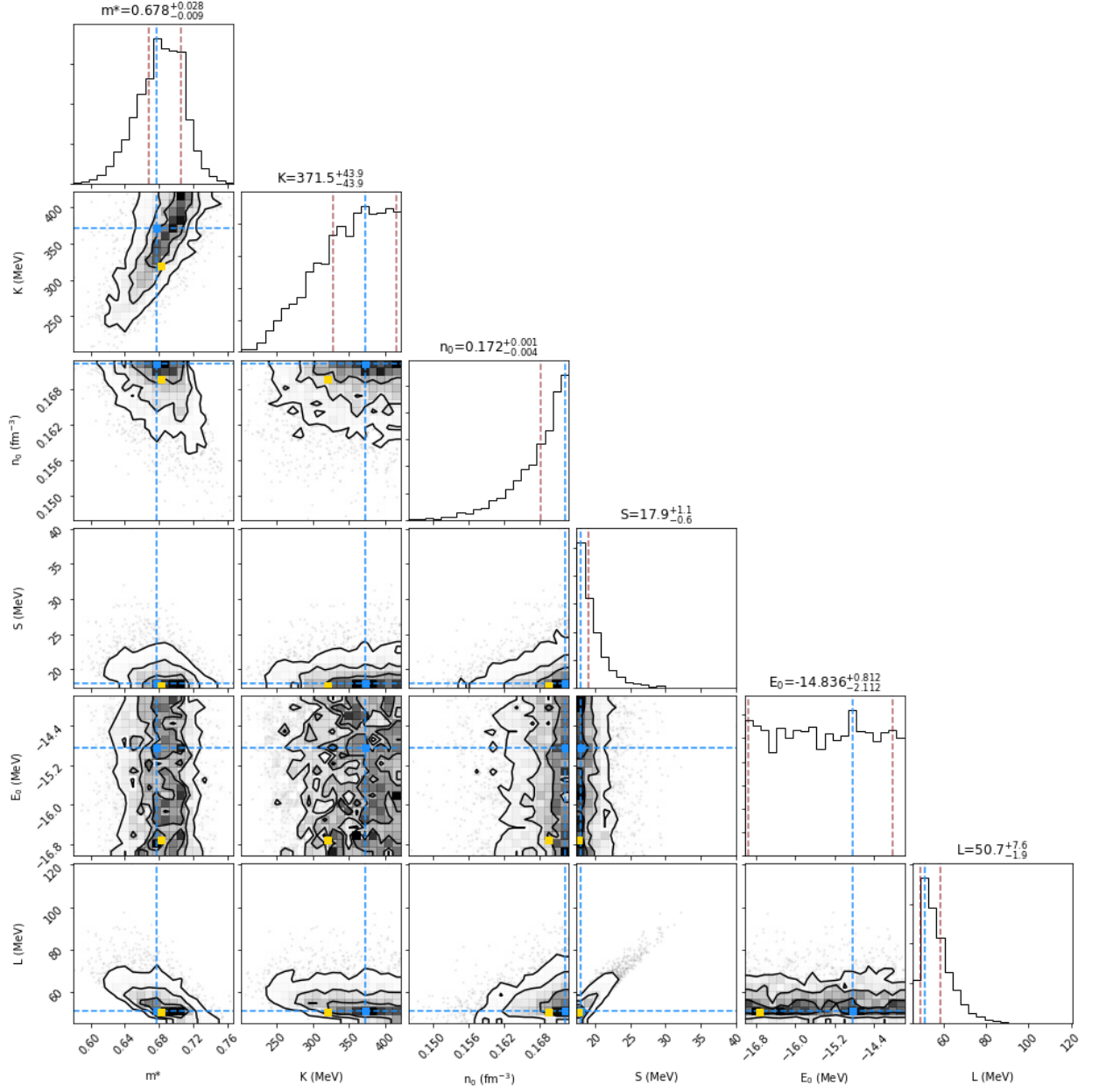
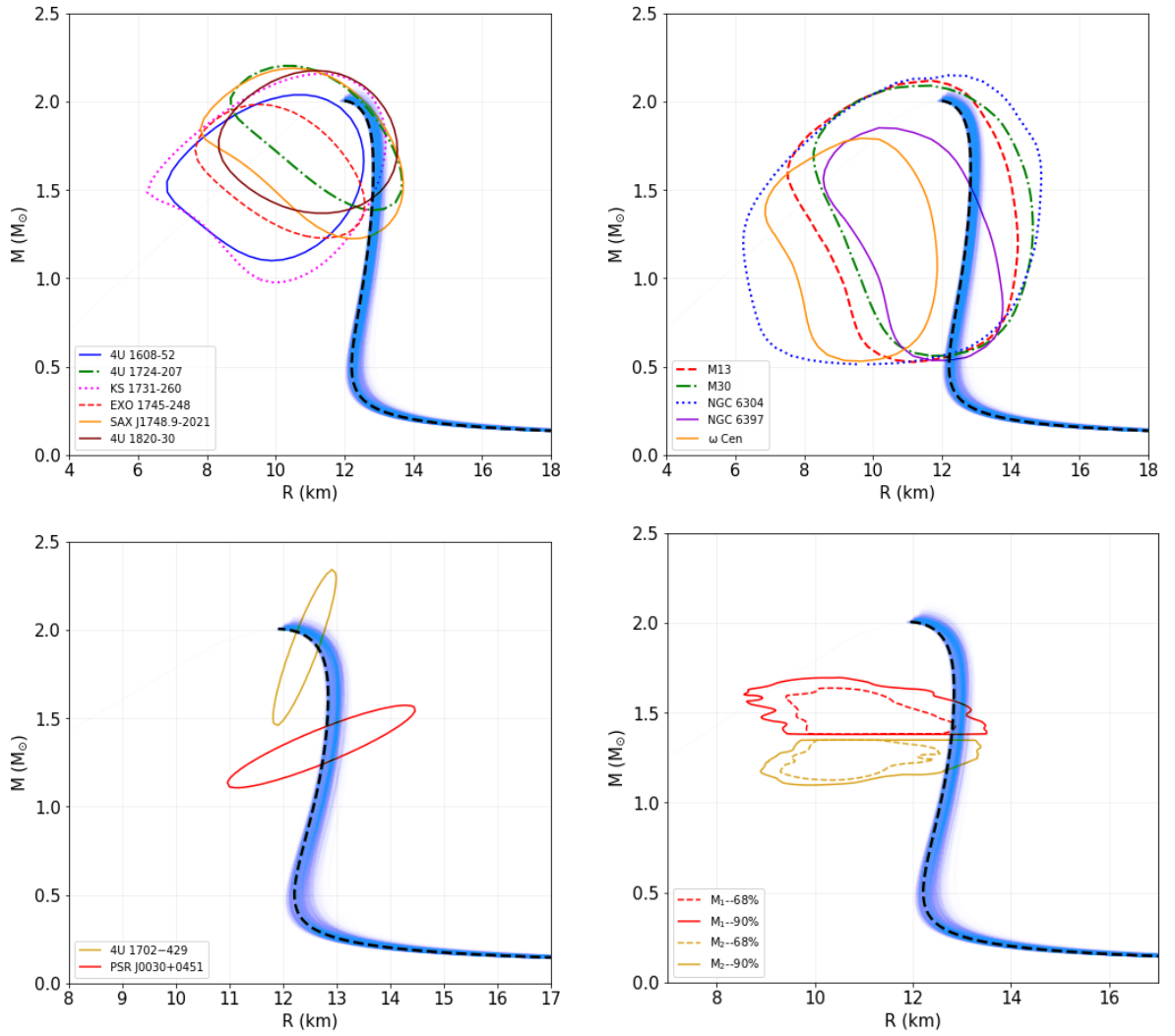
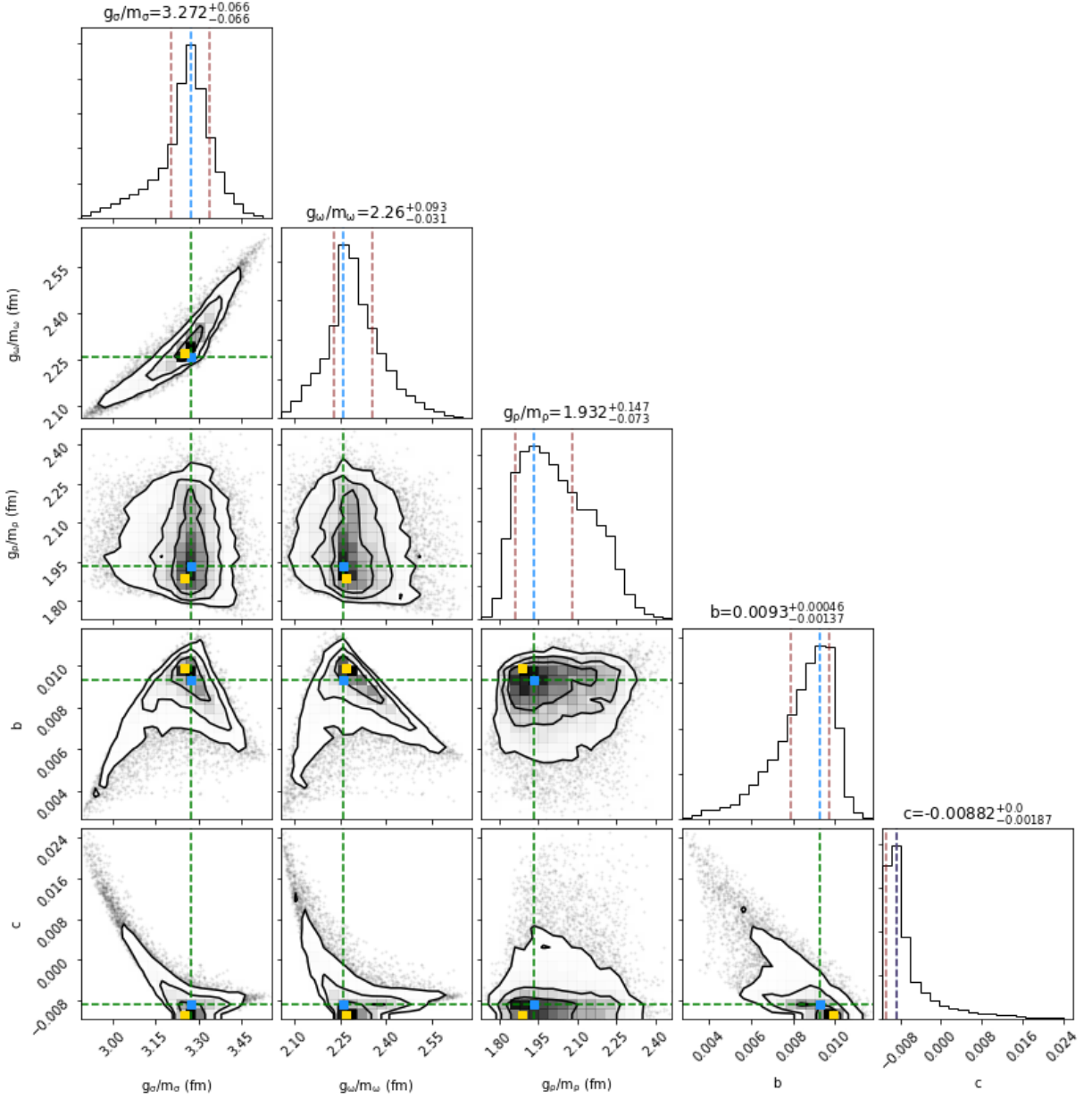


Figure 7.5.15: Same as Figure 7.5.1 for the Wide\_unif with  $\Lambda$  in the system



**Figure 7.5.16:** Same as Figure 7.5.2 for the Wide\_unif with  $\Lambda$  in the system



**Figure 7.5.17:** Distribution of RMF parameters corresponding to the empirical parameters of Fig. 7.5.1. The complete figure set (six images for the other six priors) is available in the online journal.

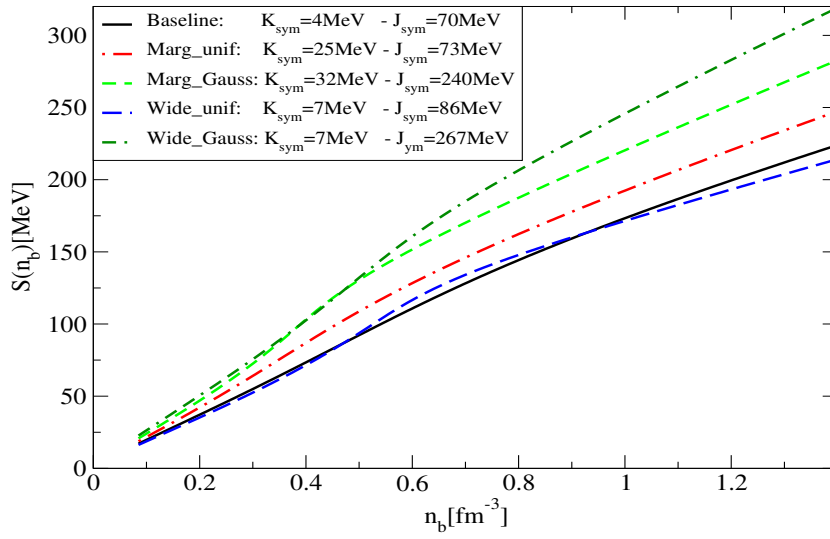


**Figure 7.5.18:** Density dependence of symmetry energy for the same EOS of Figure 7.5.9. We indicate also the high order derivatives  $K_{\text{sym}}$  and  $J_{\text{sym}}$ .

# *Neural networks vs Bayesian analysis: a study on quark matter*

The subject of this last chapter is a study of a simple EOS for quark matter, employing two different methods: the Bayesian analysis (as described in section 7.1) and a new approach based on Deep Neural Networks. Our results are presented in [Traversi & Char \(2020\)](#) (© AAS. Reproduced with permission, labelled as paper I) and in an ongoing work (paper II): the first one is focused on the comparison between the two methods while the second presents a discussion concerning the sound speed in quark matter and the conformal limit.

## **8.1 Introduction to Neural Networks**

Artificial Neural Networks (NN) are algorithms which have been developed to treat a variety of computational problems. These range from time-series predictions, classifications of data, fitting of functions to natural language understanding.

The NN paradigm differs substantially from those based on the "standard" approaches: rather than being explicitly "programmed" with rules like in conventional programming, NN generally learn from "experience" ([Peterson & Rognvaldsson, 1991](#)).

A NN is a mathematical model with a distributed architecture, i.e. it consists of an interconnected ensemble of simple processing elements, units or nodes which communicate by sending signals to each other through a large number of weighted connections, similar to the synaptic communication in the nervous system. The processing ability of the NN is stored in the strengths of these connections, the so called weights, obtained through a process of learning from a set of training patterns. Indeed the weights are adaptable parameters which are able to modify the signals that pass along them.

The main components of a NN are the following (Rumelhart & McClelland, 1986; Kröse et al., 1993):

- a set of processing units, also called "neurons";
- a state of activation  $x_k$  for each unit, which correspond to the output of that unit;
- the connections between the neurons, defined through a weight  $w_{jk}$  which quantifies the effect that the signal of unit  $j$  has on unit  $k$ ;
- an external input, called "bias" or "offset",  $\theta_k$  for every unit;
- a propagation rule to calculate the effective input  $s_k$  of a unit from its weight and bias and the output of the previous neuron;
- an activation function  $F_k$ , which is applied to the effective input  $s_k$  and provides the output of the unit  $x_k$ ;
- a learning rule to update the weights and biases;

In order to address many different kinds of problems, a large variety of NN types exist, but one can in general divide them into two broad classes: supervised and unsupervised. The first one refers to NN which attempt to understand the relationship between data and the parameter domain, while the latter corresponds to NN employed to discover “natural” groupings in a set of data independently of external constraints. However both the classes

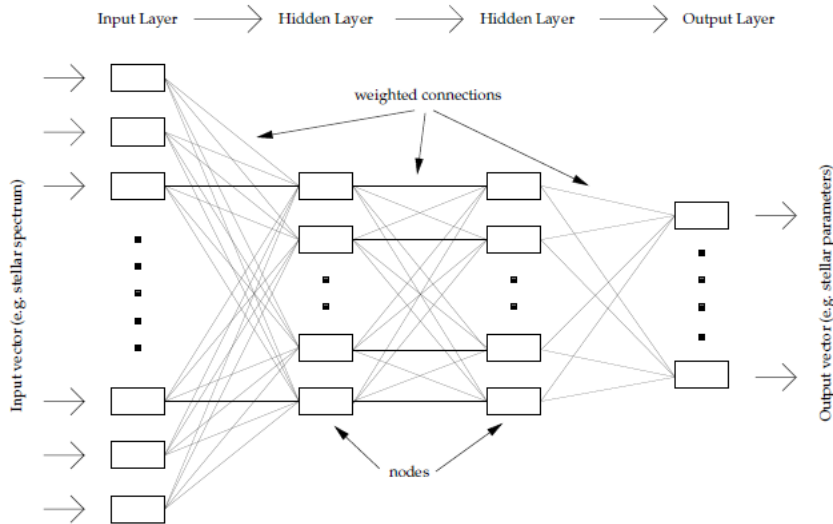


**Figure 8.1.1:** from *Bailer-Jones et al. (2001)*. Feedforward artificial NN architecture. In this case the NN consists of two hidden layers.

of NN share the idea of gathering information on a problem through the relationships that are intrinsically present in the data, rather than using a set of given rules.

A basic but very important type of supervised NN is the so called feedforward multilayer perceptron or simply feedforward NN. The historical term perceptron comes from the function performed by the units. This kind of NN can be trained to learn arbitrarily complex relationships between the data and a parameter domain and therefore it can be employed to solve both classification and interpolation problems.

Figure 8.1.1 provides an example of a multilayer Perceptron: it is composed by layers of nodes, represented as rectangles, which receive their inputs from the neurons in the layer in the left and send their output to the neurons in the right. Every node in a layer is linked with all the nodes in the adjacent layers, but no connections are present among units within a layer. Each node performs a twofold task: compute the output signal from the input and perform the progressive adjustment of the weights and biases.

Three types of units can be distinguished within a NN: the input units which receive the data from outside the NN, the output units which send the data out of the NN and the hidden units whose signals (both in input and output) remain within the NN.

In the example application of figure 8.1.1 from Bailer-Jones et al. (2001), the input vector,  $(x_1, x_2, \dots, x_i, \dots)$ , represents the stellar spectrum, while the output,  $(y_1, y_2, \dots, y_l, \dots)$ , is a vector containing stellar parameters.

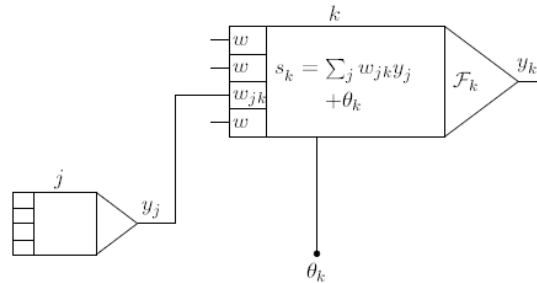


**Figure 8.1.2:** from Kröse et al. (1993). The basic components of NN. The propagation rule in this example is the "standard" weighted summation.

The  $N^{[0]}$  values of inputs layer are directly fed into the  $N^{[1]}$  units of the first hidden layer without any further operation. On the contrary, each of the hidden nodes sums the weighted signals received from its input links plus a bias and returns an output signal that is a non-linear function of this net input. Explicitly, for a unit  $k$  in the layer  $t$ , the effective input is:

$$s_k^{[t]} = \sum_{j=1}^{N_{t-1}} w_{kj}^{[t]} x_j^{[t-1]} + \theta_k^{[t]} \quad (8.1.1)$$

where  $x_j^{[t-1]}$  are the values stored in the  $(t-1)$ th layer,  $\{w_{kj}^{[t]}, \theta_k^{[t]}\}$  are the weights and biases respectively on the  $t$ -th layer and  $N_{t-1}$  is the number of nodes in the  $(t-1)$ th layer. The units with the propagation rule 8.1.1 are called sigma units.

Once the total input is evaluated, one needs a non-linear function  $F^{[t]}$  that takes  $s_k^{[t]}$  and provides the output of the unit  $k$  of the  $t$  layer,  $x_k^{[t]}$ :

$$x_k^{[t]} = F_k^{[t]}(s_k^{[t]}) \tag{8.1.2}$$

These values are then passed to the following hidden layer that performs a similar operation and this process continues until the last hidden units, whose outputs are fed into an output units layer.

The most commonly used activation functions are shown in figure 8.1.3.

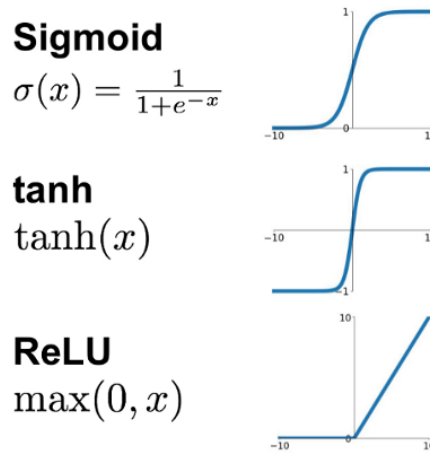


**Figure 8.1.3:** Examples of activation functions

The weights  $w_{kj}$  and the biases  $\theta_k$  appearing in equations 8.1.1 are the free parameters of the NN. They have to be opportunely adjusted to proper values in order for the NN to provide the right output to a given input. This goal is achieved by training the NN on a set of inputs, called training data, labelled with the correct target values. In this way the NN can progressively learn the relationship between the input features and associated parameters of the model. Once the NN is trained, one can obtain a reliable classification or interpolation for a new set of data provided that they are of the same type of the training data.

The supervised learning is performed through the minimization of an error function, called Loss, with respect to all of the weights and biases of the NN. Thus, first of all one has to define the Loss function  $L^{(i)} = L(\bar{y}^{(i)}, \bar{T}^{(i)})$  which for a single input vector,  $i$ , is a function of the values  $\bar{y}^{(i)}$  resulting from the output layer and the corresponding targets  $\bar{T}^{(i)}$  (or labels, the "real" value the NN tries to reproduce). The loss function typically used is the total

quadratic error:

$$L^{(i)} = \sum_{j=1}^{N_o} (y_j^{(i)} - T_j^{(i)})^2 \quad (8.1.3)$$

Then, in order to train the NN, the so called backpropagation algorithm (Rumelhart & McClelland, 1986) is exploited which consists in the evaluation, making use of the chain product rule, of the gradients of the Loss function with respect to each of the  $w_{jk}$  and  $\theta_k$  in the NN. Indeed, the latter can be calculated by propagating the error dependency back through the NN to that weight or bias. This can be carried on up to the input layer, providing the gradient vectors of the Loss  $\left(\frac{\delta L}{\delta \mathbf{w}}, \frac{\delta L}{\delta \boldsymbol{\theta}}\right)$ , with respect to the complete set of weights and biases  $(\mathbf{w}, \boldsymbol{\theta})$ . This can be finally used to update the weights and biases in different ways. The most common is the gradient descend method where the weight or bias vector is adjusted in the direction of the opposite of the gradient vector:

$$\Delta \mathbf{w} = -\alpha \frac{\delta L}{\delta \mathbf{w}} \quad , \quad \Delta \boldsymbol{\theta} = -\alpha \frac{\delta L}{\delta \boldsymbol{\theta}} \quad (8.1.4)$$

where  $\alpha$  is the learning rate and determines how large a step is made.

The Loss and the corresponding gradients are then recalculated with the new values of the weights and biases. This training algorithm is applied successively to each of the vectors in the training sample (a complete pass through the training dataset is called "epoch").

Alternatively, one can keep the weights and biases fixed and update them only after the Loss have been evaluated for all the vectors of the training data. In this case, known as "batch training", the update is performed with the Cost function, i.e. the average of the Loss over all the training examples:

$$C = \frac{1}{m} \sum_{i=1}^m (L^{(i)}) \quad (8.1.5)$$

where  $m$  is the number of training data.

Apart from the quadratic error, other examples of Cost functions are (considering for simplicity one output node) the Root Mean Square Error (RMSE)

$$RMSE = \sqrt{\frac{\sum_{i=1}^m (y^{(i)} - T^{(i)})^2}{m}} \quad (8.1.6)$$

and the Mean Square Logarithmic Error (MSLE)

$$MSLE = \frac{1}{m} \sum_{i=1}^m (\ln(y^{(i)} + 1) - \ln(T^{(i)} + 1))^2 \quad (8.1.7)$$

Finally, repeating this training process for many iterations leads to  $w_{jk}$  and  $\theta_k$  which

give an asymptotically small value of the Loss/Cost function.

In summary, the learning procedure is schematically described by the following steps (Duch & Diercksen, 1994):

1. initialize the NN parameters by setting the biases  $\theta$  to zero and the weights  $\mathbf{w}$  to small random values (other choices are also possible)
2. feed-forward pass where the output of the NN is calculated using the current values of the weights and biases,
3. backward propagation where the errors of the output are propagated back to the input layer and the weights and biases are updated as a function of the these back-propagated errors.
4. test the convergence with a stopping criterion: if this is not fulfilled then the process is repeated from the step 2.

## **8.2 EOS inference through NN: previous works**

A new method that employs deep NN to deduce the EOS of NS from a set of mass-radius,  $(M, R)$ , observational data, was firstly developed by Fujimoto et al. (2018).

This new approach is complementary to the Bayesian analysis and it allows to deal with observational  $(M_i - R_i)$  points that come with errors which introduce a shift with respect to the "real"  $M - R$  relation. Indeed the NN provides a mapping from a finite set of data with observational uncertainties onto an EOS.

First of all, one needs to generate the training data and feed them into the NN: the latter consists of a series of randomly generated EOS parameters and a set of corresponding simulated observations  $(M_i, R_i)$ , which are, respectively, the output and input of the NN.

Fujimoto et al. (2018) parametrized the EOS using a piecewise polytrope with five segments and characterizing each piece with a value of the squared sound speed  $c_s^2$ . The latter, which are the parameters of the analysis, are randomly sampled to generate  $N_{EOS}$  EOSs: for each of them, solving the TOV equation, they obtain the  $M - R$  curve and the corresponding maximum mass  $M_{max}$ , rejecting the EOSs with  $M_{max} < 1.97M_\odot$ .

At this point, for each EOS and its  $M - R$  curve, they sample  $N_o$ , equal to the number of observations employed, observational points  $(M_i^0, R_i^0)$  from a uniform distribution  $[1M_\odot, M_{max}]$ .

In order to take into account the observational error, a shift in mass  $\Delta M$  and radius  $\Delta R$  are randomly generated according to Gaussian distributions with variances  $0.1M_\odot$  and  $0.5$  km (in case real data are employed, the variances have to correspond to the experimental error). As a consequence, each training data is made of  $N_o$  pairs of "observations",

$(M_i = M_i^0 + \Delta M, R_i = R_i^0 + \Delta R)$ . This procedure is repeated  $n_s = 100$  times for each of the  $N_{EOS} = 2000$  EOSs, resulting, finally, in a training set composed by  $(N_{EOS} \times n_s)$  vectors. Once the NN is trained, it can provide one EOS as output given one observation of  $N_o$  neutron stars,  $(M_i, R_i)$  as input.

This new method was tested using independent validation data, i.e. each set of  $N_o$  points which are considered as mock data of the NS observation. For each vector of  $N_o$  observations in the validation set, the most probable EOS is reconstructed and compared with the corresponding genuine  $M - R$  curve. To provide a quantitative estimate of the accuracy, the RMS of radius deviations between the real and the reconstructed curves is evaluated for different values of the mass:  $\delta R(M) = R^{(rec)}(M) - R^0(M)$ . Fujimoto et al. (2018) found values  $\sim 0.1$  km for all the considered masses, relevantly smaller with respect to the variance of the observations,  $\Delta R \sim 0.5$  km.

In Fujimoto et al. (2020) this new method was applied for the first time to real observational data from 14 X-ray sources (Özel & Freire, 2016). They made use of the marginalized distributions with respect to  $M$  and  $R$  fitted by Gaussians. Since a Gaussian is identified by two parameters, the mean and the variance, each source is characterized by four parameters, for a total of  $2 \times 2 \times 14 = 56$ .

Unlike the previous work, in Fujimoto et al. (2020) the variances for the training set, labelled as  $\sigma_{M_i}$  and  $\sigma_{R_i}$ , are also randomly sampled from uniform distributions with ranges  $[0 - 1M_\odot)$  and  $[0, 5\text{km})$ , respectively.

They found results which are consistent both with the conventional nuclear models and with the constraints coming from GW observations. Concerning the deduced sound velocities, they obtained a value smaller than  $\frac{1}{\sqrt{3}}$ , which thus fulfill the conformal limit, in the range  $\rho \lesssim 2\rho_0$ . Above  $2\rho_0$ , the sound velocity increases up to a saturation point at  $\sim 4\rho_0$ .

Recently, Morawski & Bejger (2020) further improved the aforementioned approach: to better mimic the astrophysical observations, they sampled the points on the  $M - R$  curve using a realist mass PDF based on the available data on NS in the Galaxy. This distribution is a double-Gaussian (Alsing et al., 2018) where the main peak is located around the Chandrasekhar mass while the second at  $M \sim 2M_\odot$ .

In addition, Morawski & Bejger (2020) extended the analysis of applications of the NN to multi-messenger astrophysics investigating the problem of EOS reconstruction and simulating, using the tidal deformability as input, the case in which only data from GW measurements are considered.

Finally, the relation between the NN method and the Bayesian analysis was discussed in Fujimoto et al. (2018). This comparison will be also one of the main subject of our work in section 8.4.

In the NN approach, given the parameters  $\theta$  in the parameter space  $\Theta$ , the probability to generate an EOS is described by  $Pr(\theta)$ . The data  $D = \{(M_i, R_i)\}$  for each EOS are then sampled from the observational distribution  $Pr(D|\theta)$ . Finally the loss function  $\ell(\theta, D)$  "connects" the output parameters  $\theta$  with the input data  $D$ , through the NN  $f(D|\mathbf{W})$ , where  $\mathbf{W}$  are the fitting parameters. Thus, putting all the element together, one finds that the training process consists in minimizing the total loss function:

$$L[f] = \int \delta\theta \delta D Pr(\theta) Pr(D|\theta) \ell(\theta, f(D)) \quad (8.2.1)$$

Using the definitions from the Bayesian analysis, here  $Pr(\theta)$  is the prior distribution of the EOS and  $Pr(D|\theta)$  is the likelihood function. Therefore the posterior PDF is just  $Pr(\theta|D) = Pr(\theta)Pr(D|\theta)$ . To calculate the most probable EOS, one can use the maximum a posteriori estimator (MAP),

$$f_{MAP}(D) = \arg_{\theta} \max Pr(\theta) Pr(D|\theta) \quad (8.2.2)$$

and the result is an approximation of the  $f$  that minimizes 8.2.1. Therefore [Fujimoto et al. \(2018\)](#) concluded that the Bayesian analysis can be regarded as a limit of the more general NN approach.

A different application of the machine learning and NN has been suggested by [Ferreira & Providência \(2019\)](#): they used Support Vector Machines Regression and NN to mimic the non-linear maps between NS observables and the EOS. The purpose is to study the impact of the different nuclear matter parameters on the NS observables and analyze the correlations.

Once the non-linear functions between the empirical parameters and the NS observables is learned, one can measure how much the prediction error on the test set changes as a consequence of randomly permuting the value of each empirical parameter. The more the prediction error increases, the more important is the impact of that parameter on the non-linear map.

### 8.3 Abstracts

This work concerns the study of the quark matter and the structure of the resulting QsS within the two family scenario (see 3.3). The EOS is modelled using the CSS parametrization

(Drago et al. (2019), see the discussion of section 3.2.5 and 3.2.6):

$$p = c_s^2(e - e_0) \tag{8.3.1}$$

where  $e_0$  is the energy density at zero pressure. To constrain the parameters of the EOS, we employ the mass and radius ( $M - R$ ) PDFs from a set X-ray sources and also the mass and tidal deformability estimates ( $M - \Lambda$ ) from GW events. We use two different parameter estimation methods, i.e. the Bayesian analysis and NN based method described in chapter 8.2.

In paper I (8.4), we present the results obtained using both the approaches, in the case in which the sound velocity is fixed at  $c_s^2 = \frac{1}{3}$  and the only parameter is  $e_0$ , and in a second case where we allow also  $c_s^2$  to change freely. The main focus of paper I is the comparison between the two inference methods: we find that the respective results and the estimated errors are consistent among each other and therefore the new NN approach is a powerful recipe complementary to the standard Bayesian analysis.

In paper II (8.5), we concentrate on the values obtained for the sound speed in the two parameter case. Indeed, the difficulties to reconcile the current high masses measurements with the conformal limit suggested by QCD calculations, is present in many models and has been matter of discussion in the recent years (see section 3.2.5). We find that not only this is possible in the context of the two families scenario, but it is also suggested as the most valuable solution to fit the observations. Indeed, we obtain that the most probable value of the squared sound speed indicated by our Bayesian analysis sit very close to  $c_s^2 = \frac{1}{3}$ .

## 8.4 *Structure of Quark Star: A Comparative Analysis of Bayesian Inference and Neural Network based modelling*

The link between astrophysical observations and nuclear physics is usually expressed through the one-to-one relation between the EOS and the ( $M - R$ ) sequence, calculated by solving the TOV equations (see the Introduction of this thesis and chapter 1.4). Recently, the tidal deformability ( $\Lambda$ ) has also been added as a complimentary observable to the radii measurements (Hinderer (2008); Damour & Nagar (2009); Hinderer et al. (2010), see chapter 4). Thus, the EOS can also be mapped into the  $M - \Lambda$  plane. The most widely adopted approach to estimate the EOS is to build a model containing a number of parameters. The latter can be partially constrained a priori by physical considerations and then, they are systematically updated using the observational data through the Bayesian inference methods (for further details see chapters 7.1, 7.5.2 and 8.4.3). Unfortunately, the performances of this

analysis are limited by the existence of only a few observational points, which are also not optimally distributed throughout the  $M - R$  plane to investigate the whole possible EOS range. Therefore, it is very useful to develop new methodologies which can be complimentary to the standard method for parameter estimation. Lately, approaches based on machine learning have gained popularity as an alternative procedure with applications in many branches of physics, e.g. high energy physics or astrophysical data analysis. In particular, as explained in details in chapter 8.2, Deep learning methods employing NN have been used to infer the EOS of dense matter (Fujimoto et al., 2018, 2020; Morawski & Bejger, 2020).

In this work, we want to present a comparative study between the NN based prediction and the Bayesian parameter estimation. In addition, we study the properties and the structure of Qs within the two families scenario, as a followup work to the previous analysis on HSs described in chapter 7.

#### 8.4.1 Quark Stars within the two families scenario

The two families scenario is based on the hypothesis of strange quark matter being absolutely stable and this allows to obtain an EOS branch made of very massive Qs with maximum mass of about  $\sim 2.2M_{\odot}$  (see chapter 3.3). The latter are here the objects of our investigations. For simplicity, we use a CSS parametrization to describe the EOS of Qs (Alford et al. (2013); Zdunik & Haensel (2013); Chamel et al. (2013); Drago et al. (2019), see sections 3.2.4, 3.2.5 and 3.2.6) where the relations between the energy density, the pressure and baryon density are:

$$p = c_s^2 (e - e_0), \quad (8.4.1)$$

$$p = \frac{c_s^2 e_0}{c_s^2 + 1} \left( \left( \frac{n}{n_0} \right)^{c_s^2 + 1} - 1 \right). \quad (8.4.2)$$

Here,  $n_0$  and  $e_0$  are the baryon density and the energy density at zero pressure, respectively. Three are the main quantities contained in this parameterization:  $n_0$ , the speed of sound  $c_s$  and the energy per baryon  $(E/A)_3 = e_0/n_0$ . The accepted range of the energy per baryon is due to the limits for the stability of the two-flavor and three-flavor (or strange) quark matter. The absolute stability of strange quark matter is realized with the condition  $(E/A)_3 < 930$  MeV, while, in order to prevent the decay of  $\text{Fe}^{56}$  in two-flavor quark matter  $(E/A)_3 > 830$  MeV (Weissenborn et al. (2011); Drago et al. (2019), for further details see section 3.2.6). Concerning the speed of sound, in hadronic matter it is usually less than  $\sqrt{1/3}$  because the EOS is soft, but in quark matter theoretical calculations suggest that at high densities it should tend to the conformal limit of  $\sqrt{1/3}$ , required by the asymptotic freedom of QCD (Bedaque & Steiner, 2015). The validity of this theoretical constraint is currently an object

of discussion and many papers have tested it against the recent astrophysical data on massive pulsars and tidal deformability limits inferred from the GW signal from BNS mergers (Reed & Horowitz, 2020; Annala et al., 2020; Marczenko, 2020). We will further discuss the conformal limit in the context of the two families scenario in chapter 8.5

### **Calculation of the Structure**

The structure of a static QS is modelled using the TOV equations of 1.4.1 and 1.4.2 described in section 1.4.

In addition, we calculate the tidal deformability of the QS, defined as in equation 4.1.3:

$$\Lambda = \frac{2}{3}k_2 \left( \frac{R}{M} \right)^5, \quad (8.4.3)$$

where  $k_2$  is called tidal Love number and it associated to the quadrupolar tidal perturbation. The  $k_2$  can be evaluated through the expression:

$$\begin{aligned} k_2 = & \frac{8C^5}{5}(1-2C)^2[2+2C(y-1)-y] \\ & \times \left\{ 2C[6-3y+3C(5y-8)] + 4C^3[13-11y+C(3y-2)+2C^2(1+y)] \right. \\ & \left. + 3(1-2C)^2[2-y+2C(y-1)] \ln(1-2C) \right\}^{-1}. \end{aligned} \quad (8.4.4)$$

where,  $y$  is the solution of the equation:

$$\frac{dy}{dr} = -\frac{y^2}{r} - \frac{r+4\pi r^3(p-e)}{r(r-2m)}y + \frac{4(m+4\pi r^3p)^2}{r(r-2m)^2} + \frac{6}{r-2m} - \frac{4\pi r^2}{r-2m} \left[ 5e+9p + \frac{e+p}{(dp/de)} \right]. \quad (8.4.5)$$

for  $r = R$ . Since the QSs present a sharp discontinuity of the energy density in correspondence with the surface, the value of  $y(R)$  needs a correction term as:

$$y = y(R) - \frac{4\pi R^3 e_-}{M}. \quad (8.4.6)$$

where  $e_-$  represents the energy density just inside the surface (Hinderer et al., 2010; Postnikov et al., 2010; Takátsy & Kovács, 2020).

#### **8.4.2 Observational Data: Candidate Quark Stars**

Here, we list the sources employed in our analysis. We use some of the X-ray sources from Özel et al. (2016) selected on the basis of their masses.

Three types of binaries are possible, in the context of the two families scenario: HS-HS,

HS-QS, QS-QS. For each of the different combinations we have provided an estimate of the threshold mass in De Pietri et al. (2019) (described in chapter 5): we found for the HS-HS case  $M_{thr} \sim 2.5M_{\odot}$ . Since GW170817 did not result in a prompt collapse, we can interpret it only as a HS-QS merger (for further details see section 5.6). Therefore we have to classify the high-mass component of this binary as a QS and we label it as GW170817\_1. Next, we marginalize the PDF of the mass for this object from the multidimensional posterior and find a mean value of  $1.49M_{\odot}$ . Thus, one can hypothetically identify as QSs all the sources having a mean of the marginalized mass PDF,  $M \gtrsim M_{GW170817\_1}$ . Explicitly, we have used 4U 1820–30, 4U 1724–07, 4U 1702–429, J0437–4715, SAX J1748.9 2021, GW170817\_1, GW190425\_1 and GW190425\_2.

As in chapter 7.5, we mimic the posterior of the sources which do not have a full distribution available, with the bivariate Gaussian distribution of equation 7.5.5: in this case 4U 1702–429 (Nättilä et al., 2017) and J0437–4715 (Gonzalez-Caniulef et al., 2019). The first one, as before, has  $\mu_R = 12.4\text{km}$ ,  $\mu_M = 1.9M_{\odot}$ ,  $\sigma_R = 0.4\text{km}$ ,  $\sigma_M = 0.3M_{\odot}$  and  $\rho = 0.9$ , to represent the correlation between the measurements. For J0437–4715, we use  $\mu_R = 13.6\text{km}$ ,  $\mu_M = 1.44M_{\odot}$ ,  $\sigma_R = 0.85\text{km}$ ,  $\sigma_M = 0.07M_{\odot}$  and  $\rho = 0.0$ , because in this case the mass and radius measurements are independent. We have selected this particular source although its mass is lower than  $M_{GW170817\_1}$ , because its radius is larger than  $\sim 13\text{ km}$  and, in our scheme, HSs can not be characterized by such large radius. As a consequence, J0437–4715 is interpreted as a QS.

Concerning the GW sources, we directly use the PDF for their individual  $\Lambda$ s, because the corresponding  $M - R$  posterior (which we employed in Traversi et al. (2020) for GW170817) is calculated assuming certain universal relations which are not valid for QSs and also postulating the same EOS for both the component of the binary <sup>1</sup>.

The same set of sources is obtained also following a second criterion. As explained in section 3.3.2, at a given baryonic mass, QSs have a lower gravitational mass than HSs, of about  $0.1M_{\odot}$  smaller. Therefore the transition from HSs to QSs is energetically favoured and it implies the existence of a minimum mass for the QSs branch,  $M_{min}^{QS} \sim M_{max}^{HS} - 0.1M_{\odot}$  and the coexistence of both HSs and QSs in the range  $[M_{min}^{QS}, M_{max}^{HS}]$ . In this interval HSs and QSs can have the same mass but different radii.

To identify the QSs, we first select J0437–4715 as QS, again because of its radius: the central value of its mass is  $\sim 1.45M_{\odot}$  which we choose as a guess for  $M_{min}^{QS}$ . Thus  $M_{max}^{HS}$  is fixed to  $M_{min}^{QS} + 0.1 \sim 1.55M_{\odot}$  and all the sources with masses  $\gtrsim 1.55M_{\odot}$  can be interpreted as QSs (as before the masses are intended as the mean values of the marginalized distributions of the sources). This criterion is fulfilled by all the sources which we have selected in this work apart from GW170817\_1, whose mass ( $\sim 1.49M_{\odot}$ ) falls in the coexistence region

---

<sup>1</sup>The data from GW170817 and GW190425 can be found at <https://dcc.ligo.org/LIGO-P1800115/public> and, <https://dcc.ligo.org/LIGO-P2000026/public>

$[M_{min}^{QS}, M_{max}^{HS}]$ . However, GW170817\_1 is a QS because of the phenomenological reasons previously described.

### 8.4.3 Bayesian Inference

We follow the Bayesian framework described in section 7.5.2. In this case we have:

$$P(e_0, c_s^2 | \text{data}) = CP(\text{data} | e_0, c_s^2)P(e_0)P(c_s^2), \quad (8.4.7)$$

where  $P(e_0)$ ,  $P(c_s^2)$  are the priors probability for  $e_0$  and  $c_s^2$  and

$$P(\text{data} | e_0, c_s^2) = \prod_{i=1}^{N-3} P_i(M_i, R_i | e_0, c_s^2) \prod_{j=1}^{N-5} P_j(M_j, \Lambda_j | e_0, c_s^2) \quad (8.4.8)$$

is the likelihood function that expresses the probability to generate this  $N$  observations provided a particular set of parameters for the EOS. Again, to estimate the the probability of the realization of  $(M, R)$  or  $(M, \Lambda)$  for a particular source given an EOS, we take the maximum among the likelihoods calculated for each configuration of the  $M - R$  or  $M - \Lambda$  sequences associated to that EOS:

$$P_i(M_i, R_i | \text{data}) = P_{\max}(M_i, R_i | e_0, c_s^2, e_c) \quad \text{or,} \quad P_i(M_i, \Lambda_i | \text{data}) = P_{\max}(M_i, \Lambda_i | e_0, c_s^2, e_c), \quad (8.4.9)$$

Here, the  $M - R$  and  $M - \Lambda$  curves for a given EOS are parameterized using the central energy density ( $e_c$ ) of the QS. Finally, we perform the Markov-Chain Monte Carlo (MCMC) simulations in order to populate the PDF of equation 8.4.7 exploiting the python emcee package (Foreman-Mackey et al. (2013), see section 7.1).

### 8.4.4 Deep Learning

Deep learning is mainly used to generate a complex non-linear mapping connecting the input and output. It exploits trained NN in order to predict the most probable output for a given input. Concerning the EOS inference, the advantage of NN consists in their multilayered structure that is able to reproduce the non-linear nature of the inversion mapping linking the  $M - R$  relation to the EOS, avoiding the uncertainties connected to the assumption of a specific fitting function. This non-linear mapping is expressed trough the transformation of equations 8.1.1 and 8.1.2, which are applied iteratively between subsequent layers (for an basic introduction on NN see section 8.1). Then, for the training procedure, one has to choose and progressively minimize a loss function.

In this work, we mostly follow the method developed in Fujimoto et al. (2018, 2020) and described in chapter 8.2.

### Preparation of Training, Validation and Test Data

In order to generate the training and the validation data set, we randomly choose a number ( $N_{\text{EOS}}$ ) of parameter sets, we build the corresponding EOSs and evaluate the  $M - R$  and  $M - \Lambda$  sequences. Since our QSs are massive, we consider only the configurations on the curves having masses within  $[1.3M_{\odot}, M_{\text{max}}]$ . Then, using a uniform distribution of mass in the aforementioned range, we sample 8 data points which represents the sources listed in section 8.4.2. We now have 5  $(M_i^0, R_i^0)$  points and 3  $(M_i^0, \Lambda_i^0)$  points. Since we want the NN to learn the observational uncertainties associated with the sources and to connect with the "true" sequence, we need to introduce shifts on the points sampled on the curves. Using the set of  $(\sigma_M, \sigma_R)$  and  $(\sigma_M, \sigma_{\Lambda})$  obtained from the marginalized distribution of the observational data, we construct Gaussian distributions for the mass having mean at  $M_i^0$  and standard deviation  $\sigma_M^i$ , for the radius having mean at  $R_i^0$  and standard deviation  $\sigma_R^i$  and for the tidal deformability having mean at  $\Lambda_i^0$  and standard deviation  $\sigma_{\Lambda}^i$ . Those distributions are then used to sample 5 new couples of  $(M_i, R_i)$  and 3 couples of  $(M_i, \Lambda_i)$ . In such manner, the errors of the real observational data is taken into account. Next, this last step is repeated, for each of the sampled EOS, a large number ( $N_s$ ) of times, in order to finally generate  $N_{\text{EOS}} \times N_s$  training data. The latter are vectors composed of 16 entries including the masses, radii and tidal deformabilities  $(M_i, M_j, R_i, \Lambda_j; i = 1, 2, \dots, 5; j = 6, 7, 8)$ . The validation and the test set are produced by repeating the same procedure but with smaller  $N_{\text{EOS}}$  and  $N_s = 1$ . Finally, our training set is characterized by a size of  $2000 \times 100$  in the 1D case and of  $10000 \times 100$  in 2D whereas the validation and test set are  $1000 \times 1$  in both cases. Once the NN is trained, it should be able to return the value of the "real" EOS parameters when fed with the mean values of the marginalized PDFs of the masses and radii/tidal deformabilities of the chosen sources.

### Features of the Neural Network

In this section, we describe the details of the NN built for our analysis. We use Scikit-learn (Pedregosa et al., 2011) and the Keras (Chollet, 2015) Python package with TensorFlow (Abadi et al., 2016) as a backend. In Table 8.1, we summarize the structure of our NN.

Layer index	nodes	activation
0	16	N/A
1	50	ReLU
2	50	ReLU
3	50	ReLU
4	1/2	tanh

**Table 8.1:** Construction of the NN in this study. 16 neurons at the input layer correspond to 5 pairs of mass and radius and 3 pairs of mass and tidal deformability.

	Bayes 1P	NN 1P	Bayes 2P	NN 2P
$e_0$ (MeV fm <sup>-3</sup> )	191.84	191.04	183.48	191.29
$c_s^2$	1/3	1/3	0.306	0.38
$M_{max}(M_\odot)$	2.18	2.19	2.13	2.37
$R_{M_{max}}$ (km)	12.01	12.03	12.00	12.42
$R_{1.6}$ (km)	12.10	12.12	12.20	12.26
$\Lambda_{1.6}$	368	373	382	417

**Table 8.2:** Features of the most probable EOS obtained with the Bayesian analysis (Bayes) and the NN method (NN) in the one parameter (1P) and two parameter (2P) case. The inferred values are specified together with the corresponding maximum mass ( $M_{max}$ ) star and its radius ( $R_{M_{max}}$ ) and for the  $1.6M_\odot$  configuration, the radius ( $R_{1.6}$ ) and the tidal deformability ( $\Lambda_{1.6}$ ).

The number of neurons contained in the input layer is the same as the observable of the selected sources (here 16), while in the output layer the number of neurons equals the one of the EOS parameters (here 1 or 2). To normalize the features of the training, validation and test set, we use the 'StandardsScaler' function of Scikit-learn while the labels (the corresponding EOS parameters) are normalized with the uniform normalization ( $y_{norm} = \frac{y-y_{min}}{y_{max}-y_{min}}$ ).

For the output layer, we chose 'tanh' as activation function in order to obtain a normalized output which can be converted back to the standard parameter values afterwards. For the inner layers, we use the common 'ReLU' function (see Figure 8.1.3). As loss function, we select the mean squared logarithmic error (MSLE) of equation 8.1.7.

To optimize our NN, we employ the standards 'Adam' algorithm (Kingma & Ba, 2014) along with the mini-batch training with a size of 128. Finally, we chose the Glorot uniform distribution (Glorot & Bengio, 2010) as initialization for the NN parameters. In addition, for the 2-parameter case, we include a 'l2' regularization. The selected learning rate is  $\alpha = 0.005$ . Because of our limited computational resources, we could not perform the hyperparameter tuning which we plan to include in future analyses.

The errors in the NN prediction are estimated using the root mean squared error of equation 8.1.6 estimated on the test set. In the 2D analysis, we calculate the RMSEs separately for each of the EOS parameters then we construct a 2D Gaussian using the RMSEs as sigmas. From that distribution, we calculate the 68% CI and the corresponding quantities.

#### 8.4.5 Results and discussions

In the following, we present the results of the Bayesian and the NN analyses with the methodology described in sections 8.4.3 and 8.4.4 respectively for two different cases: in the first, we keep the  $c_s^2$  fixed and we vary only the  $e_0$ , and then considering both of them as

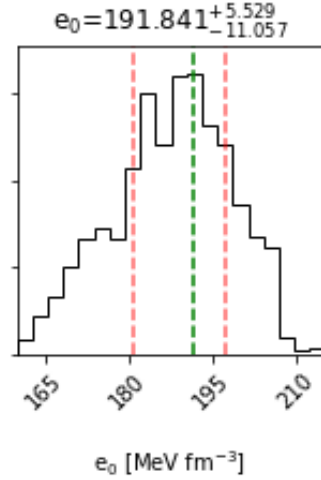


**Figure 8.4.1:** PDF for the parameter  $e_0$  from the Bayesian analysis. The green line is placed on the mode of the distribution, while the red line represent the 68% CI.

free parameters. The goal of this last case is to understand which value of the  $c_s^2$  is the most suitable to fit the astrophysical data within our model. Only after that, we check whether or not the result from our analysis is able to fulfill the conformal limit indicated by QCD calculations.

Since the most massive pulsar which has been observed up to now has a mass of  $2.14^{+0.10}_{-0.09} M_\odot$  (Cromartie et al. (2019), see section 2.3.1), we impose a strict lower bound of  $2.05 M_\odot$  (the lower edge of the 68% CI) for the maximum mass in our study. We employ all the sources described in section 8.4.2. The resulting one and two dimensional PDFs for the EOS parameters are visualized using the python corner.py package (Foreman-Mackey, 2016) and the features of the most probable EOSs are summarized in Table 8.2.

### **One parameter case: $e_0$**

First of all, we describe the simplest case in which the only parameter is  $e_0$ , having a prior range between 160 and  $232 \text{ MeV fm}^{-3}$ , that corresponds to the acceptable interval in  $(E/A)_3$  for the Witten conjecture to hold true. The value of squared speed of sound is kept fixed at  $c_s^2 = 1/3$ . We see immediately that values of  $e_0$  larger than  $\sim 220 \text{ MeV fm}^{-3}$ , leading to the softest possible EOSs, are ruled out "a-priori" by the maximum mass limit. Figure 8.4.1 shows the most probable  $e_0$  from the Bayesian calculation, along with the  $1\sigma$  error. The PDF peaks at  $191.841 \text{ MeV fm}^{-3}$ . The sequence corresponding to most likely value of  $e_0$  has a maximum mass of  $2.18 M_\odot$ , and a radius for the  $1.6 M_\odot$  configuration  $R_{1.6} = 12.10 \text{ km}$ . From our trained NN, we obtain the predicted value  $e_0 = 191.04 \text{ MeV fm}^{-3}$ , basically equivalent to the result from the Bayesian analysis, with an error estimated on the test

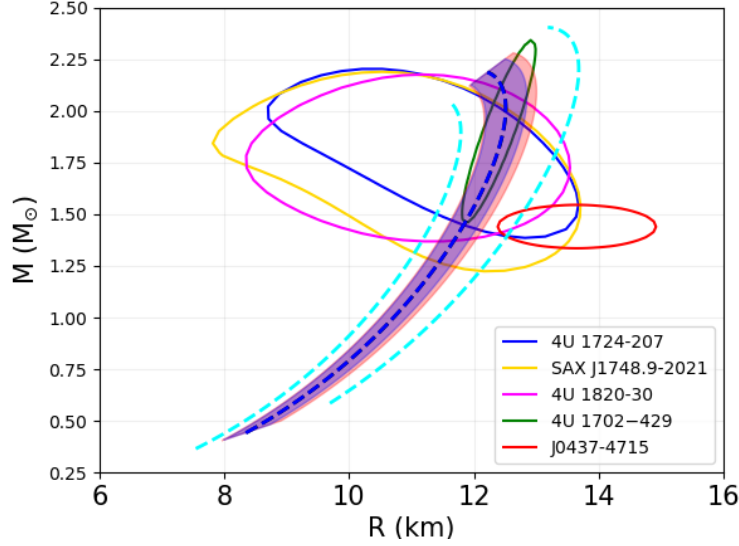


**Figure 8.4.2:** Comparison between the  $M$ - $R$  curve obtained with the two methods employed. The red and blue shaded regions correspond to the 68% CI predicted by the Bayesian analysis and NN respectively. The two most probable configurations, which are indistinguishable, are plotted as the dashed blue line. Finally, the dashed cyan lines represents the border of the allowed parameter space.

set of  $\text{RMSE} = 10.03 \text{ MeV fm}^{-3}$ . This EOS is characterized by  $M_{max} = 2.19M_{\odot}$  and  $R_{1.6} = 12.12 \text{ km}$ . In Figures 8.4.2 and 8.4.3, we show the comparison between the 68% CI from the distributions of the sources and the one from the PDFs obtained with the Bayesian calculation (shaded red) and with the NN (shaded blue), in the  $M - R$  and  $M - \Lambda$  planes, respectively. The dashed cyan line represents the allowed parameter space. Notice that the most probable curve from the Bayesian inference is coincident with the predicted value from the NN (both dashed blue) and also the errors are very similar. Moreover, the maximum masses of the most likely EOSs are consistent with the range suggested in Rezzolla et al. (2018). The outcomes of our analyses is exactly what we expect when comparing the two methods.

At 68% CI, the results are not compatible with the source J0437-4715 and also the GW170817\_1. The reason is that these two sources point in different directions: while GW170817\_1 indicates a small radius, J0437-4715 suggests a larger radius. Thus, our results sit on the intermediate values which allow the EOSs to be consistent with both the sources at 90% CI.

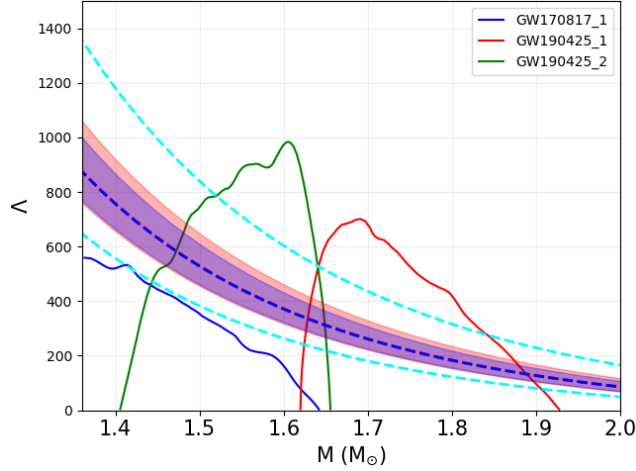


**Figure 8.4.3:** Comparison between the  $M$ - $\Lambda$  curve obtained with the two methods employed. The red and blue shaded regions correspond to the 68% CI predicted by the Bayesian analysis and NN respectively. The two most probable configurations, which are indistinguishable, are plotted as the dashed blue line. Finally, the dashed cyan lines represent the border of the allowed parameter space.

### Two parameter case: $e_0$ and $c_s^2$

Here we describe the case where also the speed of sound is treated as a free parameter and we try to understand how much its value can deviate from the QCD conformal limit, when it is determined by the observational data. The prior range for  $e_0$  is the same as before, i.e.  $[160 - 232] \text{ MeV fm}^{-3}$ , while for  $c_s^2$  the interval is  $[0.1, 1]$ . Contrary to the previous case, the range in  $e_0$  is not narrowed a priori due to the maximum mass limit, because here an increase of  $c_s^2$  allows also EOSs with  $e_0 > 220 \text{ MeV fm}^{-3}$  to reach masses exceeding  $2.05M_\odot$ . On the other hand, the maximum mass constraint forces a lower limit for squared speed of sound at about 0.26.

The joint posterior for  $e_0$  and  $c_s^2$  resulting from the Bayesian analysis is shown in figure 8.4.4 along with the most probable values and the  $1\sigma$  (39.3%), 68% and 90% CI contours. In addition, we display the marginalized PDFs with the most likely solutions and the  $1\sigma$  errors. The posterior discloses a correlation among the EOS parameters. From the plots one can see the existence of two classes of solutions, the first with low and the second with high values of  $(e_0, c_s^2)$ . The latter consists of points which are inside the 68% CI, but they are individually less probable with respect to the ones belonging to the low  $(e_0, c_s^2)$  class. This is the reason why the  $e_0$  marginalized distributions has a peak that is quite far from the high likelihood region of the joint posterior. The most probable values of the 2D PDF are  $e_0 = 183.48 \text{ MeV fm}^{-3}$  and  $c_s^2 = 0.306$ , but there are other points characterized by very similar probabilities in the vicinity of the maximum.

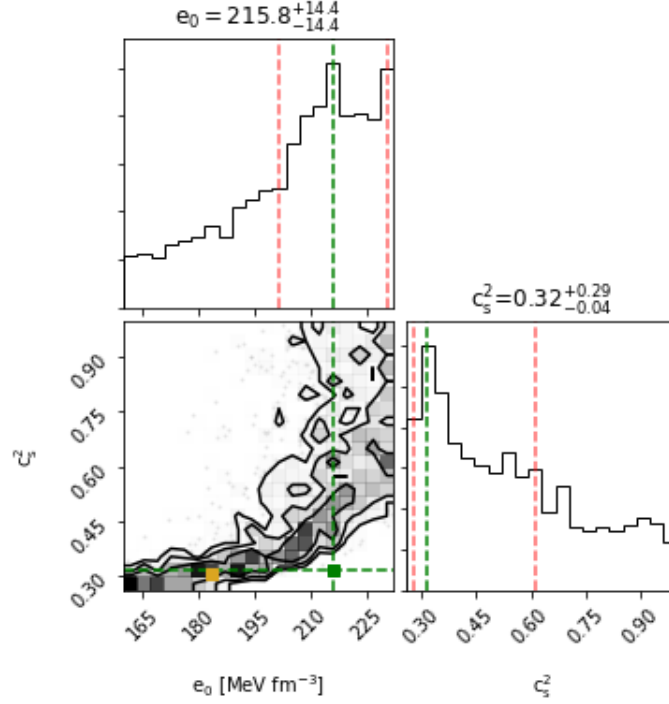


**Figure 8.4.4:** Joint PDF from the Bayesian analysis for the parameters  $e_0$  and  $c_s^2$ . In addition, the marginalized distributions where the green lines are placed on the modes, while the red line represent the 68% CI. The yellow point indicates the maximum of the 2D posterior.

Figure 8.4.5 shows the  $M - R$  sequences inferred through the Bayesian analysis (shaded red). Here the aforementioned classes of solutions are distinguishable: the first one has not too large maximum masses  $\sim 2.1 - 2.2M_\odot$  and radii in the interval  $R_{1.6} \sim 11.6 - 12.9$  km, allowing, in this case, the 68% CI to overlap also with J0437-4715; contrarily, the second class can reach both extremely big maximum mass up to  $\sim 3.25M_\odot$  and have rather small radii  $R_{1.6} \lesssim 11.7$  km. The preferred EOS, displayed as a red dashed line in Figures 8.4.5 and 8.4.6, belongs to the low  $(e_0, c_s^2)$  class and therefore the conformal constraint is fulfilled. This EOS is characterized by  $M_{max} = 2.13M_\odot$  and  $R_{1.6} = 12.20$  km. For what concerns the NN results, we find the optimal solution at  $e_0 = 191.29$  MeV fm $^{-3}$ ,  $c_s^2 = 0.38$ . Despite this point is not exactly coincident with the absolute maximum of the Bayesian PDF, it is one of the several high likelihood modes of the posterior and sits well inside the largest probability region. The cause of the existence of multiple relevant combinations of EOS parameters, all belonging to the first class, is that the  $M - R$  curves corresponding to each of them are superimposed for the majority of the sequences. This is evident looking at the red and blue dashed lines in Figure 8.4.5, which represent the favoured EOSs obtained with

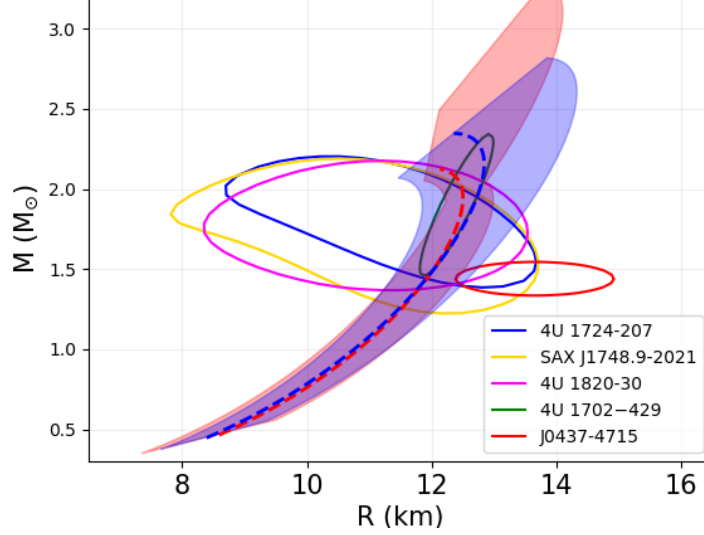


**Figure 8.4.5:** Comparison between the  $M$ - $R$  curves obtained with the two methods employed. The red and blue shaded regions correspond to the 68% CI predicted by the Bayesian analysis and NN respectively. The two most probable configurations are plotted as the dashed red (Bayes) and blue (NN) lines.

the two methods. The NN sequence has indeed a  $R_{1.6} = 12.26$  km, similar to the red curve, but it is characterized by a larger maximum mass  $M_{max} = 2.37M_{\odot}$ . We want to underline that, with a total mass as the one of GW190425 and the most likely parameters obtained in this work, the outcome of a double QSs binary merger would be a prompt collapse.

As in the  $1P$  case and for the same reasons previously explained, our results for  $M - R$  and  $M - \Lambda$  PDFs are not consistent with the 68% CI from the distribution for GW170917\_1 PDF and they are only marginally compatible with J0437-4715.

The RMSEs for the EOS parameters estimated by the NN on the test set are  $15.5 \text{ MeV fm}^{-3}$  for  $e_0$  and  $0.13$  for  $c_s^2$ . As discussed before, the error is calculated as the 68% CI of the 2D Gaussian constructed from the individual RMSEs. This approximation is the major drawback of our NN method: the absence of an explicit PDF prevents the correlation among the parameters to be seen. As a consequence, it is impossible to obtain the two types of solutions as provided by the Bayesian approach and the inferred 68% CIs for the  $M$ - $R$  and the  $M$ - $\Lambda$  points are considerably larger.

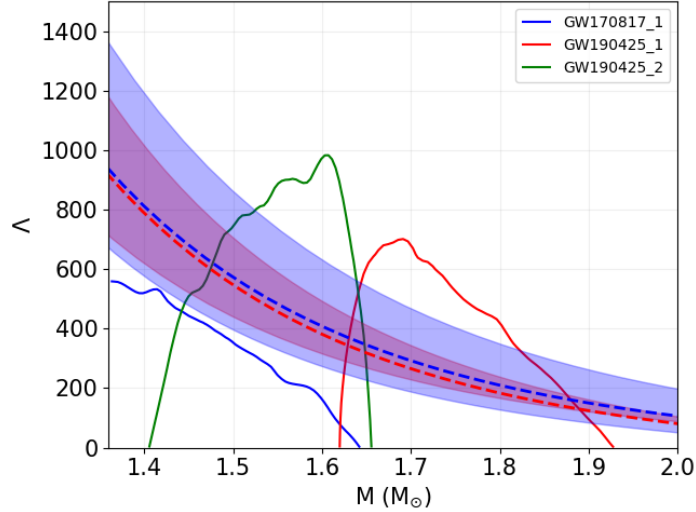


**Figure 8.4.6:** Comparison between the  $M$ - $\Lambda$  curves obtained with the two methods employed. The red and blue shaded regions correspond to the 68% CI predicted by the Bayesian analysis and NN respectively. The two most probable configurations are plotted as the dashed red (Bayes) and blue (NN) lines.

#### 8.4.6 Summary and Conclusions

In this analysis, we parameterized the EOS for quark matter with a CSS model characterized by two parameters ( $c_s^2, e_0$ ). We employed the  $M - R$  PDF of five X-ray sources and the  $M - \Lambda$  posterior from three GW sources to infer the most probable parameter set using both the Bayesian method and the NN prediction approach. For what concerns the NN calculations, we used the marginalized distributions of the PDFs of the sources approximated with Gaussians, when incorporating the observational uncertainties. While the results from these two approaches are consistent with each other, the NN method is unable to reveal the correlation existing between the predicted parameters. Differently to the previous works of Fujimoto et al. (2018, 2020), we tried to give a quantitative comparison between the two adopted methods performing both the analyses using the same model. In addition, we have incorporated the tidal deformabilities on par of the radius without turning it into other equivalent variables while performing the NN predictions in the same way as Morawski & Bejger (2020). Both the approaches predict an incompatibility of our model with GW170817\_1 and J0437-4715 at the 68% level despite the other employed sources are in agreement with the predictions. The consistency between the results from the two methods encourage to acknowledge the NN based prediction as an proficient complimentary approach to the standard Bayesian inference. One of the criticism of our study can be the approximation adopted to incorporate the errors of the observations in the NN framework.

Ideally, it would be more rigorous to use the full PDF instead of a double Gaussian calculated from marginalized data. For the future we intend to improve this aspect by studying a computationally efficient way to incorporate the comprehensive data sets. In this manner the correlation between the  $M - R$  and  $M - \Lambda$  measurements of the sources will be automatically included.

Finally, we also plan to refine our NN method to incorporate an investigation of the correlations existing in our parameter space and, as a consequence, to obtain a improved estimate of the errors.

## 8.5 Speed of sound and quark matter

After the observation of NS with masses  $\sim 2M_{\odot}$  it became clear that the EOS of dense matter must be stiff enough to support such a large mass against the collapse to BH. The stiffness of the EOS for nucleonic matter is controlled by the adiabatic index or correspondingly by the speed of sound  $c_s$ , defined as the derivative of pressure  $p$  with respect to the energy density  $e$  at fixed entropy. An interesting result found in [Bedaque & Steiner \(2015\)](#) (and re-analyzed recently in [Reed & Horowitz \(2020\)](#)) is that, while asymptotically the high density the speed of sound reaches the QCD conformal limit of  $c_s^2 = 1/3$ , at the densities corresponding to the core of NS this constraint seems to be violated:  $c_s$  has to increase to values appreciably larger than the conformal limit and then it should decrease and reach the conformal bound from above<sup>2</sup>. Actually, if one considers the now very popular hypothesis of twin stars ([Alvarez-Castillo & Blaschke, 2017](#); [Christian & Schaffner-Bielich, 2020](#)),  $c_s$  must basically be set to the causal limit  $c_s = 1$  (see the discussion of section 3.2.5). Notice that this deduced behaviour is different from the case of zero density and finite temperature matter for which lattice QCD has unequivocally established that  $c_s$  is always below the conformal bound ([Karsch, 2007](#)). This behaviour is predicted also by many weak couplings and strong couplings models, see [Bedaque & Steiner \(2015\)](#).

Two are the existing proposed solutions to explain the tension between the requirement, coming from astrophysical observations, to have values of  $c_s^2$  much larger than 1/3 and the need to recover the conformal limit at high densities:

- a physical mechanism exists, able to rapidly increase  $c_s$  at densities close to  $\sim 2n_0$  and which then is switched off at larger densities, allowing to reach the conformal constraint from above. Several are the examples for this kind of explanation in the

---

<sup>2</sup>Note that while in [Bedaque & Steiner \(2015\)](#) a CSS EOS with  $c_s = 1/3$  is matched with nuclear physics EOSs at  $2n_0$ , in the more recent [Annala et al. \(2020\)](#), the matching is performed starting from  $1.1n_0$  and a new scheme for the interpolated EOS is employed. This allows to explain the existence of massive configurations, contemporary avoiding to violate the conformal limit. However this implies that the calculations of chiral effective field theory break down below  $2n_0$ , see [Tews et al. \(2018\)](#).

literature, see [Hoyos et al. \(2016\)](#); [Tews et al. \(2018\)](#); [Ma & Rho \(2019\)](#); [Khaidukov & Simonov \(2018\)](#); [McLerran & Reddy \(2019\)](#); [Marczenko \(2020\)](#).

- the conformal limit is never violated within the two families scenario.

In the second case, QSs exist as self-bound objects resembling a giant nuclear drops with a pressure profile ending at the surface with a large finite value of the energy density  $e_0$ . The maximum mass of this type of compact stars depends on the speed of sound as ordinary NS but also on the value of  $e_0$ . In particular, when employing the simple CSS parameterization of equation 8.4.2,  $p = c_s^2(e - e_0)$  ([Alford et al., 2013](#); [Zdunik & Haensel, 2013](#); [Chamel et al., 2013](#); [Drago et al., 2019](#))<sup>3</sup> one finds that the maximum mass  $m_{max} \propto e_0^{-1/2}$  ([Lattimer & Prakash, 2011](#)). On the contrary, no similarly simple scaling exists for  $c_s$ . One can obtain numerically that approximately  $m_{max}(x, e_0) = (e_n/e_0)^{1/2}(0.113144 + 3.26855x - 1.043x^2 + 0.131752x^3)$  where  $e_n = 150 \text{ MeVfm}^{-3}$  is the nuclear matter energy density and  $x = c_s^2/(1/3)$ . Figure 8.5.1 shows the contour plot of  $m_{max}$ . One can see that when the conformal limit is fulfilled, i.e. for  $x = 1$ ,  $2M_\odot \lesssim m_{max} \lesssim 2.5M_\odot$  if  $1 \lesssim e_0/e_n \lesssim 1.5$ . Therefore, when QSs are considered, it is not required that the squared speed of sound exceeds  $1/3$  in order to produce configurations with masses larger than  $2M_\odot$ . Moreover, even for a smaller value of the sound velocity,  $x \sim 0.75$ , it is possible to reach the  $\sim 2M_\odot$  limit when  $e_0$  is equal to the nuclear matter density  $e_n$ . Although this value is very unlikely, it is still remarkable that a window for  $c_s$  and  $e_0$  exists, allowing for massive QSs even if  $c_s$  is below the conformal limit. Similarly, [Dondi et al. \(2017\)](#) by employing the chiral color dielectric model, found that it is possible to fulfill the  $2M_\odot$  limit with an EOS for quark matter having a  $c_s$  that approaches  $1/3$  from below. Thus, the tension between astrophysical data and the theoretical constraints on the speed of sound in dense matter ([Bedaque & Steiner, 2015](#)) is removed within the two families scenario, unless future observations will prove the existence of stars with masses above  $\sim 2.5M_\odot$ .

A related problem concerns the radii of compact stars. One can find that the radius of the maximum mass configuration scales according to  $r_{max}(x, e_0) = (e_n/e_0)^{1/2}(7.06161 + 9.39851x - 3.41955x^2 + 0.465928x^3)$ . The range of values of  $r_{max}$  for a given  $m_{max}$  is displayed in Figure 8.5.1: one can see how the radius increases together with  $m_{max}$ , up to  $\sim 15 \text{ km}$  when  $e_0/e_n = 1$  and  $m_{max} = 3M_\odot$ . Within the two families scenario, massive stars with rather large radii are interpreted as QSs.

On the other hand, HSs, if the conformal limit is assumed to be valid also in hadronic matter, can reach a maximum mass of about  $1.9M_\odot$  ([Bedaque & Steiner, 2015](#)). Actually, the predicted appearance of new degree of freedom such as hyperons and  $\Delta$ s can lower the speed of sound of hadronic matter leading to a reduction of both the the maximum mass

---

<sup>3</sup>Note that this basic prescription gives EOSs very similar to the ones found within the popular MIT bag model (see section 3.2.4), where the role of  $e_0$  is played by the bag constant and the squared sound speed is  $\sim 1/3$  because the  $u$  and  $d$  quarks are massless while the  $s$  quark has a mass of  $\sim 100 \text{ MeV}$  which is small with respect to the chemical potential, see [Alford et al. \(2005\)](#).

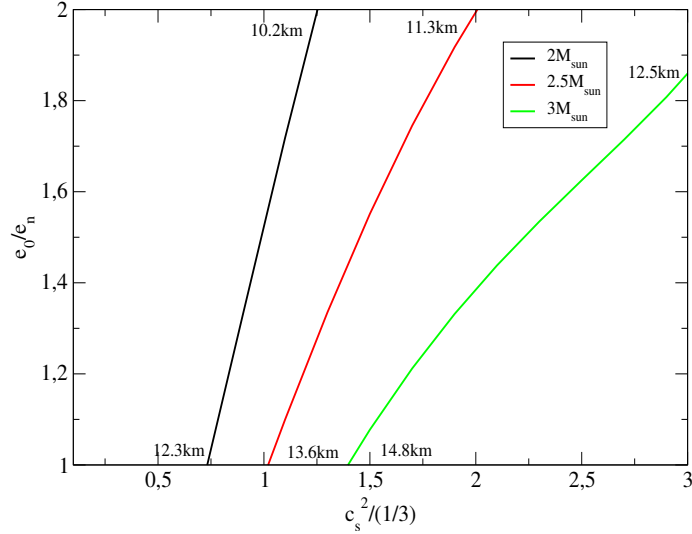


**Figure 8.5.1:** Maximum mass and corresponding radius for QSs as function of the energy density ant zero pressure  $e_0$  and the speed of sound  $c_s$

and the radii of HSs.

The analysis discussed above establishes which are the possible values of  $m_{max}$  within the two families scenario by using the CSS parametrization for quark matter. Clearly, these predictions need to be compared with the available astrophysical observations. This investigation was performed in [Traversi & Char \(2020\)](#), described in chapter 8.4, where we obtained the PDFs of  $e_0$  and  $c_s^2$  through a Bayesian analysis employing a selected sample of data, interpreted as QSs within the two families scenario. As discussed in section 8.4.5, the largest likelihood region corresponds to solutions having low values of  $c_s^2$  and also not too big values of  $e_0$ . The most probable parameter set of the joint PDF, shown in Figure 8.4.4, is placed at  $e_0 = 183.48 \text{ MeV fm}^{-3}$ ,  $c_s^2 = 0.306$ . This is a important result: directly from the data, we infer that, within the two families scenario, not only the favoured values of  $c_s$  are distant from the causal bound but even the violation of the conformal limit seems to be unnecessary.

Moreover, the maximum mass corresponding to the most probable solution is  $M_{max} = 2.13M_\odot$ , which is inside the interval suggested by the GW data and it is very close to the central value of the mass of MSP J0740+6620 ([Cromartie et al. \(2019\)](#), see section 2.3.1).

### 8.5.1 What if GW190814 has a $2.6M_\odot$ compact star component?

Finally, we want to discuss the possibility that the binary system whose merger has produced GW190814 [Abbott et al. \(2020b\)](#) was composed by a BH and a compact star, thus implying

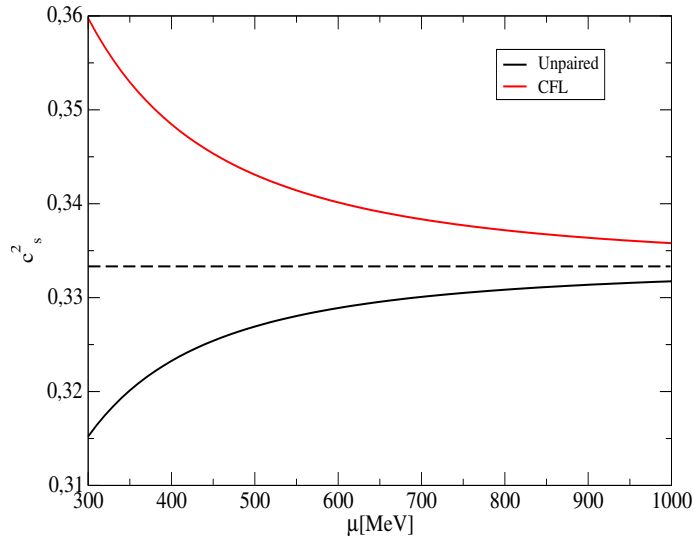


**Figure 8.5.2:** Speed of sound as a function of the quark chemical potential for unpaired quark matter and CFL matter.

a value of  $m_{max}$  larger than  $2.5M_{\odot}$ . Indeed, this detection allowed to identify the component of the binary as a  $23M_{\odot}$  BH and a compact companion of  $\sim 2.6M_{\odot}$ , whose nature remains rather uncertain. As a matter of fact, the mass of the companion falls within the BH lower mass gap and, at the same time, such a massive NS challenges the previous astrophysical limits and the constraints from nuclear physics (Fattoyev et al., 2020). Recently, Bombaci et al. (2020) suggested that this object could actually be a QS. It is clear, from the previous discussion and from the results in Figure 8.5.1, that to obtain a QS with  $M = 2.6M_{\odot}$ , a violation of the conformal limit is required also in dense quark matter. Namely, for a certain interval of densities,  $c_s^2$  must be larger than  $1/3$ . Bombaci et al. (2020) proposed a solution in terms a color superconducting state for quark matter, namely the CFL phase. Indeed, the superconducting gap is able to change the density dependence of the speed of sound as displayed in Figure 8.5.2 and behaves also as an effective reduction of  $e_0$  (through the bag constant). Differently from the simple CSS EOS, with a strange quark having a finite mass  $m_s$  and with a superconducting gap  $\Delta$ , an additional term proportional to  $m_s^2 - 4\Delta^2$  appears in the gran-potential (Alford et al., 2005). One finds that, for  $\Delta > m_s/2$ , as the chemical potential increases,  $c_s$  will reach the conformal limit from above. The example plotted in Figure 8.5.2 is characterized by  $m_s = 100$  MeV,  $\Delta = 80$  MeV and  $a_4 = 0.7$  (pQCD correction parameter, see sections 3.2.4 and 3.2.6). In this way, as shown in Bombaci et al. (2020), values of  $m_{max}$  larger than  $2.5M_{\odot}$  can be obtained and the violation of conformal symmetry at low density is justified through a physical mechanism. Moreover, we underline that the deviations from the conformal constraint are quite small and that actually the most relevant effect to raise the maximum mass comes from the value of  $e_0$ , that is lowered by the presence of a large superconducting gap.

### 8.5.2 Summary

We have proved that the existence of compact stars, having masses up to  $2.5M_{\odot}$  does not inevitably require the violation of the conformal bound in dense matter. However, one has to renounce the assumption that all the compact stars belongs to only one family and hypothesize the existence of two distinct branches, HSs and QSs, in the M-R plot. Some astrophysical sources can be identified as QSs (with a certain degree of uncertainty), within the two families scenario. A Bayesian analysis employing such selected set of sources has allowed to estimate the PDFs of the two parameters of the EOS model, namely  $e_0$  and  $c_s^2$ . Remarkably, the presently available observational data suggest that the PDF of  $c_s^2$  actually has a peak at a value close to  $1/3$ .

In the case compact stars having masses larger than  $2.5M_{\odot}$  are observed in future, then even the two families scenario would require a violation of the conformal limit. A plausible mechanism has been suggested which relies on the appearance of a sizable superconducting gap.

Finally, while in this work we performed the Bayesian analysis by using the simple CSS model, we plan, in future investigations, to exploit more sophisticated models, which will allow to include a density dependence of  $c_s$  such as e.g. a parametrization with piecewise CSS models or the color dielectric model of [Dondi et al. \(2017\)](#).

---

# Conclusions

This thesis is focused on the problem concerning the Equation of State (EOS) of Neutron Stars (NS): we have employed different methods in order to constrain the EOS on the basis of astrophysical observations. In particular, the emphasis is given to the difficulties in reconciling the measurements of big masses ( $\sim 2M_{\odot}$ ) and rather small radii of NS. Moreover, the recent gravitational wave detections from binary NS (BNS) merger events (GW170917, GW190425) provided new additional information on the EOS through the dimensionless tidal deformability ( $\tilde{\Lambda}$ ) and the ejected matter powering heavy elements nucleosynthesis. The resulting Kilonova suggested the presence of a strong shocked component in the ejecta favouring again small radii.

After giving an overview of available constraints from theory (chapter 1), laboratory experiments, mass-radius ( $M - R$ ) measurements (chapter 2) and BNS merger observations (chapter 4), we describe the EOSs employed in our works and the models proposed to disentangle the apparent contradictions among different experimental evidence (chapter 3). We investigate the possibility for new degrees of freedom and quark matter to appear in NS and in particular, the eventual existence of two branches of compact objects, one of which containing quark matter. This is the case of the "two families scenario" which is based on the hypothesis of quark matter being absolutely stable: in this model, the first class is composed by very compact hadronic stars (HSs) containing hyperons and  $\Delta$  resonances and having a maximum mass of about  $1.6M_{\odot}$ , while the second class is made of Quark Stars (QSs). The latter are big and have a larger radius.

The phenomenological implications and signatures of this model in the context of the merger of two compact stars are studied in [De Pietri et al. \(2019\)](#) presented in chapter 5. In this work, we analyzed the features of the different possible types of merger, i.e. HS-HS, HS-QS, QS-QS, in terms of the chirp mass  $M_{chirp}$  and the mass asymmetry  $q = \frac{m_2}{m_1}$ . Then, we estimated the threshold mass,  $M_{thr}$ , and the supramassive maximum mass  $M_{supra}$  for each combination and discussed the outcome of the merger. The HS-HS case is studied in details by performing hydrodynamic simulations of the merger using LORENE and the Einstein

---

Toolkit (ET) and employing two EOSs, SFHo and the hadronic EOS of the two families scenario, labelled as SFHo-HD. The  $M_{thr}$  found for the two models are very different, being  $\sim 2.84M_{\odot}$  for the first one and  $\sim 2.5M_{\odot}$  for the second. This implies that a signature of the two families scenario would be the observation of prompt collapse, suggested by the absence of a Kilonova, for a binary with a total mass  $M_{thr}^{SFHo-HD} < M_{tot} < M_{tot}^{GW170817} \sim 2.74M_{\odot}$ . In the opposite case of  $M_{tot} < M_{thr}^{SFHo-HD}$ , two ways allow to distinguish among the EOSs: first,  $\tilde{\Lambda}$  can be up to a factor 2 smaller in the case of SFHo-HD; second the GW post-merger signal is characterized by a main peak  $f_2$  of about 1kHz larger for SFHo-HD since it contains more degrees of freedom which make it softer. Subsequently, if the remnant reaches a relevant fraction of strangeness, a deconfinement process is triggered which converts the HS into a QS and consequently  $f_2$  is shifted to smaller frequencies. A relevant part of our study regards the estimate of both the dynamically ejected mass and the mass of the disk,  $M_{disk}$ . For both the EOSs, the maximum for the dynamical ejecta corresponds to a  $M_{tot}$  slightly smaller than the respective  $M_{thr}$ . The value is larger than  $10^{-2}M_{\odot}$  and the ejection is mainly due to the shock waves. On the other hand,  $M_{disk}$  for SFHo-HD is up to an order of magnitude smaller leading to a suppression of the purple component of the associated Kilonova.

Finally, we discussed the interpretation of GW170817: using the calculated values of the threshold masses together with the results from a population synthesis analysis, we concluded that in the two families scenario the event was a mixed HS-QS merger. However, a question remains open: what is the fate of the quark matter eventually ejected during a QS-QS or a HS-QS merger? This problem is the subject of [Bucciantini et al. \(2019\)](#), described in chapter 6: here we analyzed in detail the QS-QS merger, studying the process of fragmentation of a QS into strangelets, self-bound lumps of strange matter, in order to infer the typical size of the ejected fragments. Then we considered the possibility of the evaporation of these nuggets into neutrons evaluating the timescales of evaporation given the thermodynamic conditions in the post-merger phase obtained through an explicit QS-QS merger simulation. We found that 93% of the mass of the quark matter ejected evaporates and this process takes place within 15 ms from the collision. As a consequence, a QS-QS merger can generate a Kilonova signal with the same features as the one from a standard NS-NS merger. Moreover, the flux of the remaining strangelets is too low either to be directly detected and to influence the evolution of stars. Therefore, the strong arguments against the possible existence of QSs have been disproved.

Moreover, despite the available experimental data are still unable to provide a definitive answer on the EOS problem, they can be exploited in a more direct way to set important constraints. In addition, one can also infer, from statistical point of view, the theories which are favoured because of their ability to reproduce the data, or if the latter suggests the need for new different models. This was the aim of the Bayesian analysis of [Traversi et al. \(2020\)](#) in chapter 7.

---

In this work we combined the prior knowledge about the saturation properties of nuclear matter with the data from a set of astrophysical X-ray sources and from GW170817. For the first time, we performed this kind of analysis using a Relativistic Mean Field (RMF) theory, the non-linear Walecka model. The Lagrangian contains five coupling constants associated to the mesons interaction terms, which are directly linked through algebraic relations to the saturation density  $n_0$ , the binding energy  $E_0$ , the incompressibility  $K$ , the effective mass  $m^*$  and the symmetry energy  $S$  at saturation. The latter are the parameters constrained through the Bayesian inference. We explored different priors divided in two classes: the informed priors which considers the limit from laboratory experiments and the agnostic priors, where the parameters have larger ranges. Finally, the model is extended to include the  $\Lambda$  hyperons with fixed coupling constant.

We found the joint Posterior Distribution Functions (PDFs) for the nuclear empirical parameters and, from the most probable value and the 68% Confidence Interval (CI), we deduced the preferred range for the NS radii and the maximum mass. In addition, through the calculation of the Bayes Factor, we provided a quantitative comparison among the models. We obtained that the constraints on the saturation parameters in the informed priors prevent the NS radius  $R_{1.4}$  to go below  $\sim 12.5$  km. This evidence suggests a tension between nuclear physics and the astrophysical data. Indeed, the favoured model is agnostic: the resulting EOS is characterized by a smaller radius  $R_{1.4} \sim 12$  km and by a strong reduction of the effective mass at  $\sim 2 - 3n_0$ . This features is a hint of a phase transition to a chiral symmetry restored phase.

Finally, the inclusion of  $\Lambda$ s shifts the radius to  $\sim 14$  km, revealing the inability of this simple model to explain the astrophysical data.

In order to explore a different solution, we performed a similar statistical analysis in chapter 8 (in Traversi & Char (2020)) employing a simple model for Qs, the Constant Speed of Sound (CSS) parameterization, again in the context of the two families scenario. This EOS contains two parameters: the energy density at zero pressure  $e_0$ , and the squared speed of sound in quark matter  $c_s^2$ .

Besides the Bayesian analysis, here we made use of a second new parameter estimation method based on Neural Networks (NNs): the latter provides a mapping from a finite set of data with observational uncertainties onto an EOS. Thus, once trained, the NN can return the most probable EOS as output given the real data as input. To constrain the EOS, we employed the  $(M - R)$  PDFs from a set of X-ray sources and also the mass and tidal deformability estimates  $(M - \Lambda)$  from GW170817 and GW190425.

The scope of the works is twofold. First, in Traversi & Char (2020), we compared between the two inference methods: we found that both the results and the estimated errors are consistent with each other and thus the new NN recipe is a powerful complementary approach to the standard Bayesian analysis. Secondly, in an ongoing work, we focus on the result obtained for the sound speed in quark matter: the most probable value is, for both the

---

employed methods, very close to  $c_s^2 = \frac{1}{3}$ , the conformal limit suggested by QCD calculations.

A common outlook from the collection of my Ph.D. works is the indication of a deficit from the standard EOSs in the ability to describe the whole set of available experimental evidence and the need for solutions based on the appearance of a new phase of matter. Indeed, in chapter 7, we found that, using a simple standard model, the commonly accepted knowledge from nuclear physics provides results incompatible with the observations and the situation is worsened by the inclusion of new degrees of freedom. For this reason, even adopting a formalism which do not include "a priori" the possibility of phase transitions, a data-driven investigation of the parameter space points the result toward this type of solutions. Moreover, as investigated in chapter 5 and 8, only a scenario consisting of two branches of compact objects can easily accommodate big masses with small radii, suggested both by direct  $M - R$  measurements and by the indirect analysis of the ejecta from GW170817. Indeed, this kind of solutions can have a branch characterized by small radii and thus eject a relevant amount of matter without violating the constraints on  $\tilde{\Lambda}$  (see chapter 5). Moreover, as seen in chapter 6, the conditions of density and temperature found in the post-merger phase determine the evaporation of the eventual unbound quark matter, restoring the necessary conditions for the r-processes to take place.

The different types of models with two classes of EOSs can be distinguished both through phenomenological signatures and theoretically by the value of the sound speed in quark matter. Indeed, the difficulties to reconcile the current high mass measurements with the debated conformal limit is present in many models. On the other hand, as we found in chapter 8, in the two families scenario, not only this is possible but it is also suggested as the most valuable solution to fit the observations.

At present, many issues, both concerning theoretical principles and data interpretation, are still subjects of discussion and a shared solution for the challenging EOS problem has yet to be found. However, in the last years, many different methods to test and constrain the EOS have been developed and are constantly improving. These approaches reveals to be complementary (see for example chapter 8) and their ability to provide different and equally valuable information will be proven as essential to shed light on the EOS puzzle.

# Appendices



# A

## *Numerical relativity and Einstein Toolkit*

In GR, gravity is the manifestation of the space-time curvature.

Therefore, the Poisson equation, that in Newtonian gravity gives the relation between the gravitational potential and the mass density, must be reformulated in different terms.

In particular, the question is how the curvature of space-time is influenced by matter and energy. As requested by the principles of GR, this new equation has to be written in a covariant form. Starting from the Poisson equation:

$$\nabla^2\Phi = 4\pi G\rho \tag{A.1}$$

one has to generalize the right hand side to a tensor which contains information on mass and energy, i.e. the energy momentum tensor,  $T_{\mu\nu}$ . Concerning the left hand side, it has to be substituted with a second order derivative of the metric, the variable expressing the geometric properties of space-time. A candidate is the Ricci tensor  $R_{\mu\nu}$ :

$$\begin{aligned} R_{\mu\nu} &= R_{\mu\lambda\nu}^{\lambda} \\ R_{\sigma\mu\nu}^{\rho} &= \delta_{\mu}^{\rho}\Gamma_{\nu\sigma}^{\rho} - \delta_{\nu}^{\rho}\Gamma_{\mu\sigma}^{\rho} - \Gamma_{\mu\lambda}^{\rho}\Gamma_{\nu\sigma}^{\lambda} - \Gamma_{\nu\lambda}^{\rho}\Gamma_{\mu\sigma}^{\lambda} \\ \Gamma_{\mu,\nu}^{\lambda} &= \frac{1}{2}(\delta_{\mu}g_{\nu\sigma} + \delta_{\nu}g_{\sigma\mu} - \delta_{\sigma}g_{\mu\nu}) \end{aligned} \tag{A.2}$$

However, from the energy conservation principle:

$$\nabla^{\mu}T_{\mu\nu} = 0 \tag{A.3}$$

and thus the left hand side must also have a vanishing covariant derivative: this requirement does not hold true for the Ricci tensor, but it is satisfied by another (0, 2) tensor built from

it, the so called Einstein tensor:

$$G_{\mu\nu} = R_{\mu\nu} - \frac{1}{2}Rg_{\mu\nu} \quad (\text{A.4})$$

The proportionality constant is calculated by imposing the Poisson equation as Newtonian limit. Finally one gets the Einstein Equations (EEs):

$$G_{\mu\nu} = 8\pi GT_{\mu\nu} \quad (\text{A.5})$$

To describe the dynamical evolution during the merger through a simulation, one has to solve equations A.5, which means computing the temporal evolution of both matter and curvature. Moreover, physical "constraints", i.e. the conservation equations generalized to tensorial form have to be added: the latter, together with the EOS, represent the General Relativistic Hydrodynamic Equations (GRHD).

Our simulations (see chapter 5) are performed with the open source software `Einstein Toolkit`, that contains a set of modules providing different functionalities; the most important is the `CACTUS` module which is in turn divided in sub-modules called `Thorns`. To solve numerically hyperbolic differential equations such as EEs and GRHD, the first step is to represent continuous space-time functions at discrete time steps (Maione, 2016). Secondly one has to create, for each function, a discrete 3D Cartesian spatial grid: the latter covers a region that is much bigger than the initial separation between the NS and that will be evolved in time during the simulation.

The evolution equations must be written as a system of partial differential equations (PDEs) :

$$\delta_t U_i(t, \vec{x}) = f(U_i(t, \vec{x}), \delta_{\vec{x}} U_i(t, \vec{x}), \delta_{\vec{x}}^2 U_i(t, \vec{x}), t, \vec{x}) \quad (\text{A.6})$$

where  $U_i$  are the components of the evolved vector: their values at  $t_{n+1} = t_n + \Delta t$  are obtained from the knowledge of the previous temporal step  $t_n$ . Once the initial conditions are set for each point in the grid, the computation is performed using the `Mo1` thorn inside `Cactus`, which employs the "method of lines": this consists in approximating, for each grid point, the derivatives in the right end side of the equation A.6, leaving only the dependence on  $t$ . Finally one obtains a system of ordinary differential equations, solved through the

---

fourth order Runge-Kutta numerical method:

$$\begin{aligned}
U_i^0 &= U_i^n \\
U_i^1 &= U_i^0 + \frac{1}{2}\Delta t f(U_i^0) \\
U_i^2 &= U_i^0 + \frac{1}{2}\Delta t f(U_i^1) \\
U_i^3 &= U_i^0 + \Delta t f(U_i^2) \\
U_i^4 &= \frac{1}{6}(-2U_i^0 + 2U_i^1 + 4U_i^3 + \Delta t f(U_i^3)) \\
U_i^{n+1} &= U_i^4
\end{aligned} \tag{A.7}$$

From the previous argument, it became clear that the first step to solve the EEs is to rewrite them separating the temporal coordinate from the spatial ones, making use of the so called 3 + 1 formalism. The space-time is sliced into 3D non-intersecting, space-like surfaces  $\Sigma$  having a Riemannian signature (+, +, +). These are level surfaces of the time coordinate  $t$ .

The evolution from a hypersurface to the next is described by means of two kinematical variables, the "lapse function"  $\alpha$  and the "shift vector"  $\beta^i$ .

The first one is strictly positive and it is defined by:

$$\alpha = -\sqrt{\nabla^\mu t \nabla_\mu t} \tag{A.8}$$

or:

$$n^\mu = -\alpha \nabla^\mu t \tag{A.9}$$

where  $n$  is a unit vector which is normal to the surface and points in the positive time direction. One can interpret the lapse function as an estimate of the rate of variation of the coordinate time along  $n^\mu$ . The induced metric on each hypersurface is:

$$\gamma_{\mu\nu} = g_{\mu\nu} + n_\mu n_\nu \tag{A.10}$$

where  $\gamma_{ij} = g_{ij}$  and  $\gamma^{0\mu} = 0$ . Thus the tensors  $\gamma$  and  $n$  can be exploited to decompose any 4D tensor in a time-like and a spatial part, applying the spatial-projector operator:

$$\gamma_\nu^\mu := g^{\mu\alpha} \gamma_{\alpha\nu} = g_\nu^\mu + n^\mu n_\nu = \delta_\nu^\mu + n^\mu n_\nu \tag{A.11}$$

and the time-projection operator:

$$N_\nu^\mu := -n^\mu n_\nu \tag{A.12}$$

Therefore, any 4-vector can be expressed as:

$$U^\mu = \gamma_\nu^\mu U^\nu + N_\nu^\mu U^\nu \tag{A.13}$$

The evolution is performed along the time coordinate basis vector  $t$ , which is written as the linear superposition of a time-like term, parallel to  $n$ , and spatial term orthogonal to  $n$

$$t = e_t = \delta_t := \alpha n + \beta \tag{A.14}$$

where  $\beta$  is the aforementioned shift vector and the components of  $n$  are given by:

$$n_\mu = (-\alpha, 0, 0, 0) \quad , \quad n^\mu = \frac{1}{\alpha}(1, -\beta^i) \tag{A.15}$$

Finally, in the 3 + 1 formulation, the line element is:

$$ds^2 = -(\alpha^2 - \beta_i \beta^i) dt^2 + 2\beta_i dx^i dt + \gamma_{ij} dx^i dx^j \tag{A.16}$$

This means that the lapse function expresses the proper time between two adjacent hypersurfaces ( $\beta^i = 0 = dx^i$ ) and the shift vector is linked to the change of coordinates of a point from  $\Sigma_t$  to  $\Sigma_{t+dt}$ .

The 3 + 1 formulation is used to decompose the EEs, so that they can be written as an initial value problem that can be solved numerically. This form is denominated ADM formulation (from Arnowitt, Deser, Misner).

First of all, one needs to convert the 4D operators and tensors to 3D objects, defined on the spatial surfaces, applying the spatial-projector:

- the Riemann tensor:

$${}^{(3)}R^\mu_{\nu\kappa\sigma} = \partial_\kappa {}^{(3)}\Gamma^\mu_{\nu\sigma} + \partial_\sigma {}^{(3)}\Gamma^\mu_{\nu\kappa} + {}^{(3)}\Gamma^\mu_{\lambda\kappa} {}^{(3)}\Gamma^\lambda_{\nu\sigma} + {}^{(3)}\Gamma^\mu_{\lambda\sigma} {}^{(3)}\Gamma^\lambda_{\nu\kappa} \tag{A.17}$$

- the Ricci tensor and scalar:

$${}^{(3)}R_{\alpha\beta} = {}^{(3)}R^\mu_{\alpha\mu\beta} \quad , \quad {}^{(3)}R = {}^{(3)}R^\mu_\mu \tag{A.18}$$

- the covariant derivative:

$$D_\nu = \gamma^\mu_\nu \nabla_\mu = (\delta^\mu_\nu + n_\nu n^\mu) \nabla_\mu \tag{A.19}$$

- the connection coefficients:

$${}^{(3)}T^\alpha_{\delta\gamma} = \frac{1}{2} \gamma^{\alpha\beta} (\partial_\beta \gamma_{\gamma\delta} + \partial_\gamma \gamma_{\delta\beta} - \partial_\delta \gamma_{\beta\gamma}) \tag{A.20}$$

However, the projection implies a loss of part of information: concerning the Riemann tensor, this gap can be filled by defining another tensor, the so called extrinsic curvature  $K_{\mu\nu}$ , which is purely spatial and expresses the time derivative of the spatial metric or, in

---

other terms, the curvature of  $\Sigma_t$ :

$$K_{\mu\nu} = -\gamma_\mu^\lambda \nabla_\lambda n_\nu = -(\delta_\mu^\lambda + n^\lambda n_\mu) \nabla_\lambda n_\nu = \frac{1}{2} L_n \gamma_{\mu\nu} \quad (\text{A.21})$$

where  $L_n$  denotes the Lie derivative.

From the projections of the Riemann tensor, one finds the following equations:

- the Gauss equation, when projecting all the four indices into  $\Sigma$ :

$$R_{\mu\nu\rho\sigma} + K_{\mu\rho} K_{\nu\sigma} - K_{\mu\sigma} K_{\nu\rho} = \gamma_\mu^\alpha \gamma_\nu^\beta \gamma_\rho^\gamma \gamma_\sigma^\delta {}^{(4)}R_{\alpha\beta\gamma\delta} \quad (\text{A.22})$$

- the Codazzi equation, with a contraction with  $n^\mu$  and three spatial projections:

$$D_\mu K_{\nu\rho} - D_\nu K_{\mu\rho} = \gamma_\nu^\gamma \gamma_\mu^\alpha \gamma_\rho^\beta n^\delta {}^{(4)}R_{\gamma\alpha\beta\delta} \quad (\text{A.23})$$

- the Ricci equation, with two contractions with  $n^\mu$  and two spatial projections:

$$L_n K_{\mu\nu} = n^{\sigma\rho} \gamma_\mu^\beta \gamma_\nu^\gamma {}^{(4)}R_{\gamma\sigma\beta\rho} - \frac{1}{\alpha} D_\mu D_{n\alpha} - K_\nu^\rho K_{\mu\rho} \quad (\text{A.24})$$

From [A.22](#) and [A.10](#), after contracting with the spatial metric, one gets:

$$2n^\mu n^\nu {}^{(4)}G_{\mu\nu} = R + K^2 - K_{\mu\nu} K^{\mu\nu} \quad (\text{A.25})$$

Once projected, the energy momentum tensor becomes:

$$S_{\mu\nu} = \gamma_\mu^\alpha \gamma_\nu^\beta T_{\alpha\beta} \quad (\text{A.26})$$

thus the total energy density measured by the normal observer is:

$$e = n^\mu n^\nu T_{\mu\nu} \quad (\text{A.27})$$

The Hamiltonian constraint is written in terms of this energy density as:

$$R + K^2 - K_{\mu\nu} K^{\mu\nu} = 16\pi e \quad (\text{A.28})$$

In a similar way the momentum constraint, using the Codazzi equations, can be expressed as:

$$D_\nu H_\mu^\nu - D_\mu K = 8\pi j_\mu \quad (\text{A.29})$$

where:

$$j_\mu = -\gamma_\mu^\nu n^\rho T_{\nu\rho} \quad (\text{A.30})$$

These identities are not explicitly solved during the simulations, but they give a way to

keep numerical errors under control while computing the EEs. Finally, one can write the actual EEs, i.e. the equations describing the evolution of the 3D metric and of the extrinsic curvature.

After applying some non-trivial algebra, one obtains:

$$\delta_t K_{ij} = -D_i D_j \alpha + \alpha(R_{ij} - 2K_{ik} K_j^k + K K_{ij}) - 8\pi\alpha(R_{ij} - \frac{1}{2}\gamma_{ij}(S - e)) + L_\beta K_{ij} \quad (\text{A.31})$$

and, from A.21:

$$\delta_t \gamma_{ij} = -2\alpha K_{ij} + L_\beta \gamma_{ij} \quad (\text{A.32})$$

A.31 and A.32 with the addition of the constraints, constitute the set of ADM equations. Unfortunately, these equations, being weakly hyperbolic, cannot be employed in numerical simulations because they would be affected by numerical instabilities. Therefore, in order to obtain a set of strongly hyperbolic equations, one has to define new variables. The first one is the conformally related metric:

$$\tilde{\gamma}_{ij} = \psi^{(-4)} \gamma_{ij} = e^{-4\Phi} \gamma_{ij} \quad (\text{A.33})$$

Here  $\psi = e^\Phi$  is the so called conformal factor and  $\Phi = \frac{1}{12} \ln \gamma$ ,  $|\tilde{\gamma}_{ij}| = 1$ .

To replace the extrinsic curvature, the trace-free extrinsic curvature is introduced:

$$A_{ij} = K_{ij} - \frac{1}{3}\gamma_{ij}K \quad (\text{A.34})$$

and subsequently re-scaled as:

$$\tilde{A}_{ij} = e^{-4\Phi} A_{ij} \quad (\text{A.35})$$

After some calculations, the evolution equations for  $\Phi$  and  $K$  can be expressed as:

$$\partial_t \Phi = -\frac{1}{6}\alpha K + \beta^i \partial_i \Phi + \frac{1}{6}\partial_i \beta^i \quad (\text{A.36})$$

and

$$\partial_t K = -\gamma^{ij} D_j D_i \alpha + \alpha(\tilde{A}_{ij} \tilde{A}^{ij} + \frac{1}{3}K^2) + 4\pi\alpha(\rho + S) + \beta^i \partial_i K \quad (\text{A.37})$$

The EEs A.31 and A.32 are then reformulated as the evolution of the new variables:

$$\partial_t \tilde{\gamma}_{ij} = -2\alpha \tilde{A}_{ij} + \beta^k \partial_k \tilde{\gamma}_{ij} + \tilde{\gamma}_{ik} \partial_j \beta^k + \tilde{\gamma}_{kj} \partial_i \beta^k - \frac{2}{3}\tilde{\gamma}_{ij} \partial_k \beta^k \quad (\text{A.38})$$

$$\begin{aligned} \partial_t \tilde{A}_{ij} = & e^{-4\Phi} (-(D_i D_j \alpha)^{TF} + \alpha(R_{ij}^{TF} - 8\pi S_{ij}^{TF})) + \alpha(K \tilde{A}_{ij} - 2\tilde{A}_{ij} - 2\tilde{A}_{il} \tilde{A}_j^l) \\ & + \beta^k \partial_k \tilde{\gamma}_{ij} + \tilde{\gamma}_{ik} \partial_j \beta^k + \tilde{\gamma}_{kj} \partial_i \beta^k - \frac{2}{3}\tilde{\gamma}_{ij} \partial_k \beta^k \end{aligned} \quad (\text{A.39})$$

Equations A.36, A.37, A.38 and A.39, together with the constraint which defines the

conformal connection

$$\tilde{\Gamma}^i = -\tilde{\gamma}^{ij} \quad (\text{A.40})$$

and the corresponding evolution equation

$$\begin{aligned} \partial_t \tilde{\Gamma}^i &= -2\tilde{A}^{ij} \partial_j \alpha + 2\alpha (\tilde{\Gamma}_{jk}^i \tilde{A}^{kj} - \frac{2}{3} \tilde{\gamma}^{ij} \partial_j K - 8\pi \tilde{\gamma}^{ij} S_j + 6\tilde{A}^{ij} \partial_j \Phi) \\ &+ \beta^j \partial_j \tilde{\Gamma}^i - \tilde{\Gamma}^j \partial_j \beta^i + \frac{2}{3} \tilde{\Gamma}^i \partial_j \beta^j + \frac{1}{3} \tilde{\gamma}^{li} \beta_{,jl}^j + \tilde{\gamma}^{li} \beta_{,lj}^i \end{aligned} \quad (\text{A.41})$$

form the set of EEs in the BSSN-OK formulation.

To solve the EEs, besides the curvature, also matter must be evolved.

Let us introduce a fluid with 4-velocity  $u$ : its direction is different both from the unit vector  $n$  and from the coordinate  $t$ . The real goal consists in calculating  $u$  spacial projection, i.e. the 3-velocity of the fluid,  $v$ . The Eulerian observer measures the 3-velocity of the fluid as the ratio between  $u$  projected on a hypersurface normal to  $n$ ,  $\gamma_\mu^i u^\mu = u^i$ , and its Lorentz factor, measured by  $n$ ,  $W = -n_\mu u^\mu = \alpha u^t$ :

$$v = \frac{\gamma \cdot u}{-n \cdot u} \quad (\text{A.42})$$

The components of the 3-velocity written in terms of  $\alpha$  and  $\beta^i$  are:

$$v^i = \frac{u^i}{W} + \frac{\beta^i}{\alpha} = \frac{1}{\alpha} \left( \frac{u^i}{u^t} + \beta^i \right), \quad v_i = \frac{u_i}{W} = \frac{u_i}{\alpha u^t} \quad (\text{A.43})$$

Then, one writes the energy momentum tensor of an ideal fluid as:

$$T^{\mu\nu} = \rho h u^\mu u^\nu + p g^{\mu\nu} \quad (\text{A.44})$$

where  $\epsilon$  is the energy density,  $p$  the pressure,  $\rho$  the mass density and  $h = 1 + \epsilon + \frac{p}{\rho}$  the relativistic specific enthalpy.

For the task of evolving the hydrodynamical variables, one has to solve the equations for the conservation of energy and momentum and of baryon number,

$$\nabla_\mu T^{\mu\nu} = 0 \quad (\text{A.45})$$

$$\nabla_\mu (\rho u^\mu) = 0 \quad (\text{A.46})$$

Finally, in order to close the system, an additional equation, i.e. the EOS, has to be provided.

The hydrodynamical evolution in the ET is performed by the thorn GRHydro (derived from WHISKY, [Moesta et al. \(2013\)](#)).

The GRHD equations are implemented by exploiting the Valencia formulation, that consists

in replacing the usual thermodynamical primitive variables,  $\rho$ ,  $\epsilon$  and  $v^i$  with a different set of variables denoted as "conserved variables". Since these parameters enable to express the GRHD equations in conservative form:

$$\partial_t \mathbf{U} = \partial_i \mathbf{F}^{(i)}(\mathbf{U}) = \mathbf{S}(\mathbf{U}) \quad (\text{A.47})$$

they are automatically conserved in the numerical computation. Here  $\mathbf{U}$  contains the conserved variables,  $\mathbf{F}^i$  are the fluxes and  $\mathbf{S}$  is the source term, which depends only on  $\mathbf{U}$ , but not on its derivatives.

Explicitly, the conserved variables are:

$$\mathbf{U} = \begin{pmatrix} D \\ S_j \\ \tau \end{pmatrix} = \begin{pmatrix} \sqrt{\gamma} W \rho \\ \sqrt{\gamma} \rho h W^2 v_j \\ \sqrt{\gamma} (\rho h W^2 - p) - D \end{pmatrix}$$

and the associated fluxes:

$$F^i = \begin{pmatrix} D(\alpha v^i - \beta^i) \\ S_j(\alpha v^i - \beta^i) + p \delta_j^i \\ \tau(\alpha v^i - \beta^i) + p v^i \end{pmatrix}$$

while the source terms are given by:

$$\mathbf{S} = \begin{pmatrix} 0 \\ T^{\mu\nu}(\partial_\mu g_{\nu j} + \Gamma_{\mu\nu}^\sigma g_{\sigma j}) \\ \alpha(T^{\mu 0} \partial_\mu \log \alpha - T^{\mu\nu} \Gamma_{\nu\mu}^0) \end{pmatrix}$$

A possible issue of non-linear, hyperbolic PDE is that they can develop shocks, i.e. discontinuities of the computed variables, which have to be properly treated in the code. The main trick consists in evolving the volume average in a cell of the quantities contained in  $\mathbf{U}$ . In a simple explanatory one dimensional case and using a scalar function  $u(x, t)$ :

$$\tilde{u}^n = \frac{1}{\Delta x} \int_{x^{i-1/2}}^{x^{i+1/2}} u(x, t^n) dx \quad (\text{A.48})$$

thus the equation [A.47](#) is written simply as:

$$\partial_t u(x, t) + \partial_x f(u(x, t)) = 0 \quad (\text{A.49})$$

The flux function on the boundaries is defined as:

$$\hat{F}_{j+1/2} \simeq \int_{t^n}^{t^{n+1}} F(u(x_{j+1/2}, t)) dt \quad (\text{A.50})$$

and then the equation [A.49](#) must be discretized. The latter becomes an expression for  $\tilde{u}$  at

---

the evolved time given as a function of  $\tilde{u}$  calculated at the previous temporal step:

$$\tilde{u}_j^{n+1} = \tilde{u}_j^n - \frac{\Delta t}{\Delta x} (\hat{F}_{j+1/2} - \hat{F}_{j-1/2}) \quad (\text{A.51})$$

The procedure to solve the equation, can be summarized by three steps:

- the reconstruction of the piecewise-polynomial function from the cell average. If  $u(x, t)$  is sufficiently smooth, the integral [A.48](#) represents a good approximation of  $u(x, t)$  at the midpoint of the interval. Thus the quantity:

$$\sum_{i=1}^N \tilde{u}_i^n \Delta x \quad (\text{A.52})$$

where  $i$  is the cell index, is almost the same as the integral of the  $u$  over the whole grid. The so called Godunov's description consists in approximating the hydrodynamical quantities using piecewise constant functions. This method leads to a system of Riemann problems characterized by discontinuous initial conditions, such as:

$$u_0 = \begin{cases} u_L & \text{if } x < 0 \\ u_R & \text{if } x > 0 \end{cases} \quad (\text{A.53})$$

The solution is evaluated exactly at  $(x_{j+1/2}, t)$ .

- the evolution of the hyperbolic equations. Given the Riemann problem, with initial conditions:

$$\tilde{u}(x_{j\pm 1/2}, t^n) \begin{cases} u_L(x, t^n) & \text{for } x < x_{j\pm 1/2} \\ u_R(x, t^n) & \text{for } x > x_{j\pm 1/2} \end{cases} \quad (\text{A.54})$$

and its solution  $\tilde{u}(x_{j+1/2}, t)$  for  $t \in (t^n, t^{n+1})$ , the flux becomes:

$$\hat{F}_{j\pm 1/2} = \frac{1}{\Delta t} \int_{t^n}^{t^{n+1}} F(\tilde{u}(x_{j+1/2}, t)) dt \quad (\text{A.55})$$

This expression is then inserted in equation [A.51](#), thus the right hand side of the evolution equation for the conserved variable is written.

Moreover, the value of  $u$  at  $t_n$  is known and therefore all the conserved variables are evaluated at the initial time. At this step, the computation consists in inverting the system which contains the definition of the conserved variables as functions of the thermodynamical ones. This task is performed in `GRHydro` using a 1D Newton-Raphson scheme. Once the usual hydrodynamical parameters are found, one can write

the energy-momentum tensor and thus calculate the right hand-side of the BSSN-OK equations which evolve the curvature. In this way one obtains a set of equations, the BSSN-OK and the hydrodynamical ones for  $\tilde{u}$  from  $t_n$  to  $t_{n+1}$ , written in the requested form. These equations are coupled and need to be evolved together. This numerical calculation is performed by `Mo1` with the fourth order Runge-Kutta method.

- average

The solution evaluated for  $t^{n+1}$  is averaged over each cell of the grid in order to get:

$$\tilde{u}_i^{n+1} = \frac{1}{\Delta x} \int_{x_{i-1/2}}^{x_{i+1/2}} \tilde{u}(x, t^{n+1}) dx \quad (\text{A.56})$$

Finally, the procedure must be iterated to get the solutions for each time step.

The hydrodynamical equations previously explained are coupled also to the EOS, which must be included in the calculations. Concerning the code, the thorn dedicated to the implementation of the EOS is `EOS_Omni` that interfaces with `GRHydro`.

# B

## *Treatment of thermodynamical integrals*

In this Appendix, the treatment of the thermodynamic integral:

$$\int_{m_e}^{\infty} dE \cdot E \sqrt{E^2 - m_e^2} \cdot \left( \frac{1}{1 + \exp \frac{E - \mu_e}{T}} - \frac{1}{1 + \exp \frac{E + \mu_e}{T}} \right) \quad (\text{B.1})$$

is discussed. Let us consider separately the two pieces:

$$\begin{aligned} & \int_{m_e}^{\infty} dE \cdot E \sqrt{E^2 - m_e^2} \cdot \frac{1}{1 + \exp \frac{E - \mu_e}{T}} \\ & \int_{m_e}^{\infty} dE \cdot E \sqrt{E^2 - m_e^2} \cdot \frac{1}{1 + \exp \frac{E + \mu_e}{T}} \end{aligned} \quad (\text{B.2})$$

With a change of variable  $x = E - \mu$ , the first part becomes:

$$\int_{m_e - \mu}^{\infty} dx \cdot \frac{(x + \mu) \cdot \sqrt{(x + \mu)^2 - m_e^2}}{1 + \exp(\frac{x}{T})} \quad (\text{B.3})$$

while  $x = E + \mu$  is chosen for the second piece and it results in:

$$\int_{m_e + \mu}^{\infty} dx \cdot \frac{(x - \mu) \cdot \sqrt{(x - \mu)^2 - m_e^2}}{1 + \exp(\frac{x}{T})} \quad (\text{B.4})$$

Summing the two terms, one can note that in the interval  $(m_e - \mu, m_e + \mu)$  only the first part is present, while in the range  $(m_e + \mu, \infty)$  both parts give a contribution. Thus, the

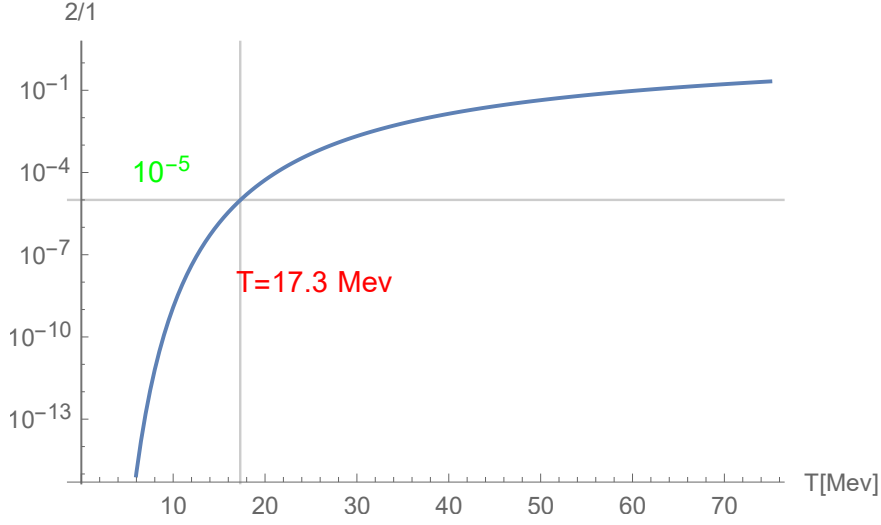


**Figure B.1:** Relative weight of the two part of the thermodynamical integral

total integral is written as:

$$\begin{aligned}
 1 &\rightarrow \int_{m_e - \mu}^{m_e + \mu} dx \cdot \frac{(x + \mu) \cdot \sqrt{(x + \mu)^2 - m_e^2}}{1 + \exp(\frac{x}{T})} + \\
 2 &\rightarrow + \int_{m_e + \mu}^{\infty} dx \cdot \frac{(x + \mu) \cdot \sqrt{(x + \mu)^2 - m_e^2} - (x - \mu) \cdot \sqrt{(x - \mu)^2 - m_e^2}}{1 + \exp(\frac{x}{T})}
 \end{aligned} \tag{B.5}$$

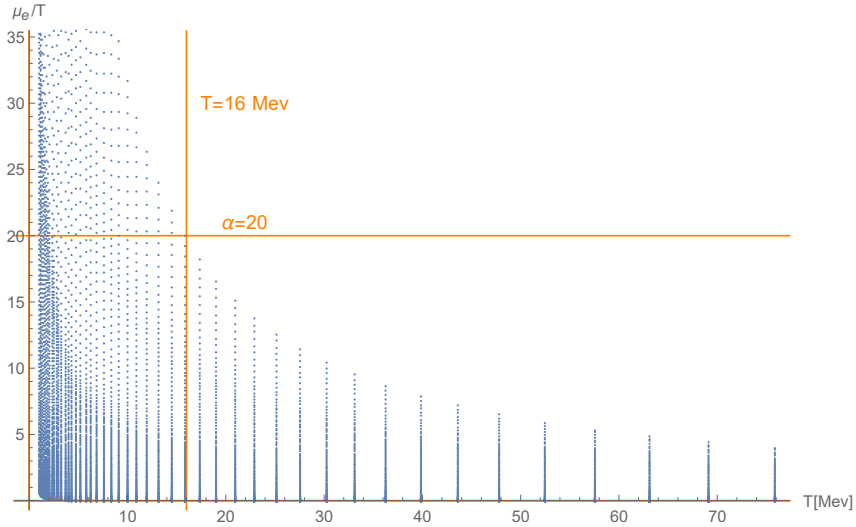


**Figure B.2:** Ratio between electron chemical potential and temperature as function of  $T$

---

Now an approximation is introduced: when  $\mu_e > \alpha T$  with  $\alpha = 20$  and the temperature is low, the second integral can be neglected.

We have checked the validity of this assumption: the ratio between 2 and 1 is calculated as a function of temperature for the limiting value of the electron chemical potential  $\mu_e = 20 \cdot T$ . As shown in figure B.1 the integral 2 become clearly negligible for  $T \lesssim 17.3$  MeV. Moreover, the ratio  $\frac{\mu_e}{T}$  characterizing the entries in the EOS table is displayed in figure B.2: one can notice that for  $T > 16$  MeV the condition  $\mu_e > 20T$  is never realized. Therefore, one can use the approximation in principle for all the temperatures as long as the limit  $\mu_e > 20T$  is fulfilled.

# C

## *Supplementary material for chapter 6*

This Appendix provides the technical details about the simulation of the rescattering process undergone by the quark matter fragments and about the analysis of their possible evaporation.

### **Rescattering and fragmentation**

The fragmentation of droplets of quark matter caused by scattering is controlled by the Weber number  $We$  and by the Ohnesorge number  $Oh$ , defined in section 6.5.2. Using these two numbers, we could estimate the smallest allowed order of magnitude of the baryon number and the size of the strangelets. However, to obtain the explicit distribution of the size of the fragments, one must perform a simulation of the re-scattering process. For that, we use the outcomes of the QS-QS merger simulations, described in section 6.3, to estimate the collisional velocities of the droplets after the ejection. Next, we exploit the Kolmogorov scaling law to calculate the velocity distribution at the level of the fragments. Through this procedure, the speeds derived from the merger simulation, at a scale of  $\sim 1$  km, can be related to the collisional velocities of the fragments which at the end of the process have a sub-millimeter size.

### *Scattering velocities*

To evaluate the initial velocities of the collisions, we firstly investigate the changes in the scalar velocity of the particles in a time range of few milliseconds after the merger. Obviously, these changes are dependent on the time interval between two consecutive measurements, here 0.0788 ms, but the aim of our simulation is only to infer the general features of the

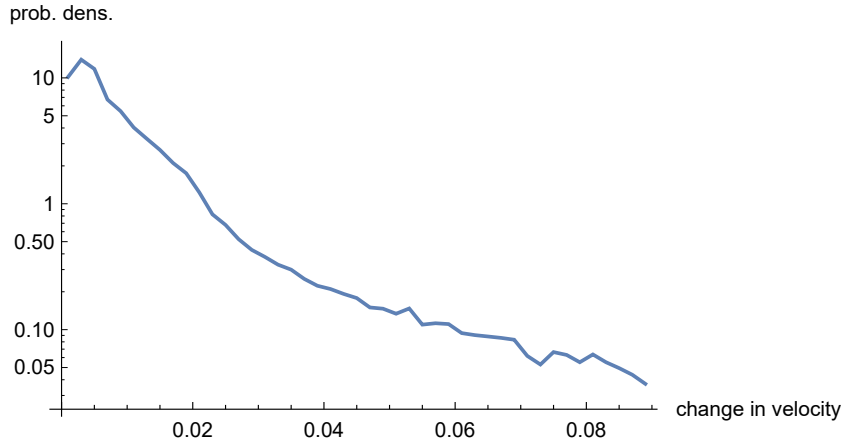


**Figure C.1:** Distribution of the changes in the scalar velocity of the particles (about 1 km size) in units of  $c$

distribution of fragments without any ambition of precision. The scale of the velocities derived in this way has a value comparable or slightly larger than the one characterizing the turbulent velocities in a NS-NS merger (Giacomazzo et al., 2015; Kiuchi et al., 2015). This is an expected result, because the energy associated to a collision between two QSs, due to the absence of a crust, should overcome the one between two NS. The distribution of the change in the scalar velocities is displayed in Figure C.1.

### *Decompression*

Before carrying out the Monte Carlo simulation, one can study the outcome of the simulations of Bauswein et al. (2009, 2010b), to check if there is a clue about the time at which the fragmentation of the system will be more likely to take place. This time can be found by investigating the density evolution of the particles and it corresponds to the presence of a decompression phase. We are considering the simulation with a bag constant  $B = 60\text{MeV}/\text{fm}^3$  having the equilibrium density, where the pressure is zero, at  $\rho_{eq} \sim 4.5 \times 10^{14}\text{g}/\text{cm}^3$ . Unfortunately, the nature of hydrodynamical simulations prevents the possibility to probe the regime of the spinodal instability that is present at much lower densities and that would lead to the starting of a spontaneous fragmentation. However, we can analyze the minimum densities found during the evolution of the particles and the corresponding timescales. The results are shown in Figures C.2: one can see that the minimum densities are considerably lower than  $\rho_{eq}$  and the corresponding time is about 1 – 2 ms after the merger (happening at about 2.5 ms). It is interesting to note the presence of a sort of periodic behavior, indicating that, for few milliseconds after the merger, the system oscillates, reaching rather low densities. This phenomenon takes place exactly at the same time at which we see the most violent change in the velocities, suggesting this as the

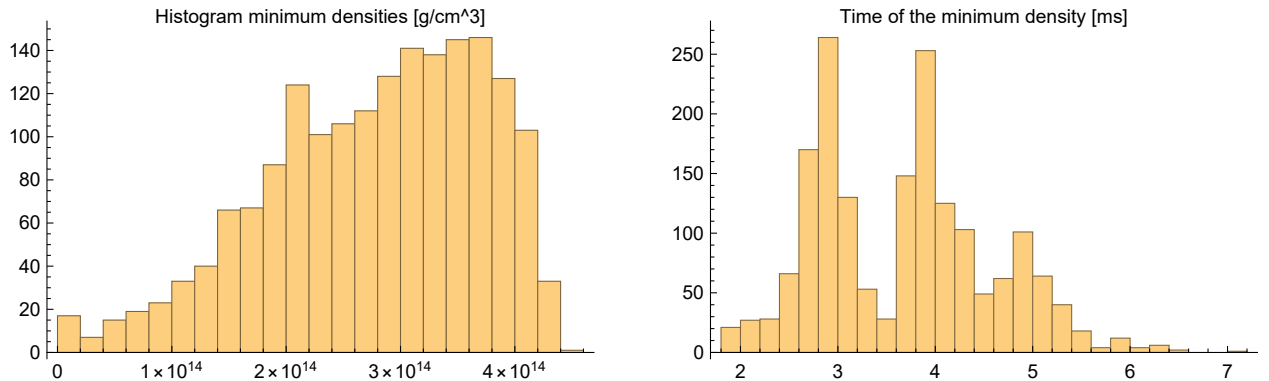


**Figure C.2:** Left panel: distribution of the minimum densities reached by the particles during their evolution. Right panel: distribution of the times at which the minimum densities of the left panel are reached.

ideal period for the fragmentation process to happen.

#### *Simulation of scattering*

In order to sample the velocity distribution described above, we have performed a Monte Carlo simulation. We assume the size of the particles from the merger simulation, i.e.  $\sim 1$  km, as the initial size of the fragments, corresponding to a baryon number labelled as  $A_{\text{init}}$ . Then, the final distribution of the size of the droplets is derived employing an algorithm based on the following steps:

- generation of a new velocity for the collision;
- scaling of this velocity through the Kolmogorov scaling down to the size of the droplet undergoing the collision;
- calculation of  $We$  at the new scale;
- if the condition  $We > 4$  is satisfied, breaking of the fragment into a number of pieces equal to  $We$ . This method is a very basic implementation of the rule according to which the number of fragments is proportional to  $We$  (Ashgriz & Poo, 1990). This number of pieces is also influenced by the impact parameter and thus our method could lead to an overestimate. Therefore our final result can be regarded as a lower limit on the minimum size of the droplets due to the re-scattering process (without taking into account the evaporation).

This procedure is iterated a number of times ( $\sim$  few tens) similar to the number of significant changes in the scalar velocity characterizing particle, as found in the merger simulation.

---

This choice is justified also by the fact that the last iterations generate fragments small enough to get  $We \lesssim 4$ .

At the end of the Monte Carlo chain we obtained  $A_{\text{init}}/A_{\text{final}}$  fragments all with baryon number  $A_{\text{final}}$ . The final distribution  $P(A)$ , plotted in Figure 6.5.2, is the result of  $10^6$  simulated chains of collisions. We see that the  $P(A)$  is centered at a value  $A \sim 10^{24} - 10^{25}$ , that is only slightly smaller than the result obtained with the naive estimate found using  $We$  and  $Oh$ . The explicit distribution calculated here will be directly exploited for the evaporation calculations, described below.

### Evaporation

Besides the fragmentation, during the first few milliseconds, the quark matter droplets also undergo a possible evaporation, because of the high temperatures which characterize the system in this phase (see Figure 6.5.4). To calculate the total evaporated mass, one firstly needs to evaluate the timescale for total evaporation corresponding to a given temperature and baryon number as shown in Figure 6.5.3 and expressed in equation 6.5.5:  $\tau_A = C(T)\text{Log}A$ , where  $C(T)$  can be estimated numerically.

From this equation, we can also extract the timescale for a partial evaporation:

$$\tau_A(f) = C(T)(\text{Log}A - \text{Log}(fA)) = -C(T)\text{Log}f, \quad (\text{C.1})$$

where  $f$  is the strangelet fraction that has NOT evaporated.

For instance, 99% evaporation corresponds to  $f = 0.01$ , because the resulting strangelet has baryon number equal to  $0.01 A$ . It is important to underline that  $\tau_A(f)$  is a function of  $A$  only in the limit  $f > 1/A$ , i.e. basically for a total evaporation, but for all the other cases it is independent from  $A$ . This result is also evident looking at the value for the percentage of evaporated matter listed in Table 6.1. At this point, one is able to evaluate the probability that each ejected droplet, with a given  $A$ , evaporates at least up to a fraction  $f$ , leading to a remaining strangelet with a maximum baryon number of  $fA$ . For this purpose, one has to study the thermal evolution on each of the trajectories to check whether the time that a certain particle spends above a given temperature is long enough to evaporate it up to the fraction  $f$ . Following this procedure, we find the probability that strangelets with initial baryon number  $A$  evaporate at least up to the fraction  $f$ . This quantity, labelled as  $R_A(f)$ , can be considered as a cumulative probability, linked to the corresponding probability distribution function,  $E_A(f)$ , by the relation:

$$R_A(f) = \int_{1/A}^f df' E_A(f') + R_A(1/A), \quad (\text{C.2})$$

where  $R_A(1/A)$  represents the probability of total evaporation of a droplet with baryon num-

ber  $A$ . We then evaluate the numerical value of the probability distribution of evaporation from its cumulative, using the derivative:

$$E_A(f) = \partial R_A(f) / \partial f. \quad (\text{C.3})$$

At this point, we define the distribution of the baryon numbers of the fragments after the evaporation as  $Q(A)$ . This is a function of  $P(A)$ :

$$\begin{aligned} Q(A) &= \int_1^\infty dA' P(A') \int_{1/A'}^1 df E_{A'}(f) \delta(A - fA') \\ &= \int_1^\infty dA' P(A') E_{A'}(f = A/A') / A'. \end{aligned} \quad (\text{C.4})$$

This relation fulfill the sum-rule for the number of fragments:

$$\int_1^\infty dA Q(A) = \int_1^\infty dA P(A) [1 - R_A(1/A)] \quad (\text{C.5})$$

suggesting that the number of fragments after evaporation corresponds to the number of fragments before evaporation minus the number of totally evaporated fragments.

### Quark star-hadronic star merger

To estimate the ejection of quark matter during a HS-QS merger, we also performed a relativistic hydrodynamical simulations of these event using the same scheme as in [Bauswein et al. \(2009, 2010b\)](#) (see section 6.3). We choose a symmetric binary with both the components having a mass of  $1.35 M_\odot$ . The EOS for the HS is the same used in [De Pietri et al. \(2019\)](#), while for the QS we employ a EOS based on the MIT bag model (see chapters 3.2.4 and 3.3.1). The simulation lasts until few milliseconds after the merger, when the remnant collapses to BH since the expected conversion process to quark phase, as in [Herzog & Ropke \(2011\)](#), is not included. However, we can safely assume that the dynamics of the ejection of matter would not be modified during the first milliseconds of the post-merger phase by the deconfinement process, which becomes more relevant at later times. The study of the mass ejection in our simulation reveals that no quark matter has become unbound, as evident from Figure C.3. Instead, the only ejected matter comes from the HS that gets disrupted during the collision, because the hadronic matter is less bound with respect to the quark matter. On the other hand, despite the larger radius of the QS determines a stronger tidal deformation, no matter becomes unbound from the tail and the QS, during the merger, remains gravitationally bound. Moreover, we underline that the case  $q = 1$  investigated here is the one for which both  $\tilde{\Lambda}$  and the tidal deformability of the QS have the biggest possible value (see Figure 5.6.1). This implies that the ejection of quark matter is even more unlikely for binaries with  $q \neq 1$ .

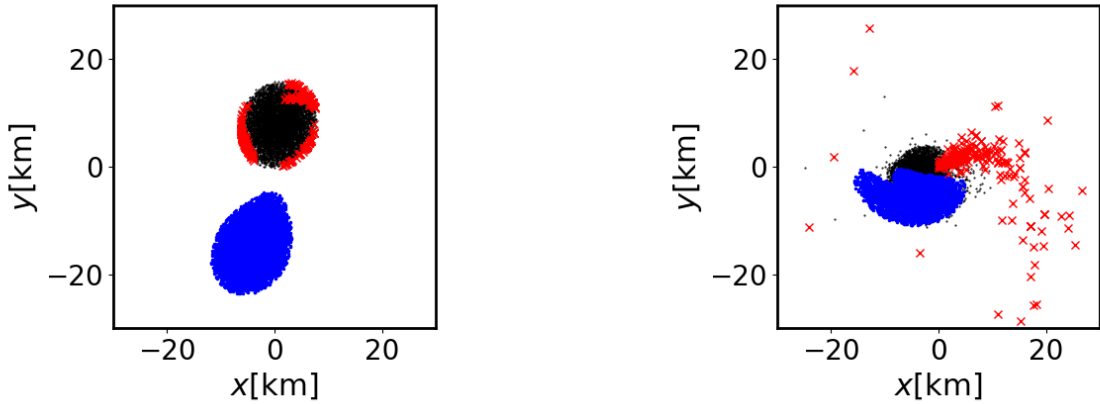


**Figure C.3:** Snapshots from the HS-QS simulation just before (left) and after (right) the merger. Blue dots represent quark matter, while hadronic matter is shown with black markers. (Note that we display only a subset of the particles, which is the reason why the stellar surfaces seems less smooth.) The red cross mark the fluid elements which become eventually unbound. From the right panel is evident that only hadronic matter is ejected.

For a second simulation we selected a symmetric binary, where the components have a mass of  $1.2M_{\odot}$ . This is a rather unrealistic system within the two families scenario, since  $1.2M_{\odot}$  is below the minimum mass for the QS branch. However it is useful to check this case because it favours quark matter ejection and this merger does not result in a early collapse. We obtain an amount of unbound quark matter smaller than  $10^{-4}M_{\odot}$ , a significantly smaller value compared to several  $10^{-3} M_{\odot}$  of mass ejected from the HS. Note that this amount of quark matter corresponds to just a few particles and it could be due to a numerical artifact. Clearly, in this work we cannot give a full survey of all the combinations of binary masses and EOSs and therefore we cannot completely exclude that other systems could lead to a bigger amount of ejecta from the QS, but, even in that case, we expect the thermodynamical and mechanical properties of the strangelets to be similar to those found in a QS-QS merger and discussed in chapter 6.5.

---

# *Bibliography*

- Aasi, J., et al. 2015, *Class. Quant. Grav.*, 32, 074001, doi: 10.1088/0264-9381/32/7/074001
- Abadi, M., Barham, P., Chen, J., et al. 2016, in 12th {USENIX} Symposium on Operating Systems Design and Implementation ({OSDI} 16), 265–283
- Abbott, B., et al. 2020a, *Astrophys. J. Lett.*, 892, L3, doi: 10.3847/2041-8213/ab75f5
- Abbott, B. P., et al. 2017a, *Astrophys. J.*, 850, L40, doi: 10.3847/2041-8213/aa93fc
- . 2017b, *Astrophys. J.*, 848, L13, doi: 10.3847/2041-8213/aa920c
- . 2017c, *Phys. Rev. Lett.*, 119, 161101, doi: 10.1103/PhysRevLett.119.161101
- . 2017d, *Astrophys. J.*, 848, L12, doi: 10.3847/2041-8213/aa91c9
- . 2017e, *Astrophys. J.*, 850, L39, doi: 10.3847/2041-8213/aa9478
- . 2018, *Phys. Rev. Lett.*, 121, 161101, doi: 10.1103/PhysRevLett.121.161101
- . 2019, *Phys. Rev.*, X9, 011001, doi: 10.1103/PhysRevX.9.011001
- Abbott, R., et al. 2020b, *Astrophys. J. Lett.*, 896, L44, doi: 10.3847/2041-8213/ab960f
- Abdo, A., et al. 2013, *Astrophys. J. Suppl.*, 208, 17, doi: 10.1088/0067-0049/208/2/17
- Abrahamyan, S., et al. 2012, *Phys. Rev. Lett.*, 108, 112502, doi: 10.1103/PhysRevLett.108.112502
- Acernese, F., et al. 2015, *Class. Quant. Grav.*, 32, 024001, doi: 10.1088/0264-9381/32/2/024001

- 
- Ademard, G., et al. 2014, *Eur. Phys. J. A*, 50, 33, doi: 10.1140/epja/i2014-14033-x
- Adriani, O., et al. 2015, *Phys. Rev. Lett.*, 115, 111101, doi: 10.1103/PhysRevLett.115.111101
- . 2017, *Riv. Nuovo Cim.*, 40, 473, doi: 10.1393/ncr/i2017-10140-x
- Agathos, M., Zappa, F., Bernuzzi, S., et al. 2020, *Phys. Rev. D*, 101, 044006, doi: 10.1103/PhysRevD.101.044006
- Agrawal, B., Sulaksono, A., & Reinhard, P.-G. 2012, *Nucl. Phys. A*, 882, 1, doi: 10.1016/j.nuclphysa.2012.03.004
- Aichelin, J. 1991, *Phys. Rept.*, 202, 233, doi: 10.1016/0370-1573(91)90094-3
- Aichelin, J., & Schaffner-Bielich, J. 2010, *The Quest for the Nuclear Equation of State*, ed. R. Stock, doi: 10.1007/978-3-642-01539-7\_4
- Akmal, A., Pandharipande, V. R., & Ravenhall, D. G. 1998a, *Phys. Rev.*, C58, 1804, doi: 10.1103/PhysRevC.58.1804
- . 1998b, *Phys. Rev. C*, 58, 1804, doi: 10.1103/PhysRevC.58.1804
- Alberico, W., Gervino, G., & Lavagno, A. 1994, *Phys. Lett. B*, 321, 177, doi: 10.1016/0370-2693(94)90460-X
- Alcock, C., & Farhi, E. 1985, *Phys. Rev.*, D32, 1273, doi: 10.1103/PhysRevD.32.1273
- Alcock, C., Farhi, E., & Olinto, A. 1986, *Astrophys. J.*, 310, 261, doi: 10.1086/164679
- Alcock, C., Farhi, E., & Olinto, A. 1986, *Astrophys. J.*, 310, 261, doi: 10.1086/164679
- Alcubierre, M., Brügmann, B., Diener, P., et al. 2003, *Phys. Rev. D*, 67, 084023, doi: 10.1103/PhysRevD.67.084023
- Alcubierre, M., Brügmann, B., Dramlitsch, T., et al. 2000, *Phys. Rev. D*, 62, 044034, doi: 10.1103/PhysRevD.62.044034
- Alexander, K. D., et al. 2017, *Astrophys. J.*, 848, L21, doi: 10.3847/2041-8213/aa905d
- Alford, M., Braby, M., Paris, M. W., & Reddy, S. 2005, *Astrophys. J.*, 629, 969, doi: 10.1086/430902
- Alford, M. G., Burgio, G. F., Han, S., Taranto, G., & Zappalà, D. 2015, *Phys. Rev.*, D92, 083002, doi: 10.1103/PhysRevD.92.083002

- 
- Alford, M. G., & Han, S. 2014, EPJ Web Conf., 80, 00038, doi: 10.1051/epjconf/20148000038
- Alford, M. G., Han, S., & Prakash, M. 2013, Phys. Rev., D88, 083013, doi: 10.1103/PhysRevD.88.083013
- Alford, M. G., Schmitt, A., Rajagopal, K., & Schäfer, T. 2008, Rev. Mod. Phys., 80, 1455, doi: 10.1103/RevModPhys.80.1455
- AlGendy, M., & Morsink, S. M. 2014, Astrophys. J., 791, 78, doi: 10.1088/0004-637X/791/2/78
- Allen, G., Goodale, T., Lanfermann, G., et al. 2011, Cactus Users' Guide. <http://www.cactuscode.org/Guides/Stable/UsersGuide/UsersGuideStable.pdf>
- Alsing, J., Silva, H. O., & Berti, E. 2018, Mon. Not. Roy. Astron. Soc., 478, 1377, doi: 10.1093/mnras/sty1065
- Alvarez-Castillo, D., Ayriyan, A., Benic, S., et al. 2016, Eur. Phys. J., A52, 69, doi: 10.1140/epja/i2016-16069-2
- Alvarez-Castillo, D., & Blaschke, D. 2015, Phys. Part. Nucl., 46, 846, doi: 10.1134/S1063779615050032
- . 2017, Phys. Rev. C, 96, 045809, doi: 10.1103/PhysRevC.96.045809
- Amati, L., Bozzo, E., Della Valle, M., Gotz, D., & O'Brien, P., eds. 2018, pp.113–292
- Ambartsumyan, V. A., & Saakyan, G. S. 1960, Soviet Astronomy, 4, 187
- Amsler, C., Doser, M., Antonelli, M., et al. 2008, Physics Letters B, 667, 1, doi: 10.1016/j.physletb.2008.07.018
- Angeli, I., Gangrsky, Y. P., Marinova, K., et al. 2009, J. Phys. G, 36, 085102, doi: 10.1088/0954-3899/36/8/085102
- Angeli, I., & Marinova, K. 2013, Atom. Data Nucl. Data Tabl., 99, 69, doi: 10.1016/j.adt.2011.12.006
- Anglani, R., Casalbuoni, R., Ciminale, M., et al. 2014, Rev. Mod. Phys., 86, 509, doi: 10.1103/RevModPhys.86.509
- Anile, A. M. 2005, Relativistic Fluids and Magneto-fluids
- Annala, E., Gorda, T., Kurkela, A., Näätä, J., & Vuorinen, A. 2020, Nature Phys., doi: 10.1038/s41567-020-0914-9

- 
- Annala, E., Gorda, T., Kurkela, A., & Vuorinen, A. 2018, *Phys. Rev. Lett.*, 120, 172703, doi: 10.1103/PhysRevLett.120.172703
- Antoniadis, J., Tauris, T. M., Ozel, F., et al. 2016. <https://arxiv.org/abs/1605.01665>
- Antoniadis, J., et al. 2013, *Science*, 340, 6131, doi: 10.1126/science.1233232
- Arcones, A., Janka, H.-T., & Scheck, L. 2007, *Astron. Astrophys.*, 467, 1227, doi: 10.1051/0004-6361:20066983
- Arzoumanian, Z., et al. 2018, *Astrophys. J. Suppl.*, 235, 37, doi: 10.3847/1538-4365/aab5b0
- Ashgriz, N., & Poo, J. 1990, *Journal of Fluid Mechanics*, 221, 183
- Audi, G., Wapstra, A. H., & Thibault, C. 2002, *Nucl. Phys.*, A729, 337, doi: 10.1016/j.nuclphysa.2003.11.003
- Avancini, S., Marinelli, J., Menezes, D., de Moraes, M., & Providencia, C. 2007, *Phys. Rev. C*, 75, 055805, doi: 10.1103/PhysRevC.75.055805
- Backer, D. C., Kulkarni, S. R., Heiles, C., Davis, M. M., & Goss, W. M. 1982, *Nature*, 300, 615, doi: 10.1038/300615a0
- Bailer-Jones, C., Gupta, R., & Singh, H. 2001. <https://arxiv.org/abs/astro-ph/0102224>
- Baiotti, L. 2019, *Prog. Part. Nucl. Phys.*, 109, 103714, doi: 10.1016/j.pnpnp.2019.103714
- Baiotti, L., Giacomazzo, B., & Rezzolla, L. 2008, *Phys. Rev.*, D78, 084033, doi: 10.1103/PhysRevD.78.084033
- Baiotti, L., Hawke, I., Montero, P. J., et al. 2005, *Phys. Rev. D*, 71, 024035, doi: 10.1103/PhysRevD.71.024035
- Baker, J., Campanelli, M., & Lousto, C. O. 2002, *Phys. Rev. D*, 65, 044001, doi: 10.1103/PhysRevD.65.044001
- Balberg, S., & Gal, A. 1997, *Nucl. Phys. A*, 625, 435, doi: 10.1016/S0375-9474(97)81465-0
- Balberg, S., Lichtenstadt, I., & Cook, G. B. 1999, *Astrophys. J. Suppl.*, 121, 515, doi: 10.1086/313196

- 
- Baldo, M., Bombaci, I., & Burgio, G. 1997, *Astron. Astrophys.*, 328, 274. <https://arxiv.org/abs/astro-ph/9707277>
- Baldo, M., Burgio, G., & Schulze, H. 1998, *Phys. Rev. C*, 58, 3688, doi: 10.1103/PhysRevC.58.3688
- . 2000, *Phys. Rev. C*, 61, 055801, doi: 10.1103/PhysRevC.61.055801
- Banik, S., & Bandyopadhyay, D. 2003, *Phys. Rev. D*, 67, 123003, doi: 10.1103/PhysRevD.67.123003
- Banik, S., Hanauske, M., & Bandyopadhyay, D. 2005, *J. Phys. G*, 31, S841, doi: 10.1088/0954-3899/31/6/026
- Banik, S., Hanauske, M., Bandyopadhyay, D., & Greiner, W. 2004, *Phys. Rev. D*, 70, 123004, doi: 10.1103/PhysRevD.70.123004
- Banik, S., Hempel, M., & Bandyopadhyay, D. 2014, *Astrophys. J. Suppl.*, 214, 22, doi: 10.1088/0067-0049/214/2/22
- Baran, V., Colonna, M., Greco, V., & Di Toro, M. 2005, *Phys. Rept.*, 410, 335, doi: 10.1016/j.physrep.2004.12.004
- Barish, B., Liu, G., & Lane, C. 1987, *Phys. Rev. D*, 36, 2641, doi: 10.1103/PhysRevD.36.2641
- Barnes, J., & Kasen, D. 2013, *Astrophys. J.*, 775, 18, doi: 10.1088/0004-637X/775/1/18
- Bass, S. A., Gyulassy, M., Stöcker, H., & Greiner, W. 1999, *Journal of Physics G Nuclear Physics*, 25, R1, doi: 10.1088/0954-3899/25/3/013
- Baubock, M., Ozel, F., Psaltis, D., & Morsink, S. M. 2015, *Astrophys. J.*, 799, 22, doi: 10.1088/0004-637X/799/1/22
- Bauböck, M., Berti, E., Psaltis, D., & Özel, F. 2013, *Astrophys. J.*, 777, 68, doi: 10.1088/0004-637X/777/1/68
- Baumgarte, T. W., & Shapiro, S. L. 1998, *Phys. Rev. D*, 59, 024007, doi: 10.1103/PhysRevD.59.024007
- Bauswein, A., Bastian, N.-U. F., Blaschke, D. B., et al. 2019, *Phys. Rev. Lett.*, 122, 061102, doi: 10.1103/PhysRevLett.122.061102
- Bauswein, A., Baumgarte, T. W., & Janka, H. T. 2013a, *Phys. Rev. Lett.*, 111, 131101, doi: 10.1103/PhysRevLett.111.131101

- 
- Bauswein, A., Goriely, S., & Janka, H. T. 2013b, *Astrophys. J.*, 773, 78, doi: 10.1088/0004-637X/773/1/78
- Bauswein, A., Janka, H., Hebeler, K., & Schwenk, A. 2012, *Phys. Rev. D*, 86, 063001, doi: 10.1103/PhysRevD.86.063001
- Bauswein, A., & Janka, H. T. 2012, *Phys. Rev. Lett.*, 108, 011101, doi: 10.1103/PhysRevLett.108.011101
- Bauswein, A., Janka, H. T., & Oechslin, R. 2010a, *Phys. Rev.*, D82, 084043, doi: 10.1103/PhysRevD.82.084043
- Bauswein, A., Janka, H. T., Oechslin, R., et al. 2009, *Phys. Rev. Lett.*, 103, 011101, doi: 10.1103/PhysRevLett.103.011101
- Bauswein, A., Just, O., Janka, H.-T., & Stergioulas, N. 2017, *Astrophys. J.*, 850, L34, doi: 10.3847/2041-8213/aa9994
- Bauswein, A., Oechslin, R., & Janka, H. T. 2010b, *Phys. Rev.*, D81, 024012, doi: 10.1103/PhysRevD.81.024012
- Bauswein, A., & Stergioulas, N. 2015, *Phys. Rev.*, D91, 124056, doi: 10.1103/PhysRevD.91.124056
- . 2017, *Mon. Not. Roy. Astron. Soc.*, 471, 4956, doi: 10.1093/mnras/stx1983
- Bauswein, A., Stergioulas, N., & Janka, H.-T. 2016, *Eur. Phys. J.*, A52, 56, doi: 10.1140/epja/i2016-16056-7
- Baym, G., Pethick, C., & Sutherland, P. 1971, *Astrophys. J.*, 170, 299, doi: 10.1086/151216
- Becker, W., Trumper, J., Lommen, A. N., & Backer, D. C. 2000, *Astrophys. J.*, 545, 1015, doi: 10.1086/317839
- Bedaque, P., & Steiner, A. W. 2015, *Phys. Rev. Lett.*, 114, 031103, doi: 10.1103/PhysRevLett.114.031103
- Bednarek, I., Haensel, P., Zdunik, J., Bejger, M., & Manka, R. 2012, *Astron. Astrophys.*, 543, A157, doi: 10.1051/0004-6361/201118560
- Belczynski, K., Kalogera, V., & Bulik, T. 2002, *Astrophys. J.*, 572, 407, doi: 10.1086/340304
- Belczynski, K., Kalogera, V., Rasio, F. A., et al. 2008, *Astrophys. J. Suppl.*, 174, 223, doi: 10.1086/521026

- 
- Benic, S. 2014, *Eur. Phys. J. A*, 50, 111, doi: 10.1140/epja/i2014-14111-1
- Benic, S., Blaschke, D., Alvarez-Castillo, D. E., Fischer, T., & Typel, S. 2015, *Astron. Astrophys.*, 577, A40, doi: 10.1051/0004-6361/201425318
- Berezhiani, Z., Bombaci, I., Drago, A., Frontera, F., & Lavagno, A. 2003, *Astrophys. J.*, 586, 1250, doi: 10.1086/367756
- Bertsch, G., & Das Gupta, S. 1988, *Phys. Rept.*, 160, 189, doi: 10.1016/0370-1573(88)90170-6
- Bhattacharyya, A., Ghosh, S. K., Hanauske, M., & Raha, S. 2005a, *Phys. Rev. C*, 71, 048801. <https://arxiv.org/abs/astro-ph/0406509>
- Bhattacharyya, S., Strohmayr, T. E., Miller, M. C., & Markwardt, C. B. 2005b, *Astrophys. J.*, 619, 483, doi: 10.1086/426383
- Blaschke, D., & Alvarez-Castillo, D. E. 2016, *AIP Conf. Proc.*, 1701, 020013, doi: 10.1063/1.4938602
- Blaschke, D., Ayriyan, A., Alvarez-Castillo, D. E., & Grigorian, H. 2020, *Universe*, 6, 81, doi: 10.3390/universe6060081
- Blaschke, D., Ayriyan, A., Friesen, A., & Grigorian, H., eds. 2018
- Blattel, B., Koch, V., & Mosel, U. 1993, *Reports on Progress in Physics*, 56, 1, doi: 10.1088/0034-4885/56/1/001
- Bodmer, A. R. 1971, *Phys. Rev.*, D4, 1601, doi: 10.1103/PhysRevD.4.1601
- Bogdanov, S. 2013, *Astrophys. J.*, 762, 96, doi: 10.1088/0004-637X/762/2/96
- Bogdanov, S., Heinke, C. O., Özel, F., & Güver, T. 2016, *Astrophys. J.*, 831, 184, doi: 10.3847/0004-637X/831/2/184
- Bogdanov, S., Rybicki, G. B., & Grindlay, J. E. 2007, *Astrophys. J.*, 670, 668, doi: 10.1086/520793
- Bogdanov, S., et al. 2019, *Astrophys. J. Lett.*, 887, L26, doi: 10.3847/2041-8213/ab5968
- Boguta, J. 1982, *Phys. Lett. B*, 109, 251, doi: 10.1016/0370-2693(82)90428-2
- Boguta, J., & Bodmer, A. R. 1977, *Nucl. Phys.*, A292, 413, doi: 10.1016/0375-9474(77)90626-1
- Bombaci, I. 2017a, *JPS Conf. Proc.*, 17, 101002, doi: 10.7566/JPSCP.17.101002

- 
- . 2017b, "The Hyperon Puzzle in Neutron Stars", booktitle = "Proceedings of the 12th International Conference on Hypernuclear and Strange Particle Physics (HYP2015), doi: 10.7566JPSCP.17.101002
- Bombaci, I., & Datta, B. 2000, *Astrophys. J. Lett.*, 530, L69, doi: 10.1086/312497
- Bombaci, I., Drago, A., Logoteta, D., Pagliara, G., & Vidana, I. 2020. <https://arxiv.org/abs/2010.01509>
- Bombaci, I., Logoteta, D., Panda, P. K., Providencia, C., & Vidana, I. 2009, *Phys. Lett.*, B680, 448, doi: 10.1016/j.physletb.2009.09.039
- Bombaci, I., Logoteta, D., Providencia, C., & Vidana, I. 2011, *Astron. Astrophys.*, 528, A71, doi: 10.1051/0004-6361/201015783
- Bombaci, I., Logoteta, D., Vidana, I., & Providência, C. 2016, *Eur. Phys. J. A*, 52, 58, doi: 10.1140/epja/i2016-16058-5
- Bombaci, I., Lugones, G., & Vidana, I. 2007, *Astron. Astrophys.*, 462, 1017, doi: 10.1051/0004-6361:20065259
- Bombaci, I., Panda, P. K., Providencia, C., & Vidana, I. 2008, *Phys. Rev. D*, 77, 083002, doi: 10.1103/PhysRevD.77.083002
- Bombaci, I., Parenti, I., & Vidana, I. 2004, *Astrophys. J.*, 614, 314, doi: 10.1086/423658
- Bonanno, L., & Sedrakian, A. 2012, *Astron. Astrophys.*, 539, A16, doi: 10.1051/0004-6361/201117832
- Bonazzola, S., Gourgoulhon, E., & Marck, J.-A. 1998, *Phys. Rev. D*, 58, 104020, doi: 10.1103/PhysRevD.58.104020
- Bondi, H. 1964, *Proc. Roy. Soc. Lond. A*, A282, 303, doi: 10.1098/rspa.1964.0234
- Botta, E., Bressani, T., & Garbarino, G. 2012, *Eur. Phys. J. A*, 48, 41, doi: 10.1140/epja/i2012-12041-6
- Bovard, L., Martin, D., Guercilena, F., et al. 2017, *Phys. Rev.*, D96, 124005, doi: 10.1103/PhysRevD.96.124005
- Braje, T. M., Romani, R. W., & Rauch, K. P. 2000, *Astrophys. J.*, 531, 447, doi: 10.1086/308448
- Brandt, S. R., Brendal, B., Gabella, W. E., et al. 2020, "The Einstein Toolkit, The "Turing" release, ET\_2020\_05, Zenodo, doi: 10.5281/zenodo.3866075

- 
- Breu, C., & Rezzolla, L. 2016, *Mon. Not. Roy. Astron. Soc.*, 459, 646, doi: 10.1093/mnras/stw575
- Brown, B., Shen, G., Hillhouse, G., Meng, J., & Trzcinska, A. 2007, *Phys. Rev. C*, 76, 034305, doi: 10.1103/PhysRevC.76.034305
- Brown, E. F., Bildsten, L., & Rutledge, R. E. 1998, *Astrophys. J. Lett.*, 504, L95, doi: 10.1086/311578
- Brown, G., Lee, C.-H., Park, H.-J., & Rho, M. 2006, *Phys. Rev. Lett.*, 96, 062303, doi: 10.1103/PhysRevLett.96.062303
- Brown, G., Thorsson, V., Kubodera, K., & Rho, M. 1992, *Phys. Lett. B*, 291, 355, doi: 10.1016/0370-2693(92)91386-N
- Brown, J. D., Diener, P., Sarbach, O., Schnetter, E., & Tiglio, M. 2009, *Phys. Rev. D*, 79, 044023, doi: 10.1103/PhysRevD.79.044023
- Buballa, M., & Carignano, S. 2015, *Prog. Part. Nucl. Phys.*, 81, 39, doi: 10.1016/j.pnpnp.2014.11.001
- Bucciantini, N., Drago, A., Pagliara, G., & Traversi, S. 2019. <https://arxiv.org/abs/1908.02501>
- Burbidge, M. E., Burbidge, G. R., Fowler, W. A., & Hoyle, F. 1957, *Rev. Mod. Phys.*, 29, 547, doi: 10.1103/RevModPhys.29.547
- Burdin, S., Fairbairn, M., Mermod, P., et al. 2015, *Phys. Rept.*, 582, 1, doi: 10.1016/j.physrep.2015.03.004
- Burgio, F., & Zappalà, D. 2016, *PoS, MPCS2015*, 008, doi: 10.22323/1.262.0008
- Burgio, G. F., Drago, A., Pagliara, G., Schulze, H. J., & Wei, J. B. 2018, *Astrophys. J.*, 860, 139, doi: 10.3847/1538-4357/aac6ee
- Buss, O., Gaitanos, T., Gallmeister, K., et al. 2012, *Phys. Rept.*, 512, 1, doi: 10.1016/j.physrep.2011.12.001
- Cai, B.-J., Fattoyev, F. J., Li, B.-A., & Newton, W. G. 2015, *Phys. Rev.*, C92, 015802, doi: 10.1103/PhysRevC.92.015802
- Capano, C. D., Tews, I., Brown, S. M., et al. 2020, *Nature Astron.*, 4, 625, doi: 10.1038/s41550-020-1014-6
- Caraveo, P. A. 2014, *Ann. Rev. Astron. Astrophys.*, 52, 211, doi: 10.1146/annurev-astro-081913-035948

- 
- Carignano, S., & Buballa, M. 2020, *Phys. Rev. D*, 101, 014026, doi: 10.1103/PhysRevD.101.014026
- Carson, Z., Steiner, A. W., & Yagi, K. 2019, *Phys. Rev. D*, 99, 043010, doi: 10.1103/PhysRevD.99.043010
- Centelles, M., Roca-Maza, X., Vinas, X., & Warda, M. 2009, *Phys. Rev. Lett.*, 102, 122502, doi: 10.1103/PhysRevLett.102.122502
- Chajeccki, Z., et al. 2014. <https://arxiv.org/abs/1402.5216>
- Chamel, N., Fantina, A. F., Pearson, J. M., & Goriely, S. 2013, *Astron. Astrophys.*, 553, A22, doi: 10.1051/0004-6361/201220986
- Chang, P., Bildsten, L., & Wasserman, I. 2005, *Astrophys. J.*, 629, 998, doi: 10.1086/431730
- Char, P., & Banik, S. 2014, *Phys. Rev. C*, 90, 015801, doi: 10.1103/PhysRevC.90.015801
- Char, P., Drago, A., & Pagliara, G. 2019, in *Xiamen-CUSTIPEN Workshop on the EOS of Dense Neutron-Rich Matter in the Era of Gravitational Wave Astronomy Xiamen, China, January 3-7, 2019*. <https://arxiv.org/abs/1905.04681>
- Char, P., Traversi, S., & Pagliara, G. 2020, *Particles*, 3, 621, doi: 10.3390/particles3030040
- Chatterjee, D., & Vidaña, I. 2016, *Eur. Phys. J.*, A52, 29, doi: 10.1140/epja/i2016-16029-x
- Chatziioannou, K., Clark, J. A., Bauswein, A., et al. 2017, *Phys. Rev. D*, 96, 124035, doi: 10.1103/PhysRevD.96.124035
- Chen, L.-W., Ko, C. M., & Li, B.-A. 2005, *Phys. Rev. Lett.*, 94, 032701, doi: 10.1103/PhysRevLett.94.032701
- Chen, L.-W., Ko, C. M., Li, B.-A., Xu, C., & Xu, J. 2014, *Eur. Phys. J. A*, 50, 29, doi: 10.1140/epja/i2014-14029-6
- Chen, L.-W., Ko, C. M., Li, B.-A., & Xu, J. 2010, *Phys. Rev. C*, 82, 024321, doi: 10.1103/PhysRevC.82.024321
- Chen, Y., Guo, H., & Liu, Y. 2007, *Phys. Rev. C*, 75, 035806, doi: 10.1103/PhysRevC.75.035806
- Chollet, F. 2015, *Keras*, <https://github.com/fchollet/keras>, GitHub

- 
- Chornock, R., et al. 2017, *Astrophys. J.*, 848, L19, doi: 10.3847/2041-8213/aa905c
- Christian, J.-E., & Schaffner-Bielich, J. 2020, *Astrophys. J. Lett.*, 894, L8, doi: 10.3847/2041-8213/ab8af4
- Christian, J.-E., Zacchi, A., & Schaffner-Bielich, J. 2018a, *The European Physical Journal A*, 54, doi: 10.1140/epja/i2018-12472-y
- . 2018b, *Eur. Phys. J.*, A54, 28, doi: 10.1140/epja/i2018-12472-y
- Ciolfi, R., & Siegel, D. M. 2015, *Astrophys. J.*, 798, L36, doi: 10.1088/2041-8205/798/2/L36
- Clark, B. C., Kerr, L. J., & Hama, S. 2003, *Phys. Rev. C*, 67, 054605, doi: 10.1103/PhysRevC.67.054605
- Clayton, D. D. 1983, *Principles of stellar evolution and nucleosynthesis*
- Coll, B. 1976, *Annales de L'Institut Henri Poincare Section (A) Physique Theorique*, 25, 363
- Colonna, M., Baran, V., & Di Toro, M. 2014, *Eur. Phys. J. A*, 50, 30, doi: 10.1140/epja/i2014-14030-1
- Colucci, G., & Sedrakian, A. 2013, *Phys. Rev. C*, 87, 055806, doi: 10.1103/PhysRevC.87.055806
- Cook, G. B., Shapiro, S. L., & Teukolsky, S. A. 1994, *Astrophys. J.*, 424, 823, doi: 10.1086/173934
- Coulter, D., et al. 2017, *Science*, 358, 1556, doi: 10.1126/science.aap9811
- Cowperthwaite, P. S., et al. 2017, *Astrophys. J.*, 848, L17, doi: 10.3847/2041-8213/aa8fc7
- Cozma, M., Leifels, Y., Trautmann, W., Li, Q., & Russotto, P. 2013, *Phys. Rev. C*, 88, 044912, doi: 10.1103/PhysRevC.88.044912
- Cromartie, H. T., et al. 2019, *Nat. Astron.*, 4, 72, doi: 10.1038/s41550-019-0880-2
- Dalitz, R. 1960, in *9th International Annual Conference on High Energy Physics*, Vol. Vol.1, 587-608
- Dall'Osso, S., Stratta, G., Guetta, D., et al. 2011, *Astron. Astrophys.*, 526, A121, doi: 10.1051/0004-6361/201014168
- Damen, E., Magnier, E., Lewin, W. H. G., et al. 1990, *Astron. Astrophys.*, 2237, 103

- 
- Damour, T., & Nagar, A. 2009, *Phys. Rev. D*, 80, 084035, doi: 10.1103/PhysRevD.80.084035
- Danielewicz, P. 1984a, *Annals Phys.*, 152, 239, doi: 10.1016/0003-4916(84)90092-7
- . 1984b, *Annals Phys.*, 152, 305, doi: 10.1016/0003-4916(84)90093-9
- Danielewicz, P., Lacey, R., & Lynch, W. G. 2002, *Science*, 298, 1592, doi: 10.1126/science.1078070
- Danielewicz, P., & Lee, J. 2014, *Nucl. Phys. A*, 922, 1, doi: 10.1016/j.nuclphysa.2013.11.005
- D’Avanzo, P. 2015, *Journal of High Energy Astrophysics*
- Davidson, P. 2015, *Turbulence* (Oxford University Press)
- De Filippo, E., & Pagano, A. 2014, *Eur. Phys. J. A*, 50, 32, doi: 10.1140/epja/i2014-14032-y
- De Pietri, R., Drago, A., Feo, A., et al. 2019, *Astrophys.J.*, 881, 122, doi: 10.3847/1538-4357/ab2fd0
- De Pietri, R., Feo, A., Font, J. A., et al. 2018, *Phys. Rev. Lett.*, 120, 221101, doi: 10.1103/PhysRevLett.120.221101
- De Pietri, R., Feo, A., Maione, F., & Löffler, F. 2016a, *Phys. Rev. D*, 93, 064047, doi: 10.1103/PhysRevD.93.064047
- De Pietri, R., Feo, A., Maione, F., & Löffler, F. 2016b, *Phys. Rev.*, D93, 064047, doi: 10.1103/PhysRevD.93.064047
- de Rujula, A., & Glashow, S. L. 1984, *Nature*, 312, 734, doi: 10.1038/312734a0
- De Vries, H., De Jager, C., & De Vries, C. 1987, *Atom. Data Nucl. Data Tabl.*, 36, 495, doi: 10.1016/0092-640X(87)90013-1
- Demorest, P., Pennucci, T., Ransom, S., Roberts, M., & Hessels, J. 2010, *Nature*, 467, 1081, doi: 10.1038/nature09466
- Dexheimer, V., Negreiros, R., & Schramm, S. 2015, *Phys. Rev. C*, 91, 055808, doi: 10.1103/PhysRevC.91.055808
- Dexheimer, V., & Schramm, S. 2008, *Astrophys. J.*, 683, 943, doi: 10.1086/589735
- Dhiman, S. K., Kumar, R., & Agrawal, B. 2007, *Phys. Rev. C*, 76, 045801, doi: 10.1103/PhysRevC.76.045801

- 
- Di Toro, M., Drago, A., Gaitanos, T., Greco, V., & Lavagno, A. 2006, Nucl. Phys., A775, 102, doi: 10.1016/j.nuclphysa.2006.04.007
- Di Toro, M., et al. 2009, Prog. Part. Nucl. Phys., 62, 389, doi: 10.1016/j.ppnp.2008.12.038
- Djapo, H., Schaefer, B.-J., & Wambach, J. 2010, Phys. Rev. C, 81, 035803, doi: 10.1103/PhysRevC.81.035803
- Dondi, N. A., Drago, A., & Pagliara, G. 2017, EPJ Web Conf., 137, 09004, doi: 10.1051/epjconf/201713709004
- Drago, A., Lavagno, A., Metzger, B., & Pagliara, G. 2016a, Phys. Rev., D93, 103001, doi: 10.1103/PhysRevD.93.103001
- Drago, A., Lavagno, A., & Pagliara, G. 2004, Phys. Rev. D, 69, 057505, doi: 10.1103/PhysRevD.69.057505
- . 2014a, Phys. Rev., D89, 043014, doi: 10.1103/PhysRevD.89.043014
- Drago, A., Lavagno, A., Pagliara, G., & Pigato, D. 2014b, Phys. Rev., C90, 065809, doi: 10.1103/PhysRevC.90.065809
- . 2016b, Eur. Phys. J., A52, 40, doi: 10.1140/epja/i2016-16040-3
- Drago, A., Lavagno, A., & Parenti, I. 2007, Astrophys. J., 659, 1519, doi: 10.1086/512112
- Drago, A., Moretti, M., & Pagliara, G. 2019, Astron. Nachr., 340, 189, doi: 10.1002/asna.201913586
- Drago, A., & Pagliara, G. 2015, Phys. Rev., C92, 045801, doi: 10.1103/PhysRevC.92.045801
- . 2018, Astrophys. J., 852, L32, doi: 10.3847/2041-8213/aaa40a
- Drago, A., Pagliara, G., Popov, S. B., Traversi, S., & Wiktorowicz, G. 2018a, Universe, 4, 50, doi: 10.3390/universe4030050
- Drago, A., Pagliara, G., & Traversi, S. 2018b, Mem. Soc. Ast. It., 89, 236. <https://arxiv.org/abs/1802.01696>
- Drago, A., & Tambini, U. 1999, J. Phys. G, 25, 971, doi: 10.1088/0954-3899/25/5/302
- Duch, W., & Diercksen, G. H. F. 1994, Computer Physics Communications, 82, 91, doi: 10.1016/0010-4655(94)90158-9
- Duerr, H.-P. 1956, Phys. Rev., 103, 469, doi: 10.1103/PhysRev.103.469

- 
- Dutra, M., Lourenço, O., Avancini, S. S., et al. 2014, *Phys. Rev.*, C90, 055203, doi: 10.1103/PhysRevC.90.055203
- Einfeldt, B. 1988, *SIAM Journal on Numerical Analysis*, 25, 294, doi: 10.1137/0725021
- Erler, J., Birge, N., Kortelainen, M., et al. 2012, *Nature*, 486, 509, doi: 10.1038/nature11188
- Essick, R., Landry, P., & Holz, D. E. 2020, *Phys. Rev. D*, 101, 063007, doi: 10.1103/PhysRevD.101.063007
- Fai, G. I., & Randrup, J. 1982, *Nucl. Phys. A*, 381, 557, doi: 10.1016/0375-9474(82)90376-1
- Falanga, M., Bozzo, E., Lutovinov, A., et al. 2015, *Astron. Astrophys.*, 577, A130, doi: 10.1051/0004-6361/201425191
- Farhi, E. 1986, *Nucl. Phys. A*, 450, 505C, doi: 10.1016/0375-9474(86)90583-X
- Fasano, M., Abdelsalhin, T., Maselli, A., & Ferrari, V. 2019, *Phys. Rev. Lett.*, 123, 141101, doi: 10.1103/PhysRevLett.123.141101
- Fattoyev, F., Horowitz, C., Piekarewicz, J., & Reed, B. 2020. <https://arxiv.org/abs/2007.03799>
- Fattoyev, F., Piekarewicz, J., & Horowitz, C. 2018, *Phys. Rev. Lett.*, 120, 172702, doi: 10.1103/PhysRevLett.120.172702
- Feo, A., De Pietri, R., Maione, F., & Löffler, F. 2017, *Class. Quant. Grav.*, 34, 034001, doi: 10.1088/1361-6382/aa51fa
- Fernández, R., & Metzger, B. D. 2013, *Mon. Not. Roy. Astron. Soc.*, 435, 502, doi: 10.1093/mnras/stt1312
- Ferreira, M., & Providência, C. 2019. <https://arxiv.org/abs/1910.05554>
- Fiorella Burgio, G., & Fantina, A. F. 2018, *Nuclear Equation of state for Compact Stars and Supernovae*, Vol. 457, 255–335, doi: 10.1007/978-3-319-97616-7\_6
- Fischer, T., Whitehouse, S. C., Mezzacappa, A., Thielemann, F. K., & Liebendorfer, M. 2010, *Astron. Astrophys.*, 517, A80, doi: 10.1051/0004-6361/200913106
- Fischer, T., Bastian, N.-U. F., Wu, M.-R., et al. 2018, *Nature Astron.*, 2, 980, doi: 10.1038/s41550-018-0583-0
- Flanagan, E. E., & Hinderer, T. 2008, *Phys. Rev. D*, 77, 021502, doi: 10.1103/PhysRevD.77.021502

- 
- Fonseca, E., et al. 2016, *Astrophys. J.*, 832, 167, doi: 10.3847/0004-637X/832/2/167
- Foreman-Mackey, D. 2016, *The Journal of Open Source Software*, 24, doi: 10.21105/joss.00024
- Foreman-Mackey, D., Hogg, D. W., Lang, D., & Goodman, J. 2013, *Publ. Astron. Soc. Pac.*, 125, 306, doi: 10.1086/670067
- Fortin, M., Avancini, S. S., Providência, C., & Vidaña, I. 2017, arXiv e-prints, arXiv:1701.06373. <https://arxiv.org/abs/1701.06373>
- Fortin, M., Zdunik, J. L., Haensel, P., & Bejger, M. 2015, *Astron. Astrophys.*, 576, A68, doi: 10.1051/0004-6361/201424800
- Fraga, E. S., Kurkela, A., & Vuorinen, A. 2014, *Astrophys. J.*, 781, L25, doi: 10.1088/2041-8205/781/2/L25
- Fraga, E. S., Pisarski, R. D., & Schaffner-Bielich, J. 2001, *Phys. Rev. D*, 63, 121702, doi: 10.1103/PhysRevD.63.121702
- Friedman, J., Parker, L., & Ipser, J. 1986, *Astrophys. J.*, 304, 115, doi: 10.1086/164149
- Frohn, A., & Roth, N. 2000, *Dynamics of Droplets* (Springer Science & Business Media), doi: 10.1007/978-3-662-04040-9
- Fuchs, C., Faessler, A., Zabrodin, E., & Zheng, Y.-M. 2001, *Phys. Rev. Lett.*, 86, 1974, doi: 10.1103/PhysRevLett.86.1974
- Fuchs, C., & Wolter, H. 2006, *Eur. Phys. J. A*, 30, 5, doi: 10.1140/epja/i2005-10313-x
- Fujibayashi, S., Kiuchi, K., Nishimura, N., Sekiguchi, Y., & Shibata, M. 2018, *Astrophys. J.*, 860, 64, doi: 10.3847/1538-4357/aabafd
- Fujimoto, M. Y., & Taam, R. E. 1986, *Astrophys. J.*, 305, 246, doi: 10.1086/164244
- Fujimoto, Y., Fukushima, K., & Murase, K. 2018, *Phys.Rev.D*, 98, 023019, doi: 10.1103/PhysRevD.98.023019
- . 2020, *Phys. Rev. D*, 101, 054016, doi: 10.1103/PhysRevD.101.054016
- Furnstahl, R. 2002, *Nucl. Phys. A*, 706, 85, doi: 10.1016/S0375-9474(02)00867-9
- Gaidarov, M., Antonov, A., Sarriguren, P., & de Guerra, E. 2012, *Phys. Rev. C*, 85, 064319, doi: 10.1103/PhysRevC.85.064319
- Gaidarov, M., Antonov, A., Sarriguren, P., & Moya De Guerra, E. 2015, *AIP Conf. Proc.*, 1606, 180, doi: 10.1063/1.4891131

- 
- Gale, C., Jeon, S., & Schenke, B. 2013, *Int. J. Mod. Phys. A*, 28, 1340011, doi: 10.1142/S0217751X13400113
- Gale, C., Welke, G., Prakash, M., Lee, S., & Das Gupta, S. 1990, *Phys. Rev. C*, 41, 1545, doi: 10.1103/PhysRevC.41.1545
- Galloway, D. K., & Lampe, N. 2012, *Astrophys. J.*, 747, 75, doi: 10.1088/0004-637X/747/1/75
- Galloway, D. K., Muno, M. P., Hartman, J. M., et al. 2008, *Astrophys. J. Suppl.*, 179, 360, doi: 10.1086/592044
- Gandolfi, S., Carlson, J., & Reddy, S. 2012, *Phys. Rev. C*, 85, 032801, doi: 10.1103/PhysRevC.85.032801
- Gandolfi, S., Lippuner, J., Steiner, A. W., et al. 2019, *J. Phys.*, G46, 103001, doi: 10.1088/1361-6471/ab29b3
- Garpman, S., Glendenning, N., & Karant, Y. 1979, *Nucl. Phys. A*, 322, 382, doi: 10.1016/0375-9474(79)90433-0
- Gendreau, K. C., Arzoumanian, Z., & et al., P. W. A. 2016, in *Space Telescopes and Instrumentation 2016: Ultraviolet to Gamma Ray*, ed. J.-W. A. den Herder, T. Takahashi, & M. Bautz, Vol. 9905, International Society for Optics and Photonics (SPIE), 420 – 435, doi: 10.1117/12.2231304
- Gentile, N., Aufderheide, M., Mathews, G., Swesty, F., & Fuller, G. 1993, *Astrophys. J.*, 414, 701, doi: 10.1086/173116
- Gerlach, U. H. 1968, *Phys. Rev.*, 172, 1325, doi: 10.1103/PhysRev.172.1325
- Giacomazzo, B., Perna, R., Rezzolla, L., Troja, E., & Lazzati, D. 2013, *Astrophys. J.*, 762, L18, doi: 10.1088/2041-8205/762/2/L18
- Giacomazzo, B., Zrake, J., Duffell, P., MacFadyen, A. I., & Perna, R. 2015, *Astrophys. J.*, 809, 39, doi: 10.1088/0004-637X/809/1/39
- Glendenning, N. 1982a, *Phys. Lett. B*, 114, 392, doi: 10.1016/0370-2693(82)90078-8
- . 1985, *Astrophys. J.*, 293, 470, doi: 10.1086/163253
- Glendenning, N. K. 1982b, *Physics Letters B*, 114, 392, doi: [https://doi.org/10.1016/0370-2693\(82\)90078-8](https://doi.org/10.1016/0370-2693(82)90078-8)
- . 1989, *Journal of Physics G: Nuclear and Particle Physics*, 15, L255, doi: 10.1088/0954-3899/15/11/006

- 
- . 1997, *Compact stars: Nuclear physics, particle physics, and general relativity*
- . 2000, *Compact stars*, 2nd edn. (Springer)
- Glendenning, N. K., & Kettner, C. 2000, *Astronomy & Astrophysics*, 353, L9. <https://arxiv.org/abs/astro-ph/9807155>
- Glendenning, N. K., & Moszkowski, S. A. 1991, *Phys. Rev. Lett.*, 67, 2414, doi: 10.1103/PhysRevLett.67.2414
- Glendenning, N. K., & Schaffner-Bielich, J. 1998, *Phys. Rev. Lett.*, 81, 4564, doi: 10.1103/PhysRevLett.81.4564
- Glorot, X., & Bengio, Y. 2010, in *Proceedings of Machine Learning Research*, Vol. 9, *Proceedings of the Thirteenth International Conference on Artificial Intelligence and Statistics*, ed. Y. W. Teh & M. Titterton (Chia Laguna Resort, Sardinia, Italy: PMLR), 249–256. <http://proceedings.mlr.press/v9/glorot10a.html>
- Gomes, R., Dexheimer, V., Schramm, S., & Vasconcellos, C. 2015, *Astrophys. J.*, 808, 8, doi: 10.1088/0004-637X/808/1/8
- Gonzalez-Caniulef, D., Guillot, S., & Reisenegger, A. 2019, *Mon. Not. Roy. Astron. Soc.*, 490, 5848, doi: 10.1093/mnras/stz2941
- Goodman, J., & Weare, J. 2010, *Communications in Applied Mathematics and Computational Science*, 5, 65, doi: 10.2140/camcos.2010.5.65
- Goriely, S., Bauswein, A., & Janka, H. T. 2011, *Astrophys. J.*, 738, L32, doi: 10.1088/2041-8205/738/2/L32
- Goriely, S., Bauswein, A., Just, O., Pllumbi, E., & Janka, H.-T. 2015, *Mon. Not. Roy. Astron. Soc.*, 452, 3894, doi: 10.1093/mnras/stv1526
- Goriely, S., Sida, J. L., Lemaître, J. F., et al. 2013, *Phys. Rev. Lett.*, 111, 242502, doi: 10.1103/PhysRevLett.111.242502
- Gottlieb, O., Nakar, E., Piran, T., & Hotokezaka, K. 2018, *Mon. Not. Roy. Astron. Soc.*, 479, 588, doi: 10.1093/mnras/sty1462
- Gourgoulhon, E., Grandclément, P., Taniguchi, K., Marck, J.-A., & Bonazzola, S. 2001, *Phys. Rev. D*, 63, 064029, doi: 10.1103/PhysRevD.63.064029
- Gourgoulhon, E., Haensel, P., Livine, R., et al. 1999, *Astron. Astrophys.*, 349, 851. <https://arxiv.org/abs/astro-ph/9907225>

- 
- Gregory, P. C. 2005, *Bayesian Logical Data Analysis for the Physical Sciences: A Comparative Approach with ‘Mathematica’ Support* (Cambridge University Press)
- Greif, S., Raaijmakers, G., Hebel, K., Schwenk, A., & Watts, A. 2019, *Mon. Not. Roy. Astron. Soc.*, 485, 5363, doi: 10.1093/mnras/stz654
- Grindlay, J., Camilo, F., Heinke, C., et al. 2002, *Astrophys. J.*, 581, 470, doi: 10.1086/344150
- Gross-Boelting, T., Fuchs, C., & Faessler, A. 1999, *Nucl. Phys. A*, 648, 105, doi: 10.1016/S0375-9474(99)00022-6
- Guillot, S., & Rutledge, R. E. 2014, *Astrophys. J. Lett.*, 796, L3, doi: 10.1088/2041-8205/796/1/L3
- Guillot, S., Rutledge, R. E., & Brown, E. F. 2011, *Astrophys. J.*, 732, 88, doi: 10.1088/0004-637X/732/2/88
- Guillot, S., Servillat, M., Webb, N. A., & Rutledge, R. E. 2013, *Astrophys. J.*, 772, 7, doi: 10.1088/0004-637X/772/1/7
- Gupta, N., & Arumugam, P. 2012, *Phys. Rev. C*, 85, 015804, doi: 10.1103/PhysRevC.85.015804
- Gusakov, M., Haensel, P., & Kantor, E. 2014, *Mon. Not. Roy. Astron. Soc.*, 439, 318, doi: 10.1093/mnras/stt2438
- Güven, H., Bozkurt, K., Khan, E., & Margueron, J. 2020, *Phys. Rev. C*, 102, 015805, doi: 10.1103/PhysRevC.102.015805
- Guver, T., & Özel, F. 2013, *Astrophys. J. Lett.*, 765, L1, doi: 10.1088/2041-8205/765/1/L1
- Guver, T., Özel, F., Cabrera-Lavers, A., & Wroblewski, P. 2010a, *Astrophys. J.*, 712, 964, doi: 10.1088/0004-637X/712/2/964
- Guver, T., Wroblewski, P., Camarota, L., & Özel, F. 2010b, *Astrophys. J.*, 719, 1807, doi: 10.1088/0004-637X/719/2/1807
- Haensel, P., Paczynski, B., & P. Amsterdamski, P. 1991, *Astrophys. J.*, 375, 209, doi: 10.1086/170182
- Haensel, P., & Zdunik, J. L. 1989, *Nature*, 340, 617, doi: 10.1038/340617a0
- Haensel, P., Zdunik, J. L., & Schaeffer, R. 1986, *Astron. Astrophys.*, 160, 121

- 
- Haensel, Potekhin, Y. 2007, *Nuutron stars 1: Equation of state and structure*, Vol. 326 (Springer)
- Hambaryan, V., Neuhäuser, R., Suleimanov, V., & Werner, K. 2014, in *Journal of Physics Conference Series*, Vol. 496, *Journal of Physics Conference Series*, 012015, doi: 10.1088/1742-6596/496/1/012015
- Han, K., Ashenfelter, J., Chikanian, A., et al. 2009, *Phys. Rev. Lett.*, 103, 092302, doi: 10.1103/PhysRevLett.103.092302
- Hanauske, M., Zschesche, D., Pal, S., et al. 2000, *Astrophys. J.*, 537, 958, doi: 10.1086/309052
- Harten, A., Lax, P., & Leer, B. 1983, *SIAM Review*, 25, 35, doi: 10.1137/1025002
- Hartle, J. B., & Sabbadini, A. G. 1977, *Astrophys. J.*, 213, 831, doi: 10.1086/155214
- Hartnack, C., Oeschler, H., & Aichelin, J. 2006, *Phys. Rev. Lett.*, 96, 012302, doi: 10.1103/PhysRevLett.96.012302
- Hartnack, C., Puri, R. K., Aichelin, J., et al. 1998, *Eur. Phys. J. A*, 1, 151, doi: 10.1007/s100500050045
- Hashimoto, O. 2004, in *International Symposium on A New Era of Nuclear Structure Physics*, 35–42, doi: 10.1142/9789812702401\_0005
- Hebeler, K., Lattimer, J. M., Pethick, C. J., & Schwenk, A. 2013, *Astrophys. J.*, 773, 11, doi: 10.1088/0004-637X/773/1/11
- Hebeler, K., & Schwenk, A. 2010, *Phys. Rev. C*, 82, 014314, doi: 10.1103/PhysRevC.82.014314
- Heinimann, O., Hempel, M., & Thielemann, F.-K. 2016, *Phys. Rev. D*, 94, 103008, doi: 10.1103/PhysRevD.94.103008
- Heinke, C., et al. 2014, *Mon. Not. Roy. Astron. Soc.*, 444, 443, doi: 10.1093/mnras/stu1449
- Heiselberg, H., Madsen, J., & Riisager, K. 1986, *Phys. Scripta*, 34, 556, doi: 10.1088/0031-8949/34/6A/011
- Heiselberg, H., & Pethick, C. J. 1993, *Phys. Rev.*, D48, 2916, doi: 10.1103/PhysRevD.48.2916
- Heiselberg, H., & Pethick, C. J. 1993, *PRD*, 48, 2916, doi: 10.1103/PhysRevD.48.2916

- 
- Heiselberg, H., Pethick, C. J., & Staubo, E. F. 1993, *Phys. Rev. Lett.*, 70, 1355, doi: 10.1103/PhysRevLett.70.1355
- Hempel, M. 2011, *Manual for the supernova EOS tables - v1.0*, Department of Physics, University of Basel
- Hempel, M., Fischer, T., Schaffner-Bielich, J., & Liebendorfer, M. 2012, *Astrophys. J.*, 748, 70, doi: 10.1088/0004-637X/748/1/70
- Hempel, M., & Schaffner-Bielich, J. 2010, *Nucl. Phys.*, A837, 210, doi: 10.1016/j.nuclphysa.2010.02.010
- Herzog, M., & Ropke, F. K. 2011, *Phys. Rev.*, D84, 083002, doi: 10.1103/PhysRevD.84.083002
- Hessels, J. W., Ransom, S. M., Stairs, I. H., et al. 2006, *Science*, 311, 1901, doi: 10.1126/science.1123430
- Hinderer, T. 2008, *Astrophys. J.*, 677, 1216, doi: 10.1086/533487
- Hinderer, T., Lackey, B. D., Lang, R. N., & Read, J. S. 2010, *Phys. Rev.*, D81, 123016, doi: 10.1103/PhysRevD.81.123016
- Hinze, J. O. 1955, *AICHE Journal*, 1, 289
- Hoffman, R. D., Muller, B., & Janka, H. T. 2008, *Astrophys. J.*, 676, L127, doi: 10.1086/587621
- Hofmann, F., Keil, C., & Lenske, H. 2001, *Phys. Rev. C*, 64, 034314, doi: 10.1103/PhysRevC.64.034314
- Hofmann, M., Mattiello, R., Sorge, H., Stöcker, H., & Greiner, W. 1995, *Physical Review C*, 51, 2095, doi: 10.1103/PhysRevC.51.2095
- Hogg, D. W., Bovy, J., & Lang, D. 2010, arXiv e-prints. <https://arxiv.org/abs/1008.4686>
- Hogg, D. W., & Foreman-Mackey, D. 2018, *Astrophys. J. Suppl.*, 236, 11, doi: 10.3847/1538-4365/aab76e
- Horikawa, Y., Thies, M., & Lenz, F. 1980, *Nuclear Physics A*, 345, 386, doi: 10.1016/0375-9474(80)90346-2
- Hornick, N., Tolos, L., Zacchi, A., Jan-Erik, C., & Schaffner-Bielich, J. 2018, *Phys. Rev. C*, 98, 065804

- 
- Horowitz, C., & Piekarewicz, J. 2001, *Phys. Rev. Lett.*, 86, 5647, doi: 10.1103/PhysRevLett.86.5647
- . 2002, *Phys. Rev. C*, 66, 055803, doi: 10.1103/PhysRevC.66.055803
- Horowitz, C., Pollock, S., Souder, P., & Michaels, R. 2001, *Phys. Rev. C*, 63, 025501, doi: 10.1103/PhysRevC.63.025501
- Horvath, J. 2010, *Int. J. Mod. Phys. D*, 19, 523, doi: 10.1142/S0218271810016531
- Hotokezaka, K., Kiuchi, K., Kyutoku, K., et al. 2013a, *Phys. Rev.*, D88, 044026, doi: 10.1103/PhysRevD.88.044026
- . 2013b, *Phys. Rev.*, D87, 024001, doi: 10.1103/PhysRevD.87.024001
- Hotokezaka, K., & Piran, T. 2015, *Mon. Not. Roy. Astron. Soc.*, 450, 1430, doi: 10.1093/mnras/stv620
- Hoyos, C., Jokela, N., Rodríguez Fernández, D., & Vuorinen, A. 2016, *Phys. Rev. D*, 94, 106008, doi: 10.1103/PhysRevD.94.106008
- Hsiang, L.-P., & Faeth, G. 1995, *Int.J.Multiphase Flow*, 21, 545
- Huber, H., Weigel, M., & Weber, F. 1999, *Z. Naturforsch. A*, 54, 77, doi: 10.1515/zna-1999-0110
- Hulse, R., & Taylor, J. 1975, *Astrophys. J. Lett.*, 195, L51, doi: 10.1086/181708
- Huovinen, P., & Ruuskanen, P. 2006, *Ann. Rev. Nucl. Part. Sci.*, 56, 163, doi: 10.1146/annurev.nucl.54.070103.181236
- Iida, K., & Sato, K. 1998, *Phys. Rev.*, C58, 2538, doi: 10.1103/PhysRevC.58.2538
- Jacobs, D. M., Starkman, G. D., & Lynn, B. W. 2015, *Mon. Not. Roy. Astron. Soc.*, 450, 3418, doi: 10.1093/mnras/stv774
- Jaminon, M., & Mahaux, C. 1989, *Phys. Rev. C*, 40, 354, doi: 10.1103/PhysRevC.40.354
- Jastrzebski, J., Trzcinska, A., Lubinski, P., et al. 2004, *Int. J. Mod. Phys. E*, 13, 343, doi: 10.1142/S0218301304002168
- Jiang, G.-S., & Shu, C.-W. 1996, *Journal of Computational Physics*, 126, 202, doi: <https://doi.org/10.1006/jcph.1996.0130>
- Jiang, J.-L., Tang, S.-P., Wang, Y.-Z., Fan, Y.-Z., & Wei, D.-M. 2020, *Astrophys. J.*, 892, 1, doi: 10.3847/1538-4357/ab77cf

- 
- Just, O., Bauswein, A., Pulpillo, R. A., Goriely, S., & Janka, H. T. 2015, *Mon. Not. Roy. Astron. Soc.*, 448, 541, doi: 10.1093/mnras/stv009
- Kampfer, B. 1981, *J. Phys. A*, 14, L471, doi: 10.1088/0305-4470/14/11/009
- Kaplan, D., & Nelson, A. 1986, *Phys. Lett. B*, 175, 57, doi: 10.1016/0370-2693(86)90331-X
- Kaplan, D. L., Bhalerao, V. B., van Kerkwijk, M. H., et al. 2013, *Astrophys. J.*, 765, 158, doi: 10.1088/0004-637X/765/2/158
- Karsch, F. 2007, *Nucl. Phys. A*, 783, 13, doi: 10.1016/j.nuclphysa.2006.11.035
- Kasen, D., Badnell, N. R., & Barnes, J. 2013, *Astrophys. J.*, 774, 25, doi: 10.1088/0004-637X/774/1/25
- Kasen, D., Fernandez, R., & Metzger, B. 2015, *Mon. Not. Roy. Astron. Soc.*, 450, 1777, doi: 10.1093/mnras/stv721
- Kasliwal, M., et al. 2017, *Science*, 358, 1559, doi: 10.1126/science.aap9455
- Kastaun, W., & Galeazzi, F. 2015, *Phys. Rev.*, D91, 064027, doi: 10.1103/PhysRevD.91.064027
- Katayama, T., & Saito, K. 2014. <https://arxiv.org/abs/1410.7166>
- . 2015, *Phys. Lett. B*, 747, 43, doi: 10.1016/j.physletb.2015.03.039
- Khaidukov, Z., & Simonov, Y. A. 2018. <https://arxiv.org/abs/1811.08970>
- Khan, E., & Margueron, J. 2013. <https://arxiv.org/abs/1304.4721>
- Kingma, D. P., & Ba, J. 2014. <https://arxiv.org/abs/1412.6980>
- Kiuchi, K., Cerdá-Durán, P., Kyutoku, K., Sekiguchi, Y., & Shibata, M. 2015, *Phys. Rev.*, D92, 124034, doi: 10.1103/PhysRevD.92.124034
- Kiuchi, K., Kyutoku, K., Shibata, M., & Taniguchi, K. 2019, *Astrophys. J.*, 876, L31, doi: 10.3847/2041-8213/ab1e45
- Kiziltan, B., Kottas, A., De Yoreo, M., & Thorsett, S. E. 2013, *Astrophys. J.*, 778, 66, doi: 10.1088/0004-637X/778/1/66
- Klähn, T., Łastowiecki, R., & Blaschke, D. 2013, *Phys. Rev. D*, 88, 085001, doi: 10.1103/PhysRevD.88.085001
- Klahn, T., et al. 2006, *Phys. Rev. C*, 74, 035802, doi: 10.1103/PhysRevC.74.035802

- 
- Klos, B., et al. 2007, *Phys. Rev. C*, 76, 014311, doi: 10.1103/PhysRevC.76.014311
- Kluzniak, W., & Lee, W. H. 2002, *Mon. Not. Roy. Astron. Soc.*, 335, L29, doi: 10.1046/j.1365-8711.2002.05819.x
- Knorren, R., Prakash, M., & Ellis, P. 1995, *Phys. Rev. C*, 52, 3470, doi: 10.1103/PhysRevC.52.3470
- Koch, J., & Ohtsuka, N. 1985, *Nucl. Phys. A*, 435, 765, doi: 10.1016/0375-9474(85)90187-3
- Kohley, Z., & Yennello, S. 2014, *Eur. Phys. J. A*, 50, 31, doi: 10.1140/epja/i2014-14031-0
- Kojo, T., Powell, P. D., Song, Y., & Baym, G. 2015, *Phys. Rev. D*, 91, 045003, doi: 10.1103/PhysRevD.91.045003
- Kolmogorov, A. N. 1949, *Dokl. Akad. Nauk SSSR*, 66, 825
- Koranda, S., Stergioulas, N., & Friedman, J. L. 1997, *Astrophys. J.*, 488, 799, doi: 10.1086/304714
- Korobkin, O., Rosswog, S., Arcones, A., & Winteler, C. 2012, *Mon. Not. Roy. Astron. Soc.*, 426, 1940, doi: 10.1111/j.1365-2966.2012.21859.x
- Kortelainen, M., Lesinski, T., More, J., et al. 2010, *Phys. Rev. C*, 82, 024313, doi: 10.1103/PhysRevC.82.024313
- Kosov, D., Fuchs, C., Martemyanov, B., & Faessler, A. 1998, *Phys. Lett. B*, 421, 37, doi: 10.1016/S0370-2693(97)01598-0
- Kreim, S., Hempel, M., Lunney, D., & Schaffner-Bielich, J. 2013, *Int. J. Mass Spectr. Ion Process.*, 349-350, 63, doi: 10.1016/j.ijms.2013.02.015
- Kröse, B., Krose, B., van der Smagt, P., & Smagt, P. 1993, doi: 10.1118/493
- Krüger, T., Tews, I., Hebeler, K., & Schwenk, A. 2013, *Phys. Rev.*, C88, 025802, doi: 10.1103/PhysRevC.88.025802
- Kutta, W. 1901, *Z. Math. Phys.*, 46, 435
- Kämpfer, B. 1981, *Phys. Lett. B*, 101, 366, doi: 10.1016/0370-2693(81)90065-4
- Köppel, S., Bovard, L., & Rezzolla, L. 2019, *Astrophys. J.*, 872, L16, doi: 10.3847/2041-8213/ab0210

- 
- Lamb, F. K., Boutloukos, S., Van Wassenhove, S., et al. 2009, *Astrophys. J. Lett.*, 705, L36, doi: 10.1088/0004-637X/705/1/L36
- Landry, P., & Essick, R. 2019, *Phys. Rev. D*, 99, 084049, doi: 10.1103/PhysRevD.99.084049
- Lasota, J.-P., Haensel, P., & Abramowicz, M. A. 1996, *Astrophys. J.*, 456, 300, doi: 10.1086/176650
- Lastowiecki, R., Blaschke, D., Grigorian, H., & Typel, S. 2012, *Acta Phys. Polon. Supp.*, 5, 535, doi: 10.5506/APhysPolBSupp.5.535
- Lattimer, J., & Prakash, M. 2001, *Astrophys. J.*, 550, 426, doi: 10.1086/319702
- . 2004, *Science*, 304, 536, doi: 10.1126/science.1090720
- Lattimer, J. M. 2012, *Ann. Rev. Nucl. Part. Sci.*, 62, 485, doi: 10.1146/annurev-nucl-102711-095018
- Lattimer, J. M., & Lim, Y. 2013, *Astrophys. J.*, 771, 51, doi: 10.1088/0004-637X/771/1/51
- Lattimer, J. M., & Prakash, M. 2007, *Phys.Rept.*, 442, 109, doi: 10.1016/j.physrep.2007.02.003
- . 2011, 275, doi: 10.1142/9789814329880\_0012
- Lattimer, J. M., Prakash, M., Masak, D., & Yahil, A. 1990, *Astrophys. J.*, 355, 241, doi: 10.1086/168758
- Lattimer, J. M., & Steiner, A. W. 2014, *Eur. Phys. J. A*, 50, 40, doi: 10.1140/epja/i2014-14040-y
- Lattimer, J. M., & Swesty, F. D. 1991, *Nuclear Physics A*, 535, 331, doi: [https://doi.org/10.1016/0375-9474\(91\)90452-C](https://doi.org/10.1016/0375-9474(91)90452-C)
- Lavagno, A. 2010, *Phys. Rev. C*, 81, 044909, doi: 10.1103/PhysRevC.81.044909
- Lazzati, D., Perna, R., Morsony, B. J., et al. 2018, *Phys. Rev. Lett.*, 120, 241103, doi: 10.1103/PhysRevLett.120.241103
- Le Fèvre, A., Leifels, Y., Reisdorf, W., Aichelin, J., & Hartnack, C. 2016, *Nucl. Phys. A*, 945, 112, doi: 10.1016/j.nuclphysa.2015.09.015
- Leahy, D. A., Morsink, S. M., & Cadeau, C. 2008, *Astrophys. J.*, 672, 1119, doi: 10.1086/523794

- 
- Leahy, D. A., Morsink, S. M., & Chou, Y. 2011, *Astrophys. J.*, 742, 17, doi: 10.1088/0004-637X/742/1/17
- Leahy, D. A., Morsink, S. M., Chung, Y.-Y., & Chou, Y. 2009, *Astrophys. J.*, 691, 1235, doi: 10.1088/0004-637X/691/2/1235
- Lefebvre, A. 1988, *Atomization and Sprays, Combustion* (Hemisphere Publishing Corporation) (Taylor & Francis)
- Lehner, L., Liebling, S. L., Palenzuela, C., et al. 2016, *Class. Quant. Grav.*, 33, 184002, doi: 10.1088/0264-9381/33/18/184002
- Lewin, W. H. G., van Paradijs, J., & Taam, R. E. 1993, *Space Sci. Rev.*, 62, 223, doi: 10.1007/BF00196124
- Li, B.-A. 2002, *Nucl. Phys. A*, 708, 365, doi: 10.1016/S0375-9474(02)01018-7
- Li, B.-A., Chen, L.-W., & Ko, C. M. 2008, *Phys. Rept.*, 464, 113, doi: 10.1016/j.physrep.2008.04.005
- Li, B.-A., & Ko, C. 1997, *Nucl. Phys. A*, 618, 498, doi: 10.1016/S0375-9474(97)00124-3
- Li, B.-A., Ramos, A., Verde, G., & Vidana, I. 2014, *Eur. Phys. J. A*, 50, 9, doi: 10.1140/epja/i2014-14009-x
- Li, J. J., Sedrakian, A., & Weber, F. 2018, *Phys. Lett.*, B783, 234, doi: 10.1016/j.physletb.2018.06.051
- Li, Z. H., & Schulze, H.-J. 2008, *Phys. Rev.*, C78, 028801, doi: 10.1103/PhysRevC.78.028801
- Li, Z.-X., Mao, G.-J., Zhuo, Y.-Z., & Greiner, W. 1997, *Phys. Rev. C*, 56, 1570, doi: 10.1103/PhysRevC.56.1570
- Lim, Y., & Holt, J. W. 2018, *Phys. Rev. Lett.*, 121, 062701, doi: 10.1103/PhysRevLett.121.062701
- Lim, Y., Hyun, C. H., Kwak, K., & Lee, C.-H. 2015, *Int. J. Mod. Phys. E*, 24, 1550100, doi: 10.1142/S0218301315501001
- Lindblom, L. 1984, *Astrophys. J.*, 278, 364, doi: 10.1086/161800
- . 1992, *Astrophys. J.*, 398, 569, doi: 10.1086/171882
- Lindblom, L. 1998, *Phys. Rev. D*, 58, 024008, doi: 10.1103/PhysRevD.58.024008

- 
- . 2010, *Phys. Rev.*, D82, 103011, doi: 10.1103/PhysRevD.82.103011
- . 2015, *AIP Conf. Proc.*, 1577, 153, doi: 10.1063/1.4861951
- Lipparini, E., & Stringari, S. 1989, *Physics Reports*, 175, 103, doi: 10.1016/0370-1573(89)90029-X
- Liu, G., & Barish, B. 1988, *Physical Review Letter*, 61, 271, doi: 10.1103/PhysRevLett.61.271
- Liu, X.-D., Osher, S., & Chan, T. 1994, *Journal of Computational Physics*, 115, 200, doi: <https://doi.org/10.1006/jcph.1994.1187>
- Lo, K. H., Coleman Miller, M., Bhattacharyya, S., & Lamb, F. K. 2013, *Astrophys. J.*, 776, 19, doi: 10.1088/0004-637X/776/1/19
- Lo, K. H., Miller, M. C., Bhattacharyya, S., & Lamb, F. K. 2018, *Astrophys. J.*, 854, 187, doi: 10.3847/1538-4357/aaa95b
- Loffler, F., et al. 2012, *Class. Quant. Grav.*, 29, 115001, doi: 10.1088/0264-9381/29/11/115001
- Logoteta, D., Vidana, I., & Bombaci, I. 2019, *Eur. Phys. J.*, A55, 207, doi: 10.1140/epja/i2019-12909-9
- Lommen, A. N., Zepka, A., Backer, D. C., et al. 2000, *Astrophys. J.*, 545, 1007, doi: 10.1086/317841
- Lonardoni, D., Lovato, A., Gandolfi, S., & Pederiva, F. 2015, *Phys. Rev. Lett.*, 114, 092301, doi: 10.1103/PhysRevLett.114.092301
- London, R. A., Taam, R. E., & Howard, W. M. 1986, *Astrophys. J.*, 306, 170, doi: 10.1086/164330
- Lopes, L. L., & Menezes, D. P. 2014, *Phys. Rev. C*, 89, 025805, doi: 10.1103/PhysRevC.89.025805
- Lourenço, O., Dutra, M., Lenzi, C. H., Flores, C. V., & Menezes, D. P. 2019, *Phys.Rev.C*, 99, 045202, doi: 10.1103/PhysRevC.99.045202
- Lugones, G. 2016, *Eur. Phys. J. A*, 52, 53, doi: 10.1140/epja/i2016-16053-x
- Lugones, G., Benvenuto, O., & Vucetich, H. 1994, *Phys. Rev. D*, 50, 6100, doi: 10.1103/PhysRevD.50.6100
- Lyons, N., O'Brien, P., Zhang, B., et al. 2010, *Mon. Not. Roy. Astron. Soc.*, 402, 705, doi: 10.1111/j.1365-2966.2009.15538.x

- 
- Lü, H.-J., Zhang, B., Lei, W.-H., Li, Y., & Lasky, P. D. 2015, *Astrophys. J.*, 805, 89, doi: 10.1088/0004-637X/805/2/89
- Ma, Y.-L., & Rho, M. 2019, *Phys. Rev. D*, 100, 114003, doi: 10.1103/PhysRevD.100.114003
- MacFadyen, A., & Woosley, S. E. 1999, *Astrophys. J.*, 524, 262, doi: 10.1086/307790
- Macher, J., & Schaffner-Bielich, J. 2005, *Eur. J. Phys.*, 26, 341, doi: 10.1088/0143-0807/26/3/003
- Mackay, D. J. C. 2003, *Information Theory, Inference and Learning Algorithms* (Cambridge University Press)
- Madej, J., Joss, P. C., & Rozanska, A. 2004, *The Astrophysical Journal*, 602, 904, doi: 10.1086/379761
- Madsen, J. 1988, *Phys. Rev. Lett.*, 61, 2909, doi: 10.1103/PhysRevLett.61.2909
- . 2002, *J. Phys. G*, 28, 1737, doi: 10.1088/0954-3899/28/7/327
- Madsen, J., Heiselberg, H., & Riisager, K. 1986, *Phys. Rev.*, D34, 2947, doi: 10.1103/PhysRevD.34.2947
- Maione, F. 2016, PhD thesis, University of Parma
- Maione, F., De Pietri, R., Feo, A., & Löffler, F. 2017, *Phys. Rev.*, D96, 063011, doi: 10.1103/PhysRevD.96.063011
- Maione, F., Pietri, R. D., Feo, A., & Löffler, F. 2016, *Classical and Quantum Gravity*, 33, 175009. <http://stacks.iop.org/0264-9381/33/i=17/a=175009>
- Majczyna, A., Madej, J., Joss, P., & Rozanska, A. 2005, *Astron. Astrophys.*, 430, 643, doi: 10.1051/0004-6361:20034048
- Malik, T., Alam, N., Fortin, M., et al. 2018, *Phys.Rev.C*, 98, 035804, doi: 10.1103/PhysRevC.98.035804
- Manchester, R. N., Hobbs, G. B., Teoh, A., & Hobbs, M. 2005, *Astron. J.*, 129, 1993, doi: 10.1086/428488
- Marczenko, M. 2020. <https://arxiv.org/abs/2005.14535>
- Margalit, B., & Metzger, B. D. 2017, *Astrophys. J.*, 850, L19, doi: 10.3847/2041-8213/aa991c

- 
- Margueron, J., Hoffmann Casali, R., & Gulminelli, F. 2018a, *Phys. Rev.*, C97, 025805, doi: 10.1103/PhysRevC.97.025805
- . 2018b, *Phys. Rev.*, C97, 025806, doi: 10.1103/PhysRevC.97.025806
- Maslov, K. A., Kolomeitsev, E. E., & Voskresensky, D. N. 2015, *Phys. Lett.*, B748, 369, doi: 10.1016/j.physletb.2015.07.032
- Masuda, K., Hatsuda, T., & Takatsuka, T. 2013, *Astrophys. J.*, 764, 12, doi: 10.1088/0004-637X/764/1/12
- McLerran, L., & Reddy, S. 2019, *Phys. Rev. Lett.*, 122, 122701, doi: 10.1103/PhysRevLett.122.122701
- Metzger, B. D., & Fernández, R. 2014, *Mon. Not. Roy. Astron. Soc.*, 441, 3444, doi: 10.1093/mnras/stu802
- Metzger, B. D., Giannios, D., Thompson, T. A., Bucciantini, N., & Quataert, E. 2011, *Mon. Not. Roy. Astron. Soc.*, 413, 2031, doi: 10.1111/j.1365-2966.2011.18280.x
- Metzger, B. D., Martinez-Pinedo, G., Darbha, S., et al. 2010, *Mon. Not. Roy. Astron. Soc.*, 406, 2650, doi: 10.1111/j.1365-2966.2010.16864.x
- Migdal, A. B., Chernoutsan, A. I., & Mishustin, I. N. 1979, *Physics Letters B*, 83, 158, doi: 10.1016/0370-2693(79)90674-9
- Millener, D. 2009, in 18th Indian-Summer School: Strangeness and Hypernuclei, doi: 10.1007/978-3-540-72039-3\_2
- Miller, M., & Lamb, F. K. 1998, *Astrophys. J. Lett.*, 499, L37, doi: 10.1086/311335
- Miller, M. C. 2013. <https://arxiv.org/abs/1312.0029>
- Miller, M. C., et al. 2019, *Astrophys. J. Lett.*, 887, L24, doi: 10.3847/2041-8213/ab50c5
- Mintz, B., Fraga, E., Pagliara, G., & Schaffner-Bielich, J. 2010, *Phys. Rev. D*, 81, 123012, doi: 10.1103/PhysRevD.81.123012
- Mishustin, I., Hanauske, M., Bhattacharyya, A., et al. 2003, *Phys. Lett. B*, 552, 1, doi: 10.1016/S0370-2693(02)03108-8
- Miyatsu, T., Katayama, T., & Saito, K. 2012, *Phys. Lett. B*, 709, 242, doi: 10.1016/j.physletb.2012.02.009
- Moesta, Mundim, Faber, et al. 2013, doi: 10.1088/0264-9381/31/1/015005

- 
- Möller, P., Nix, J. R., Myers, W. D., & Swiatecki, W. J. 1995, *Atomic Data and Nuclear Data Tables*, 59, 185, doi: 10.1006/adnd.1995.1002
- Morawski, F., & Bejger, M. 2020, *Astronomy & Astrophysical*, doi: 10.1051/0004-6361/202038130
- Morsink, S. M., & Leahy, D. A. 2011, *Astrophys. J.*, 726, 56, doi: 10.1088/0004-637X/726/1/56
- Morsink, S. M., Leahy, D. A., Cadeau, C., & Braga, J. 2007, *Astrophys. J.*, 663, 1244, doi: 10.1086/518648
- Most, E. R., Papenfort, L. J., Dexheimer, V., et al. 2019, *Phys. Rev. Lett.*, 122, 061101, doi: 10.1103/PhysRevLett.122.061101
- Most, E. R., Weih, L. R., Rezzolla, L., & Schaffner-Bielich, J. 2018, *Phys. Rev. Lett.*, 120, 261103, doi: 10.1103/PhysRevLett.120.261103
- Mueller, H., & Serot, B. D. 1996, *Nucl. Phys.*, A606, 508, doi: 10.1016/0375-9474(96)00187-X
- Mukherjee, A. 2009, *Phys. Rev. C*, 79, 045811, doi: 10.1103/PhysRevC.79.045811
- Muno, M. P., Ozel, F., & Chakrabarty, D. 2002, *Astrophys. J.*, 581, 550, doi: 10.1086/344152
- . 2003, *Astrophys. J.*, 595, 1066, doi: 10.1086/377447
- Möller, P., Myers, W. D., Sagawa, H., & Yoshida, S. 2012, *Phys. Rev. Lett.*, 108, 052501, doi: 10.1103/PhysRevLett.108.052501
- Mösta, P., Mundim, B. C., Faber, J. A., et al. 2014, *Classical and Quantum Gravity*, 31, 015005. <http://stacks.iop.org/0264-9381/31/i=1/a=015005>
- Nakamura, K., Horie, H., Takahashi, T., & Tanimori, T. 1985, *Phys. Lett. B*, 161, 417, doi: 10.1016/0370-2693(85)90790-7
- Nakamura, S., Sato, T., Lee, T.-S., Szczerbinska, B., & Kubodera, K. 2010, *Phys. Rev. C*, 81, 035502, doi: 10.1103/PhysRevC.81.035502
- Nakamura, T., Oohara, K., & Kojima, Y. 1987, *Progress of Theoretical Physics Supplement*, 90, 1, doi: 10.1143/PTPS.90.1
- Nakano, H., Healy, J., Lousto, C. O., & Zlochower, Y. 2015, *Phys. Rev. D*, 91, 104022, doi: 10.1103/PhysRevD.91.104022

- 
- Nambu, Y., & Jona-Lasinio, G. 1961, *Physical Review*, 122, 345, doi: 10.1103/PhysRev.122.345
- Nandi, R., & Char, P. 2018, *Astrophys. J.*, 857, 12, doi: 10.3847/1538-4357/aab78c
- Nandi, R., Char, P., & Pal, S. 2019, *Phys.Rev.C*, 99, 052802, doi: 10.1103/PhysRevC.99.052802
- Nath, N., Strohmayer, T. E., & Swank, J. H. 2002, *Astrophys. J.*, 564, 353, doi: 10.1086/324132
- Negreiros, R., Tolos, L., Centelles, M., Ramos, A., & Dexheimer, V. 2018, *Astrophys. J.*, 863, 104, doi: 10.3847/1538-4357/aad049
- Newman, E., & Penrose, R. 1962, *Journal of Mathematical Physics*, 3, 566, doi: 10.1063/1.1724257
- Nicholl, M., et al. 2017, *Astrophys. J.*, 848, L18, doi: 10.3847/2041-8213/aa9029
- Niebergal, B., Ouyed, R., & Jaikumar, P. 2010, *Phys. Rev.*, C82, 062801, doi: 10.1103/PhysRevC.82.062801
- Nishizaki, S., Takatsuka, T., & Yamamoto, Y. 2001, *Prog. Theor. Phys.*, 105, 607, doi: 10.1143/PTP.105.607
- Nättilä, J., Miller, M. C., Steiner, A. W., et al. 2017, *Astron. Astrophys.*, 608, A31, doi: 10.1051/0004-6361/201731082
- Nättilä, J., & Pihajoki, P. 2018, *Astron. Astrophys.*, 615, A50, doi: 10.1051/0004-6361/201630261
- Nättilä, J., Steiner, A., Kajava, J., Suleimanov, V., & Poutanen, J. 2016, *Astron. Astrophys.*, 591, A25, doi: 10.1051/0004-6361/201527416
- O'Connell, J., & Sealock, R. 1990, *Phys. Rev. C*, 42, 2290, doi: 10.1103/PhysRevC.42.2290
- Oechslin, R., Janka, H.-T., & Marek, A. 2007, *Astron. Astrophys.*, 467, 395, doi: 10.1051/0004-6361:20066682
- Oertel, M., Hempel, M., Klähn, T., & Typel, S. 2017, *Rev. Mod. Phys.*, 89, 015007, doi: 10.1103/RevModPhys.89.015007
- Oertel, M., Providência, C., Gulminelli, F., & Raduta, A. R. 2015, *J. Phys. G*, 42, 075202, doi: 10.1088/0954-3899/42/7/075202

- 
- Ono, A., Danielewicz, P., Friedman, W., Lynch, W., & Tsang, M. 2003, *Phys. Rev. C*, 68, 051601, doi: 10.1103/PhysRevC.68.051601
- Ono, A., Horiuchi, H., Maruyama, T., & Ohnishi, A. 1992, *Prog. Theor. Phys.*, 87, 1185, doi: 10.1143/PTP.87.1185
- Oppenheimer, J., & Volkoff, G. 1939, *Phys. Rev.*, 55, 374, doi: 10.1103/PhysRev.55.374
- Oset, E., & Salcedo, L. 1987, *Nucl. Phys. A*, 468, 631, doi: 10.1016/0375-9474(87)90185-0
- Ozel, F. 2006, *Nature*, 441, 1115, doi: 10.1038/nature04858
- . 2013, *Rept. Prog. Phys.*, 76, 016901, doi: 10.1088/0034-4885/76/1/016901
- Ozel, F., Baym, G., & Guver, T. 2010, *Phys. Rev. D*, 82, 101301, doi: 10.1103/PhysRevD.82.101301
- Özel, F., & Freire, P. 2016, *Ann. Rev. Astron. Astrophys.*, 54, 401, doi: 10.1146/annurev-astro-081915-023322
- Ozel, F., Gould, A., & Guver, T. 2012a, *Astrophys. J.*, 748, 5, doi: 10.1088/0004-637X/748/1/5
- Ozel, F., & Psaltis, D. 2009, *Phys. Rev.*, D80, 103003, doi: 10.1103/PhysRevD.80.103003
- Özel, F., Psaltis, D., Guver, T., et al. 2016, *Astrophys. J.*, 820, 28, doi: 10.3847/0004-637X/820/1/28
- Ozel, F., Psaltis, D., Narayan, R., & Villarreal, A. S. 2012b, *Astrophys. J.*, 757, 55, doi: 10.1088/0004-637X/757/1/55
- Paar, N., Moustakidis, C. C., Marketin, T., Vretenar, D., & Lalazissis, G. 2014, *Phys. Rev. C*, 90, 011304, doi: 10.1103/PhysRevC.90.011304
- Pagliara, G., Herzog, M., & Röpke, F. K. 2013, *Phys. Rev.*, D87, 103007, doi: 10.1103/PhysRevD.87.103007
- Pal, S., Hanauske, M., Zakout, I., Stoecker, H., & Greiner, W. 1999, *Phys. Rev. C*, 60, 015802, doi: 10.1103/PhysRevC.60.015802
- Palenzuela, C., Liebling, S. L., Neilsen, D., et al. 2015, *Phys. Rev.*, D92, 044045, doi: 10.1103/PhysRevD.92.044045
- Pandharipande, V., Pethick, C., & Thorsson, V. 1995, *Phys. Rev. Lett.*, 75, 4567, doi: 10.1103/PhysRevLett.75.4567

- 
- Paulucci, L., & Horvath, J. E. 2014, *Phys. Lett.*, B733, 164, doi: 10.1016/j.physletb.2014.04.036
- Paulucci, L., Horvath, J. E., & Benvenuto, O. 2017, *Int. J. Mod. Phys. Conf. Ser.*, 45, 1760042, doi: 10.1142/S2010194517600424
- Pechenick, K. R., Ftaclas, C., & Cohen, J. M. 1983, *Astrophys. J.*, 274, 846, doi: 10.1086/161498
- Pedregosa, F., Varoquaux, G., Gramfort, A., et al. 2011, *Journal of machine learning research*, 12, 2825
- Perego, A., Radice, D., & Bernuzzi, S. 2017, *Astrophys. J.*, 850, L37, doi: 10.3847/2041-8213/aa9ab9
- Perego, A., Rosswog, S., Cabezón, R. M., et al. 2014, *Mon. Not. Roy. Astron. Soc.*, 443, 3134, doi: 10.1093/mnras/stu1352
- Perillo Isaac, M., et al. 1998, *Phys. Rev. Lett.*, 81, 2416, doi: 10.1103/PhysRevLett.81.2416
- Peterson, C., & Rognvaldsson, T. 1991, in 1991 CERN School of Computing, 0113–170
- Pian, E., et al. 2017, *Nature*, 551, 67, doi: 10.1038/nature24298
- Piekarewicz, J. 2004, *Phys. Rev. C*, 69, 041301, doi: 10.1103/PhysRevC.69.041301
- Piekarewicz, J., Agrawal, B., Colo, G., et al. 2012, *Phys. Rev. C*, 85, 041302, doi: 10.1103/PhysRevC.85.041302
- Pili, A. G., Bucciantini, N., Drago, A., Pagliara, G., & Del Zanna, L. 2016, *Mon. Not. Roy. Astron. Soc.*, 462, L26, doi: 10.1093/mnrasl/slw115
- Postnikov, S., Prakash, M., & Lattimer, J. M. 2010, *Phys. Rev.*, D82, 024016, doi: 10.1103/PhysRevD.82.024016
- Potekhin, A. 2014, *Phys. Usp.*, 57, 735, doi: 10.3367/UFNe.0184.201408a.0793
- Poutanen, J., & Beloborodov, A. M. 2006, *Mon. Not. Roy. Astron. Soc.*, 373, 836, doi: 10.1111/j.1365-2966.2006.11088.x
- Poutanen, J., & Gierlinski, M. 2003, *Mon. Not. Roy. Astron. Soc.*, 343, 1301, doi: 10.1046/j.1365-8711.2003.06773.x
- Poutanen, J., Nätttilä, J., Kajava, J. J., et al. 2014, *Mon. Not. Roy. Astron. Soc.*, 442, 3777, doi: 10.1093/mnras/stu1139

- 
- Press, W. H., Flannery, B. P., Teukolsky, S., & Vetterling, W. T. 2007, *Numerical recipes, The art of scientific computing* (Cambridge University Press)
- Price, P. B., Guo, S. L., Ahlen, S. P., & Fleischer, R. L. 1984, *Physical Review Letter*, 52, 1265, doi: 10.1103/PhysRevLett.52.1265
- Providência, C., & Rabhi, A. 2013, *Physical Review C*, 87, 055801, doi: 10.1103/PhysRevC.87.055801
- Psaltis, D., & Chakrabarty, D. 1999, *Astrophys. J.*, 521, 332, doi: 10.1086/307525
- Psaltis, D., Özel, F., & DeDeo, S. 2000, *Astrophys. J.*, 544, 390, doi: 10.1086/317208
- Psaltis, D., & Özel, F. 2014, *Astrophys. J.*, 792, 87, doi: 10.1088/0004-637X/792/2/87
- Radice, D., Galeazzi, F., Lippuner, J., et al. 2016, *Mon. Not. Roy. Astron. Soc.*, 460, 3255, doi: 10.1093/mnras/stw1227
- Radice, D., Perego, A., Hotokezaka, K., et al. 2018a, *Astrophys. J.*, 869, 130, doi: 10.3847/1538-4357/aaf054
- Radice, D., Perego, A., Zappa, F., & Bernuzzi, S. 2018b, *Astrophys. J.*, 852, L29, doi: 10.3847/2041-8213/aaa402
- Raduta, A. R., Gulminelli, F., & Oertel, M. 2014. <https://arxiv.org/abs/1406.0395>
- Raithel, C. A., Özel, F., & Psaltis, D. 2016, *Astrophys. J.*, 831, 44, doi: 10.3847/0004-637X/831/1/44
- Raithel, C. A., & Özel, F. 2019, *Astrophys. J.*, 885, 121, doi: 10.3847/1538-4357/ab48e6
- Raithel, C. A., Özel, F., & Psaltis, D. 2017, *Astrophys. J.*, 844, 156, doi: 10.3847/1538-4357/aa7a5a
- Rappold, C., et al. 2013, *Nucl. Phys. A*, 913, 170, doi: 10.1016/j.nuclphysa.2013.05.019
- Rawls, M. L., Orosz, J. A., McClintock, J. E., et al. 2011, *Astrophys. J.*, 730, 25, doi: 10.1088/0004-637X/730/1/25
- Ray, L. 1979, *Phys. Rev. C*, 19, 1855, doi: 10.1103/PhysRevC.20.1212
- Ray, L., & Hodgson, P. 1979, *Phys. Rev. C*, 20, 2403, doi: 10.1103/PhysRevC.20.2403

- 
- Read, J. S., Lackey, B. D., Owen, B. J., & Friedman, J. L. 2009, *Phys. Rev.*, D79, 124032, doi: 10.1103/PhysRevD.79.124032
- Reed, B., & Horowitz, C. 2020, *Phys. Rev. C*, 101, 045803, doi: 10.1103/PhysRevC.101.045803
- Reinhard, P.-G., & Nazarewicz, W. 2010, *Phys. Rev. C*, 81, 051303, doi: 10.1103/PhysRevC.81.051303
- Reisdorf, W., et al. 2012, *Nucl. Phys. A*, 876, 1, doi: 10.1016/j.nuclphysa.2011.12.006
- Rezzolla, L., Baiotti, L., Giacomazzo, B., Link, D., & Font, J. A. 2010a, *Class. Quant. Grav.*, 27, 114105, doi: 10.1088/0264-9381/27/11/114105
- . 2010b, *Classical and Quantum Gravity*, 27, 114105, doi: 10.1088/0264-9381/27/11/114105
- Rezzolla, L., Giacomazzo, B., Baiotti, L., et al. 2011, *Astrophys. J.*, 732, L6, doi: 10.1088/2041-8205/732/1/L6
- Rezzolla, L., & Kumar, P. 2015, *Astrophys. J.*, 802, 95, doi: 10.1088/0004-637X/802/2/95
- Rezzolla, L., Most, E. R., & Weih, L. R. 2018, *Astrophys. J.*, 852, L25, doi: 10.3847/2041-8213/aaa401
- Rezzolla, Z. 2013, *Relativistic hydrodynamics*, 1st edn. (Oxford, university press)
- Rhoades, Clifford E., J., & Ruffini, R. 1974, *Phys. Rev. Lett.*, 32, 324, doi: 10.1103/PhysRevLett.32.324
- Rijken, T. A., Nagels, M. M., & Yamamoto, Y. 2010, *Nuclear Physics A*, 835, 160, doi: 10.1016/j.nuclphysa.2010.01.189
- Rikovska-Stone, J., Guichon, P. A., Matevosyan, H. H., & Thomas, A. W. 2007, *Nucl. Phys. A*, 792, 341, doi: 10.1016/j.nuclphysa.2007.05.011
- Riley, T. E., et al. 2019, *Astrophys. J. Lett.*, 887, L21, doi: 10.3847/2041-8213/ab481c
- Riley, T. E., Watts, A. L., Bogdanov, S., et al. 2019, *A NICER View of PSR J0030+0451: Nested Samples for Millisecond Pulsar Parameter Estimation*, Zenodo, doi: 10.5281/zenodo.3386449
- Roberts, L. F., Kasen, D., Lee, W. H., & Ramirez-Ruiz, E. 2011, *Astrophys. J.*, 736, L21, doi: 10.1088/2041-8205/736/1/L21

- 
- Roberts, L. F., Woosley, S. E., & Hoffman, R. D. 2010, *Astrophys. J.*, 722, 954, doi: 10.1088/0004-637X/722/1/954
- Roberts, M. S. E., McLaughlin, M. A., Gentile, P. A., et al. 2015, in . <https://arxiv.org/abs/1502.07208>
- Roca-Maza, X., Centelles, M., Vinas, X., & Warda, M. 2011, *Phys. Rev. Lett.*, 106, 252501, doi: 10.1103/PhysRevLett.106.252501
- Roca-Maza, X., Centelles, M., Viñas, X., et al. 2013, *Phys. Rev. C*, 88, 024316, doi: 10.1103/PhysRevC.88.024316
- Romani, R. W., Filippenko, A. V., Silverman, J. M., et al. 2012, *Astrophys. J. Lett.*, 760, L36, doi: 10.1088/2041-8205/760/2/L36
- Rowlinson, A., O'Brien, P. T., Metzger, B. D., Tanvir, N. R., & Levan, A. J. 2013, *Mon. Not. Roy. Astron. Soc.*, 430, 1061, doi: 10.1093/mnras/sts683
- Ruiz, M., Lang, R. N., Paschalidis, V., & Shapiro, S. L. 2016, *Astrophys. J. Lett.*, 824, L6, doi: 10.3847/2041-8205/824/1/L6
- Ruiz, M., & Shapiro, S. L. 2017, *Phys. Rev.*, D96, 084063, doi: 10.1103/PhysRevD.96.084063
- Ruiz, M., Shapiro, S. L., & Tsokaros, A. 2018, *Phys. Rev.*, D97, 021501, doi: 10.1103/PhysRevD.97.021501
- Rumelhart, D. E., & McClelland, J. L. 1986
- Runge, C. 1895, *Mathematische Annalen*, 46, 167, doi: 10.1007/BF01446807
- Russotto, P., Cozma, M., Fevre, A., et al. 2014, *Eur. Phys. J. A*, 50, 38, doi: 10.1140/epja/i2014-14038-5
- Rutledge, R. E., Bildsten, L., Brown, E. F., Pavlov, G. G., & Zavlin, V. E. 2001, *Astrophys. J.*, 551, 921, doi: 10.1086/320247
- Rybicki, G. B., Heinke, C. O., Narayan, R., & Grindlay, J. E. 2006, *Astrophys. J.*, 644, 1090, doi: 10.1086/503701
- Sagert, I., Fischer, T., Hempel, M., et al. 2009, *Phys. Rev. Lett.*, 102, 081101, doi: 10.1103/PhysRevLett.102.081101
- Sagert, I., Tolos, L., Chatterjee, D., Schaffner-Bielich, J., & Sturm, C. 2012, *Phys. Rev.*, C86, 045802, doi: 10.1103/PhysRevC.86.045802

- 
- Sammarruca, F. 2009, *Phys. Rev. C*, 79, 034301, doi: 10.1103/PhysRevC.79.034301
- Schaeffer, R., Zdunik, L., & Haensel, P. 1983, *Astronomy & Astrophysics*, 126, 121
- Schaffner, J. 1996, in *International Conference on Nuclear Physics at the Turn of Millennium: Structure of Vacuum and Elementary Matter*, 278–285. <https://arxiv.org/abs/nucl-th/9605010>
- Schaffner, J., Dover, C. B., Gal, A., Greiner, C., & Stoecker, H. 1993, *Phys. Rev. Lett.*, 71, 1328, doi: 10.1103/PhysRevLett.71.1328
- Schaffner, J., & Mishustin, I. N. 1996, *Phys. Rev. C*, 53, 1416, doi: 10.1103/PhysRevC.53.1416
- Schaffner-Bielich, J., Hanauske, M., Stoecker, H., & Greiner, W. 2002, *Phys. Rev. Lett.*, 89, 171101, doi: 10.1103/PhysRevLett.89.171101
- Schertler, K., Greiner, C., Schaffner-Bielich, J., & Thoma, M. H. 2000, *Nucl. Phys.*, A677, 463, doi: 10.1016/S0375-9474(00)00305-5
- Schramm, S., Dexheimer, V., Negreiros, R., Steinheimer, J., & Schürhoff, T. 2013. <https://arxiv.org/abs/1310.5804>
- Schramm, S., Negreiros, R., Steinheimer, J., Schurhoff, T., & Dexheimer, V. 2012, *Acta Phys. Polon. B*, 43, 749, doi: 10.5506/APhysPolB.43.749
- Schramm, S., & Zschesche, D. 2003, *J. Phys. G*, 29, 531, doi: 10.1088/0954-3899/29/3/307
- Schulze, H., Baldo, M., Lombardo, U., Cugnon, J., & Lejeune, A. 1998, *Phys. Rev. C*, 57, 704, doi: 10.1103/PhysRevC.57.704
- Schulze, H., Lejeune, A., Cugnon, J., Baldo, M., & Lombardo, U. 1995, *Phys. Lett. B*, 355, 21, doi: 10.1016/0370-2693(95)00665-8
- Schulze, H.-J., Polls, A., Ramos, A., & Vidana, I. 2006, *Phys. Rev. C*, 73, 058801, doi: 10.1103/PhysRevC.73.058801
- Schulze, H.-J., & Rijken, T. 2011, *Phys. Rev. C*, 84, 035801, doi: 10.1103/PhysRevC.84.035801
- Schürhoff, T., Schramm, S., & Dexheimer, V. 2010, *Astrophys. J.*, 724, L74, doi: 10.1088/2041-8205/724/1/L74
- Seidov, Z. F. 1971, *Soviet Astronomy*, 15, 347

- 
- Sekiguchi, Y., Kiuchi, K., Kyutoku, K., & Shibata, M. 2011, *Phys. Rev. Lett.*, 107, 211101, doi: 10.1103/PhysRevLett.107.211101
- . 2015a, *Phys. Rev.*, D91, 064059, doi: 10.1103/PhysRevD.91.064059
- . 2015b, *Phys. Rev. D*, 91, 064059, doi: 10.1103/PhysRevD.91.064059
- Sekiguchi, Y., Kiuchi, K., Kyutoku, K., Shibata, M., & Taniguchi, K. 2016a, *Phys. Rev.*, D93, 124046, doi: 10.1103/PhysRevD.93.124046
- . 2016b, *Phys. Rev. D*, 93, 124046, doi: 10.1103/PhysRevD.93.124046
- Shapiro, I. I. 1964, *Phys. Rev. Lett.*, 13, 789, doi: 10.1103/PhysRevLett.13.789
- Shen, H., Toki, H., Oyamatsu, K., & Sumiyoshi, K. 1998, *Nucl. Phys.*, A637, 435, doi: 10.1016/S0375-9474(98)00236-X
- Shetty, D., Yennello, S., Botvina, A., et al. 2004, *Phys. Rev. C*, 70, 011601, doi: 10.1103/PhysRevC.70.011601
- Shibata, M., Fujibayashi, S., Hotokezaka, K., et al. 2017, *Phys. Rev.*, D96, 123012, doi: 10.1103/PhysRevD.96.123012
- Shibata, M., & Nakamura, T. 1995, *Phys. Rev. D*, 52, 5428, doi: 10.1103/PhysRevD.52.5428
- Shibata, M., & Taniguchi, K. 2006, *Phys. Rev.*, D73, 064027, doi: 10.1103/PhysRevD.73.064027
- Shibata, M., & Uryu, K. 2002, *Prog. Theor. Phys.*, 107, 265, doi: 10.1143/PTP.107.265
- Shlomo, S., Kolomietz, V. M., & Colò, G. 2006, *European Physical Journal A*, 30, 23, doi: 10.1140/epja/i2006-10100-3
- Siegel, D. M. 2019, *Eur. Phys. J. A*, 55, 203, doi: 10.1140/epja/i2019-12888-9
- Siegel, D. M., & Metzger, B. D. 2017, *Phys. Rev. Lett.*, 119, 231102, doi: 10.1103/PhysRevLett.119.231102
- . 2018, *Astrophys. J.*, 858, 52, doi: 10.3847/1538-4357/aabaec
- Sivia, S. 2006, *Data analysis : a Bayesian tutorial* (Oxford University Press)
- Sotani, H., Iida, K., Oyamatsu, K., & Ohnishi, A. 2014, *PTEP*, 2014, 051E01, doi: 10.1093/ptep/ptu052
- Stairs, I. H. 2003, *Living Rev. Rel.*, 6, 5, doi: 10.12942/lrr-2003-5

- 
- Steiner, A., & Gandolfi, S. 2012, *Phys. Rev. Lett.*, 108, 081102, doi: 10.1103/PhysRevLett.108.081102
- Steiner, A. W., Gandolfi, S., Fattoyev, F. J., & Newton, W. G. 2015, *Phys. Rev. C*, 91, 015804, doi: 10.1103/PhysRevC.91.015804
- Steiner, A. W., Heinke, C. O., Bogdanov, S., et al. 2018, *Mon. Not. Roy. Astron. Soc.*, 476, 421, doi: 10.1093/mnras/sty215
- Steiner, A. W., Hempel, M., & Fischer, T. 2013a, *Astrophys. J.*, 774, 17, doi: 10.1088/0004-637X/774/1/17
- Steiner, A. W., Lattimer, J. M., & Brown, E. F. 2010, *Astrophys. J.*, 722, 33, doi: 10.1088/0004-637X/722/1/33
- . 2013b, *Astrophys. J. Lett.*, 765, L5, doi: 10.1088/2041-8205/765/1/L5
- . 2016, *Eur. Phys. J.*, A52, 18, doi: 10.1140/epja/i2016-16018-1
- Steiner, A. W., Prakash, M., Lattimer, J. M., & Ellis, P. J. 2005, *Phys. Rept.*, 411, 325, doi: 10.1016/j.physrep.2005.02.004
- Stergioulas, N. 2003, *Living Rev. Rel.*, 6, 3, doi: 10.12942/lrr-2003-3
- Stergioulas, N., & Friedman, J. 1995, *Astrophys. J.*, 444, 306, doi: 10.1086/175605
- Stone, J., Stone, N., & Moszkowski, S. 2014, *Phys. Rev. C*, 89, 044316, doi: 10.1103/PhysRevC.89.044316
- Stratta, G., et al. 2017, in . <https://arxiv.org/abs/1712.08153>
- Strobel, K., Schaab, C., & Weigel, M. K. 1999, *Astron. Astrophys.*, 350, 497. <https://arxiv.org/abs/astro-ph/9908132>
- Strohmayer, T. E., Zhang, W., & Swank, J. H. 1997, *Astrophys. J. Lett.*, 487, L77, doi: 10.1086/310880
- Strohmayer, T. E., Zhang, W., Swank, J. H., et al. 1996, *Astrophys. J. Lett.*, 469, L9, doi: 10.1086/310261
- Sturm, C. T., et al. 2001, *Phys. Rev. Lett.*, 86, 39, doi: 10.1103/PhysRevLett.86.39
- Sulaksono, A., & Agrawal, B. 2012, *Nucl. Phys. A*, 895, 44, doi: 10.1016/j.nuclphysa.2012.09.006
- Suleimanov, V., Poutanen, J., & Werner, K. 2011, *Astron. Astrophys.*, 527, A139, doi: 10.1051/0004-6361/201015845

- 
- . 2012, *Astron. Astrophys.*, 545, A120, doi: 10.1051/0004-6361/201219480
- Sztajno, M., Fujimoto, M. Y., van Paradijs, J., et al. 1987, *Monthly Notices of the Royal Astronomical Society*, 226, 39, doi: 10.1093/mnras/226.1.39
- Takami, K., Rezzolla, L., & Baiotti, L. 2014, *Phys. Rev. Lett.*, 113, 091104, doi: 10.1103/PhysRevLett.113.091104
- . 2015, *Phys. Rev.*, D91, 064001, doi: 10.1103/PhysRevD.91.064001
- Takatsuka, N., & Yamamoto. 2002, *The European Physical Journal, A*, 13, doi: 10.1007/s10050-002-8744-y
- Takatsuka, T., Nishizaki, S., & Tamagaki, R. 2008, *Prog. Theor. Phys. Suppl.*, 174, 80, doi: 10.1143/PTPS.174.80
- Takátsy, J., & Kovács, P. 2020, *Phys. Rev. D*, 102, 028501, doi: 10.1103/PhysRevD.102.028501
- Tamii, A., von Neumann-Cosel, P., & Poltoratska, I. 2014, *Eur. Phys. J. A*, 50, 28, doi: 10.1140/epja/i2014-14028-7
- Tamii, A., et al. 2011, *Phys. Rev. Lett.*, 107, 062502, doi: 10.1103/PhysRevLett.107.062502
- Tanaka, M., & Hotokezaka, K. 2013, *Astrophys. J.*, 775, 113, doi: 10.1088/0004-637X/775/2/113
- Tanaka, M., et al. 2018, *Astrophys. J.*, 852, 109, doi: 10.3847/1538-4357/aaa0cb
- Taranto, G., Baldo, M., & Burgio, G. 2013, *Phys. Rev. C*, 87, 045803, doi: 10.1103/PhysRevC.87.045803
- Tarbert, C., et al. 2014, *Phys. Rev. Lett.*, 112, 242502, doi: 10.1103/PhysRevLett.112.242502
- Taurines, A., Vasconcellos, C., Malheiro, M., & Chiapparini, M. 2000, *Mod. Phys. Lett. A*, 15, 1789, doi: 10.1142/S0217732300002024
- Tauris, T. M., et al. 2017, *Astrophys. J.*, 846, 170, doi: 10.3847/1538-4357/aa7e89
- Terashima, S., et al. 2008, *Phys. Rev. C*, 77, 024317, doi: 10.1103/PhysRevC.77.024317
- Tews, I., Carlson, J., Gandolfi, S., & Reddy, S. 2018, *Astrophys. J.*, 860, 149, doi: 10.3847/1538-4357/aac267

- 
- Thomas, A., Whittenbury, D., Carroll, J., Tsushima, K., & Stone, J. 2013, EPJ Web Conf., 63, 03004, doi: 10.1051/epjconf/20136303004
- Thorne, K. S. 1980, Rev. Mod. Phys., 52, 299, doi: 10.1103/RevModPhys.52.299
- Thorsson, V., Prakash, M., & Lattimer, J. M. 1994, Nucl. Phys. A, 572, 693, doi: 10.1016/0375-9474(94)90407-3
- Todd-Rutel, B., & Piekarewicz, J. 2005, Phys. Rev. Lett., 95, 122501, doi: 10.1103/PhysRevLett.95.122501
- Toki, H., Hirata, D., Sugahara, Y., Sumiyoshi, K., & Tanihata, I. 1995, Nucl. Phys., A588, c357, doi: 10.1016/0375-9474(95)00161-S
- Traversi, S., & Char, P. 2020. <https://arxiv.org/abs/2007.10239>
- Traversi, S., Char, P., & Pagliara, G. 2020, Astrophys. J., 897, 165, doi: 10.3847/1538-4357/ab99c1
- Trippa, L., Colo, G., & Vigezzi, E. 2008, Phys. Rev. C, 77, 061304, doi: 10.1103/PhysRevC.77.061304
- Trzcinska, A., Jastrzebski, J., Lubinski, P., et al. 2001, Phys. Rev. Lett., 87, 082501, doi: 10.1103/PhysRevLett.87.082501
- Tsang, M., Friedman, W., Gelbke, C., et al. 2001, Phys. Rev. Lett., 86, 5023, doi: 10.1103/PhysRevLett.86.5023
- Tsang, M., Zhang, Y., Danielewicz, P., et al. 2009, Phys. Rev. Lett., 102, 122701, doi: 10.1103/PhysRevLett.102.122701
- Tsang, M., et al. 2004, Phys. Rev. Lett., 92, 062701, doi: 10.1103/PhysRevLett.92.062701
- . 2012, Phys. Rev. C, 86, 015803, doi: 10.1103/PhysRevC.86.015803
- Typel, S., & Brown, B. A. 2001, Phys. Rev. C, 64, 027302, doi: 10.1103/PhysRevC.64.027302
- Typel, S., & Wolter, H. H. 1999, Nucl. Phys., A656, 331, doi: 10.1016/S0375-9474(99)00310-3
- Uechi, S. T., & Uechi, H. 2009, Adv. High Energy Phys., 2009, 640919, doi: 10.1155/2009/640919
- van Dalen, E., Colucci, G., & Sedrakian, A. 2014, Phys. Lett. B, 734, 383, doi: 10.1016/j.physletb.2014.06.002

- 
- van Kerkwijk, M., Breton, R., & Kulkarni, S. 2011, *Astrophys. J.*, 728, 95, doi: 10.1088/0004-637X/728/2/95
- van Paradijs, J. 1979, *Astrophys. J.*, 234, 609, doi: 10.1086/157535
- van Putten, M. H. P. M., Lee, G. M., Della Valle, M., Amati, L., & Levinson, A. 2014, *Mon. Not. Roy. Astron. Soc.*, 444, 58, doi: 10.1093/mnrasl/slu113
- Verbiest, J. P. W., Bailes, M., van Straten, W., et al. 2008, *Astrophys. J.*, 679, 675, doi: 10.1086/529576
- Vidana, I., Logoteta, D., Providencia, C., Polls, A., & Bombaci, I. 2011, *EPL*, 94, 11002, doi: 10.1209/0295-5075/94/11002
- Vidana, I., Polls, A., Ramos, A., Engvik, L., & Hjorth-Jensen, M. 2000a, *Phys. Rev. C*, 62, 035801, doi: 10.1103/PhysRevC.62.035801
- Vidana, I., Polls, A., Ramos, A., Hjorth-Jensen, M., & Stoks, V. 2000b, *Phys. Rev. C*, 61, 025802, doi: 10.1103/PhysRevC.61.025802
- Villar, V. A., Berger, E., Metzger, B. D., & Guillochon, J. 2017, *Astrophys. J.*, 849, 70, doi: 10.3847/1538-4357/aa8fcb
- Vincent, F. H., et al. 2018, *Astrophys. J.*, 855, 116, doi: 10.3847/1538-4357/aab0a3
- Walecka, J. 1974, *Annals Phys.*, 83, 491, doi: 10.1016/0003-4916(74)90208-5
- Wang, M., Audi, G., Wapstra, A., et al. 2012, *Chinese Physics C*, 36, 1603, doi: 10.1088/1674-1137/36/12/003
- Warda, M., Vinas, X., Roca-Maza, X., & Centelles, M. 2009, *Phys. Rev. C*, 80, 024316, doi: 10.1103/PhysRevC.80.024316
- Watts, A. L. 2012, *Ann. Rev. Astron. Astrophys.*, 50, 609, doi: 10.1146/annurev-astro-040312-132617
- Watts, A. L., & Reddy, S. 2007, *Mon. Not. Roy. Astron. Soc.*, 379, L63, doi: 10.1111/j.1745-3933.2007.00336.x
- Watts, A. L., et al. 2016, *Rev. Mod. Phys.*, 88, 021001, doi: 10.1103/RevModPhys.88.021001
- . 2019, *Sci.China Phys.Mech.Astron.*, 62, 29503, doi: 10.1007/s11433-017-9188-4
- Waxman, E., Ofek, E. O., Kushnir, D., & Gal-Yam, A. 2018, *Mon. Not. Roy. Astron. Soc.*, 481, 3423, doi: 10.1093/mnras/sty2441

- 
- Webb, N., & Barret, D. 2007, *Astrophys. J.*, 671, 727, doi: 10.1086/522877
- Weber, F. 2005, *Prog. Part. Nucl. Phys.*, 54, 193, doi: 10.1016/j.pnpnp.2004.07.001
- Weber, F., & Weigel, M. 1989, *Nucl. Phys. A*, 505, 779, doi: 10.1016/0375-9474(89)90041-9
- Wehrberger, K., Bedau, C., & Beck, F. 1989, *Nucl. Phys. A*, 504, 797, doi: 10.1016/0375-9474(89)90008-0
- Weih, L. R., Most, E. R., & Rezzolla, L. 2018, *Mon. Not. Roy. Astron. Soc.*, 473, L126, doi: 10.1093/mnrasl/slx178
- Weinberg, N., Miller, M., & Lamb, D. Q. 2001, *Astrophys. J.*, 546, 1098, doi: 10.1086/318279
- Weinberg, S. 1972, *Gravitation and cosmology* (New York: John Wiley and Sons)
- Weissenborn, S., Chatterjee, D., & Schaffner-Bielich, J. 2012a, *Phys. Rev.*, C85, 065802, doi: 10.1103/PhysRevC.85.065802, 10.1103/PhysRevC.90.019904
- . 2012b, *Nucl. Phys.*, A881, 62, doi: 10.1016/j.nuclphysa.2012.02.012
- . 2014, *Phys. Rev. C*, 90, 019904, doi: 10.1103/PhysRevC.90.019904
- Weissenborn, S., Sagert, I., Pagliara, G., Hempel, M., & Schaffner-Bielich, J. 2011, *Astrophys. J.*, 740, L14, doi: 10.1088/2041-8205/740/1/L14
- Welke, G., Prakash, M., Kuo, T., Das Gupta, S., & Gale, C. 1988, *Phys. Rev. C*, 38, 2101, doi: 10.1103/PhysRevC.38.2101
- Whittenbury, D., Carroll, J., Thomas, A., Tsushima, K., & Stone, J. 2012. <https://arxiv.org/abs/1204.2614>
- Wiktorowicz, G., Drago, A., Pagliara, G., & Popov, S. 2018, in *SN 1987A, Quark Phase Transition in Compact Objects and Multimessenger Astronomy*, 225–230, doi: 10.26119/SAO.2020.1.52363
- Wiktorowicz, G., Drago, A., Pagliara, G., & Popov, S. B. 2017, *Astrophys. J.*, 846, 163, doi: 10.3847/1538-4357/aa8629
- Wiktorowicz, G., Sobolewska, M., Lasota, J.-P., & Belczynski, K. 2017, *Astrophys. J.*, 846, 17, doi: 10.3847/1538-4357/aa821d
- Wiringa, R. B., Fiks, V., & Fabrocini, A. 1988, *Phys. Rev.*, C38, 1010, doi: 10.1103/PhysRevC.38.1010

- 
- Witten, E. 1984, *Phys. Rev.*, D30, 272, doi: 10.1103/PhysRevD.30.272
- Wolf, R., et al. 2013, *Phys. Rev. Lett.*, 110, 041101, doi: 10.1103/PhysRevLett.110.041101
- Wollaeger, R. T., Korobkin, O., Fontes, C. J., et al. 2018, *Mon. Not. Roy. Astron. Soc.*, 478, 3298, doi: 10.1093/mnras/sty1018
- Wolter, H., Prassa, V., Lalazisis, G., et al. 2009, *Prog. Part. Nucl. Phys.*, 62, 402, doi: 10.1016/j.pnpnp.2008.12.010
- Xiang, H., & Hua, G. 2003, *Phys. Rev. C*, 67, 038801, doi: 10.1103/PhysRevC.67.038801
- Xiao, Z.-G., Yong, G.-C., Chen, L.-W., et al. 2014, *Eur. Phys. J. A*, 50, 37, doi: 10.1140/epja/i2014-14037-6
- Xie, W.-J., & Li, B.-A. 2019, *Astrophys. J.*, 883, 174, doi: 10.3847/1538-4357/ab3f37
- Xu, H., et al. 2000, *Phys. Rev. Lett.*, 85, 716, doi: 10.1103/PhysRevLett.85.716
- Xu, J., Chen, L.-W., & Li, B.-A. 2015, *Phys. Rev. C*, 91, 014611, doi: 10.1103/PhysRevC.91.014611
- Yagi, K., & Yunes, N. 2016, *Class. Quant. Grav.*, 33, 13LT01, doi: 10.1088/0264-9381/33/13/13LT01
- . 2017, *Phys. Rept.*, 681, 1, doi: 10.1016/j.physrep.2017.03.002
- Yamamoto, Y., Furumoto, T., Yasutake, N., & Rijken, T. A. 2013, *Phys. Rev. C*, 88, 022801, doi: 10.1103/PhysRevC.88.022801
- . 2014, *Phys. Rev. C*, 90, 045805, doi: 10.1103/PhysRevC.90.045805
- . 2016, *Eur. Phys. J.*, A52, 19, doi: 10.1140/epja/i2016-16019-0
- Yong, G.-C., Li, B.-A., Chen, L.-W., & Zhang, X.-C. 2009, *Phys. Rev. C*, 80, 044608, doi: 10.1103/PhysRevC.80.044608
- Zabrodin, E. E., et al. 2009, *J. Phys. G*, 36, 064065, doi: 10.1088/0954-3899/36/6/064065
- Zacchi, A., Hanauske, M., & Schaffner-Bielich, J. 2016, *Phys. Rev. D*, 93, 065011, doi: 10.1103/PhysRevD.93.065011
- Zacchi, A., Tolos, L., & Schaffner-Bielich, J. 2017, *Phys. Rev. D*, 95, 103008, doi: 10.1103/PhysRevD.95.103008

- 
- Zavlin, V., Pavlov, G., & Shibanov, Y. 1996, *Astron. Astrophys.*, 315, 141. <https://arxiv.org/abs/astro-ph/9604072>
- Zavlin, V. E. 2006, *Astrophys. J.*, 638, 951, doi: 10.1086/449308
- . 2007, *Astrophys. Space Sci.*, 308, 297, doi: 10.1007/s10509-007-9297-y
- Zdunik, J., & Haensel, P. 2013, *Astron. Astrophys.*, 551, A61, doi: 10.1051/0004-6361/201220697
- Zdunik, J. L., Haensel, P., & Schaeffer, R. 1987, *Astronomy & Astrophysics*, 172, 95
- Zenihiro, J., et al. 2010, *Phys. Rev. C*, 82, 044611, doi: 10.1103/PhysRevC.82.044611
- Zhang, N.-B., & Li, B.-A. 2019, *J. Phys. G*, 46, 014002, doi: 10.1088/1361-6471/aaef54
- Zhang, Z., & Chen, L.-W. 2015, *Phys. Rev. C*, 92, 031301, doi: 10.1103/PhysRevC.92.031301

---

# *Acknowledgments*

First of all I would like to thank my supervisors Alessandro Drago and Giuseppe Pagliara for all the teachings, discussions and work done together. I also add an acknowledgment to Roberto De Pietri for his help and to Luciano Rezzolla for welcoming me to visit his group and giving me the opportunity to be part of and learn from a lively and intellectually dynamic environment. A special thought also goes to my two families; my parents for supporting me and for always giving me the freedom to make my choices and pursue my ambitions; and the second family that was born here in the Physics department, Prasanta Char, Krik Soufiane, Zhifu Feng, Mattia Soldani and the other guys from "Ping" for always making me feel at home and sharing with me the "joys and sorrows" of the Ph.D.. In particular, I thank Prasanta, who in addition to being my workmate has become a life partner for me: I will always carry with me all our philosophical discussions and our laughter, during dinners, walks on the walls and the unmissable afternoon tea break.

And finally, the biggest thanks goes to the most important person for me, Renato Martone for being my shoulder and my accomplice, but at the same time my support and my rock. Thank you for understanding me, listening to me and for every little gesture and daily attention, thank you for being able, in every situation, to always make me smile.

---

Vorrei in primo luogo ringraziare i miei supervisors Alessandro Drago e Giuseppe Pagliara per tutti gli insegnamenti, le discussioni ed il lavoro fatto insieme. Aggiungo inoltre un ringraziamento a Roberto De Pietri per l'aiuto e Luciano Rezzolla per avermi accolto in visita al suo gruppo ed avermi dato l'opportunità di confrontarmi e di imparare da un ambiente vivo ed intellettualmente dinamico.

Un pensiero speciale va inoltre alle mie due famiglie; i miei genitori per avermi sostenuta e per avermi dato, da sempre, la libertà di fare le mie scelte e perseguire le mie ambizioni; e

---

la seconda famiglia che è nata qui al dipartimento di Fisica, Prasanta Char, Krik Soufiane, Zhifu Feng, Mattia Soldani e gli altri ragazzi del "Ping" per avermi sempre fatta sentire a casa ed aver condiviso con me le "gioie e i dolori" del dottorato. In particolare ringrazio Prasanta, che oltre ad essere un compagno di lavoro è diventato per me un compagno di vita: porterò sempre con me tutte le nostre discussioni filosofiche e le nostre risate, durante cene, passeggiate sulle mura e l'immane pausa thè pomeridiana.

Ed infine il più grande ringraziamento va alla persona più importante per me, Renato Martone per essere stato la mia spalla e il mio complice, ma allo stesso tempo il mio sostegno e la mia roccia. Grazie per avermi capita, ascoltata e per ogni piccolo gesto ed attenzione quotidiana, grazie di riuscire, in ogni situazione, a strapparmi sempre un sorriso.